UNIVERSITY OF CRETE

DEPARTMENT OF CHEMISTRY

Doctoral Thesis

Development of Novel Atomic Mass Spectrometric Techniques for the Analysis of Single Particles and Single Cells

EMMANOUIL MAVRAKIS

2023

UNIVERSITY OF CRETE
DEPARTMENT OF CHEMISTRY

Doctoral Thesis

"Development of novel atomic mass spectrometric techniques for the analysis of single particles and single cells"

EMMANOUIL MAVRAKIS

Thesis Supervisor: Spiros A. Pergantis

HERAKLION 2023

«The implementation of the doctoral thesis was co-financed by Greece and the European Union (European Social Fund-ESF) through the Operational Programme «Human Resources Development, Education and Lifelong Learning» in the context of the Act "Enhancing Human Resources Research Potential by undertaking a Doctoral Research" Sub-action 2: IKY Scholarship Programme for PhD candidates in the Greek Universities».

ΠΑΝΕΠΙΣΤΗΜΙΟ ΚΡΗΤΗΣ
ΤΜΗΜΑ ΧΗΜΕΙΑΣ

ΔΙΔΑΚΤΟΡΙΚΗ ΔΙΑΤΡΙΒΗ

«Αναπτυξη νεων τεχνικων ατομικης φασματομετριας μαζας για την αναλυση
διακριτων σωματιδιων και κυτταρων»

ΜΑΥΡΑΚΗΣ ΕΜΜΑΝΟΥΗΛ

Υπεύθυνος Καθηγητής: Σπύρος Α. Περγαντής

ΗΡΑΚΛΕΙΟ 2023

«Η υλοποίηση της διδακτορικής διατριβής συγχρηματοδοτήθηκε από την Ελλάδα και την Ευρωπαϊκή Ένωση (Ευρωπαϊκό Κοινωνικό Ταμείο) μέσω του Επιχειρησιακού Προγράμματος «Ανάπτυξη Ανθρώπινου Δυναμικού, Εκπαίδευση και Δια Βίου Μάθηση», 2014-2020, στο πλαίσιο της Πράξης «Ενίσχυση του ανθρώπινου δυναμικού μέσω της υλοποίησης διδακτορικής έρευνας Υποδράση 2: Πρόγραμμα χορήγησης υποτροφιών ΙΚΥ σε υποψηφίους διδάκτορες των ΑΕΙ της Ελλάδας».

Ευρωπαϊκή Ένωση
Ευρωπαϊκό Κοινωνικό Ταμείο

Επιχειρησιακό Πρόγραμμα
Ανάπτυξη Ανθρώπινου Δυναμικού,
Εκπαίδευση και Διά Βίου Μάθηση
Με τη συγχρηματοδότηση της Ελλάδας και της Ευρωπαϊκής Ένωσης

ΕΣΠΑ 2014-2020
ανάπτυξη - εργασία - αλληλεγγύη

To my beloved people

Examination committee

Pergantis Spyridon

Professor of Chemistry, University of Crete

Lydakis – Simantiris Nikolaos

Professor of Chemistry, Hellenic Mediterranean University

Anglos Demetrios

Professor of Chemistry, University of Crete

Tsiotis Georgios

Professor of Chemistry, University of Crete

Bettmer Jörg

Professor of Chemistry, University of Oviedo

Spyros Apostolos

Associate Professor of Chemistry, University of Crete

Chatziioannou Chrysovalantou-Anastasia

Tenured Assistant Professor, University of Crete

Acknowledgments

Primarily, I would like to thank the University of Crete, which has hosted me throughout my bachelor and postgraduate studies, enabling me to become the scientist that I am today. I maintain deep appreciation for my supervisor and mentor Spiros Pergantis, professor of Analytical Chemistry in the University of Crete, who has hosted me in his research group since my first steps in Analytical Chemistry. He has been an inspiration to me ever since, and he will always have my gratitude for offering me challenges and opportunities to prove my worth in major research institutes and Analytical Chemistry conferences held internationally.

A major contributor to this dissertation and my academic progress has been professor Nikos Lydakis-Simantiris, who offered me immense expertise on several different approaches for cell manipulation, not to mention career advice and encouragement. Moreover, I would like to thank all the members of my examination committee who devoted their valuable time in reading and reviewing this dissertation, examining me and offering constructive feedback.

My academic progress would not have been possible without constructive collaboration. In this context, I would like to thank Leonidas Mavroudakis, Michail-Ioannis Chronakis, Dr. Roberto Álvarez-Fernández García, Dr. Ana Lores Padin, and professors Maria Maria Montes-Bayón and Jörg Bettmer. In addition, Daniel Rosenkratz, Fabian Kriegel, Jutta Tentschert and other scientists from the BfR institute in Berlin. Special thanks to Dr. Zenon Toprakcioglu, post-doc in the research group of Tuomas Knowles. With Zenon, I had an excellent collaboration in the field of microfluidic chip-based ICP-MS, and held constructive skype sessions on the future of this field. Moreover, I would like to thank Dr. Ioanna Kalatzi, who employed me to work on analytical projects related to metal determination in biological samples, and thus supported my phD studies.

I would like to stress on the importance of the people closest to me. My parents, Andreas and Ioanna, have always encouraged me to pursue my goals, and this phD dissertation is primarily devoted to the them. The rest of my family members, including my sister and grandmother, both named Eleni, also played their part during difficult times. This dissertation is also devoted to my friends, many of who we met and shared moments during my postgraduate studies. Last but not least, I devote this dissertation to my beloved Tenia, who raised my spirits when needed, and as an astonishing biochemist that she is, helped me in seeing solutions through the great conversations that we shared.

ABSTRACT

In response to the need for performing metal determination at the level of single particles and single cells, this dissertation reports on the development of advanced methods based on inductively-coupled plasma mass spectrometry (ICP-MS). Due to the evident advantages of microfluidics in manipulating volume-limited biological samples, including single cells/particles, emphasis is given on pairing microfluidic chips to ICP-MS. Structurally, this dissertation is comprised of 5 studies.

The first study concerns the development and application of single-cell (SC)-ICP-MS to determine the uptake of arsenate by individual *C. reinhardtii* cells, exposed to 12.5, 22.5 and 30 μg As mL^{-1}. Compared to conventional analytical schemes, SC-ICP-MS revealed the distribution of As among single cells. *C. reinhardtii* demonstrated heterogeneity with respect to As uptake, as evidenced by the broad As mass histograms that were fitted with a lognormal probability function. All exposure concentrations exhibited a similar most frequent As mass of 1.5-1.8 fg $cell^{-1}$, indicating a saturation mass reached by the majority of the cell population, while the lognormal mean As mass of 2.7-4.1 fg $cell^{-1}$ indicated that a significant portion of the cell population internalized higher amounts of arsenate. A significant cellular As amount was wall-bound, as evidenced by a 30% drop in the cellular As of washed cells.

The second study reports on the development of a data processing method (DP) that can be employed to analyze single nanoparticles (NPs) using single-particle (sp)-ICP-MS by means of μs dwell times. Herein, the developed (A) DP-^{75}μs-sp-ICP-MS is validated through comparisons with the benchmark (B) DP-5σ-^{10}ms-Syngistix™ Nano method, as well as by conducting silver (Ag) mass recovery experiments in seawater samples. Analysis of a reference 60 nm AgNP suspension showed excellent agreement between A and B in terms of NP peak area (38.8 and 37 counts for A and B, respectively) and transport efficiency (2.3 and 2.1 % for A and B, respectively). Analysis of seawater mesocosm tanks, spiked with 60 nm AgNPs, across a concentration range of 50-500 ng L^{-1}, yielded Ag mass recoveries of $83 \pm 22\%$ and $86 \pm 21\%$ for A and B, respectively. The applicability of DP-μs-sp-ICP-MS was demonstrated in a seawater mesocosm experiment, where Ag-containing NPs could be tracked at the early stages of formation.

In a third study, coupling of a microfluidic chip to ICP-MS was accomplished using a combination of commercially available components, including a pneumatic high-efficiency nebulizer and a spray chamber designed to allow for the addition of a laminar flow makeup gas. To demonstrate the efficiency of this coupling, standard dilution analysis (SDA) was

employed for the first time for chip-based ICP-MS. High average recoveries (97.4-100.1%) and low average relative standard deviations (2.9-4.8%) were achieved for the determined elements (Cd, Co, Pb, Cr) across several spiked matrices and certified reference materials, whereas only 140 µL of sample is required for SDA in triplicate or 40 µL for a single analysis.

The fourth study demonstrates, for the first time, the direct coupling of a chip-based supersonic microfluidic nebulizer (chip-µf-Neb) to ICP-MS. The system exhibited efficient operation at liquid flow rates as low as 0.5 µL min^{-1}, with minimum dead volumes, while sensitive metal isotope detection was evidenced by an attained indium (In) sensitivity of 40000 cps (µg $L^{-1})^{-1}$ at 10 µL min^{-1}. The system featured a transport efficiency of 46% for Ag nanoparticles. Finally, the capabilities for conducting single-cell analysis were demonstrated with the detection of ^{80}Se, ^{75}As and $^{31}P^{16}O$ in single *Chlamydomas reinhardtii* cells.

The fifth study reports on the use of inertial microfluidics for cell focusing and size-based sorting of cell populations prior to SC-ICP-MS detection. Microfluidic chips with spiral channels were operated at a range of Reynolds and Dean numbers, while multiple outlet channels allowed for collection of cell-enriched and cell-free samples. A high degree of cell focusing was achieved for *C. reinhardtii*, as 80% of the infused cells were collected from a single outlet. Individual sorting of BMDMS cells (diameter of 12 µm) and *C. reinhardtii* cells (diameter of 7 µm) at a De of 69.9 indicated that the 2 cell lines could be collected with 100% and 70% purity, respectively, when present in the same cell suspension; thus, equipping SC-ICP-MS with flow cytometry capabilities.

Keywords: inductively-coupled plasma mass spectrometry (ICP-MS), single-cell analysis, single-particle analysis, SC-ICP-MS, sp-ICP-MS, µs-sp-ICP-MS, microfluidics, standard dilution analysis, chip-based ICP-MS, supersonic microfluidic nebulizer, cell sorting, inertial microfluidics, spiral channels

Table of Contents

ABBREVIATIONS

a:	particle diameter or particle size (for a spherical particle)
AFM:	atomic force microscopy
Ag-b-NPs:	silver-based nanoparticles
Ag:	Silver
Ag_2S:	Silver sulfide
ANOVA:	analysis of variance
b:	Average background signal intensity
"*b* from 3σ-criterion (10ms)":	determination of b by applying a 3σ criterion on sp-ICP-MS data acquired using a 10 ms dwell time
"*b* from 3σ-criterion (75µs)":	determination of b by applying a 3σ criterion on sp-ICP-MS data acquired using a 75 µs dwell time
BMDMS:	Bone marrow-derived macrophages cells
BPEI:	branched polyethylenimine
C. reinhardtii:	*Chlamydomonas reinhardtii* cells
CeO:	Cerium oxide
chip-µf-Neb:	chip-based supersonic microfluidic nebulizer
CPE:	cloud-phase extraction
CPI:	Consumer Products Inventory
CRMs:	certified reference materials
CSP_s:	Coomasie stainable particles
CTCs:	Circulating tumor cells
cVSSI:	capillary vibrating sharp-edge spray ionization
De:	Dean number
De_c:	Critical Dean number
Diss. Ag:	dissolved Ag species
DLS:	dynamic light scattering
DP-µs-sp-ICP-MS:	data processing method for sp-ICP-MS analyses conducted using µs-scale dwell times

DP-^{75}µs-sp-ICP-MS: data processing method for sp-ICP-MS analyses conducted using a 75 µs dwell time

DP-5σ-^{10}ms-Syngistix™ Nano: data processing method of Syngistix™ Nano for sp-ICP-MS analysis conducted using a 10 ms dwell time

DP: data processing method

DRC: Dynamic reaction cell

Dwell time: the specified measurement interval in which a single intensity data point is recorded for an elemental isotope

D_h: Hydraulic diameter

$\frac{dv}{dy}$: Velocity gradient

EC50: Half-maximal effective concentration

EDTA Ethylenediaminetetraacetic acid

EOF: electro-osmotic flow

ESI-MS: Electrospray ionization mass spectrometry

FACS: fluorescence-activated flow cytometry

FFF: field flow fractionation

F_{dean}: Drag force due to Dean flow

f_{lift}: Coefficient of lift

F_{Shear}: Shear-gradient lift

F_{WL}: Wall-lift

GSH: glutathione

H: height

h/w: height-to-width or aspect ratio

HDX-MS: Hydrogen-deuterium exchange mass spectrometry

HEN: High-efficiency nebulizer

ICP-MS: inductively-coupled plasma mass spectrometry

ICP-OES: inductively coupled plasma optical emission spectroscopy

ICP-TOF-MS: inductively-coupled plasma time-of-flight mass spectrometry

In: Indium

IS: internal standard

K_{sp}: Solubility product constant

LC-MS: liquid chromatography mass spectrometry

LIF: laser-induced fluorescence

LODs: limits of detection

L_D: Limit of detection for Poisson-distributed data, serving as a peak detection threshold for DP-µs-sp-ICP-MS

L_I: Channel length required for particle or cell focusing

L_M: migration distance

λ: Length fraction

MCE: microchip capillary electrophoresis

MEMSs: micro-electro-mechanical systems

ms-sp-ICP-MS: single-particle ICP-MS using ms-scale dwell times

10 ms-sp-ICP-MS: single-particle ICP-MS analysis conducted using a 10ms dwell time

MSPME: magnetic solid phase microextraction

μ: fluid dynamic viscosity (Pa s)

µF: microfludic

µs-sp-ICP-MS: single-particle ICP-MS using µs-scale dwell times

75 µs-sp-ICP-MS single-particle ICP-MS analysis conducted using a 75µs dwell time

µs-sp-ICP-MS/MS: µs-sp-ICP-MS analysis using triple quadrupole inductively-coupled plasma mass spectrometry

µTAS: miniaturized chemical analysis system

NaCl: Sodium chloride

nanoESI: nanoelectrospray ionization

NOM: natural organic matter

NPs: nanoparticles

P-G: Poisson-Gaussian

PA: Peak Area

PCs: phytochelatines

PDMS: poly(dimethylsiloxane)

PEEK: polyetheretherketone

PFA: perfluoroalkoxy

PMMA: polymethyl methacrylate

PO: Phosphorus oxide

PrmIS: primary internal standard

PTFE: polytetrafluoroethylene

PVP: polyvinylpyrrolidone

$\boldsymbol{R}$**:** spiral radius of curvature

RBCs: Red blood cells

RCF: Relative centrifugal force

Re: Reynolds number

$\mathbf{R_f}$**:** Inertial force ratio

$\boldsymbol{R_p}$**:** Particle Reynolds number

$\boldsymbol{\rho}$**:** density (kg m^{-3})

S/B: signal-to-background ratio

SC-ICP-MS: single-cell inductively-coupled plasma mass spectrometry

SDA: standard dilution analysis

SecIS secondary internal standard

sp-ICP-MS: single-particle inductively-coupled plasma mass spectrometry

sp. PCC 6803: *Synechocystis sp. PCC 6803*

TE: transport efficiency

TEM: transmission electron microscopy

TPE: Thermoplastic elastomer

Trizma Tris(hydroxymethyl)aminomethane

$\boldsymbol{V_d}$**:** average dean velocity

$\boldsymbol{V_f}$**:** Volume fraction

$\boldsymbol{V_{max}}$**:** Maximum linear velocity (m s^{-1})

$\boldsymbol{V_p}$**:** Particle lateral migration velocity (m s^{-1})

WBCs: White blood cells

XPS: X-ray photoelectron spectra

1 Chapter 1. General Introduction-Motivation

Studies on single cells have demonstrated cellular heterogeneity, even within isogenic populations, in terms of size, gene expression and growth rate.[1,2] Therefore, bulk analysis of whole cell populations may be misleading in determining parameters of cellular response.[3] Such parameters may be the uptake and metabolism of metal species. Supposing a cellular system undergoing Pt drug treatment is found to have doubled its average Pt concentration, does it mean that all the cells have doubled their Pt concentration, or is it because 20% of the cells (possibly rare cells) have increased their Pt content 6-fold, while the 80% remains unaffected? The previous example serves to underscore the importance of studying metal uptake on a per cell basis.

The motivation for this dissertation is the development of advanced analytical techniques based on atomic mass spectrometry for the determination of metals and metalloids in individual particles, these either being single cells (SC) and/or individual metal-containing nanoparticles (NPs). The latter finding increasing use in daily commodities, such as cosmetics and textiles, and in turn causing concern with respect to their effects on aquatic ecosystems.[4] For the development of the methodologies presented in this dissertation, emphasis has been on the technical aspects of sampling of individual cells and particles into the ICP-MS detector, and development and application of appropriate data treatment methodologies (i.e. handling millions of raw MS data points) for accurate quantitation. Due to the evident capabilities of microfluidic devices for the manipulation of volume-limited samples of biological interest, including single cells,[5] novel ways to interface microfluidic chips to ICP-MS are established in order to conduct sensitive, accurate, and efficient analysis of samples, ranging from digested biological tissue and cell populations to single cells. Microfluidic chips have also been demonstrated to offer label-free size-based sorting of cells and particles, without the application of external forces.[6] This dissertation shows possibilities to employ spiral chips for size-based sorting of cells prior to single-cell metal analysis.

1.1 Literature

[1] H.N. Joensson, H. Andersson Svahn, Droplet microfluidics-A tool for single-cell analysis, Angew. Chemie - Int. Ed. 51 (2012) 12176–12192. https://doi.org/10.1002/anie.201200460.

[2] S.J. Altschuler, L.F. Wu, Cellular Heterogeneity: Do Differences Make a Difference?, Cell. (2010). https://doi.org/10.1016/j.cell.2010.04.033.

[3] -CELL ANALYSIS for Quantitative Biology, (n.d.).

[4] K. Flores, R.S. Turley, C. Valdes, Y. Ye, J. Cantu, J.A. Hernandez-Viezcas, J.G. Parsons, J.L. Gardea-Torresdey, Environmental applications and recent innovations in single particle inductively coupled plasma mass spectrometry (SP-ICP-MS), Appl. Spectrosc. Rev. 56 (2021) 1–26. https://doi.org/10.1080/05704928.2019.1694937.

[5] J. El-Ali, P.K. Sorger, K.F. Jensen, Cells on chips, Nature. 442 (2006) 403–411. https://doi.org/10.1038/nature05063.

[6] J. Zhang, S. Yan, D. Yuan, G. Alici, N.T. Nguyen, M. Ebrahimi Warkiani, W. Li, Fundamentals and applications of inertial microfluidics: A review, Lab Chip. 16 (2016) 10–34. https://doi.org/10.1039/c5lc01159k.

2 Chapter 2. Investigating the Uptake of Arsenate by *Chlamydomonas reinhardtii* Cells using Single Cell ICP-MS

2.1 Introduction

2.1.1 Chlamydomonas reinhardtii and arsenate uptake

Arsenic (As) is a metalloid that is universally distributed in aquatic ecosystems.[1] Although its concentration in fresh waters does not typically exceed 10 µg As L^{-1}, excessive concentrations above 50 µg As L^{-1} have been reported for groundwater in several countries, thus raising concerns for public health, especially for regions where a significant population consumes As contaminated water. In its greatest scale, this problem has been reported for the Bengal Basin in India.[2]

It has been suggested that algae can be used for arsenic remediation due to their high surface-to-volume ratio.[3] In this context, there is a need to study microalgae in the presence of arsenic so as to elucidate their tolerance, accumulation capacity, as well as their underlying mechanisms of tolerance to arsenic species. In natural waters, As occurs in two inorganic forms, that is, arsenite and arsenate, containing As^{3+} and As^{5+}, respectively. It has been postulated that that freshwater algae tend to uptake arsenate, reduce it to arsenite, and convert it to dimethyl-arsenic compounds. [4]

An algal cell line that has been studied with respect to its interaction with arsenate is *Chlamydomonas reinhardtii*, a unicellular eukaryotic green alga which has extensively been used as a model to study processes such as photosynthesis and respiration, as well as heavy metal homeostasis and tolerance of photosynthetic organisms.[5,6]. Under exposure to arsenate polluted medium, it has been reported that *C. reinhardtii* cells will uptake arsenate and continue to grow, provided that arsenate is present at sub-lethal concentrations.[7–10] This was demonstrated by Kobayashi et al who observed that although arsenate-exposed cells exhibited reduced growth relative to control cells across 5 days of cultivation, these cells finally reached the growth levels of controls even in the presence of 1 mM arsenate (corresponding to 75 µg As mL^{-1}).[8] Even though this exposure concentration is excessive, considering that a median 50% effective concentration (EC50) of 33.5 µg As mL^{-1} has been reported for *C. reinhardtii* cells,[7] it showed that cells could progressively increase their tolerance to arsenate. Growth and photosynthesis inhibition are toxic effects that are induced by the presence of arsenate.[8,11] For instance, Kobayashi et al reported almost complete inhibition of photosynthesis for cells exposed to 0.5 mM of

arsenate (corresponding to 37.5 μg As mL^{-1}).[8] However, when *C. reinhardtii* were exposed to 37.5 μg As mL^{-1} along with a cadmium (Cd) concentration of 5.6 μg Cd mL^{-1}, the initial 40% suppression of photosynthetic yield was partly recovered, reaching 75% of the photosynthetic yield of control cells. Thus, it was shown that arsenate toxicity was relieved in the presence of Cd, a finding which was related to increased levels of thiol-containing biomolecules such as glutathione (GSH) and phytochelatines (PCs). However, arsenate alone was not indicated to cause GSH and PC synthesis in *C. reinhardtii,* as is the case for other cells isolated from plant species.[8] Nevertheless, it has been shown that arsenate tends to be reduced to arsenite via various reductases, including glutathione.[10] Arsenate can enter cells through phosphate transporters due its structural similarity with phosphate, and thus the first step towards detoxification is its reduction to arsenite. [7,10,11] Competitive uptake of phosphate and arsenate has been evidenced by an order of magnitude higher arsenate accumulation in cells growing under phosphorus deprived conditions.[7] Speciation experiments of cells grown in arsenate over the course of 6-7 days have shown that 15-30% of the internalized arsenic was found as arsenite, with phosphorus deprived cells exhibiting the highest arsenate reduction rates.[7,10] On a subsequent step, arsenite can be transformed to dimethyl-arsenic species, as was shown for a mutant *C. reinhardtii* strain cultivated for 48 hours in the presence of arsenite.[9]

For all of these reported studies, conventional analytical schemes were used in order to determine As uptake by this unicellular photosynthetic green algae. These included acid digestion of large numbers of cells, followed by the use of an atomic spectrometric technique for As determination, i.e., atomic absorption spectrometry for total As detection.[7–9] The intracellular As content could be differentiated from the wall-bound As through cell washing steps, i.e. using phosphate buffers. These conventional methods allow for reporting cellular arsenic uptake values as As mass per dry cell weight or, if the number of digested cells is known, mean As mass per cell. However, this mean As mass per cell may not be representative of how As is distributed in the cell population, especially if the analyzed cell population has a broad As distribution, as implied by recent studies on the exhibited heterogeneity of cell populations. Thus, techniques that can report As content per cell are required in order to examine uptake on a per cell basis.

2.1.2 Introduction to SC-ICP-MS

The potential of inductively-coupled plasma mass spectrometry (ICP-MS) for the analysis of individual cells was showcased by the group of Houk, who observed the detection of bacteria cells, previously incubated in uranium (U), to occur as individual spike $^{238}U^{+}$ signals above a constant background.[12] This indicated that the processes of atomization and ionization of intact cells resembled that of metal-containing nanoparticles (NPs). Analysis of individual cells using time-resolved ICP-MS, typically known as SC-ICP-MS, has experienced immense growth thanks to the rapid advancement of sp-ICP-MS, allowing for the analysis of individual particles in colloidal suspensions.[13] This is because the principles of sp-ICP-MS are directly applicable to SC-ICP-MS.

As would be observed for the analysis of a colloidal suspension using sp-ICP-MS, nebulization of a cell suspension into an ICP-MS results in the detection of sharp transient signals, observed as individual spikes in the recorded signal intensity. Each detected spike results from the introduction of a single cell, which undergoes atomization and ionization of its constituent elements in the ICP.[14,15] The target analyte ions resulting from a single cell are extracted from the ICP as a cloud of ions, and subsequently detected by the MS detector as a discrete signal spike above a continuous background signal. The continuous background signal may either reflect the concentration of the dissolve analyte species present in the suspension, or the noise of the detector if the dissolved analyte concentration is below detection.[16] Detection of dissolved analyte species is registered as a continuous background signal, because the analyte mass is homogenously distributed within the volume of sample that is introduced, thus resulting in a continuous flux of metal ions. Provided that a single cell contains a detectable analyte amount, its detection will be registered as a signal spike due to its higher ion flux compared to that of the background.

SC-ICP-MS allows for simultaneous determination of the metal content present in the cell and that occurring as dissolved in the suspension. The dissolved analyte concentration can be quantitated from the intensity of the continuous background signal by employing an external calibration curve, while the intensity of each signal spike can be related to the elemental content of a cell after appropriate determination of the target analyte sensitivity. The latter means establishing a relationship between the ICP-MS signal and the absolute analyte amount detected per dwell time. Determination of the analyte transport efficiency is required, which is typically 1-5% for conventional nebulization systems. Several methodologies have been used to calculate the transport efficiency for single cell analysis,

including nebulization of suspensions of certified metal-containing NPs[17], metal-doped polystyrene beads mimicking the physical properties of a cell[18], detection of an intrinsic cellular element for direct measurement of the cell transport efficiency [19], as well as the waste collection approach.[20] Upon transport efficiency determination, the analyte mass contained in a single cell m_c can be determined using the following expression: [15]

$$m_c = nFtI/b \qquad (Eq.1)$$

, where n stands for the transport efficiency, F the liquid flow rate, t the instrument dwell time, I the net intensity of a cell detection event following background subtraction, and b the slope of the calibration curve, established through the introduction of dissolved analyte standard solutions. Moreover, in order to minimize probability of coincidental cell detection, optimization of the sample flow rate as well as the cell number concentration is required.

Cell detection events, registered as signal spikes, can be identified and separated from the background intensity using statistical iterative exclusion approaches, based on which intensities greater than 3 or 5 multiples of the standard deviation (3σ or 5σ) of the background intensity are considered cellular events.[15,21,22] In case SC-ICP-MS analysis is conducted using ms-scale dwell times, the intensity of a cell detection event can be captured within a single dwell time, resulting in a single intensity data point that can be related to cellular content. When μs-resolution is used, the full time profile of a single cell can be captured, and the intensities of several dwells need to be summed in order to quantitate the given cell detection event.[14,16]

SC-ICP-MS analysis has been used for several applications, ranging from the analysis of relatively robust algal cells to the analysis of fragile mammalian cells.[23–26] The scope of applications becomes even broader if SC-ICP-MS analysis is conducted by means of time-of-flight mass spectrometry. This is because ICP-TOF-MS provides multi-elemental capabilities per single cell. The capability of ICP-TOF-MS in conducting multiplexed analysis of 20 antibodies per single cell was initially demonstrated by Bandura et al, who improved the existing TOF technology to provide potential for its use in single-cell analysis.[27] This technology was endorsed as mass cytometry (commercialized as CyTOF by Fluidigm), and brought clear advantages over the conventional fluorescence-activated flow cytometry (FACS) in eliminating problems of overlapping fluorescence signals when multiple biomarkers are required to be screened per cell.[28,29] While mass cytometry has been demonstrated to enable detection of metal labels of high atomic masses (>75 amu), and thus lanthanide-dopped biomarkers have been used for antibody detection, i.e., Tb (159

amu), Ho (165 amu), more recent ICP-TOF-MS instruments seem to have the capacity to detect elements in the low mass range as well, i.e., Mg, P, Mn; ultimately providing possibilities to complement metal uptake with cell volume information.[30] Recently, quadrupole-based ICP-MS has been showcased to enable detection of 2 isotopes per individual cell, i.e., that of the tagged biomarker binding to the cell and that of the target analyte, a workflow which previously could not be conducted due to the mismatch between the ms-scale settling time of the quadrupole, when switching between 2 masses, and the µs-scale duration of a cell detection event. Dual-analyte detection became possible by reducing the quadrupole settling time to a few hundreds of µs and using a collision cell gas to elongate the transient signal of a cell detection event (up to 5 ms).[31]

2.1.3 Objective

While several studies have reported on the uptake of arsenate by *Chlamydomonas reinhardtii* cells, conventional analytical schemes have been used, involving acid digestion of an ensemble of cells and the use of an atomic spectrometric technique to report a mean value of As content per cell. However, this value has little biological relevance, if As is broadly distributed among the cells. Hence, the objective of this study is to demonstrate a methodology that will enable determination of As uptake on a per cell basis in order to examine the distribution of As within the cell population. To this end, *C. reinhardtii* cells are cultivated in increasing sub-lethal concentrations of arsenate, i.e., 12.5, 22.5 and 30 µg As mL^{-1}, and the As amount, present within the cells or dissolved in the suspension, is simultaneously quantitated using SC-ICP-MS. Cells incubated in arsenate are also analyzed following cell washing with EDTA in order to differentiate between the cell wall-bound As and the As internalized by the cells. Values of the arsenic content per cell are represented as mass histograms that are modelled with suitable probability functions. Novel analytical metrics derived from the modelled distributions are used to describe the uptake pattern of As by *C. reinhardtii* cells across the range of arsenate incubation concentrations. Bulk analysis of cells using Conventional-ICP-MS is also conducted in order to validate the trends determined using SC-ICP-MS.

2.2 Materials and Methods

2.2.1 Cell Cultivation

The cells that were used in this study were the wild-type strain *Chlamydomonas reinhardtii* CC-1690 purchased from Chlamydomonas Resource Center, University of Minnesota, USA. *C. reinhardtii* cell colonies were transferred from agar plates into 3 L of cultivation medium (tris-acetate phosphate, TAP, pH 7.0, supplemented with acetic acid as a carbon source) and cultivated for 5 days under continuous illumination (~2500 lux) and stirring at 25 °C. Subsequently, the cell culture was examined under a microscope for the presence of organisms other than *C. reinhardtii*. Axenic cultures were used to inoculate fresh TAP media, which were spiked with appropriate volumes of sodium arsenate solution so that the final calculated concentration would be 0 (control), 15, 22.5 and 30 µg As mL^{-1}. All the cell cultures were grown under identical conditions for 5 days, at which point cells were harvested by centrifugation (4000 x g, 5 min, 4°C). To completely remove remaining of the TAP media within the cell pellet, cells were resuspended in a washing buffer containing 150 mM NaCl, 4 mM $MgCl_2 \cdot 6H_2O$, 20 mM Trizma base, pH 7.0, and subjected to a second replicate centrifugation step. Finally, cells were transferred into a high-density sucrose solution (0.8 M sucrose, 50 mM Trizma base, pH 7.0), used as a cryoprotectant, and stored in small aliquots at -80 °C until used. Samples that had been thawed for analysis, were not refrozen and re-analyzed.

2.2.2 Single Cell-ICP-MS Analysis

Analysis was carried out on cells prepared as described above (unwashed cells) and on cells which were subsequently treated with EDTA solution (50 mM Trizma, 1 mM EDTA, pH 7) in order to remove any arsenate adsorbed to the cell wall (washed cells). For quantitation of the cell populations, a Neubauer hemocytometer was used. Subsequently, appropriate volumes of stock cell suspensions were diluted in deionized water at a number concentration of 10^5 cells mL^{-1} and analyzed within 10 min of dilution. Arsenic determination in cells was carried out using a NexION 350 X ICP-MS (Perkin Elmer, Shelton, CT, US) equipped with a High-Efficiency Introduction System appropriate for nebulization of cells. The introduction system comprised of a PFA nebulizer (Elemental Scientific Inc.), fitted onto the Asperon™ spray chamber (Perkin Elmer, Shelton, CT, US). The nebulizing and spray chamber makeup gas flow were 0.3 and 0.52 L min^{-1}, respectively. A peristaltic pump was used to deliver samples at a flow rate of 19.4 µL min^{-1}. The instrument was operated in Time-Resolved

Analysis mode with a dwell time of 50 μs. Bulk analysis of cells was carried out using conventional ICP-MS, following cell digestion of millions of cells per arsenate exposure condition. The obtained total As concentration was normalized by the number of digested cells in order to express the As mass per cell, as derived from conventional ICP-MS.

Data acquisition during SC-ICP-MS analysis, as well as most data processing operations, were performed using the Syngistix™ Single-cell Application Module Software v1.2 (Perkin Elmer). The software's signal integration is based on an iterative algorithm in which cell events are discriminated from the dissolved element signal and integrated. An essential attribute of this software is the option to manually set the threshold signal, above which cell events are counted and integrated. Details about how this was set in the present study are provided in section 2.2.3. In addition, the data for constructing histograms and investigating detected cell event profiles were treated with OriginPro and Microsoft Excel software. In order to analyze the cell event profiles, i.e., the signal spikes above a constant background signal, a manual procedure was followed using an Excel spreadsheet, and analysis was conducted for a single replicate SC-ICP-MS analysis of *Chlamydomonas reinhardtii* cells incubated in 22.5 ppm of As. More specifically, the raw ICP-MS intensity data of a single replicate SC-ICP-MS acquisition were loaded as x, y data in a spreadsheet, where y represented the ICP-MS recorded intensity and x the time in μs. Subsequently, time-x data points with y-intensities below 3 counts (i.e., the background threshold intensity) were filtered. This allowed for identifying the set of y-intensity data points that corresponded to each cell event, by isolating groups of data points that were adjacent in time. The time profile of each peak was determined from its isolated data points, plus two baseline points of 3 count intensity.

In order to quantitate cellular As, a mass flux calibration curve[21,32] was established using dissolved standards of 1, 10 and 50 ng As per mL and applying a transport efficiency value, which was determined to be 9.9±0.9% when using 60 nm monodispersed gold (Au) nanoparticles (NIST 8013). The obtained calibration parameters allowed for the use of the following equation for quantitating As in each cell detection event:

$$m_{cell} = \frac{PA}{m} \qquad (Eq.2)$$

where m_{cell} is the mass per cell event (fg As cell^{-1}), PA is the integrated cell event intensity (counts) and m (counts fg^{-1}) is the slope of the mass flux calibration curve (**Figure SI1. 1**).

2.2.3 SC-ICP-MS parameter selection and limit of detection determination.

The fundamental condition for conducting SC-ICP-MS analysis is that each detection event corresponds to a single cell, and therefore coincidental detection of multiple cells is unwanted. Meeting this condition is dependent on the instrument dwell time and the number of cells introduced into the plasma per unit of time. A detector dwell time of 50 μs, with no settling time between consecutive data points, was selected for maximum instrument capability in terms of temporal resolution and signal-to-background (S/B) ratios. Cell suspensions were prepared at concentrations of 10^5 cells mL^{-1} in order to statistically preclude multiple cell detection. Prediction of multiple cell events was based on Poisson statistics, as has been done for particle events upon nebulization of particle suspensions using a pneumatic nebuliser[33]. The Poisson distribution is a discrete probability function that expresses the probability of a number of events k, if these events occur at a constant mean rate λ, and provided that the occurrence of one event is independent from the other. The probability function is determined by the following expression:

$$P = \frac{e^{-\lambda}\lambda^{k}}{\kappa!} \qquad (Eq.3)$$

Herein λ is defined as the rate of cell introduction to the plasma and k the number of occurrences, i.e., zero, single, double, etc cell detection events within a measurement time. If a cell event lasts no more than 1 ms, then given the sample uptake rate (19.4 μL min^{-1}) and the cell number concentration (10^5 cells mL^{-1}) there is a 3.1% and 0.05% probability to register single and double cell events, respectively. Considering that these probabilities further decrease when a transport efficiency (TE) below 100% is applied (9.9% in this study), it is statistically unlikely to detect multiple cell events. However, statistics do not account for cell aggregation due to biological or cell culture growth conditions.

As is the case in single particle ICP-MS, a threshold value should be determined in order to discriminate between the continuous signal, deriving from the background or dissolved element, and the cell detection events. Among the most widely used strategies is the iterative 3σ approach introduced by Pace et al[21,32], according to which all signals above the threshold, determined by triple the standard deviation (3σ) added to the background mean (m), correspond to nanoparticles. The validity of this approach relies on the assumption that the dissolved or background signal is normally distributed. Yet in this study, the use of short dwell time (50 μs) and the extremely low concentration levels of dissolved As in the cell suspensions deviate significantly from the assumed normal distribution of the

blank and thus render the 3σ approach for calculating the Limit of Detection (L_D) inappropriate. This is demonstrated in **Figure SI1. 2**, where the ^{75}As intensity recorded per dwell time for a SC-ICP-MS acquisition of control *Chlamydomonas reinhardtii* is transformed into a histogram, with the horizontal axis being the ^{75}As intensity in counts and the vertical axis the frequency, i.e., the number of dwell times that recorded a given As intensity. The observed frequency of each As recorded intensity (counts) is contrasted with the theoretical frequencies determined for a Poisson distribution of the same mean value, i.e., 0.00168 counts. The mean value was calculated by averaging the intensity data of the whole acquisition. Since the ^{75}As distribution is not normally distributed but is related to that of Poisson, a more suitable formula for L_D calculation was used that incorporates Poisson statistics. Herein, the Limit of Detection is calculated as:

$$L_D = b + 2.71 + 3.29\sqrt{b} \qquad (Eq. 4)$$

; b standing for the average background intensity (counts). The above formula has been established by IUPAC for "well-known" blanks, and has been derived from the normal approximation of the Poisson distribution.[34,35] More specifically, it has been established based upon the hypothesis of a continuous signal distribution, i.e. Gaussian, but with a non-constant variance, being dependent upon the magnitude of the observed signal. The latter is the case for Poisson statistics, which evidently govern the observed mass spectrometer signals at the low count range.[36]

2.3 Results and Discussion

2.3.1 Arsenic determination in *C. reinhardtii* by SC-ICP-MS.

The detection of signal spikes for As ions (m/z 75), following the analysis of *C. reinhardtii* cell suspensions, revealed the presence of As in cells that had grown in arsenate-containing medium (**Figure 2.1**A), and its absence from cells cultivated with no arsenate added (**Figure 2.1**B). The detected signal spikes, corresponding to cell events, had a mean duration of approximately 250-350 μs as shown in **Figure 2.1**C for three cell events. The determination of all cell event duration times resulted in the frequency histogram shown in **Figure 2.1**D. So far, most SC-ICP-MS published studies have used relatively long detector dwell times (1-5 ms), and therefore the time profile of a cell event could not be determined. In the present study, we have used 50 μs detector dwell time, with no dead time, making it possible to determine the time profile of each cell event. Also, even though some studies have used 50

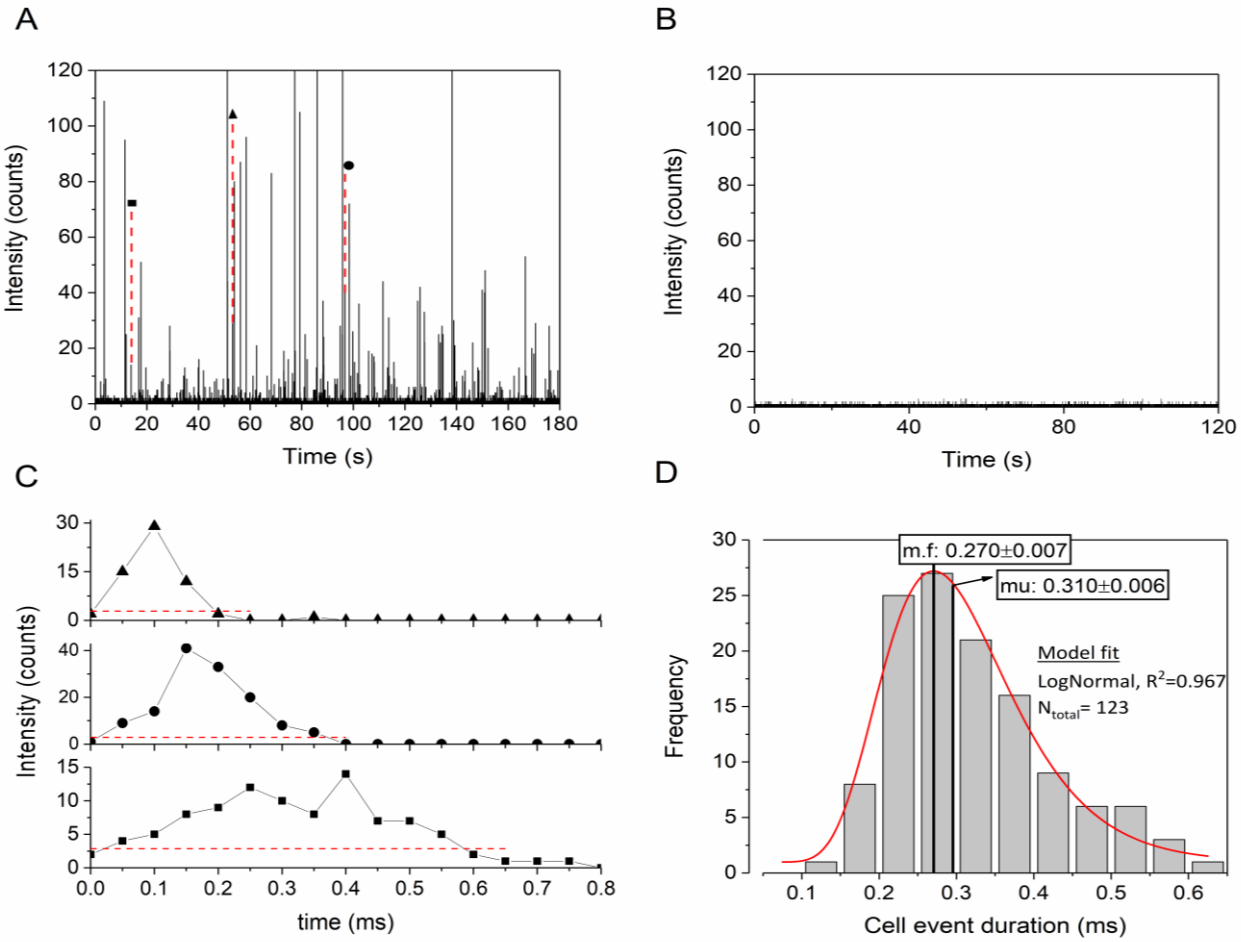

Figure 2.1 Panels (A) and (B): Time resolved ICP-MS signals obtained from washed C. reinhardtii cell suspensions, for cells grown in medium containing: (A) arsenate at 22.5 µg As mL^{-1}, (B) no arsenate for control cells. Panel (C) shows the time profile of cell events chosen from Panel A with durations close to the average (●), narrower than the average (▲) and broader than the average (■), data points obtained every 50 µs, and panel (D) a histogram showing the distribution of cell event duration times for 123 detected cell events, with m.f: most frequent duration time; mu: mean duration time.

µs dwell times, such cell event duration profiles have not been studied in detail.[18,37] Upon examination of the cell duration histogram it becomes clear that cell duration times are similar to those reported for 30-90 nm Au and Ag NPs or 1 µm-sized Si nanoparticles.[38–43]. It has been suggested that the time profile of a NP event depends on the extent of diffusion of the ion cloud upon vaporization of the corresponding NP, a view that was initially introduced by the group of Olesik, who studied the time profiles of metal-containing µm-sized droplets.[39] The metal content of these spherical monodisperse µm-sized droplets, generated by microdroplet generators, was equivalent to that of a NP, therefore droplets could be used to mimic the behavior of NPs in the plasma. More specifically, the time profile

of different metal-containing microdroplets suggested a $x^{-1/2}$ dependence on atomic mass.[39] The residence time of a NP within the plasma, which depends on the plasma gas flow rate and sampling depth, was also suggested to impact the duration profile of a NP. Moreover, the group of Günther observed that that the duration of a Au NP profile was 1.4 times less than that of a Cu profile, which was in line with Graham's law according to which the ratio of the relative diffusion velocities of 2 elements equals the ratio of the square root of their atomic masses (i.e., 1.76 for Au/Cu).[38] These data, herein, seem to indicate that the metal content of a *C. reinhardtii* cell forms a similarly sized nanoparticle upon drying in the plasma, or alternatively that signal duration for As in algal cells is governed by the element's diffusion behavior in the plasma. The latter has been also implied for other elements detected in cells.[44]

Each cell detection event (signal spike) was integrated (**Figure 2.1**C), and the resulting integration values were transformed into As mass (fg) per detected cell event. The resulting mass histograms for washed cells, showing As mass per individual cell (fg Ag per cell) per incubation concentration, i.e. 15, 22.5 and 30 µg As mL^{-1}, are displayed in **Figure 2.2**. It was not possible to construct such histograms for control samples because no cell events were detected during their analysis (**Figure 2.1**B). Each of the cell event data series, displayed as a mass histogram (**Figure 2.2**), were obtained from 9 min acquisitions resulting from the addition of three technical replicates (3 min per replicate, data shown in **Table SI1. 1**) carried out for each cell suspension. The obtained data clearly show the uptake of fg amounts of As by individual *C. reinhardtii* cells cultivated in the presence of 15, 22.5 and 30 µg As mL^{-1} as arsenate. The mass distribution of As amongst the analysed cell population provides novel information regarding As uptake by the analysed *C. reinhardtii* cells (**Figure 2.2**). High As mass dispersion amongst the washed algal cells is clearly observed by the excellent fit of the lognormal probability function to the mass histograms in all cases (**Figure 2.2**A-C). This type of lognormal As mass uptake was also observed for unwashed algal cells (**Figure SI1. 3**), indicating that the As adsorbed to the cell walls follows the same type of distribution.

Since previous studies have reported on the lognormal size distribution for C. reinhardtii cells[45], it is likely that As uptake per cell is influenced by cell size, as would also be expected for cell wall adsorption.

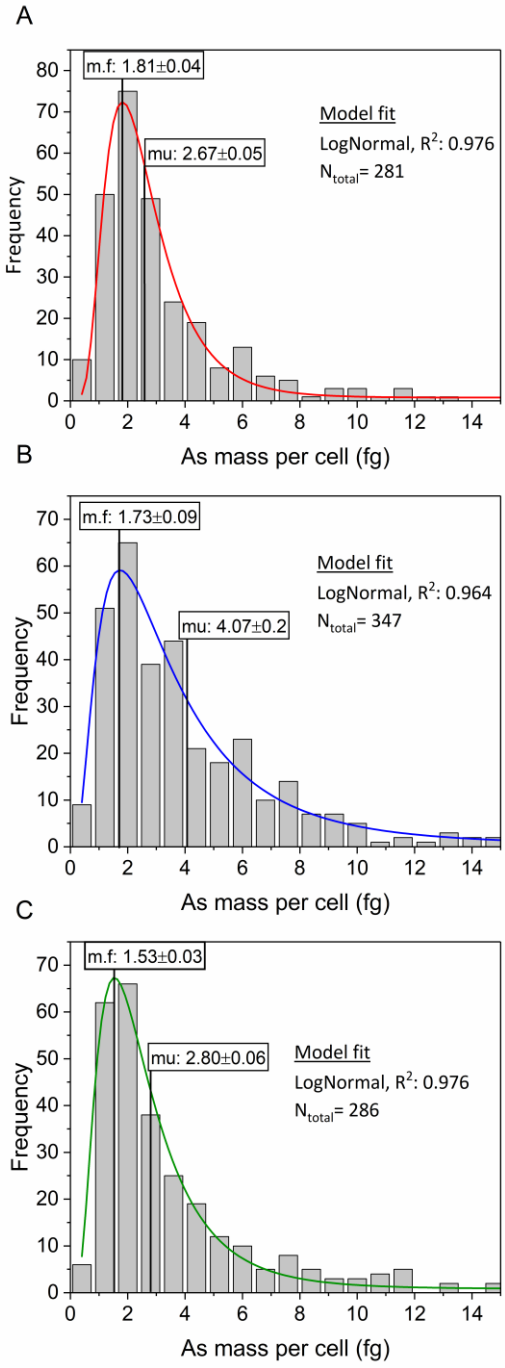

Figure 2.2 As mass distribution histograms for C. reinhardtii cells grown in 15 (A), 22.5 (B) and 30 µg mL^{-1} As (C), binned at 0.8 fg. The lognormal probability function has been fitted to the mass histogram data in all three cases. Values for mu and $m.f$ denote the lognormal mean and most frequently observed As mass per cell, respectively.

Algal cells grown in 15, 22.5 and 30 µg As mL^{-1} as arsenate were determined by SC-ICP-MS to contain a lognormal mean As mass of 2.67, 4.07 and 2.80 fg, respectively (**Figure 2.2**A-C), corresponding to 2.1-3.3×10^7 As atoms per cell. The lognormal mean mu was determined from the following expression:[45]

$$mu = e^{\mu+0.5\sigma^2} \qquad (Eq.5)$$

, where μ and σ are parameters that were exported upon fitting of the lognormal function to the data. The uncertainty of mu was obtained by error propagation of $Eq.5$.

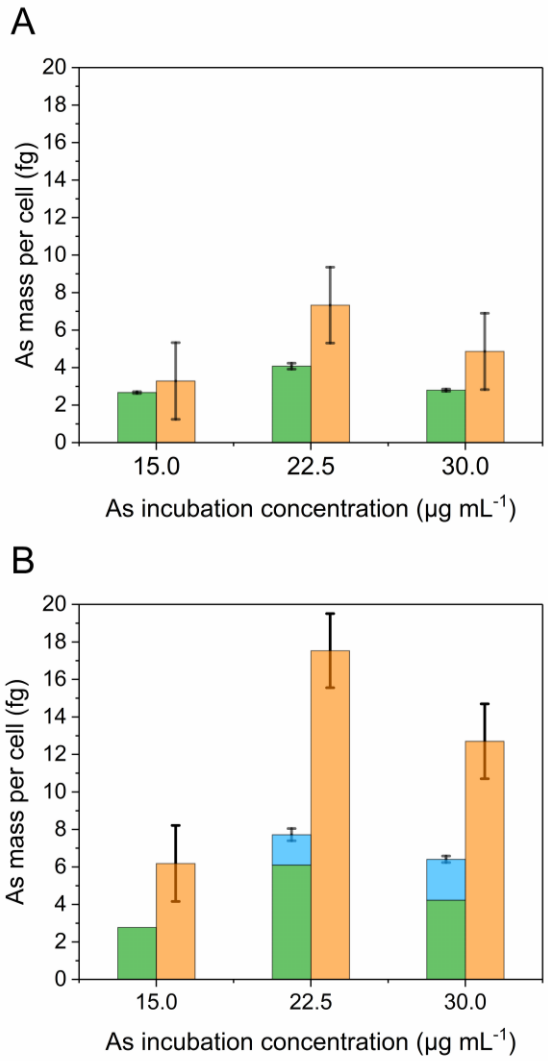

Figure 2.3 Column chart illustrating the mean As amount (fg/cell) obtained by using SC-ICP-MS (green) compared to conventional ICP-MS (orange) for washed (A) and unwashed (B) cells. Blue bars represent the dissolved As determined by using SC-ICP-MS and normalized per cell. Error bars of the mean determined by SC-ICP-MS represent the uncertainty of the lognormal mean. Error bars for conventional ICP-MS were calculated based on the 95% confidence interval of the dissolved As calibration curve. The error in the normalized dissolved As mass per cell is the standard deviation of the 3 independent replicates carried out for each cell suspension.

The observation that cells cultivated in the highest arsenate concentration did not exhibit the highest As uptake was counter-intuitive, however, the same trend was also observed when using conventional ICP-MS for bulk cell analysis. In this case, the mean As uptake values were determined to be 3.2, 7.2 and 4.8 fg As, respectively (**Figure 2.3**A); thus confirming that the highest As cultivation concentration did not correspond to the highest As uptake. This observation may be attributed to some extent to the slower cell growth rates observed for the cells grown in arsenate at 30 µg As mL^{-1} (**Figure 2.4**). After 5 days of cultivation under these conditions, the cells reached approximately 50% growth, compared to control cells and cells grown in the lower two As concentrations, i.e. 15 and 22.5 µg As mL^{-1}. This clearly shows that the presence of arsenate at high levels causes substantial cellular stress, thus retarding cell growth rate. This is further supported by Wang et al, who showed that the median (50%) effect concentration (EC50) of arsenic for *C. reinhardtii* cells, cultivated in arsenate, was 33.5 µg As per mL.[7] Similar growth inhibition has been observed in other studies for arsenate, in which case cell stress was linked to the overexpression of stress-related proteins.[46]

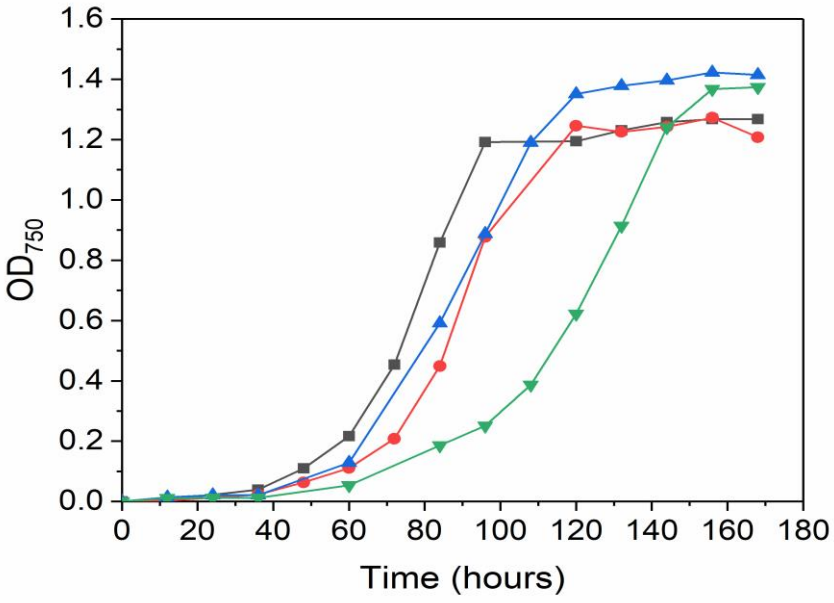

Figure 2.4 Growth curves of *C. reinhardtii* cells grown in 15 (red), 22.5 (blue), 30 (green) µg As mL^{-1} and control (black).

It is also of interest to note that a new analytical metric for metal determination in cells can now be determined using SC-ICP-MS, i.e., the most frequently detected amount of As (**Figure 2.2**). This value $m.f$ corresponds to the mode of the lognormal fit, and was determined using the following expression:

$$m.f = e^{\mu-\sigma^2} \qquad (Eq.6)$$

The expression for $m.f$ was derived by setting the first derivative of the lognormal probability function equal to 0, as $m.f$ corresponds to a global maximum.[47] The uncertainty of the $m.f$ values corresponding to the As content of each arsenate exposure concentration was derived by error propagation of $Eq.6$. The $m.f$ was determined to be 1.81, 1.73 and 1.53 fg As for arsenate exposure concentrations of 15, 22.5 and 30 μg As mL^{-1}, respectively (**Figure 2.2**). It is interesting to note that the most frequently detected As mass was similar for all three As incubation concentrations. Therefore, it may represent a steady state or saturation mass that has been reached for the majority of the cell population at each growth condition. If this is the case, then once again the mean As uptake value, as determined from the bulk analysis of cells by conventional ICP-MS, seems to have little relevance with respect to how individual cells or cell populations actually behave once grown in the presence of As. The determined by conventional ICP-MS As mean values of approximately 3-8 fg seem to indicate that all cells uptake higher amounts of As than those determined using SC-ICP-MS. Also, the higher As uptake amounts determined for only a limited number of cells by SC-ICP-MS, as seen by their lognormal uptake behavior, may be providing insight into the occurrence of cell bloating, cell aggregation, or just reflecting normal algal cell size variations. Much broader As mass distribution was mainly observed for cells cultivated in 22.5 μg As mL^{-1}; indicating the presence of a significant population of cells that had uptaken higher amounts of As. It is envisioned that following further development of SC-ICP-MS these processes will be studied extensively, and will thus be better understood.

For all the previously discussed biological reasons it is evident that it is difficult to compare the mean values determined using SC-ICP-MS to those obtained by conventional ICP-MS (**Figure 2.3**). Furthermore, from an analytical point of view, additional reasons may be contributing to the differences observed between the two approaches. One such reason may be differences in the determined transport efficiency using Au nanoparticles and the actual transport efficiency achieved for *C. reinhardtii* cells. Such differences result in potential inaccuracies of the determined mass flux entering the ICP per time. Also, when conventional ICP-MS is used to determine the metal amount per cell, the analysed cell number must be known with high accuracy. Supposing this number is underestimated, then the metal amount determined per cell will be biased to higher values. Nevertheless, the discrepancies

observed in the present study between SC and conventional ICP-MS analysis are similar in magnitude to those that have been reported in existing SC-ICP-MS literature.[19,48,49]

Differences regarding As uptake and mass distribution behavior were also observed between washed and unwashed cells cultivated under the same conditions. **Figure 2.5** shows the lognormal fit for the mass distribution for both types of cells grown under the same As concentrations (22.5 µg As mL^{-1}). From this analysis, it is observed that the As amount present in the unwashed cells shifts to lower mean amounts for washed cells, i.e. the lognormal mean drops from 6.1 to 4.1 fg As per cell; clearly indicating that a significant amount of As is wall-bound. Although evidence is not conclusive on whether the wall-bound As is quantitatively removed upon treatment of the cells with EDTA, the absence of the dissolved As species that were once detected in suspended unwashed cells (i.e., 22.5 and 30 µg As mL^{-1} in **Figure 2.3**B) provides an indication that removal of wall-bound As was close to quantitative. The use of EDTA to release metals, including arsenite (AsIII), from cell membranes has been demonstrated in previous studies.[50]

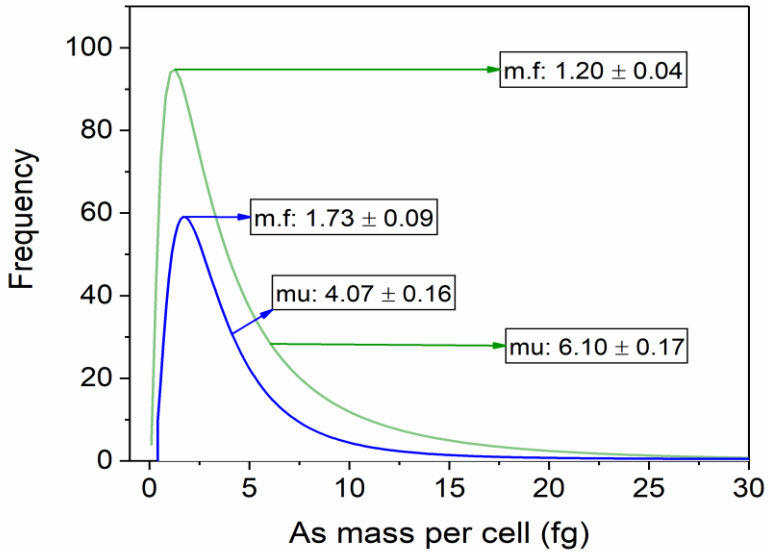

Figure 2.5 Arsenic mass distribution in washed (blue line) and unwashed (green line) *C. reinhardtii* cells incubated in 22.5 µg As mL^{-1}.

2.4 Conclusions

Herein, the uptake of arsenate by *C. reinhardtii* cells, exposed to sub-lethal concentrations of arsenate, was studied on a per cell basis by developing and applying SC-ICP-MS. This is among the first studies to showcase the application of SC-ICP-MS by means

of a 50 µs dwell time in order to quantitate the elemental content of individual cells, as well as provide insight into the time profiles of cell detection events. Results suggest high variability in As uptake as demonstrated by the lognormal distribution of As within the cell population. Novel analytical metrics were introduced, such as lognormal mean As mass per analyzed cell and the most frequent As mass amount in the analyzed cells, which were found more suitable to characterize the heterogeneous distribution of As among the cells. In addition, simultaneous determination of cell-containing As and extracellular As in a single analysis step was demonstrated. Moreover, the developed methodology featured capabilities to analyze a hundred As-containing cells per min, while only sacrificing 18000 cells per sample.

2.5 Literature

[1] P.L. Smedley, D.G. Kinniburgh, A review of the source, behaviour and distribution of arsenic in natural waters, Appl. Geochemistry. 17 (2002) 517–568. https://doi.org/10.1016/S0883-2927(02)00018-5.

[2] A. Sarkar, B. Paul, G.K. Darbha, The groundwater arsenic contamination in the Bengal Basin-A review in brief, Chemosphere. 299 (2022) 134369. https://doi.org/10.1016/j.chemosphere.2022.134369.

[3] M. Vithanage, B.B. Dabrowska, A.B. Mukherjee, A. Sandhi, P. Bhattacharya, Arsenic uptake by plants and possible phytoremediation applications: A brief overview, Environ. Chem. Lett. 10 (2012) 217–224. https://doi.org/10.1007/s10311-011-0349-8.

[4] S. Maeda, A. Ohki, T. Tokuda, M. Ohmine, Transformation of arsenic compounds in a freshwater food chain, Appl. Organomet. Chem. 4 (1990) 251–254. https://doi.org/10.1002/aoc.590040312.

[5] M. Hanikenne, Chlamydomonas reinhardtii as a eukaryotic photosynthetic model for studies of heavy metal homeostasis and tolerance, New Phytol. 159 (2003) 331–340. https://doi.org/10.1046/j.1469-8137.2003.00788.x.

[6] R.E. Webster, A.P. Dean, J.K. Pittman, Cadmium exposure and phosphorus limitation increases metal content in the freshwater alga chlamydomonas reinhardtii, Environ. Sci. Technol. 45 (2011) 7489–7496. https://doi.org/10.1021/es200814c.

[7] N.X. Wang, Y. Li, X.H. Deng, A.J. Miao, R. Ji, L.Y. Yang, Toxicity and bioaccumulation kinetics of arsenate in two freshwater green algae under different phosphate regimes, Water Res. 47 (2013) 2497–2506. https://doi.org/10.1016/j.watres.2013.02.034.

[8] I. Kobayashi, S. Fujiwara, H. Saegusa, M. Inouhe, H. Matsumoto, M. Tsuzuki, Relief of arsenate toxicity by Cd-stimulated phytochelatin synthesis in the green alga Chlamydomonas reinhardtii, Mar. Biotechnol. 8 (2006) 94–101. https://doi.org/10.1007/s10126-005-5092-3.

[9] T. Kaise, S. Fujiwara, M. Tsuzuki, T. Sakurai, T. Saitoh, C. Mastubara, Accumulation

of arsenic in a unicellular alga Chlamydomonas reinhardtii, Appl. Organomet. Chem. 13 (1999) 107–111. https://onlinelibrary.wiley.com/doi/10.1002/(SICI)1099-0739(199902)13:2%3C107::AID-AOC824%3E3.0.CO;2-9

[10] X. Yin, L. Wang, G. Duan, G. Sun, Characterization of arsenate transformation and identification of arsenate reductase in a green alga Chlamydomonas reinhardtii, J. Environ. Sci. 23 (2011) 1186–1193. https://doi.org/10.1016/S1001-0742(10)60492-5.

[11] C. Murota, H. Matsumoto, S. Fujiwara, Y. Hiruta, S. Miyashita, M. Shimoya, I. Kobayashi, M.O. Hudock, R.K. Togasaki, N. Sato, M. Tsuzuki, Arsenic tolerance in a Chlamydomonas photosynthetic mutant is due to reduced arsenic uptake even in light conditions, Planta. 236 (2012) 1395–1403. https://doi.org/10.1007/s00425-012-1689-8.

[12] F. Li, D.W. Armstrong, R.S. Houk, Behavior of bacteria in the inductively coupled plasma: Atomization and production of atomic ions for mass spectrometry, Anal. Chem. 77 (2005) 1407–1413. https://doi.org/10.1021/ac049188l.

[13] C. Degueldre, P.Y. Favarger, S. Wold, Gold colloid analysis by inductively coupled plasma-mass spectrometry in a single particle mode, Anal. Chim. Acta. 555 (2006) 263–268. https://doi.org/10.1016/j.aca.2005.09.021.

[14] M. Corte-Rodríguez, R. Álvarez-Fernández, P. García-Cancela, M. Montes-Bayón, J. Bettmer, Single cell ICP-MS using on line sample introduction systems: Current developments and remaining challenges, TrAC - Trends Anal. Chem. 132 (2020). https://doi.org/10.1016/j.trac.2020.116042.

[15] Roberto Álvarez-Fernández Garcia, Mario Corte-Rodríguez, Paula García-Cancela, Jörg Bettmer, María Montes-Bayón, Application of online sample introduction systems for single-cell analysis with ICP-MS, Antonio Canals, Miguel Ángel Aguirre, Mazaher Ahmadi, Analytical Nebulizers, Elsevier, 2023, Pages 197–216, https://doi.org/10.1016/B978-0-323-91181-8.00011-4.

[16] M. Resano, M. Aramendía, E. García-Ruiz, A. Bazo, E. Bolea-Fernandez, F. Vanhaecke, Living in a transient world: ICP-MS reinvented via time-resolved analysis for monitoring single events, Chem. Sci. (2022). https://doi.org/10.1039/d1sc05452j.

[17] M. Corte Rodríguez, R. Álvarez-Fernández García, E. Blanco, J. Bettmer, M. Montes-Bayón, Quantitative Evaluation of Cisplatin Uptake in Sensitive and Resistant Individual Cells by Single-Cell ICP-MS (SC-ICP-MS), Anal. Chem. (2017) acs.analchem.7b02746. https://doi.org/10.1021/acs.analchem.7b02746.

[18] R.C. Merrifield, C. Stephan, J.R. Lead, Quantification of Au Nanoparticle Biouptake and Distribution to Freshwater Algae Using Single Cell - ICP-MS, Environ. Sci. Technol. 52 (2018) 2271–2277. https://doi.org/10.1021/acs.est.7b04968.

[19] H. Wang, M. Wang, B. Wang, L. Zheng, H. Chen, Z. Chai, W. Feng, Interrogating the variation of element masses and distribution patterns in single cells using ICP-MS with a high efficiency cell introduction system, Anal. Bioanal. Chem. 409 (2017) 1415–1423. https://doi.org/10.1007/s00216-016-0075-y.

[20] W. Qin, H.J. Stärk, S. Müller, T. Reemtsma, S. Wagner, Determination of elemental distribution and evaluation of elemental concentration in single Saccharomyces

cerevisiae cells using single cell-inductively coupled plasma mass spectrometry, Metallomics. 13 (2021). https://doi.org/10.1093/mtomcs/mfab032.

[21] H.E. Pace, N.J. Rogers, C. Jarolimek, V.A. Coleman, C.P. Higgins, J.F. Ranville, Determining Transport Efficiency for the Purpose of Counting and Sizing Nanoparticles via Single Particle Inductively Coupled Plasma Mass Spectrometry, Anal. Chem. 83 (2011) 9361–9369.

[22] J. Tuoriniemi, G. Cornelis, M. Hassellöv, Size discrimination and detection capabilities of single-particle ICPMS for environmental analysis of silver nanoparticles, Anal. Chem. 84 (2012) 3965–3972. https://doi.org/10.1021/ac203005r.

[23] A. Lores-Padín, E. Mavrakis, B. Fernández, M. García, H. González-Iglesias, R. Pereiro, S.A. Pergantis, Gold nanoclusters as elemental label for the sequential quantification of apolipoprotein E and metallothionein 2A in individual human cells of the retinal pigment epithelium using single cell-ICP-MS, Anal. Chim. Acta. 1203 (2022). https://doi.org/10.1016/j.aca.2022.339701.

[24] Z. Chen, B. Chen, M. He, B. Hu, Droplet-Splitting Microchip Online Coupled with Time-Resolved ICPMS for Analysis of Released Fe and Pt in Single Cells Treated with FePt Nanoparticles, Anal. Chem. 92 (2020) 12208–12215. https://doi.org/10.1021/acs.analchem.0c01217.

[25] M. Corte Rodríguez, R. Álvarez-Fernández García, E. Blanco, J. Bettmer, M. Montes-Bayón, Quantitative Evaluation of Cisplatin Uptake in Sensitive and Resistant Individual Cells by Single-Cell ICP-MS (SC-ICP-MS), Anal. Chem. (2017) acs.analchem.7b02746. https://doi.org/10.1021/acs.analchem.7b02746.

[26] R. Gonzalez de Vega, S. Goyen, T.E. Lockwood, P.A. Doble, E.F. Camp, D. Clases, Characterisation of microplastics and unicellular algae in seawater by targeting carbon via single particle and single cell ICP-MS, Anal. Chim. Acta. 1174 (2021) 338737. https://doi.org/10.1016/j.aca.2021.338737.

[27] D.R. Bandura, V.I. Baranov, O.I. Ornatsky, A. Antonov, R. Kinach, X. Lou, S. Pavlov, S. Vorobiev, J.E. Dick, S.D. Tanner, Mass cytometry: Technique for real time single cell multitarget immunoassay based on inductively coupled plasma time-of-flight mass spectrometry, Anal. Chem. 81 (2009) 6813–6822. https://doi.org/10.1021/ac901049w.

[28] M.H. Spitzer, G.P. Nolan, Mass Cytometry: Single Cells, Many Features, Cell. 165 (2016) 780–791. https://doi.org/10.1016/j.cell.2016.04.019.

[29] Y.S.S. Yang, P.U. Atukorale, K.D. Moynihan, A. Bekdemir, K. Rakhra, L. Tang, F. Stellacci, D.J. Irvine, High-throughput quantitation of inorganic nanoparticle biodistribution at the single-cell level using mass cytometry, Nat. Commun. 8 (2017). https://doi.org/10.1038/ncomms14069.

[30] W. Qin, H.J. Stärk, T. Reemtsma, Ruthenium red: A highly efficient and versatile cell staining agent for single-cell analysis using inductively coupled plasma time-of-flight mass spectrometry, Analyst. 146 (2021) 6753–6759. https://doi.org/10.1039/d1an01143j.

[31] N.D. Donahue, V. Sheth, A.N. Frickenstein, A. Holden, S. Kanapilly, C. Stephan, S. Wilhelm, Absolute Quantification of Nanoparticle Interactions with Individual Human

B Cells by Single Cell Mass Spectrometry, Nano Lett. 22 (2022) 4192–4199. https://doi.org/10.1021/acs.nanolett.2c01037.

[32] H.E. Pace, N.J. Rogers, C. Jarolimek, V.A. Coleman, C.P. Higgins, J.F. Ranville, Correction to Determining Transport E ffi ciency for the Purpose of Counting and Sizing Nanoparticles via Single Particle Inductively Coupled Plasma Mass Spectrometry, Anal. Chem. 84 (2012) 4633–4633. https://doi.org/10.1021/ac300942m.

[33] J.W. Olesik, P.J. Gray, Considerations for measurement of individual nanoparticles or microparticles by ICP-MS: determination of the number of particles and the analyte mass in each particle, J. Anal. At. Spectrom. 27 (2012) 1143. https://doi.org/10.1039/c2ja30073g.

[34] L.A. Currie, International Union of Pure Nomenclature in Evaluation of Analytical Methods Including Detection Nomenclature in evaluation of analytical methods , including detect ion and quantification capabiIities (IUPAC Recommendations 1995), Pure Appl. Chem. 67 (1995) 1699–1723. https://doi.org/10.1287/isre.1120.0448.

[35] L.A. Currie, Limits for Qualitative Detection and Quantitative Determination: Application to Radiochemistry, Anal. Chem. 40 (1968) 586–593. https://doi.org/10.1021/ac60259a007.

[36] M. Tanner, D. Günther, Short transient signals, a challenge for inductively coupled plasma mass spectrometry, a review, Anal. Chim. Acta. 633 (2009) 19–28. https://doi.org/10.1016/j.aca.2008.11.041.

[37] S.I. Miyashita, A.S. Groombridge, S.I. Fujii, A. Minoda, A. Takatsu, A. Hioki, K. Chiba, K. Inagaki, Highly efficient single-cell analysis of microbial cells by time-resolved inductively coupled plasma mass spectrometry, J. Anal. At. Spectrom. 29 (2014) 1598–1606. https://doi.org/10.1039/c4ja00040d.

[38] S. Gschwind, L. Flamigni, J. Koch, O. Borovinskaya, S. Groh, K. Niemax, D. Gunther, Capabilities of inductively coupled plasma mass spectrometry for the detection of nanoparticles carried by monodisperse microdroplets, J. Anal. At. Spectrom. 26 (2011) 1166–1174. https://doi.org/10.1039/c0ja00249f.

[39] M.P. Dziewatkoski, L.B. Daniels, J.W. Olesik, Time-Resolved Inductively Coupled Plasma Mass Spectrometry Measurements with Individual, Monodisperse Drop Sample Introduction, Anal. Chem. 68 (1996) 1101–1109. https://doi.org/10.1021/ac951013b.

[40] I. Strenge, C. Engelhard, Capabilities of fast data acquisition with microsecond time resolution in inductively coupled plasma mass spectrometry and identification of signal artifacts from millisecond dwell times during detection of single gold nanoparticles, J. Anal. At. Spectrom. 31 (2016) 135–144. https://doi.org/10.1039/c5ja00177c.

[41] J. Tuoriniemi, G. Cornelis, M. Hassellöv, Improving the accuracy of single particle ICPMS for measurement of size distributions and number concentrations of nanoparticles by determining analyte partitioning during nebulisation, J. Anal. At. Spectrom. 29 (2014) 743. https://doi.org/10.1039/c3ja50367d.

[42] J. Liu, K.E. Murphy, R.I. Maccuspie, M.R. Winchester, Capabilities of single particle

inductively coupled plasma mass spectrometry for the size measurement of nanoparticles: A case study on gold nanoparticles, Anal. Chem. 86 (2014) 3405–3414. https://doi.org/10.1021/ac403775a.

[43] M.D. Montaño, J.W. Olesik, A.G. Barber, K. Challis, J.F. Ranville, Single Particle ICP-MS: Advances toward routine analysis of nanomaterials, Anal. Bioanal. Chem. 408 (2016) 5053–5074. https://doi.org/10.1007/s00216-016-9676-8.

[44] K. Shigeta, G. Koellensperger, E. Rampler, H. Traub, L. Rottmann, U. Panne, A. Okino, N. Jakubowski, Sample introduction of single selenized yeast cells (Saccharomyces cerevisiae) by micro droplet generation into an ICP-sector field mass spectrometer for label-free detection of trace elements, J. Anal. At. Spectrom. 28 (2013) 637–645. https://doi.org/10.1039/c3ja30370e.

[45] A. Garz, M. Sandmann, M. Rading, S. Ramm, R. Menzel, M. Steup, Cell-to-cell diversity in a synchronized chlamydomonas culture as revealed by single-cell analyses, Biophys. J. 103 (2012) 1078–1086. https://doi.org/10.1016/j.bpj.2012.07.026.

[46] C. Walliwalagedara, H. Van Keulen, B. Willard, R. Wei, Differential Proteome Analysis of Chlamydomonas reinhardtii Response to Arsenic Exposure, Am. J. Plant Sci. 3 (2012) 764–772.

[47] J. Soch, T.J. Faulkenberry, K. Petrykowski, A. Carsten, The Book of Statistical Proofs, (2012). https://dx.doi.org/10.5281/zenodo.4305950%0Ahttps://statproofbook.github.io/ (accessed March 12, 2023).

[48] H. Wang, B. Wang, M. Wang, L. Zheng, H. Chen, Z. Chai, Y. Zhao, W. Feng, Time-resolved ICP-MS analysis of mineral element contents and distribution patterns in single cells., Analyst. 140 (2015) 523–31. https://doi.org/10.1039/c4an01610f.

[49] X. Wei, L.L. Hu, M.L. Chen, T. Yang, J.H. Wang, Analysis of the distribution pattern of chromium species in single cells, Anal. Chem. 88 (2016) 12437–12444. https://doi.org/10.1021/acs.analchem.6b03810.

[50] J.A. Carrasco, P. Armario, E. Pajuelo, A. Burgos, M.A. Caviedes, R. López, M.A. Chamber, A.J. Palomares, Isolation and characterisation of symbiotically effective Rhizobium resistant to arsenic and heavy metals after the toxic spill at the Aznalcóllar pyrite mine, Soil Biol. Biochem. 37 (2005) 1131–1140. https://doi.org/10.1016/j.soilbio.2004.11.015.

3 Chapter 3. Development of data processing for µs-sp-ICP-MS

3.1 Introduction

3.1.1 Fundamental principles of sp-ICP-MS

For the determination of trace amounts of metals, ICP-MS has traditionally been operated by obtaining average signal intensities of the elemental isotopes, monitored throughout a several tens of seconds (s) acquisition, and relating them to total metal concentrations. If such an acquisition was viewed in time-resolved mode, a steady-state signal would be typically observed for the elemental isotopes that are monitored over the acquisition time. Since a constant signal is recorded, obtaining average elemental isotope intensities in a high time resolution fashion, i.e., using low dwell times, is not critical; dwell time defined as the specified measurement time interval in which a single intensity data point is recorded for a given elemental isotope. Even if dwell times in the range of hundreds of ms are used to monitor signal intensity per isotope, these can provide a sufficient number of intensity data points that can be averaged to report elemental concentrations with adequate precision. However, monitoring the intensity of a given isotope in a high time resolution fashion, i.e., dwell times≤ 10 ms, allows for the detection of individual metal-containing particles, a method referred as single-particle ICP-MS (sp-ICP-MS). In this dissertation, sp-ICP-MS will refer to the analysis of dilute metal-containing colloids and nanoparticles (NPs) at the level of individual particles.

Among the pioneers in the development of sp-ICP-MS were Degueldre et al, who reported the analysis of sub-micrometer sized gold (Au) colloids using ICP-MS, and introduced the fundamentals of sp-ICP-MS.[1] These authors analyzed very dilute suspensions of 5 monodisperse Au colloids, prepared at a number concentration of 400-4000 mL^{-1}, with the average diameters of the 5 differently-sized colloids being in the range of 80 to 250 nm. Analysis was conducted in time-resolved mode by monitoring the intensity of $^{197}Au^{+}$ every 10 ms, corresponding to the instrument dwell time. It was established that each single metal-containing particle reaching the plasma undergoes atomization and ionization, resulting in a cloud of ions of the constituent metal. This cloud of ions can be a fraction (n_A) of the constituent metal per particle, or represent the total metal content per particle as is the case with Au (~100% ionization efficiency). Each cloud of ions is extracted into the MS, and is recorded by the detector as a discrete signal intensity pulse above a continuous signal intensity. The continuous signal intensity, referred herein as background signal, may either

reflect the noise of the detector for the given metal isotopic mass, or detection of the dissolved metal species occurring in the colloid suspension. In the latter case, the dissolved metal species, homogenously distributed in the suspension, provide a continuous flux of metal ions, therefore yielding a continuous signal intensity. In either case, a metal-containing particle is detected as a signal pulse, as the corresponding flux of metal ions is greater than that of the background at the hundred μs-scale that a signal from an ionized particle typically lasts. [2,3] The magnitude or area of the recorded signal pulse S_A is a function of the number of metal atoms (N_M) that are present in the analyzed particle or of the fraction of the metal in the particle considered (in case the particle has multi-metal components), while the frequency (f) of the recorded signal pulses is related to the particle number concentration in the colloid suspension. With the assumption of a spherical particle consisting entirely of Au, the particle signal S_A is expressed as:

$$S_A = \pi n_A n_C \rho (6M_M)^{-1} A_v \alpha^3 \qquad (Eq. 1)$$

, where n_C represents the detection efficiency of the cloud of ions resulting from the ionization of a Au particle, ρ the density of Au, M_M the molecular weight of Au, A_v the Avogadro constant, and d the diameter of the analyzed particle. The particle number concentration of the analyzed colloid is related to the frequency of the recorded ion clouds $f(S_{A)}$, via the following expression:

$$f(S_A) = N_{col} Q_{col} n_{neb} \qquad (Eq. 2)$$

, where N_{col} represents the colloid number concentration, Q_{col} the colloid suspension introduction rate, and n_{neb} the transport efficiency due to losses of particles within the nebulizing argon flow during colloid introduction to the ICP. Based on $Eq. 1$, the recorded signal S_A scales with particle diameter, a relation which was experimentally supported by the cubic relationship that was exhibited by the average colloid size in the analyzed suspension and the recorded average S_A. Thus, it was revealed that the particle size distribution of an analyzed colloid can be evaluated on the basis of the distribution of the recorded signals, i.e., the number of S_A signals recorded throughout a given time-resolved acquisition. A particular advantage of the described sp-ICP-MS method was that it allowed for tracking colloids down to a minimum number concentration of 10^3 mL^{-1} (corresponding to the detection of 1 signal pulse over a 20 s time-resolved acquisition); thus, demonstrating sensitive colloid detection even at extremely low particle number concentrations. This is because single particles can be individually detected by sp-ICP-MS, independent of the

colloid dilution, even if they are present at extremely low number concentration. This detection capability is not offered when ICP-MS is operated in conventional mode (high ms dwell time acquisition), as described previously, because the signal of a single nm-sized Au particle would be lost amongst the higher background signal recorded when dwell times of hundreds of ms are used.

In an attempt to determine uranium dioxide particles across a wide size range (100-10000 nm), the same authors investigated the influence of particle size on particle atomization within the ICP.[4] This was investigated by determining the residence time of each particle size within the ICP, for which complete particle sublimation and analyte atomization could occur, and comparing it to the maximum residence time dictated by the ICP operating conditions, i.e., the argon flow through the torch. Through that study, it was indicated that the ICP could atomize particles up to 6000 nm, however, it is possible that resulting ion signals may exceed the pulse counting limit of the electron multiplier detector, thus causing detector shutdown and resulting in loss of signals from these particle sizes.

3.1.2 Critical considerations for sp-ICP-MS analyses

Since the introduction of the principle of sp-ICP-MS[1,4], further development of the technique has focused on addressing critical aspects such as calibration and data processing approaches, required in order for sp-ICP-MS to become a powerful technique for nanomaterial characterization.[3]

Calibration approaches are required in order to determine metal mass per nanoparticle (NP) as well as the size of each metal-containing NP in an unknown sample, assuming NPs of a certain shape, i.e., spherical. In order to relate the recorded ICP-MS signal to NP mass and thus NP size, the ICP-MS response to the analyte amount per NP, that is, the sensitivity m, needs to be determined. The determined sensitivity is a function of the analyte mass introduced per dwell time and the detection efficiency n_C, relating to loss of ions upon transmission to the detector, as reported in $Eq.1$. Straight-forward ways to determine the sensitivity m involve the introduction of suspensions of well-characterized spherical monodisperse NPs, containing the same analyte as the target analyte in the unknown NPs, in order to establish a direct relationship between ICP-MS response versus analyte mass per NP size.[5] Other ways involve the introduction of monodispersed aqueous droplets of a well-defined volume, containing the target analyte in dissolved form, using micro-droplet generators.[6,7] In this case, the analyte mass flux introduced per dwell time is known

because of the defined droplet volume, the detection of which occurs as that of a NP, i.e. as a discrete signal intensity pulse. A less-intuitive way for the determination of sensitivity m through the introduction of dissolved standard solutions of the target analyte was introduced by Pace et al.[8,9] This method assumes that the analyte ions resulting from NP ionization and those from the ionization of dissolved species share the same detection efficiency n_C. However, determination of n_{neb} is required in order to account for the incomplete transport of the analyte mass, present either as NPs or as dissolved in solution, via nebulization. n_{neb} is defined as the number of droplets, containing either a NP or dissolved ions, that make their way into the ICP versus the number of droplets generated via nebulization. If n_{neb} is determined, then the mass of the introduced dissolved analyte (mass (fg)/dwell time) can be calculated; thus, allowing for the determination of the sensitivity m and subsequently the analyte mass per NP. The mass of a NP can be determined by using the following relation:

$$M_{NP} = \frac{f^{-1}(I_{NP}-b)}{m} \qquad (Eq.3)$$

, where M_{NP} is the mass of a single NP, f is the analyte mass of the NP, I_{NP} and b represent the NP intensity of the registered signal pulse and the average intensity of the background signal, respectively, and m the ICP-MS sensitivity (typically expressed in counts fg^{-1}) determined with either of the 3 aforementioned approaches. For a NP of spherical geometry, the mass of a NP can be converted to size (nm) using the following relation:

$$NP_{size} = \sqrt[3]{\frac{6M_{NP}}{\pi\rho}} \qquad (Eq.4)$$

, where ρ stands for the density of the particle.

Determination of n_{neb} allows, in turn, for the determination of the nanoparticle number concentration in the analyzed colloid. Several ways have been introduced to determine n_{neb}, one of which is known as the particle counting method or “particle frequency method”.[8–11] Upon aspirating a suspension of well-characterized monodispersed NPs, at a known number concertation, n_{neb} can be determined by counting the number of detected NP signals, with reference to the number of NPs that should be detected considering a n_{neb} of 100%.[8] This method assumes that the NPs in the reference NP suspension used to determine n_{neb} have similar n_{neb} as the NPs present in an unknown sample. While this assumption has not been universally accepted, this method has been demonstrated to work even in cases where the reference NPs had a different metal composition from those of the target analyte NPs.[8,12,13]

Another critical consideration for the validity of sp-ICP-MS is sample dilution. For instance, in their initial demonstration of sp-ICP-MS, Degueldre et al analyzed very dilute Au colloidal suspensions, i.e., 400-4000 particles mL^{-1}. The reason for the analyzed suspensions to be sufficiently dilute is for the detected signal intensity pulses to reflect detection of individual NPs rather than multiple overlapping NPs. An upper tolerable limit of 2000 NPs detected s^{-1} was reported by Hineman et al, by considering that a typical NP signal pulse lasts no more than 0.5 ms, however, this limit does not account for random NP arrival which, in fact, occurs.[14] For a given particle number concentration, the probability of coincidental NP detection per dwell time can be determined using Poisson statistics, assuming random NP arrival to the ICP. [3,15] Since NP arrival rate to the ICP is not only a function of NP number concentration, but also of instrumental conditions such as sample introduction rate and nebulization efficiency n_{neb}, different instrumental conditions require different tolerable NP number concentrations.[13] In a study by Pace et al where coincidental NP detection was determined for different concentrations of AuNP suspensions, it was proposed that a maximum of 10% of the dwell times throughout a sp-ICP-MS acquisition should contain NPs in order for NP coincidence to be kept below 5%. This could be a practical indicator of whether or not an unknown NP-containing sample contains an excessive NP number concentration, and thus requires dilution.

The choice of dwell time for operation of sp-ICP-MS is also important for accurate NP detection. Because NP signal pulses are documented to constitute transient signals, lasting between 200-500 μs, using a dwell time in the range of 1-10 ms, results in ideally recording the intensity of a transient NP signal within a single dwell time.[2,3] Ideally because, if there is an instrument settling time set between successive dwell time measurements, there is a chance that a NP signal may be split between 2 successive dwells. This was, in fact, a limitation of the initial sp-ICP-MS analyses conducted on quadrupole-based ICP-MS which involved settling times between successive dwell times.[16] Split particle detection is even more prominent when dwell times as low as 0.1 ms are used on quadrupole-based ICP-MS instruments involving dead times. Therefore, operation of such instruments for sp-ICP-MS has been typically preferred using 5-10 ms dwell times, minimizing the chance of split-particle detection, while sufficiently low NP number concentrations have been analyzed in order to avoid multiple NP detection per dwell time.[2,12,13,17].However, advances in sp-ICP-MS have gone along with advances in instrumentation, with the newer instruments

exhibiting zero dead time between successive dwell times while also allowing for the use of even shorter dwell times, in the range of µs. [2,3,10]

Continuous sp-ICP-MS analysis using µs-scale time resolution and no dead time between successive dwell times, herein referred to as µs-sp-ICP-MS, is ideal for detecting NPs, the detection of which occurs as short transient signals. Using dwell times ≤ 100 µs, a detected transient NP signal will be comprised of several dwell time intensity readings, which can be integrated to yield the total NP intensity. One obvious advantage of µs-sp-ICP-MS is the capability to capture the time profile of a NP transient signal. Although early studies suggested that the width of the NP time profiles arises mainly from the extent of diffusion of the ion cloud, showing a dependence on isotope mass and residence time within the ICP[3,18], a recent study has demonstrated a link between the width of the detected NP time profiles and NP size.[19] Other benefits of µs-sp-ICP-MS entail decreased coincidence of NP signals, as well as enhanced NP signal-to-background ratios (S/B) compared to ms-time resolution.[20] Moreover, µs-sp-ICP-MS allowed for a deeper investigation of the limited linear range for NP size determination.[2,16,18]. In terms of this, an ICP-MS detector operating in pulse counting mode cannot cope with the increased ion flux produced from the short transient signal of an intense NP pulse, thus resulting in an underestimation of the true NP intensity, and in turn, underestimation of the true NP size. Furthermore, µs-sp-ICP-MS by means of quadrupole-based ICP-MS has allowed for monitoring 2 isotopes per NP, in instruments that allow reduction of the quadrupole settling time.[21] Monitoring 2 isotopes may enable qualitative differentiation of engineered (e.g., containing a single element) from naturally occurring NPs (e.g., containing multiple elements), while the integrated intensities of the 2 recorded transient signals per NP enable calculation of isotopic ratios. It has to be mentioned that µs-time resolution is also the case for TOF-ICP-MS detectors, lending themselves ideally to sp-ICP-MS analyses as they offer multi-elemental detection at a dwell time of 33 µs.[22]

3.1.3 Data processing for sp-ICP-MS analyses

A sp-ICP-MS analysis can provide information on both the analyte in particulate form (NPs) as well as in dissolved form. This is because the dissolved analyte produces a continuous signal, while NPs are registered as discrete signal pulses. This being the case, in a sp-ICP-MS acquisition, a major fraction of the dwell times may have registered signal intensities corresponding to the analyte in dissolved from, while the remaining fraction

registers the sum of a NP intensity plus that of dissolved analyte. In order to quantitate both analyte forms, dwell times registering intensities that correspond to NP detection events have to be separated from those that correspond to the analyte in dissolved form. Several data treatment procedures have been introduced; however, their applicability depends on the dwell time used for sp-ICP-MS acquisition, that is, ms-scale or µs-scale dwell times.

Dwell times in the range of ms, i.e., 3-20 ms, can capture the intensity of the transient signal of an individual NP within a single dwell time, thus resulting in a single intensity data point (d.p.). Using this mode of analysis, the most straightforward strategy to extract intensity d.p.s corresponding to NP detection events from those corresponding to dissolved ions is to graphically represent the recorded intensity d.p.s as a histogram, which may immediately exhibit NPs and dissolved analyte ions as distinct intensity distributions within the same graph. Such a histogram is shown in **Figure 3.1**A, for a suspension of 60 nm monodispersed silver nanoparticles (AgNPs) analysed using sp-ICP-MS with a 10 ms dwell time, where the AgNP intensities (20-70 counts (dwell time)$^{-1}$) can be clearly distinguished from the background signal. However, **Figure 3.1**B demonstrates a clear case where NP and

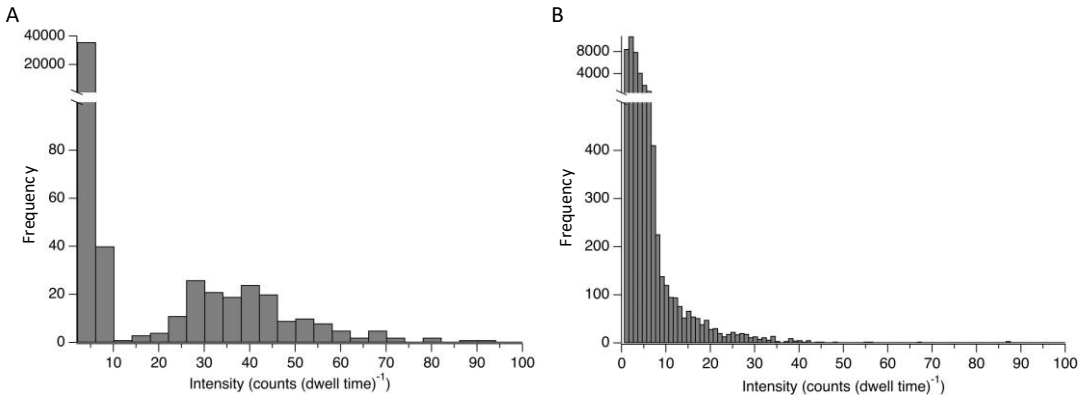

Figure 3.1 A) Histogram of the recorded intensity per dwell time, acquired upon sp-ICP-MS analysis of a 60 nm monodisperse AgNP suspension using a 10 ms dwell time*. B) Equivalent histogram for a seawater sample spiked with 500 ng L^{-1} of 60 nm AgNPs and analyzed 11 days later using sp-ICP-MS with a 10 ms dwell time.

background intensities overlap, therefore an alternative strategy is required to deconvolute the two underlying distributions. Pace et al has introduced a well-established threshold approach, where intensity d.p.s above the average plus 3 multiples of the standard deviation correspond to NP detection events.[23] The procedure is iterative, as it may have to be repeated several times in order to reach a reduced intensity dataset, which will correspond to the intensity distribution of the background signal. This method by Pace et al is hereby

referred as 3σ criterion, and its validity rests on the underlying assumption that the background follows a normal or near-normal distribution. However, further investigation on the performance of the 3σ criterion has demonstrated the occurrence of false positive signals, i.e., signals which are erroneously attributed to NP detection events, resulting in an overestimation of the determined NP number concentration. To cope with this, other authors have proposed a 5σ criterion, i.e., average plus 5 multiples of the standard deviation, as an improved threshold in order to minimize the contribution of false positives in the number of NP detection events.[16,24,25]. Application of these criteria and identification of NP detection events from the background can typically be performed using MS Excel spreadsheets, however, the extracted NP intensity distributions may contain contribution from split NP signals. In order to cope with this, Liu et al introduced a method to account for intensity d.p.s corresponding to split NP detection, when sp-ICP-MS analysis is carried out in the range of 1-20 ms dwell times.[16] By determining the expected ICP-MS response for a given Au NP, dwell times were scanned in order to find those that were adjacent in time and had registered intensities >25% of the expected ICP-MS response for the given Au NP. The intensities of these dwell times were then summed to give the total NP intensity that should have been measured in a single dwell time. However, this method can only be used in suspensions containing NPs of known shape, size and composition, for which well-characterized monodispersed NP standards also exist. A more sophisticated mathematical approach for NP identification was introduced by Cornelis and Hassellöv.[26] These authors proposed a method for mathematically deconvoluting the intensity distribution of dissolved analyte ions from that of NPs, in cases where the 2 intensity distributions overlap either because NPs occur in small sizes that are barely detectable or the background signal intensity is high. The proposed deconvolution method was based on modelling the intensity distribution of the continuous background signal with a Polyagaussian function, a compound function combining Polya and Gaussian statistics which could account for shot and flicker noise observed for dissolved analyte signals at low and high intensities, respectively.[27] The histogram data of the fitted background intensity distribution were then subtracted from the complete histogram, initially containing dissolved and NP intensities, in order to extract the NP detection events. This mathematical method pushed NP size LODs down to 10 and 15 nm for Au NPs, which could not be achieved using the σ criterion methods. In addition, along with the advances in detection electronics, allowing for uninterrupted dwell time measurements per isotope, ICP-MS manufacturers have also released software modules in

order to automate data treatment procedures for sp-ICP-MS analysis.[3] Such a module is Syngistix™ Nano Application software module v 2.5, employing a 3σ criterion in order to distinguish NP detection events from the continuous dissolved/background intensity distribution.[28,29]

Using μs-sp-ICP-MS involves capturing a NP transient signal within several dwell times, i.e., collection of multiple intensity d.p.s per NP signal, therefore the majority of the data treatment approaches developed for ms-scale sp-ICP-MS are not applicable. Analysis using μs-sp-ICP-MS typically generates millions of intensity d.p.s per acquisition, rendering NP transient signal identification and integration extremely difficult to perform using typical spreadsheet commands. For instance, 180 s of acquisition using a 75 μs dwell time consists of 2.4 million intensity d.p.s, when typical spreadsheet limits reach only a million; not to mention serious software performance drop when executing commands at the million data point levels.[10] Hence, all data treatment platforms tailored for μs-sp-ICP-MS have been built on powerful algorithms and programming languages.[30–33] The need of research groups, in the field of sp-ICP-MS, to develop their own platforms stems from the fact that there has not yet been a widely accepted platform for μs-sp-ICP-MS, both at the level of NP signal identification and integration as well as background signal determination. Tuoriniemi et al were the first to report on such a platform, built in Matlab.[30] Briefly, the procedure involved determination of intensity d.p.s that corresponded to peak maxima by finding the zero-crossing points of the first derivative of the recorded signal (i.e., the difference in signal intensity between adjacent dwells is first positive, and then negative), followed by integration of intensity d.p.s surrounding the peak maxima within a certain width, and determination of the signal intensity corresponding to the background using a 5σ criterion. Instrument manufacturers, such as Nu and Perkin Elmer, have also introduced software featuring automated real-time data processing of μs-sp-ICP-MS data, where intensity d.p.s greater than a σ or 3σ criterion are integrated as NP detection events.[29,34] For instance, in a technical note showcasing the capabilities of Nu AttoM ES in μs-sp-ICP-MS, Shaw et al reported an algorithm involving signal smoothing, determination of the peak maxima for dwell times with intensities greater than a multiple of the background σ, and determination of the nearest peak minima to ultimately define the NP transient signal.[34] Although all the aforementioned methodologies rely on a statistical σ criterion to isolate intensity d.p.s corresponding to NP detection, it has been observed for μs-sp-ICP-MS that the continuous background signal distribution follows a Poisson distribution at low average count values

rather than a Gaussian distribution; thus requiring that thresholds for NP signal identification be reinvestigated.[31,35]

Detection criteria L_D enabling decision for the occurrence of an analyte in an analyzed sample were introduced by Lloyd A. Currie, and adopted by IUPAC, for Gaussian and Poisson-distributed detection signals.[36,37] Briefly, for normally distributed signals, that is, assuming equal variances for a blank and an analyte recorded signal, a critical limit,

$$L_c = k_a \times \sigma_b \qquad (Eq.5)$$

, is defined within a 95% confidence level that the recorded signal reflects the blank, while a detection limit (L_D)

$$L_D = 2L_C \qquad (Eq.6)$$

is defined within a 95% confidence level that the recorded signal reflects the analyte; k_a representing the t-critical value of a one-sided student-t test and σ_b the standard deviation of the blank signal. For infinite degrees of freedom,

$$L_D = 3.29 \times \sigma_b \qquad (Eq.7)$$

provided that the standard deviation of the blank is well-known. If not, replicate observations of blank and analyte, i.e., $n = 2$, can yield a variance estimate of $\sigma_b/\sqrt{n}$, and thus an

$$L_D = 4.65 \times \sigma_b \qquad (Eq.8)$$

can be computed. These 2 expressions of L_D can be adjusted for low-count Poisson-distributed signals by adding a term of 2.71 for modified L_D expressions, i.e., $(Eq.9)$ and $(Eq.10)$.

$$L_D = 2.71 + 3.29\sqrt{b} \qquad (Eq.9)$$

$$L_D = 2.71 + 4.65\sqrt{b} \qquad (Eq.10)$$

$Eq.9$ and $Eq.10$ are derived from a Poisson-Gaussian (P-G) approximation; σ_b is exchanged for the square root of the average blank signal b, since a Poisson distribution presupposes equality of the mean and variance of the signal. Critical levels are defined as:

$$L_C = 1.64\sqrt{b} \qquad (Eq.11)$$

$$L_C = 2.33\sqrt{b} \qquad (Eq.12)$$

for cases of a well-known background and replicate observations, respectively. Currie et al introduced these expressions for low-count Poisson signals recorded in radiochemistry. Recently, Mozayeva et al proposed that intensity thresholds set by $Eq.9$ & 10 can be used to distinguish NP detection events from the continuous background signal, the average

value of which may constitute even a fraction of 1 count in µs-sp-ICP-MS; thus it may be approximated as a low-count Poisson-distributed blank signal b.[31] In developing an in-house data treatment method for µs-sp-ICP-MS, these authors compared the values of L_c and L_D obtained from an exact Poisson distribution of the background signal with the corresponding L_c and L_D calculated using $eq.11\ \&\ 12$ and $eq.9\ \&\ 10$, respectively. The exact L_c and L_D values derived from the Poisson treatment required calculation of the cumulative Poisson distribution for each given value of b, however, it was demonstrated that L_c and L_D can be calculated with adequate accuracy using $Eq\ 10\ \&\ 12$ for b values<5 counts (dwell time)$^{-1}$, as well as using equations $Eq\ 9\ \&\ 11$ for b values>5 counts (dwell time)$^{-1}$. Upon determination of b, a data processing method, written in "C" programming language, could isolate a silver nanoparticle (AgNP) transient signal as soon as its rising edge reached L_D, followed by its falling edge reaching L_c.[31] In a similar fashion, Lockwood et al developed a method, written in "Python", for data treatment of µs-sp-ICP-MS, enabling the use of a P-G filter for accurate NP signal identification in the presence of low intensity background signals.[32] The utility of the P-G filter was demonstrated in the analysis of a dissolved Au standard using µs-sp-ICP-MS at a dwell time of 100 µs, where the P-G filter almost completely eliminated the false positive signals that were otherwise integrated if using a Gaussian 3σ or 5σ criterion. Ultimately, the method was used to track titanium dioxide nanoparticles (TiO_2) in a freshwater sample using µs-sp-ICP-MS/MS (triple quadrupole-based ICP-MS allowing for selective monitoring of titanium (Ti) at the m/z of 64, i.e., $^{48}Ti^{16}O$).

To the best of our knowledge, none of the reported µs-sp-ICP-MS data processing methods has been validated for NP and dissolved analyte quantitation in the analyzed samples. Validation can be performed through mass balance comparisons, that is, comparing the NP and dissolved analyte mass concentration determined using µs-sp-ICP-MS with those theoretically present in the sample, i.e., through addition of known analyte amounts.

3.1.4 Chemical behavior of AgNPs in seawater

According to a recent version of the Nanotechnology Consumer Products Inventory (CPI 2013) ("Project on Emerging Nanotechnologies (2013). Consumer Products Inventory"), out of all the commercial products that contain engineered NPs, 24% make use of AgNPs, whereas a vast 49% corresponds to nanomaterials of unknown composition [39]. As a result of their extensive use, AgNPs are continuously being introduced into the environment at an

ever-increasing rate. This tendency is a reason for concern, and thus several studies have already been conducted to investigate the fate of AgNPs in environmental systems, including marine ecosystems, focusing on the potential of engineered metal-containing nanoparticles to cause harm to marine organisms [40] and human health [41].

Several studies have examined the behavior and fate of AgNPs both in freshwater and seawater systems, and have provided valuable information. One of these studies investigated the persistence of 20 nm citrate-capped AgNPs in natural freshwaters and synthetic seawater by using a combination of UV-Vis absorbance, dynamic light scattering (DLS) and atomic force microscopy (AFM) [42]. AgNPs dispersions were studied at NP concentration of 1.4×10^{10} mol L^{-1}, which corresponds to a Ag concentration of 3.7 mg L^{-1}, with the assumption of spherical monodisperse 20 nm AgNPs. Results from UV-Vis measurements have demonstrated that AgNPs exhibit the most rapid colloidal instability in the presence of seawater as the absorbance at λ_{max} diminished by 80% after just 1 hour of exposure in seawater. While agglomeration was suggested to contribute to the observed particle instability because of excessive sodium chloride concentrations and the presence of divalent cations normally present in seawater, chemical reactions of elemental Ag in NPs that suppress surface plasmon resonance and thus contribute to the disappearance of the absorbance at λ_{max} could not be excluded. More recent studies on AgNPs transformation have revealed that their dissolution occurs once nanoparticles are exposed to seawater. One such study reported on the release of ionic Ag species in ultrapure water, lake water and seawater, that had been spiked with 0.1 mg mL^{-1} of AgNPs suspensions in the form of a Ag nanopowder and incubated for 1 week [43]. More specifically, the AgNP exposed samples were filtered using alumina membrane filters (20 nm cut-off size), which resulted in the separation of the dissolved Ag species, along with AgNPs occurring in sizes below 20 nm, from the larger-sized Ag nanopowder particles. The former passed into the filtrate, whereas the latter remained on the filter membrane. Inductively coupled plasma – mass spectrometry (ICP-MS) used for the determination of the total amount of Ag recovered in the seawater filtrate showed a 5- and 10- fold increase, compared to that of lakewater and ultrapure water filtrates, respectively. This increase in the determined Ag concentration was mainly attributed to ionic species resulting from the oxidation of elemental Ag. In addition, high-resolution X-ray photoelectron spectra (XPS) obtained from the sample residues on membrane filters indicated the exclusive presence of metallic Ag, which was found to be significantly lower for seawater as opposed to lake water and ultrapure water; thus,

supporting the higher transformation of AgNPs to ionic Ag species in seawater. Another study reported on the use of UV-Vis spectroscopy and ICP-MS in order to quantitate AgNP transformation in synthetic seawater to which polyvinylpyrrolidone (PVP)-coated AgNPs had been added at concentrations ranging between 25-1500 μg Ag L^{-1} throughout a 96-hour time period [44]. These results showed a concentration-dependent AgNP dissolution rate. This was substantiated by the higher and more rapid release of ionic Ag for the lowest 25 μg Ag L^{-1} exposure concentration, in which case the recovered ionic Ag concentration reaches 83% of the total Ag input within 48 hours. A faster and higher rate of decrease in the determined AgNPs size was also observed, while dissolution rates of AgNPs were observed to decrease with increasing AgNP concentrations. To explain the slower AgNPs dissolution that occurs when high AgNP concentrations are studied, as opposed to lower ones, the authors associated the concentration of $AgCl_x^{1-x}$ species (x=2, 3) with the concentration gradient of Ag^+. More specifically, $AgCl_x^{1-x}$ complexes, such as $AgCl_2^-$, and $AgCl_3^{2-}$, are predominantly formed in seawater due to the high chloride concentration. Ag^+ is formed on the surface of AgNPs as a result of the oxidation of metallic Ag, and subsequently diffuses to the bulk solution because of the concentration gradient of Ag^+ between the surface of Ag NPs and the bulk solution. In terms of this, the dissolution of AgNPs for generation of Ag^+ supplies the formation of soluble $AgCl_x^{1-x}$ complexes, and hence the formation of $AgCl_x^{1-x}$ complexes maintains the concentration gradient of Ag^+. It is likely that higher concentration of AgNPs results in saturated concentrations of $AgCl_x^{1-x}$ complexes and thus in a decreased concentration gradient, which may explain the slower dissolution rates of AgNPs at high concentrations. Previous work from our group on a seawater microcosm experiment regarding the persistence of 60 nm Ag NPs (branched polyethylenimine (BPEI) and PVP coated), added at concentrations of 200 and 2000 ng L^{-1}, has demonstrated that particle dissolution is the predominant process when these nanoparticles are exposed to seawater [45]. This was supported by an observed decrease in NP size and Ag mass contained in the NPs, as well as the increased concentration of dissolved Ag throughout these time series experiments.

Although all of the aforementioned studies provide evidence on the dissolution of AgNPs in seawater, they still do not provide an accurate picture of AgNP transformation in natural seawater, especially because in most cases the AgNPs have been added at high concentrations, which may be environmentally irrelevant. Modelled predictions of environmental discharges of engineered nanomaterials into surface waters indicate

expected nano-Ag concentrations up to ng Ag L^{-1} levels [46,47]. To the best of our knowledge, only a limited number of publications so far reported findings on AgNPs transformations near such environmentally relevant concentrations. More specifically, previous research involving a large-scale seawater mesocosm experiment was conducted by our group, in which 100 ng Ag L^{-1} were added daily as 60 nm AgNPs (BPEI-coated) to the system up to a final concentration of 1000 ng Ag L^{-1} [48]. Results clearly suggested that NPs started to dissolve immediately once exposed to seawater. This could be observed using sp ICP-MS, even though fresh amounts of 60 nm AgNPs were added to the system each day. Further, reducing the amount of particulate Ag added to seawater to 50 ng Ag L^{-1}, Wimmer et al. have investigated the fate of silver-based NPs (citrate-coated, silver sulfide and silver chloride) in seawater at low ng Ag L^{-1} levels [49]. By using cloud-phase extraction (CPE) combined with sp ICP-MS measurements in seawater exposed to AgNPs for 72 h, they demonstrated that only 1-9 % of the initial NP number resisted dissolution. While both of these studies provide valuable insight into AgNP seawater transformation, challenges and questions still remain. More specifically, in the work of Tsiola et al., slightly elevated AgNP concentrations, 1000 ng L^{-1}, were reached during the last days of the study. Also, quantitation of dissolved Ag species was conducted using a time-consuming extraction procedure. Elaborate sample pretreatment is also required for the CPE methodology, especially when a significant number of samples need to be analyzed in short periods of time. In addition, there is a need for a complete methodology, which could rapidly provide information on the fate of AgNPs and dissolved Ag in a seawater system, at the low ng L^{-1} level, by simultaneously analyzing the sample in its native state and without the need for sample manipulation prior to analysis; ideally also offering information about the sample's nanoparticulate and ionic content in a single analysis.

3.1.5 Objective

The objective of the research described in this chapter is the development of a data processing method (DP-µs-sp-ICP-MS) which can be used to perform sp-ICP-MS analysis by means of a µs-scale dwell time (µs-sp-ICP-MS). Unlike the use of dwell times in the ms-scale, elemental isotope intensities recorded using µs-sp-ICP-MS require more advanced and specialized processing in order to yield meaningful results, including elemental mass per nanoparticle (NP), NP size, NP number concentration, as well as elemental concentration of the analyte occurring as NP or dissolved in the suspension. Despite the

considerable advancements in data processing methodologies for µs-sp-ICP-MS, the existing methodologies lack a systematic validation in quantitating NP and dissolved analyte concentration across a range of concentrations. Herein, the developed DP-µs-sp-ICP-MS is used to process sp-ICP-MS raw data obtained using a 75 µs dwell time. Evaluation of the performance of DP-µs-sp-ICP-MS is carried out by comparing the determined analytical metrics, including NP transport efficiency, NP recorded intensity, as well as particulate and dissolved silver (Ag) mass concentration, to those determined using the well-documented sp-ICP-MS analysis by means of a 10 ms dwell time. In addition, through the analysis of seawater samples containing known amounts of Ag, added as 60 nm AgNPs, determination of total Ag mass concentration recoveries allows for a systematic validation of DP-µs-sp-ICP-MS across a concentration range of 50-500 ng Ag L^{-1}. Ultimately, the developed DP-µs-sp-ICP-MS is applied to study the chemical behavior of Ag, in the form of branched-polyethyleneimine (BPEI)-coated 60 nm AgNPs and ionic, throughout an 11 day-exposure seawater mesocosm experiment.

3.2 Materials and Methods

3.2.1 Development of a data processing method for µs-sp ICP-MS

Detection of metal-containing nanoparticles (NPs) using sp ICP-MS occurs as individual transient signals, documented to typically last between 200 to 500 µs. [2,3] Due to their short duration, these NP transient signals will herein be referred as signal spikes. Handling of the raw intensity data obtained using µs-dwell times for sp ICP-MS is challenging, both at the level of accurately identifying a nanoparticle (NP) signal spike from the background as well as at the level of determining its total intensity. These challenges are less obvious when sp ICP-MS is operated using ms-scale dwell times, where the total intensity of a NP transient signal corresponds to a single intensity data point and thus NP signals can more conveniently be filtered as outliers above a background signal. Hence, development of the data processing method for µs-sp ICP-MS (DP-µs-sp-ICP-MS) involved 4 major steps, that is, identification of signal spikes from the background, determination of the average background intensity (b) corresponding to the dissolved elemental concentration, determination of the peak area (PA) for each signal spike, and filtration of signal spikes corresponding to NPs from false positive detection events. For simplicity throughout this chapter, referring to sp-ICP-MS analyses will be written in the following style: (dwell time

value in µs or ms)-sp-ICP-MS, i.e., 75 µs-sp-ICP-MS for analyses carried out using a 75 µs dwell time or 10 ms-sp-ICP-MS for analyses carried out using a 10 ms dwell time.

Identification of signal spikes and determination of their corresponding peak area (PA) was conducted on Igor Pro 9.01 (WaveMetrics) software, enabling the use of macros for identification and integration of multiple signal peaks. All raw intensity data analyzed using the developed DP-µs-sp-ICP-MS were recorded throughout 75 µs-sp ICP-MS sample analyses/acquisitions conducted on a NexION 350x ICP-MS using the Syngistix™ Nano Application software module (Perkin Elmer), which allows for acquiring continuous isotope intensity data points at a dwell time of 75 µs without the occurrence of dead time between adjacent dwell times. More specifically, the raw data, obtained in csv-type format from a 75 µs-sp ICP-MS sample analysis, were loaded onto the Igor Pro 9.01 software interface as x, y waves; y-wave being the intensity recorded per dwell time (x-wave). For instance, plotting y vs x generates the signal trace of the isotope which was monitored within a given µs-sp ICP-MS acquisition. An existing Igor Pro procedure, i.e., PeakAreasUnipolar.ipf was loaded onto the software interface in order to allow for the automated processing of the x, y dataset. For peak identification, the software scans the y-data looking for local minima and maxima, and generates 2 new waves assigned as W_MinKnots and W_MaxKnots for local minima and maxima, respectively. For an identified peak, 2 W_MinKnots data points would represent the 2 baseline points, while 1 W_MaxKnot represents the peak amplitude, that is, the maximum intensity recorded for a signal spike. Determination of W_MinKnots and

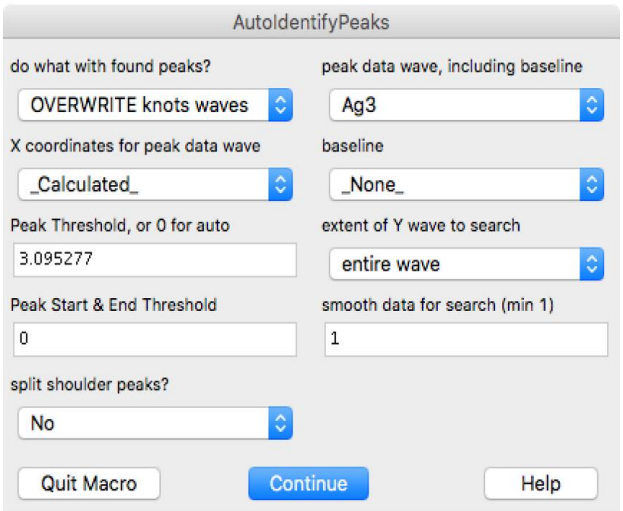

Figure 3.2 Dialog box, invoked by the peak identification macro, showing the parameters set for the identification of signal spikes detected throughout a µs-sp ICP-MS acquisition of a calibration solution containing 60 nm AgNPs.

W_MaxKnots requires the input of 2 thresholds, the Peak Threshold as well as Peak Start & End Threshold. The former relates to the rejection of signal spikes with amplitude lower than a defined intensity-y, while the latter relates to the baseline. These are shown in **Figure 3.2**, showing a dialog box invoked by the peak identification macro.

For the 75 µs-sp ICP-MS analyses conducted throughout this study, the Peak & End Threshold was set to zero because of the extremely low background intensities, the distribution of which has been demonstrated to be Poisson.[31] The latter is also supported by the recorded intensity (y-wave), comprising of positive integer values, such as 0, 1, 2, as is shown in the relevant histogram (**Figure 3.3**) of the recorded ^{107}Ag intensities, obtained during the analysis of a reference NP suspension, containing 60 nm silver nanoparticles (AgNPs) in seawater. Analysis was conducted using 75 µs-sp ICP-MS. The frequency axis in **Figure 3.3**A shows the the number of dwell times containing a given intensity, i.e., the frequency at which individual intensity d.p.s are recorded, and by expressing it as a percent relative frequency in **Figure 3.3**B, it is demonstrated that the majority of the intensity d.p.s (~98%) were found to have an intensity value of 0 counts (gray bars in **Figure 3.3**B). This

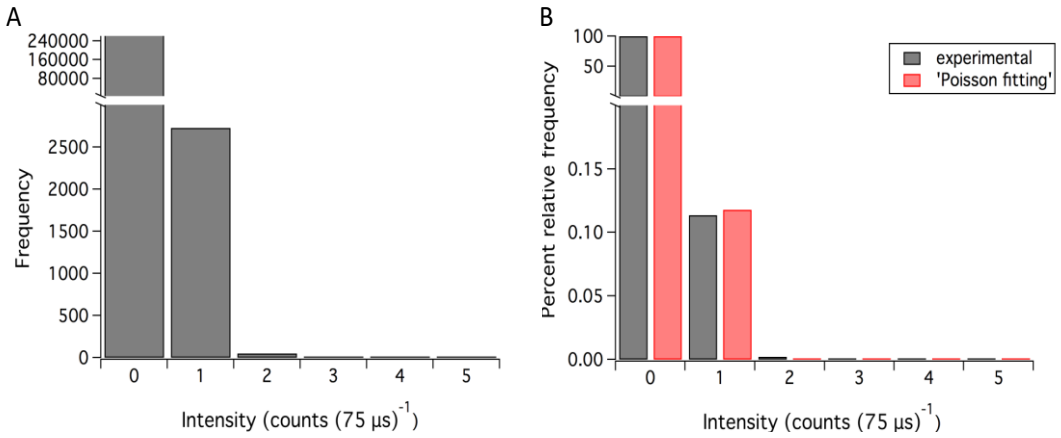

Figure 3.3 Panel A is a histogram of the ^{107}Ag intensities recorded throughout a 75 µs-sp ICP-MS acquisition of a reference NP suspension, containing 60 nm AgNPs in seawater. The absolute frequency observed for each detected intensity is subsequently transformed into a % relative frequency distribution, as shown in panel B. The % relative frequency distribution (panel B) is then compared to a theoretical Poisson distribution with an average value of 0.0068 counts, which is what was determined for the distribution of panel A. As the average value of the recorded intensity is extremely low (approaching 0 counts), and thus intensity d.p.s corresponding to the background signal exhibit the highest frequency (e.g., 0 counts), intensity d.p.s > 1 counts occur in negligible frequencies. For this reason, a limited intensity range of 0-5 counts (75 µs)$^{-1}$ is shown.

explains why the average value of the recorded intensity distribution is extremely small, e.g 0.0068 counts. Moreover, the theoretical frequency ("Poisson fitting") of the recorded intensity values was determined, assuming that these values are governed by a Poisson distribution with an average value of 0.0068 counts. It can be observed that the theoretical frequencies (red bars in **Figure 3.3**B) fit well to the frequencies observed experimentally throughout the given 75 µs-sp ICP-MS acquisition.

As we and others have observed that µs-sp ICP-MS result in Poisson distributed signal intensities [31,32], the Peak Threshold was determined using the following formula:[36]

$$L_D = 2.71 + 4.65\sqrt{b} \qquad (Eq.10)$$

, b representing the average background intensity. This formula has been proposed by Mozhayeva et al. to be used for the determination of the limit of detection in sp ICP-MS using µs dwell times, when the intensity distribution of the background signal is governed by Poisson statistics at average b intensities < 5 counts. In this study, the average b required for setting the Peak Threshold was calculated in 2 ways. The one involved extraction and subsequent averaging of the background intensity dataset obtained from the 75 µs-sp ICP-MS analysis of a given sample, according to the 3σ iterative method proposed by Pace et al.[23] This way seems to also be followed by the Syngistix™ Nano, while also allowing for a recalculation of b based on a user-set threshold, i.e., 5σ.[29] The 2nd way required a supporting 10 ms-sp ICP-MS acquisition of the same sample, previously analyzed with 75 µs-sp ICP-MS, in order to extract the average b in counts s^{-1} and subsequently determine the corresponding b in counts $(75\ \mu s)^{-1}$, a strategy which was implemented by Mozayeva et al.[31] Both ways are tested and discussed with respect to the quantitation of AgNP and dissolved Ag in seawater samples, analyzed in the framework of a mesocosm seawater experiment.

The dialog box in **Figure 3.2** also allows for setting a smoothing factor for signal smoothing prior to peak identification. A minimum value of 1 was set, as higher values resulted in a loss of low intensity signal spikes which were slightly above the Peak Threshold.

The identified set of signal spikes are subsequently integrated in order to extract the total intensity of each NP transient signal. The total intensity corresponds to the Peak Area (PA) determined by Igor Pro. **Figure 3.4** demonstrates the dialog box invoked for peak integration. The integration type can be set as either counts or trapezoidal, while measurement of the PA is carried out relative to a 0-count baseline. A 0-count baseline was

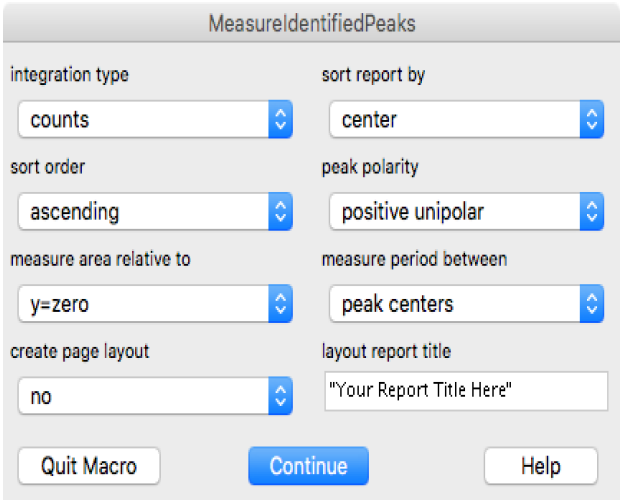

Figure 3.4 Dialog box, invoked by the peak integration macro, showing the parameters set for measurement of the peak area of the detected signal spikes detected throughout a 75 µs-sp ICP-MS acquisition of a reference suspension of 60 nm AgNPs.

used for integration because all samples analyzed in this chapter had average background intensities ~0 counts, with the highest being 0.013 counts. Counts-type integration is conducted by summing the constituent intensity data points of the transient NP signal, and trapezoidal integration by summing the area of the trapezoids contained within the transient signal. After measurement, results are accumulated in a report table, compiling the peak amplitude, PA and the integration limits (i.e., the 2 baseline points determining each signal spike).

A final processing step is needed in order to filter the signal spikes corresponding to NP detection from those which were false positives. As a NP transient signal is documented to last between 200-500 µs, quantitative NP results are reported with higher confidence when the detected signal spikes have durations within the documented range. For instance, using 75 µs-sp-ICP-MS, signal spikes determined by a total of 3 data points (2 data points found in the baseline plus 1 exceeding the L_D) are found to have a duration of 150 µs, and are thus considered false positives. The occurrence of these false-positive signal spikes could be attributed to a random fluctuation of the background, possible due to shot noise.[50] By employing an Excel macro, built in-house using Visual Basic, integrated signal spikes lasting above 150 µs were conveniently filtered as NP detection events. A baseline duration of 150 µs meant that signal spikes with only 1 dwell time intensity above the threshold, could not qualify as NP detection events. Recording the time profile of each NP detection event allowed for the investigation of a possible link between NP size and transient signal duration.

The measured peak areas (PA) of the compiled NP detection events undergo background subtraction in order to determine the net intensity corresponding to each NP detection event. Background subtraction was conducted according to the following calculation: PA-(# d.p.s × b), where # d.p.s stands for the number of intensity data points that each signal spike is comprised of, and b the average background intensity.

3.2.2 Evaluation of the data processing method for μs-sp ICP-MS

The performance of DP-μs-sp-ICP-MS was initially evaluated with respect to AgNP detection upon analysis of a reference 60 nm AgNP suspension using 75 μs-sp-ICP-MS. The reference NP suspension, which was prepared in seawater at a Ag concentration of 100 ng L^{-1}, was also analyzed using 10 ms-sp-ICP-MS, the raw data of which were processed using the Syngistix™ Nano (automated sp-ICP-MS software provided by Perkin Elmer) through the application of a 5σ criterion. Results on the determined NP transport efficiency, expressed as a percentage of the number of NPs detected relative to the number of NPs introduced, as well as the determined NP intensity, expressed as the average value of all NP intensities recorded per sp ICP-MS acquisition, are compared for the 2 methods. This was done in order to evaluate the DP-μs-sp-ICP-MS, granted that sp ICP-MS analysis using a 5-20 ms dwell time is a well-documented and accepted methodology for the analysis of NPs.[12,23,25,51–53] Also, several studies have used specifically a 10 ms dwell time to determine AgNPs in freshwater and seawater samples.[45,51,54]

3.2.3 Quantitation of nanoparticulate and ionic Ag in seawater mesocosm samples using μs sp ICP-MS

Once its potential in NP quantitation was evaluated, the DP-μs-sp-ICP-MS was used for the quantitation of nanoparticulate and ionic Ag, added at known amounts in seawater tanks. More specifically, Ag nanoparticles (Ag NP) and ionic Ag (Ag^+) were added into separate seawater systems at low parts per trillion silver concentrations (50 ng Ag L^{-1}), on a daily basis. The daily addition of AgNP and Ag^+ in the seawater tanks was part of a large-scale experiment, with the title ‘’Addressing the impacts of a low-dose addition of silver nanoparticles vs. silver ions in a coastal marine ecosystem’’, conducted under the ‘’Aquacosm’’ project (European network of mesocosm facilities). Quantitation of AgNPs and dissolved Ag on a daily basis, throughout the 11 mesocosm days, was required in order to monitor the chemical transformation of these 2 silver species. Extensive details on the

design and implementation of the seawater mesocosm experiment are provided in a study by Scheidemann et al. [55]

Samples from 9 tanks, 3 of which served as controls, 3 spiked daily with 50 ng Ag L^{-1} in the form of 60 nm branched-polyethyleneimine (BPEI)-coated AgNPs, and 3 spiked with 50 ng Ag L^{-1}as ionic silver (Ag^{+}), were analyzed daily using 75 μs-sp ICP-MS, and the generated raw data of each sample acquisition were treated using the developed DP-μs-sp-ICP-MS. The raw data obtained from the daily analysis of calibration standards prepared in seawater, including a reference suspension of 60 nm BPEI-coated AgNPs at a concentration of 100 ng Ag L^{-1}, and solutions of Ag^{+} at concentrations of 0.5-1 μg L^{-1}, were also analyzed using DP-μs-sp-ICP-MS. The 60 nm AgNP suspension served as calibrant for NP size and for the determination of the transport efficiency, while Ag^{+} standards served for the quantitation of the dissolved Ag concentration. Finally, a complete set of analytical metrics, including the mean NP size (nm), nanoparticle number concentration (parts mL^{-1}), dissolved Ag concentration (ng L^{-1}) and the observed mean duration per nanoparticle signal, are provided for each sample acquisition. The analytical metrics for each mesocosm day are derived by averaging the results obtained from the 6 individual sample acquisitions (2 acquisitions per mesocosm tank $\times$ 3 mesocosm tanks).

Data acquisition for 75-μs-sp-ICP-MS and 10-ms-sp-ICP-MS was possible by using the Syngistix™ Nano, enabling the collection of sp-ICP-MS raw data in a continuous time resolution fashion, i.e., without dead time between successive dwell times. The raw data acquired using 75-μs-sp-ICP-MS were processed using the developed DP-μs-sp-ICP-MS, while the raw data acquired using 10-ms-sp-ICP-MS were automatically processed by the Syngistix™ Nano through the application of a 5σ criterion. Quantitative results, such as Ag mass balance, AgNP size and number concentration, obtained using the latter are reprinted with permission from Michail-Ioannis Chronakis, “Investigating the occurrence and fate of metal nanoparticles in seawater systems using single particle inductively coupled plasma - mass spectrometry” (Master's degree thesis, University of Crete, Heraklion, Greece). Retrieved from https://elocus.lib.uoc.gr/dlib/e/b/3/metadata-dlib-1627642905-276941-16290.tkl l, retrieved on 21.03.2023.

3.3 Results and Discussion

3.3.1 Analysis of a reference 60 nm AgNP suspension

For proof of principle, the developed data processing method for µs-sp-ICP-MS (DP-µs-sp-ICP-MS) was evaluated for the analysis of a reference nanoparticle suspension using 75-µs-sp-ICP-MS. A ^{107}Ag intensity trace resulting from the analysis of a reference 60 nm AgNP suspension is provided in **Figure 3.5**. The suspension was prepared in seawater, at a Ag concentration of 100 ng L^{-1}, which corresponds to ~84289 NPs mL^{-1} assuming spherical monodisperse 60 nm AgNPs. The ^{107}Ag trace can be obtained by plotting the intensity d.p.s versus the number of dwell times (2.4×10^6) contained in a 3 min acquisition. Peak parameters, i.e, W_BaseKnots, W_PeakKnots corresponding to the peak minima and maxima, respectively, are appended to the graph upon completion of the signal spike

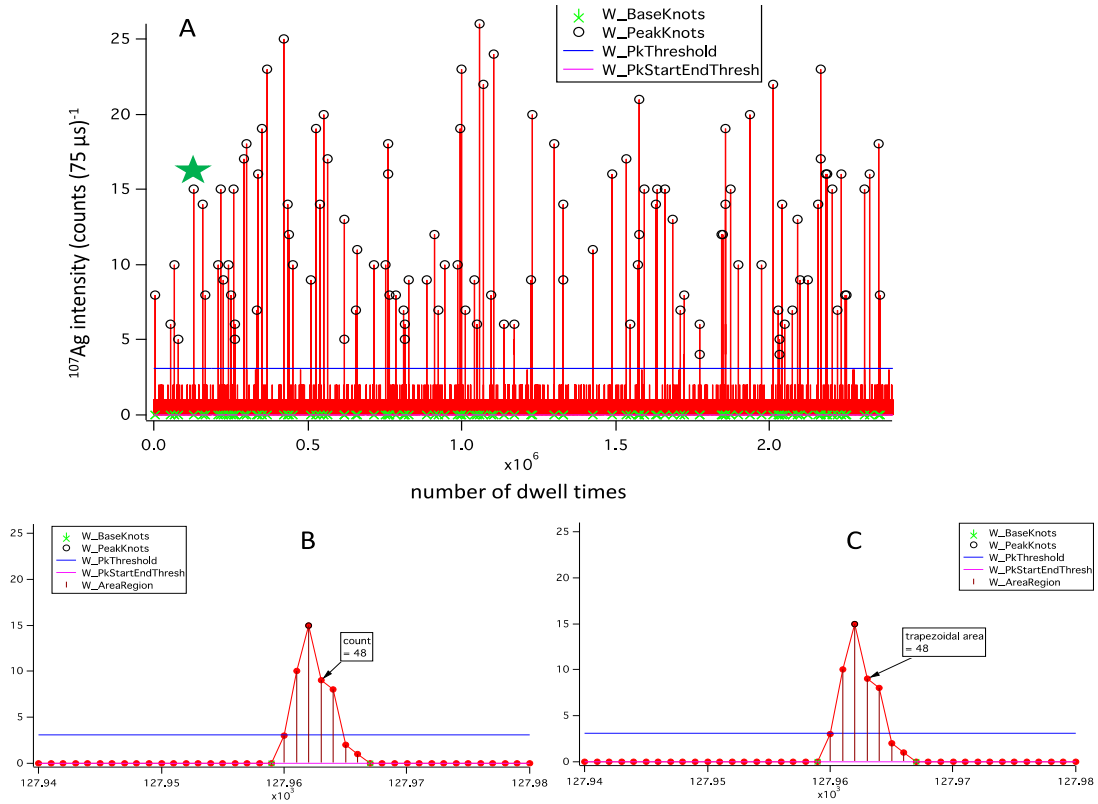

Figure 3.5 ^{107}Ag trace resulting from the analysis of a 60 nm AgNP suspension using 75 µs-sp-ICP-MS. The ^{107}Ag trace (A) is generated after the raw ICP-MS ^{107}Ag intensity data are imported into Igor Pro and further handled for signal spike identification. The AgNP suspension was prepared in seawater at a concentration of 100 ng Ag L^{-1}. Panels B, C are zoomed insets of a green asterisk-marked NP signal spike shown in panel A, with a typical duration of 600 µs, integrated using intensity data point summation (counts) or trapezoidal integration. The blue line represents the peak threshold, shown in **Figure 3.2** and determined using $Eq.10$.

identification step. For this acquisition, the average ^{107}Ag intensity was found to be 0.0068 counts, corresponding to an L_D of 3.095 (denoted as W_PkThreshold) which seems well suited in identifying all the apparent signal spikes sitting above the background intensity; the latter comprising of 0, 1, 2, 3 count values. A typical NP transient signal, marked with an asterisk in **Figure 3.5**A, is revealed in both of the 2 zoomed insets B or C. Because the transient NP signal is recorded over 8 dwell time periods, 75 µs each, its duration is found to be 600 µs. Within this 3 min acquisition, 112 NP signals were identified, showing an average duration of 611 $\pm$ 172 µs; the uncertainty expressed as the standard deviation of the duration of all identified NP signal spikes. The total intensity (NP peak area) of the NP transient signal can be determined by either summing the constituent intensity data points or by trapezoidal integration. Insets B, C indicate that both integration methods produce similar values.

By averaging the NP peak areas of the 112 NP signal spikes detected, an average value of 39.7 $\pm$ 15.3 counts was found. Moreover, by expressing the number of NPs (112) detected within the 3 min acquisition relative to the number of NPs introduced over 3 min (~5057 NPs introduced, given a concentration of ~84289 NPs mL^{-1}, and a sample introduction rate of 20 µL min^{-1}), the percentage transport efficiency (TE%) of the sample introduction system was found to be 2.2%. Results on the average NP peak area and TE% obtained using the DP-µs-sp-ICP-MS for ten replicate 75-µs-sp-ICP-MS acquisitions of a reference 60 nm AgNP suspension are compared with those obtained using the Syngistix™ Nano software for equivalent 10-ms-sp-ICP-MS acquisitions that were processed with the application of a 5σ criterion (**Table 3.1**). The two data processing methods are abbreviated as DP-^{75}µs-sp-ICP-MS and DP-5σ-^{10}ms-Syngistix™ Nano. It has to be mentioned that the raw data used for each couple of DP-^{75}µs-sp-ICP-MS and DP-5σ-^{10}ms-Syngistix™ Nano analyses were obtained on a separate analytical day using a freshly prepared 60 nm AgNP suspension, which is likely the reason for the observed day to day variation in the reported values. This is because the observed spread of the values for each technique does not reflect the technique's precision within-run replicates, but rather the technique's precision between run-replicates, i.e., the technique's reproducibility which is usually associated with greater spread of the experimental results. [56] Nevertheless, results for NP peak area and TE%, expressed as the average of 10 individual measurements, demonstrate very good agreement between the 2 methods. In addition, a significance two-sided paired-t test was employed for comparison of both methods, reporting an absolute t-value of 1.27 and 2.07

for NP peak area and TE%, respectively. The reported t-values are lower than the 2-sided t-critical values of 2.62, for 9 degrees of freedom, revealing that discrepancies between DP-^{75}µs-sp-ICP-MS and DP-5σ-^{10}ms-Syngistix™ Nano are not statistically significant. Hence, the reported comparison indicates the potential of DP-^{75}µs-sp-ICP-MS to be used as an independent data processing method for sp-ICP-MS analysis, especially when the time profiles of NP detection events need to be recorded.

Table 3.1 Comparison of DP-^{75}µs-sp-ICP-MS and DP-5σ-^{10}ms-Syngistix™ Nano with respect to the average recorded NP intensity (NP peak area) and % transport efficiency (TE%), obtained from sp-ICP-MS analyses (n=10) of a reference 60 nm AgNP at a concentration of 100 ng Ag L^{-1}. For each sp ICP-MS acquisition carried out using a 75-µs-sp-ICP-MS and processed with DP-^{75}µs-sp-ICP-MS, equivalent data were acquired using 10 ms-sp-ICP-MS and processed with DP-5σ-^{10}ms-Syngistix™ Nano. Average values ± standard deviations (σ) are calculated for n=10.

# of sp ICP-MS acquisition(s)	NP peak area (counts)		TE%	
	DP-5σ-^{10}ms-Syngistix™ Nano	DP-^{75}µs-sp-ICP-MS	DP-5σ-^{10}ms-Syngistix™ Nano	DP-^{75}µs-sp-ICP-MS
1	41.7	30.9	1.7	2.2
2	38.4	33.7	1.5	2.0
3	34.6	39.5	1.8	2.2
4	41.8	39.7	2.2	2.0
5	40.3	43.2	2.5	2.5
6	39.0	37.1	2.5	2.7
7	38.5	32.6	2.3	2.1
8	40.0	39.0	2.1	2.2
9	36.9	37.3	2.2	2.3
10	36.9	37.2	2.4	2.7
Average ± σ (n=10)	38.8 ± 2.3	37.0 ± 3.7	2.1 ± 0.3	2.3 ± 0.3

3.3.2 Optimization of DP-µs-sp-ICP-MS methods for the analysis of data obtained for AgNP treated seawater mesocosm tanks

Optimization of DP-^{75}µs-sp-ICP-MS for the requirements of the seawater mesocosm experiment was conducted on the basis of data obtained from the analysis of AgNP treated seawater tanks. The quantitation of Ag, occurring either as particulate (AgNP) or dissolved (Diss. Ag) in the AgNP treated mesocosm tanks, was explored in 2 ways using the DP-^{75}µs-sp-ICP-MS. The 2 ways differed in the procedure followed to determine the average background intensity, b, which is required for the determination of AgNP detection events

(via the determination of L_D using $Eq.10$), as well as for the dissolved Ag concentration (Diss. Ag).

The first way for determining b involves extraction of the background intensity distribution from the entire raw intensity data comprising of the background plus the NP intensities, according to the method proposed by Pace et al.[23] Initially, the average value as well as the standard deviation (σ) of the entire intensity dataset is computed, and subsequently, all intensities above the average plus 3 multiples of the standard deviation (b+3σ) are excluded; leaving a reduced original dataset which now contains intensities< b+3σ. This step is iterated until no data points in the reduced dataset can be found to have intensities> b+3σ. The final reduced dataset should represent the background distribution, and its average value correspond to b. For simplicity, this procedure will be referred to as "b from 3σ-criterion (75μs)".

The second way requires a supportive 10 ms-sp-ICP-MS acquisition of the sample, previously analyzed using 75 μs-sp-ICP-MS, and extraction of the background intensity from the 10 ms acquisition through the use of the 3σ-criterion. The average background intensity, expressed in counts $(10\ ms)^{-1}$ or counts s^{-1}, can then be recalculated to counts $(75\ \mu s)^{-1}$ in order to be used as b. The recalculation step is based on the linear relationship between dwell time and the recorded ICP-MS signal of an element in dissolved form.[3] The determined b upon recalculation can then be used to set the L_D, as well as to relate it to the dissolved Ag concentration. Out of simplicity, this procedure will be referred to as "b from 3σ-criterion (10ms)".

The two *b*-determination procedures were compared with respect to the determined Ag mass concentration (ng L^{-1}), detected as particulate (AgNP) and/or dissolved Ag (Diss. Ag). The AgNP mass concentration (μg L^{-1}) can be calculated by summing all the masses of the individual particles detected within a given volume of sample, and dividing the resulting value with the transport efficiency of the sample introduction system. The mass of each detected NP can be determined through a particle calibration, established from the analysis of a reference suspension containing 60 nm AgNPs. These constitute monodispersed NPs with an average size of 60 $\pm$ 0.5 nm; the value corresponding to the mean of a gaussian NP size distribution, as determined by the manufacturer using transmission electron microscopy (TEM). **Figure 3.6**A demonstrates the histogram of the recorded NP intensities, resulting from the analysis of the engineered 60 nm BPEI-coated AgNPs using 75 μs-sp-ICP-MS. As evidenced by the high degree of the Gaussian fitting, the recorded ICP-MS NP intensities

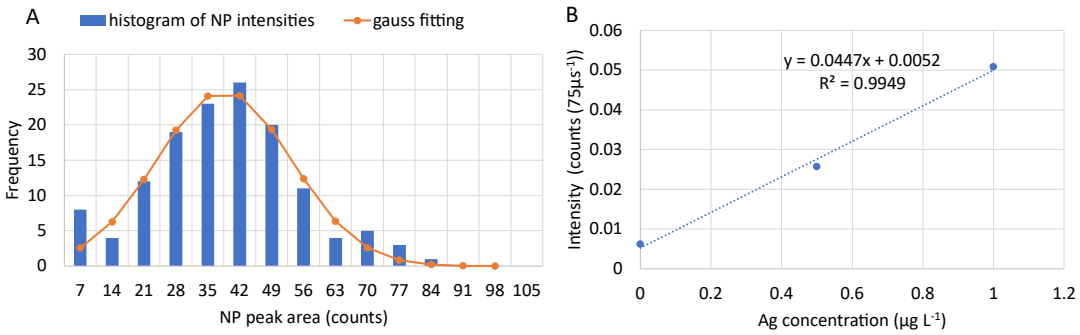

Figure 3.6 A) Histogram (blue bars) showing the distribution of the ICP-MS intensity recorded per NP. The histogram data were fitted to a Gauss distribution (orange curve), and the extracted Gaussian mean is compared to the average value derived by averaging all the recorded NP intensities. B) Calibration curve of dissolved Ag (Diss. Ag) solutions across a 0-1 µg L^{-1} concentration rage.

---

are normally distributed, thus reflecting NP monodispersity. This allows for the correlation of the recorded ICP-MS intensity per NP to the TEM-determined NP size. Hence, the detected average NP intensity was correlated to the Ag mass (fg) of a 60 nm spherical AgNP (corresponding to ~1.1 fg of Ag) in order to determine the ICP-MS sensitivity m (counts/fg), which in turn was used to calculate the Ag mass (fg) of each detected NP in the AgNP-treated seawater mesocosm tank. In parallel, the Diss. Ag can be determined directly in µg L^{-1} from a calibration curve, established by introducing Diss. Ag standard solutions (shown in **Figure 3.6**B). Summation of the mass concentration of AgNP and Diss. Ag yields the total Ag mass concentration detected in the mesocosm tank. The determined Ag mass can be subsequently compared to the Ag amounts that were added into the mesocosm tanks each day, allowing for Ag mass balance recovery calculations.

Comparison of the Ag mass balance for the 2 b-determination procedures is demonstrated in **Figure 3.7**. The black cross-marked line represents the Ag mass concentration added to the mesocosm tanks in the form of 60 nm BPEI AgNPs after spiking each day. From **Figure 3.7**, it is apparent that the determined AgNP mass concentration is equal for both procedures throughout the duration of the mesocosm experiment, indicating that discrepancies in b do not affect the quantitation of the particulate form of Ag. However, significant differences between the 2 procedures are observed for the Diss. Ag, especially after Day 3 of the experiment, when the Diss. Ag levels tend to increase as a result of the dissolution of AgNPs added on the previous days. More specifically, after Day 3, the Diss. Ag levels are consistently elevated for "b from 3σ criterion (75 µs)", exceeding the total

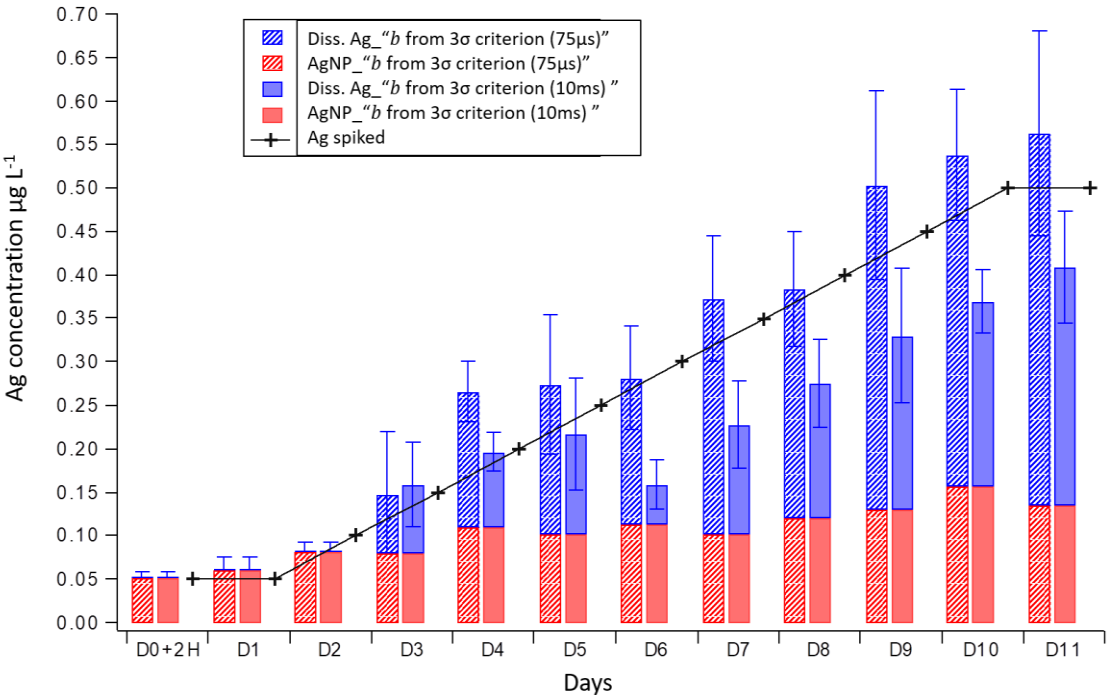

Figure 3.7 Ag mass balance for a seawater mesocosm system exposed to 60 nm Ag-BPEI NP on a daily basis, showing the determined Ag in the form of NPs (AgNP) and dissolved (Diss.Ag), as determined upon the extraction of the average dissolved intensity using the following procedures: a) "*b* from 3σ criterion (75 μs)" and b) "*b* from 3σ criterion (10 ms)". The cross-marked black line shows the Ag mass concentration spiked to the mesocosm tanks each day. Error bars represent the uncertainty in the total determined Ag concentration for n=3 mesocosm tanks.

spiked Ag mass concentration, whereas Diss. Ag levels for "*b* from 3σ criterion (10 ms)" result in an average Ag mass concentration recovery of 82.7 ± 22.4% throughout the mesocosm experiment, i.e., D0+2hours until D11. Hence, it is evident that the "*b* from 3σ criterion (75 μs)" procedure overestimates the Diss. Ag in samples containing considerable amounts of particulate and dissolved Ag, resulting in systematic and significant positive erros in total Ag recoveries. Whereas, the "*b* from 3σ criterion (10 ms)" procedure results in generally more acceptable Ag recoveries, within the limits set by the spiked Ag amount if one takes into account some Ag loss, which is to be expected, during the mesocosm experiment.

The mass concentration of the particulate form of Ag which was found to be equal between "*b* from 3σ criterion (75 μs)" and "*b* from 3σ criterion (10 ms)" can be explained by taking the example of a AgNP treated tank on D11, as this tank demonstrates the highest dissolved concentration and thus the highest b of all mesocosm days. The values of b are found to be 0.016 and 0.011 counts for "*b* from 3σ criterion (75 μs)" and "*b* from 3σ criterion

(10 ms)", respectively, therefore resulting in only slightly different L_D values of 3.30 and 3.25, accordingly. Since the recorded intensity distribution only contains integer numbers due to the Poisson nature of the recorded µs-sp-ICP-MS data, such differences do not have an impact on NP identification and thus on particulate Ag mass.

However, such reported differences in b significantly impact the Diss. Ag and thus total Ag recoveries. For instance, b values of 0.016 and 0.011 counts correspond to 0.43 and 0.27 µg Ag L^{-1} by using "*b* from 3σ criterion (75 µs)" and "*b* from 3σ criterion (10 ms)",

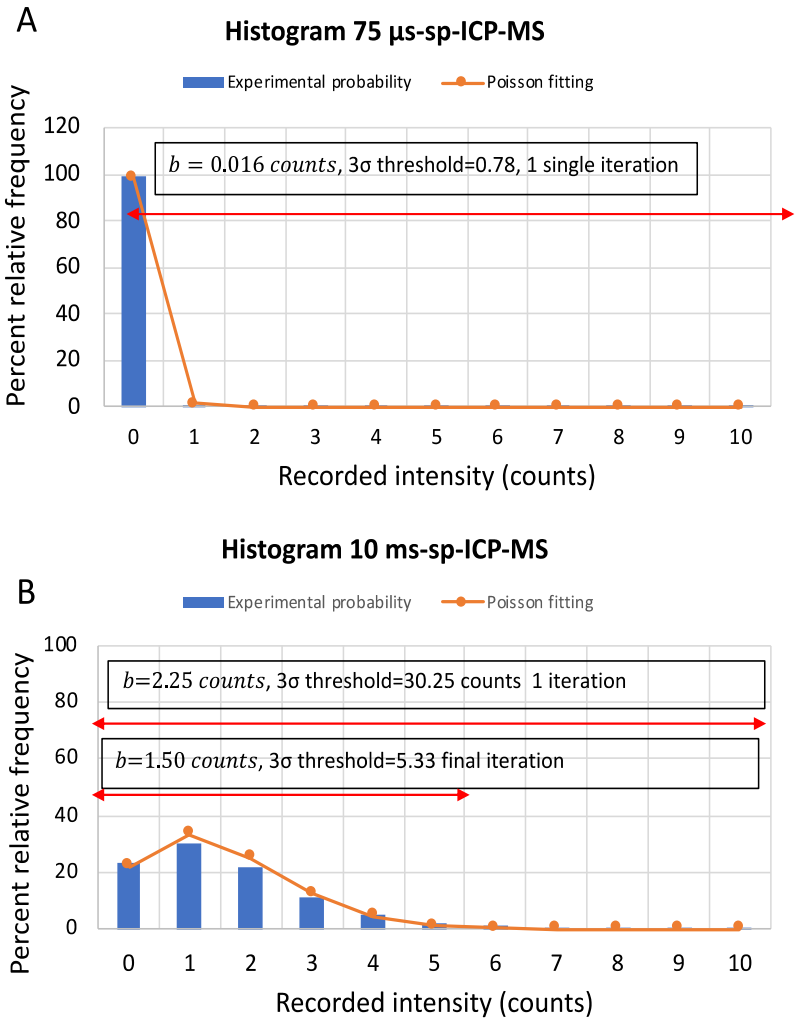

Figure 3.8 Recorded intensity histograms (intensity data obtained from the analysis of a AgNP-treated mesocosm tank on D11) showing how the average background intensity b can be computed for a 75 µs-sp-ICP-MS acquisition using "*b* from 3σ criterion (75 µs)" (A) and for B) a 10 ms-sp-ICP-MS using "*b* from 3σ criterion (10 ms)". The red bars mark the intensity data ranges from which b is derived. The NP intensity data points (i.e.,> 10 counts) have extremely low frequencies to be revealed, thus a reduced recorded intensity range, i.e., 0-10 counts, is shown for space reasons.

respectively. An explanation to the observed Diss. Ag discrepancies is graphically provided in **Figure 3.8**, showing the intensity histogram of D11 mesocosm tank obtained using 75 µs-sp-ICP-MS (A) and 10 ms-sp-ICP-MS (B), as well as the computation method used for b extraction. While both histograms fit well to a Poisson distribution, the intensity distribution of 10 ms-sp-ICP-MS approaches that of a Gauss distribution; a case of Poisson distribution for high average values.[26] Therefore, the 3σ criterion, which implies that the background signal can be separated from NP signals under the assumption that the former is normally distributed, is well suited for the extraction of b after multiple iterations of the 3σ criterion for 10 ms-sp-ICP-MS (**Figure 3.8**B). For instance, it can be observed in **Figure 3.8**B that the first iteration averages the whole intensity dataset (b of 2.25 counts (10 ms^{-1})), while the last iteration deconvolutes and averages the background signal (b of 1.50 counts (10 ms^{-1}). The b from the last iteration is subsequently recalculated to a b of 0.011 counts (75 µs)$^{-1}$, which yields a Diss. Ag of 0.27 µg Ag L^{-1}. On the other hand, the low-count Poisson distribution in A complicates extraction of b. When the 3σ criterion is performed in order to extract b directly from the 75 µs-sp-ICP-MS acquisition (**Figure 3.8**A), only 1 iteration can be performed, yielding a 3σ threshold of 0.70 counts. The procedure cannot continue as it would mean that all integers above 0 counts are excluded as outliers, thus resulting in a b of 0. Therefore, only the 1st iteration can be considered, yielding a b of 0.016 counts, which corresponds to an elevated Diss. Ag of 0.428 µg Ag L^{-1} and thus to a total Ag recovery, greatly above 100%. However, the resulting b does not reflect an entirely deconvoluted background signal, as NP intensity data points, present at much lower frequencies in histogram A, also contribute to the elevated b; possibly explaining the significantly higher Diss. Ag obtained using the "b from 3σ criterion (75 µs)" procedure. In the future, mathematical strategies achieving a more effective background exctraction are envisioned to provide accurate quantitation of dissolved metals using µs-sp-ICP-MS.

Based on the above considerations, DP-^{75}µs-sp-ICP-MS was ultimately built using the "b from 3σ criterion (10 ms)" procedure. A 6 min 10 ms-sp-ICP-MS analysis was carried out as a supporting acquisition for a tank, in addition to the main 75 µs-sp-ICP-MS. While it is understandable that a 6 min 10 ms-sp ICP-MS acquisition adds extra analytical load, requiring an extra analytical time of 6 min per mesocosm tank, it is shown in **Table 3.2** that even a 10 s 10 ms-sp ICP-MS acquisition is long enough to obtain a precise value of b. **Table 3.2** reports the statistical values, including the average background intensity (b), the standard deviation (σ) and the average plus 3 × standard deviation (b +3σ) of the extracted

background intensity distribution. Excellent agreement is observed for all statistical values between 10 ms-sp ICP-MS scan times of 360 s and 10 s, thus indicating that the intensity distribution of the background signal is very similar for both scan times. The values of b in cps, obtained using 10 ms, were recalculated to the corresponding values of b in counts per 75 µs. A typical calculation for Day 11 is provided: $149.9\,\mathrm{cps} \times 0.000075\,\mathrm{s} = 0.0112\,\mathrm{counts\ per}\ 75\,\mu s$. As can be seen, a full 6 min sp-ICP-MS acquisition is not necessary, as extremely close values of b can be acquired even for a short 10 s acquisition.

Table 3.2 Values of b, calculated from a full 10 ms-sp-ICP-MS acquisition (scan time of 360 s) and a short time segment of that acquisition (10 s) for mesocosm tank samples selected for 3 random days of exposure. σ stands for the standard deviation of the extracted background intensity distribution, while b+3σ stands for the average background intensity plus 3 multiples of the standard deviation. All values are reported in counts per sec (cps).

Scan time (s)	Day 1			Day 4			Day 11		
	b	σ	b+3σ	b	σ	b+3σ	b	σ	b+3σ
360 s	30.6	54.2	193.2	122.0	108.0	446.0	149.9	127.7	533.0
10 s	31.2	54.1	193.4	121.5	110.1	451.9	147.9	128.6	533.9

3.3.3 Comparison of DP-^{75}µs-sp-ICP-MS to DP-5σ-^{10}ms-Syngistix™ Nano for the analysis of data obtained for AgNP treated seawater mesocosm tanks

The suitability of DP-^{75}µs-sp-ICP-MS for the requirements of the mesocosm experiment was evaluated by comparing it to the DP-5σ-^{10}ms-Syngistix™ Nano with respect to the analysis of data obtained from the analysis of AgNP treated seawater mesocosm tanks. Since characterization of metal-containing NPs using 10 ms-sp-ICP-MS is well documented in the literature[45,48,51,54], analysis of the AgNP treated mesocosm tanks using DP-5σ-^{10}ms-Syngistix™ Nano was considered a benchmark for the performance of DP-^{75}µs-sp-ICP-MS data processing method.

Figure 3.9 demonstrates the Ag mass balance in the AgNP treated mesocosm tanks for the whole duration of the mesocosm experiment, as determined using DP-^{75}µs-sp-ICP-MS and DP-5σ-^{10}ms-Syngistix™ Nano. Generally, the 2 methods perform very similarly, showing a good agreement both in the AgNP and Dis. Ag mass concentration. An average total Ag recovery of 83 ± 22 % and 86 ± 21% is observed for DP-^{75}µs-sp-ICP-MS and DP-5σ-^{10}ms-Syngistix™ Nano, respectively, across the duration of the experiment.

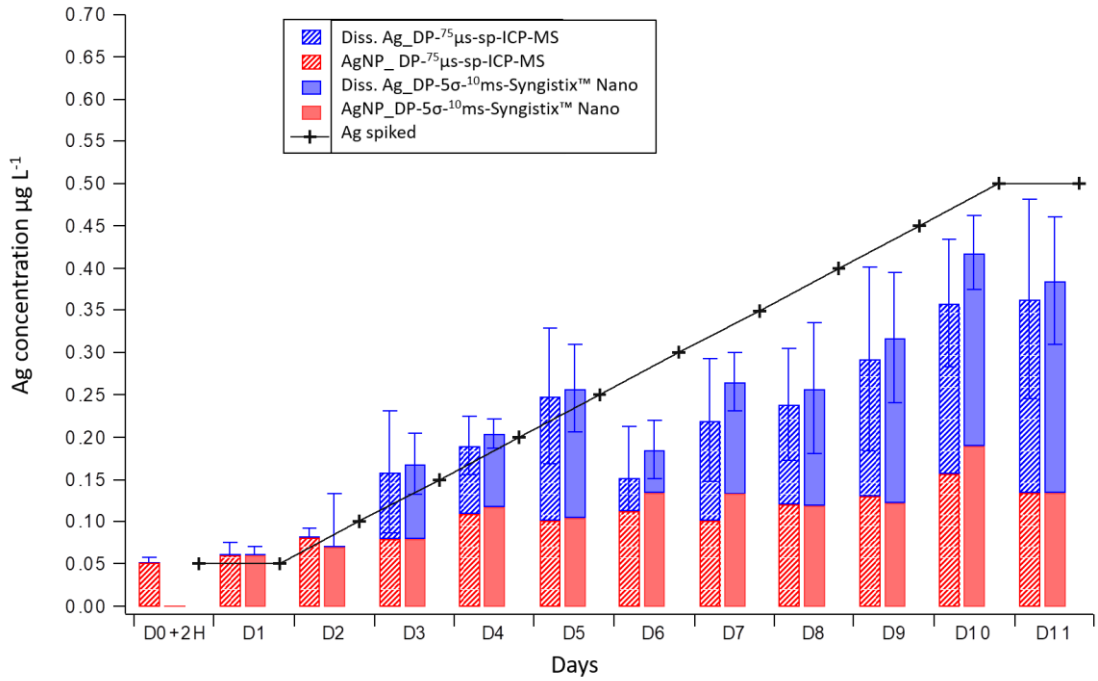

Figure 3.9 Ag mass balance for a seawater mesocosm system exposed to 60 nm Ag-BPEI NP on a daily basis, showing the determined Ag in the form of NPs (AgNPs) plus dissolved Ag (Diss. Ag), as determined using DP-^{75}µs-sp-ICP-MS and DP-5σ-^{10}ms-Syngistix™ Nano. The cross-marked black line shows the Ag mass concentration, in the form of 60 nm Ag BPEI NPs, spiked to the mesocosm tanks each day. No experimental data were recorded on D0+2H using the 10 ms dwell time. Each value represents the average for n=3 mesocosm tanks, and error bars represent ±1 standard deviation for n=3.

Comparison of the 2 methods was further conducted with respect to the determined NP number concentration (**Figure 3.10**A) as well as the average NP size (**Figure 3.10**B). Generally, DP-^{75}µs-sp-ICP-MS yields a higher NP number concentration across the mesocosm exposure days. Combined with the generally lower average NP size, it indicates that lower NP size detection limits can be attained using DP-^{75}µs-sp-ICP-MS as opposed to DP-5σ-^{10}ms-Syngistix™ Nano. This observation is in accordance with the literature supporting the use of µs-sp-ICP-MS for higher attainable signal-to-background ratios, and

thus lower NP size detection limits.[57] Nevertheless, both methods exhibit a proportional increase in the NP number concentration (**Figure 3.10**A) across days 0-6 followed by a plateau for the rest of the mesocosm days. Comparable results are also obtained for the average NP size (**Figure 3.10**B), with an average NP size of 51.2 ± 1.6 µm and 52.5 ± 2.07 across days 1-11 for DP-^{75}µs-sp-ICP-MS and DP-5σ-^{10}ms-Syngistix™ Nano, respectively.

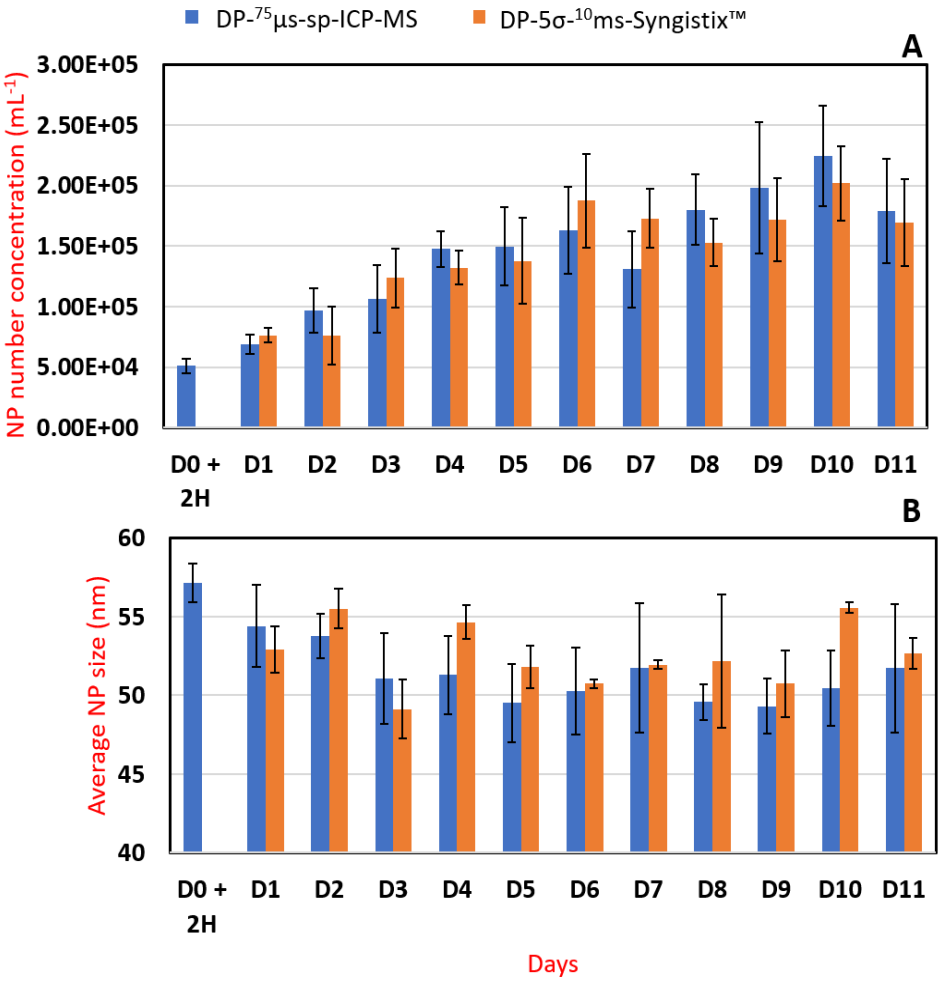

Figure 3.10 Graph A compares the determined AgNP number concentration in the AgNP treated mesocosm tanks, analyzed using DP-^{75}µs-sp-ICP-MS (blue bars) and DP-5σ-^{10}ms-Syngistix™ Nano. (orange bars). Likewise, graph B demonstrates comparison of the average NP size (nm) (n=3 tanks). Each value represents the average for n=3 mesocosm tanks, and error bars represent ±1 standard deviation for n=3. No data were recorded on D0+2hours using the 10 ms dwell time.

A slight decreasing trend across the mesocosm days is more discernible using DP-^{75}µs-sp-ICP-MS, indicative of the lower limit of detection attained with µs-sp-ICP-MS.

All the above indications support the suitability of DP-^{75}µs-sp-ICP-MS to be used in order to study the behavior of Ag, present as AgNP or Diss. Ag, in a dynamic seawater mesocosm system treated with engineered BPEI-coated AgNPs or ionic silver (Ag^+).

3.3.4 Behavior of engineered BPEI-coated AgNPs in a seawater mesocosm system

The x-axis of a ^{107}Ag trace, such as the one showed in **Figure 3.5**A, may also be presented in time units (s) instead of the number of dwell times (each dwell time corresponding to 75 µs) in order to be presented as a time-resolved sp-ICP-MS acquisition. Such an acquisition is provided in **Figure 3.11**, resulting from the analysis of a mesocosm tank 2 hours after it had been spiked with 60 nm engineered branched-polyethyleneimine (BPEI)-coated AgNPs, at a concentration of 50 ng Ag L^{-1}. Data such as those in **Figure 3.11** are acquired for each of the 11 days of the mesocosm experiment, and are used to determine the particulate and dissolved Ag mass concentration, as well as the NP number concentration, the NP size distribution, and the profile duration of each NP transient signal.

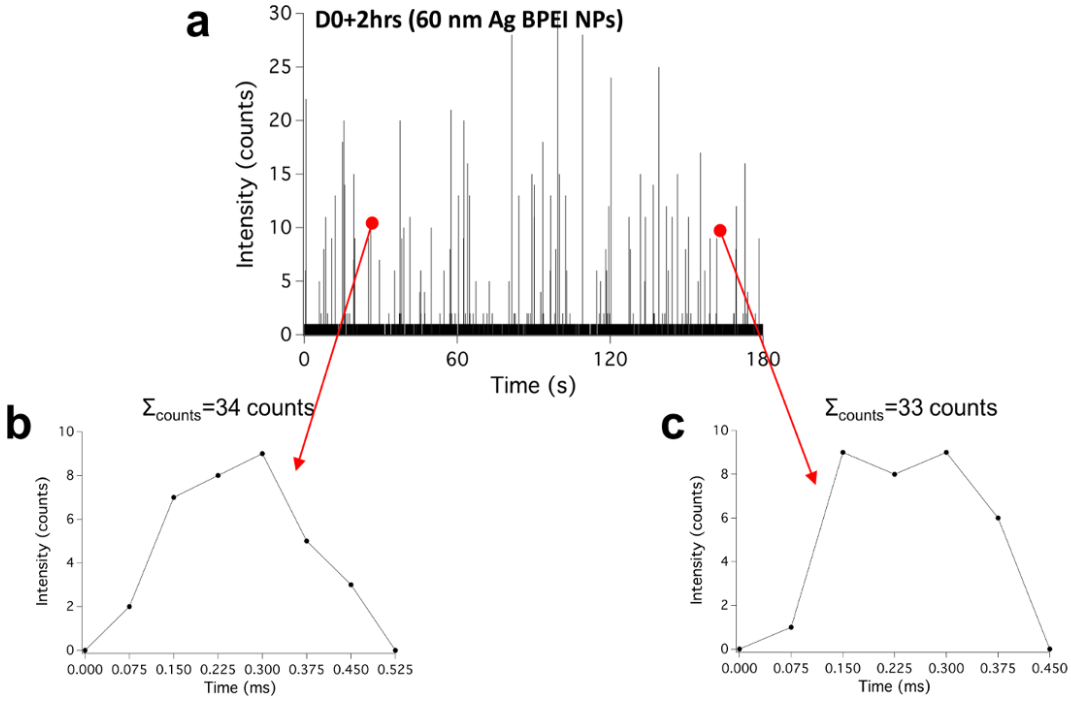

Figure 3.11 (a)$^{107}Ag^+$ time-resolved sp-ICP-MS acquisition of a seawater mesocosm tank, 2 hours after it had been spiked with 60 nm BPEI-coated AgNPs at 50 ng Ag L^{-1}; (b) and (c) show two random transient signal profiles for two detected Ag NPs as shown in (a) by the red circles.

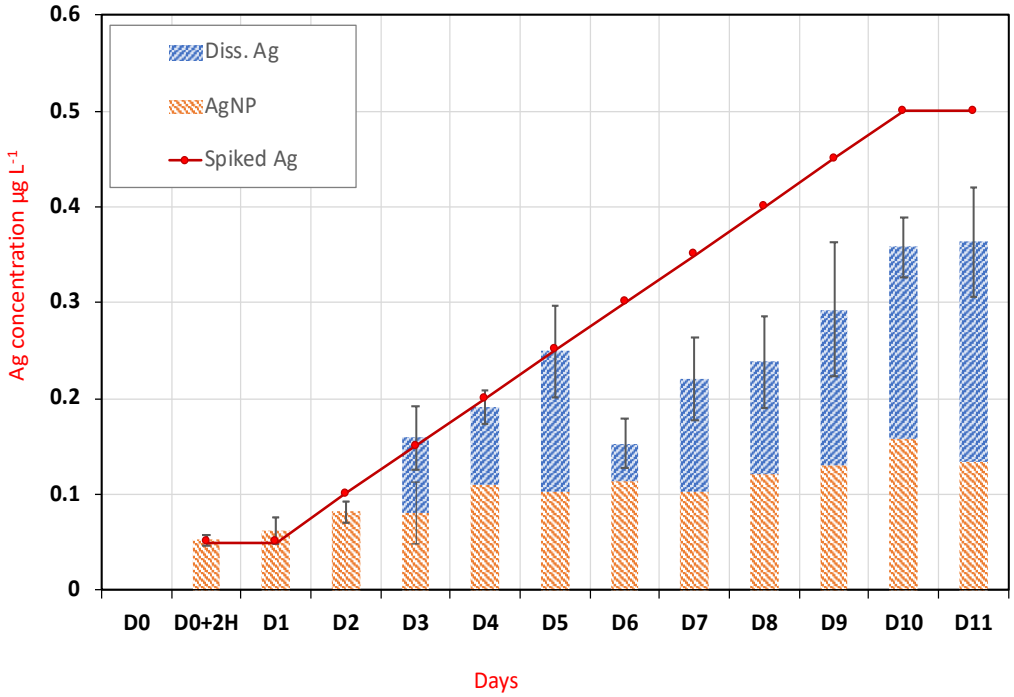

Figure 3.12 Ag mass balance for a seawater mesocosm system treated with AgNPs on a daily basis, showing the determined Ag mass concentration in the form of NPs (AgNP), plus the dissolved Ag (Diss. Ag), in comparison to the spiked Ag. The spiked Ag amount was added daily at a mass concentration of 50 ng Ag L^{-1}, in the form of 60 nm engineered BPEI-coated AgNPs. Each value represents the average for n=3 mesocosm tanks, and error bars represent ±1 standard deviation for n=3.

A summary of the chemical behavior of the engineered BPEI-coated AgNPs exposed in a seawater mesocosm system can be revealed by the Ag mass balance monitored throughout the duration of the mesocosm experiment (**Figure 3.12**). More specifically, a continuous increase in AgNP mass concentration was observed during the initial days of the experiment (Day 0 to 4), governed by the daily addition of BPEI-coated AgNPs at the 50 ng Ag L^{-1}. However, this increase leveled off in subsequent days, especially after day 6, as a result of the dissolution of the "older" BPEI-coated AgNPs that had been added during the first days of the experiment. Evidence of the dissolution of these NPs is also provided by the detection of Diss. Ag, after Day 3, followed by a gradual increase across the mesocosm days. While it is observed that the spiked Ag amount is entirely recovered across days 0-5, beyond day 6, the recovery of Ag decreases down to between 50 and 70% on average and remains at these levels throughout the rest of the exposure days. It is interesting to note that, on day 6, the Diss. Ag decreased significantly. Although currently not understood, this observation is in agreement with the results of the previously conducted mesocosm

experiment [48], in which the daily Ag spiked concertation was double that used here (100 vs 50 ng Ag L^{-1} daily), and analysis was conducted using a 10 ms dwell time. A similar decrease was also observed in that study on day 6 for the AgNPs and day 7 for the Diss. Ag. Comparing these two studies, which employ near environmentally relevant Ag concentrations, it is worth noting that they were both conducted using the same mesocosm system but 3 years apart, even though, the AgNP spiked concentrations were different. Similar Ag mass balance trends were also observed for both experiments.

To investigate the dissolution of the BPEI-coated AgNPs in more detail, their average diameter, assuming they retained a spherical shape, was calculated. A reduction in their average size from their initial 60 nm to approximately 50 nm was observed during the first 3 days of the experiment, then a constant average size was calculated for the rest of the exposure days (**Figure 3.13**a). However, because of the daily addition of "fresh" 60 nm AgNPs, the determined average NP size does not fully reveal what is occurring during the dissolution process. This is clearly reflected in the AgNP size distributions, shown for selected mesocosm days, in **Figure 3.13**b. The rapid formation of a broad size-distribution

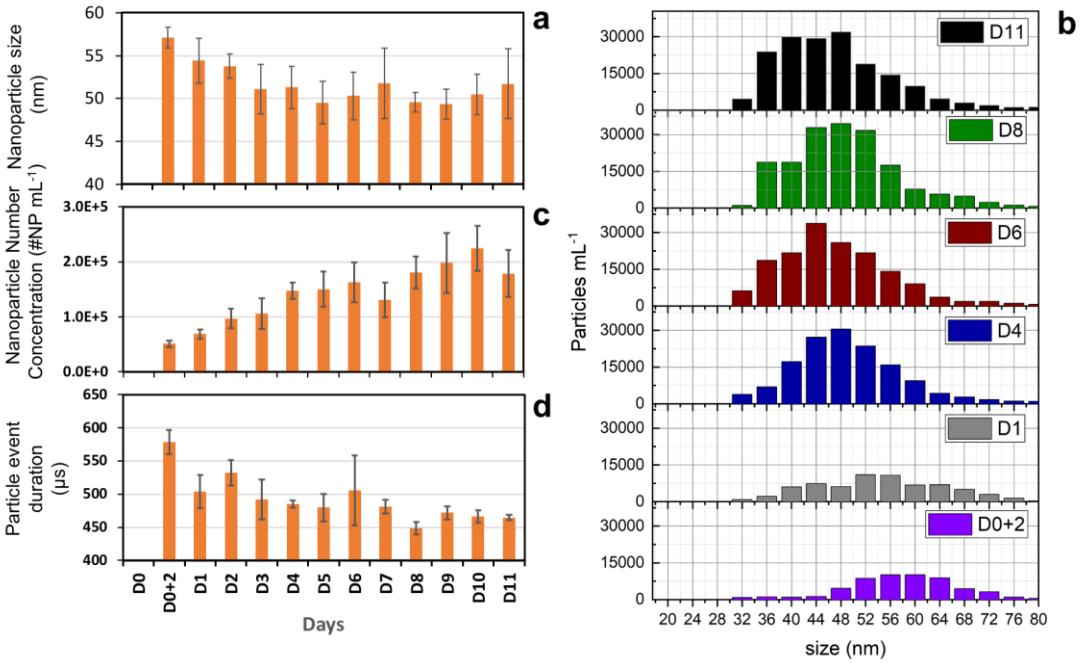

Figure 3.13 Parameters determined for a seawater mesocosm system, treated with 60 nm engineered BPEI-coated AgNPs on a daily basis, showing the average AgNP size (a), AgNP number concentration (c) and average AgNP transient signal profile duration (µs) (d). Each bar represents the average value for n=3 mesocosm tanks, and error bars represent ±1 standard deviation for n=3. Representative AgNP size distributions are shown for selected days (b).

(compared to that of the originally spiked BPEI@AgNPs, shown in **Figure SI1. 4**) supports the occurrence of dissolution that continuously produces smaller NPs coexisting with the "fresh" (60 nm) AgNPs. The size distributions also continuously grow "taller" (increase in NP numbers), as would be expected since more AgNPs are added and detected daily, and become skewed towards smaller NP sizes since the added AgNPs gradually dissolve.

The changes in the determined AgNP number concentration across the mesocosm days are shown in **Figure 3.13**c. It is apparent that the AgNP number concentration increases almost linearly for the first 4-6 days of the experiment. Subsequently, the rate of increase starts to level off, most probably as a result of the AgNPs dissolving into smaller NPs showing diameters below 30 nm, which is the size limit of detection for AgNPs in seawater using the sp ICP-MS method presented in this study. A balance, however, seems to be reached as fresh numbers of NPs are added daily. The limit of detection of 30 nm was determined by calculating the size of a spherical AgNP that corresponded to an intensity of 5 counts. An intensity of 5 counts would be the lowest possible peak area (PA) of a NP detection event registering a peak maximum>$L_D = 3.30\ counts$ (as determined for mesocosm tanks on day11 of exposure) and an ion cloud duration of 225 μs. Such a NP would comprise of 4 intensity d.p.s, e.g., 0, 1, 4, 0 counts. Transformation of AgNP intensity to AgNP size has been previously presented in section 3.3.2.

In addition, the DP-^{75}μs-sp-ICP-MS, developed and applied to the present mesocosm study, enabled the acquisition of the profile duration of each NP transient signal, a novel analytical metric which could not be provided in the study of Tsiola et al. This novel metric is provided in **Figure 3.13**d which shows the average profile duration of the recorded NP transient signals as a function of the mesocosm days. In line with the reduction in the average NP size, the average profile duration also shows a decrease, starting off at ~600 μs (n=569) on Day 0 for freshly added 60 nm AgNPs, and gradually decreasing to ~450 μs (n=1730) on Day 11. This observation demonstrates a link between NP size and NP profile duration, which has only been sparsely addressed in the literature so far.[19]

All the above figures substantiate the gradual transformation of AgNPs to dissolved Ag, possibly through the oxidation of metallic Ag for the generation of silver ions (Ag^+). This time-dependent phenomenon is efficiently monitored using sp-ICP-MS, completely accounting for both Ag forms up to day 5. However, the 50-70% recoveries of Ag noted across days 6-11 suggest a loss of Ag from the analyzed mesocosm system. Attributing this phenomenon to limitations of the analytical method is counter-intuitive, given the ~100% recoveries

obtained for Days 0-5, therefore the observed loss of Ag is more likely to be attributed to a chemical phenomenon occurring within this dynamic seawater system. An explanation for the decreased Ag mass concentration recoveries observed beyond Day 6 could be sedimentation of AgNPs as a result of their aggregation, however, formation of NP aggregates has been reported for much higher AgNP spiked concentrations (ppb and ppm Ag levels, as opposed to ppt levels used herein).[42] However, even though AgNPs may not be agglomerating with each other, the degraded AgNPs or dissolved Ag may be interacting with hetero-particles of various sizes that are present within the seawater system. For instance, the degraded AgNPs interacting with the hetero-particle may not contain enough mass of Ag to be detected, once the Ag-containing hetero-particle is atomized and ionized in the plasma. In a similar fashion, the adsorbed dissolved Ag amount, making up the Ag-containing portion of the hetero-particle, may not suffice for detection. The above occurrences may be possible if the non-Ag constituents of the hetero-particle make up enough of its overall mass to stabilize the Ag that has been adsorbed, while the adsorbed Ag quantity might not be enough to make it detectable by the used sp ICP-MS system. Also, hetero-particles of unknown size may be large enough to be removed from the mesocosm seawater system via sedimentation. In fact, as presented in Scheidemann et al, a larger area of Coomassie Stainable Particles (CSP, mm^2 L^{-1}) was measured across mesocosm days 0-5, for both the AgNP and ionic Ag^+ treated tanks but not for the controls.[55] CSP are particles produced by phytoplankton and contain polysaccharides, amino acids and other substances that tend to aggregate, ultimately forming large gels that may reach even centimeter dimensions. This increased area of CSPs in the Ag and AgNP mesocosms may have promoted hetero-agglomeration. In oceanic waters, CSPs may migrate to deeper waters due to their increased density, and so it may be possible that Ag-containing CSPs sedimented from the seawater that was sampled from the mesocosm tanks.

Overall, these results are in good agreement with the older seawater mesocosm study[48], in which case the concentration of the 60 nm engineered BPEI-coated AgNPs added daily to each seawater tank was double the one used herein, i.e., 100 ng Ag L^{-1} seawater per day, as opposed to the 50 ng Ag L^{-1} added in this study. More specifically, NP size during that study was reduced from 60 nm to approximately 48 nm after day 11. This is in good agreement with the observed reduction to 52 nm on day 11 of this study (**Figure 3.13**a). Also, the general trends of the observed mass balances were similar in both experiments, indicating a reproducible behavior for BPEI-coated AgNPs in seawater on both

occasions. However, some differences include the formation of a small number of larger Ag NPs, observed by Tsiola et al, which again may have resulted because of the double amount of Ag NPs added daily in this previous study.

3.3.5 Behavior of Ionic Ag in a Seawater Mesocosm System

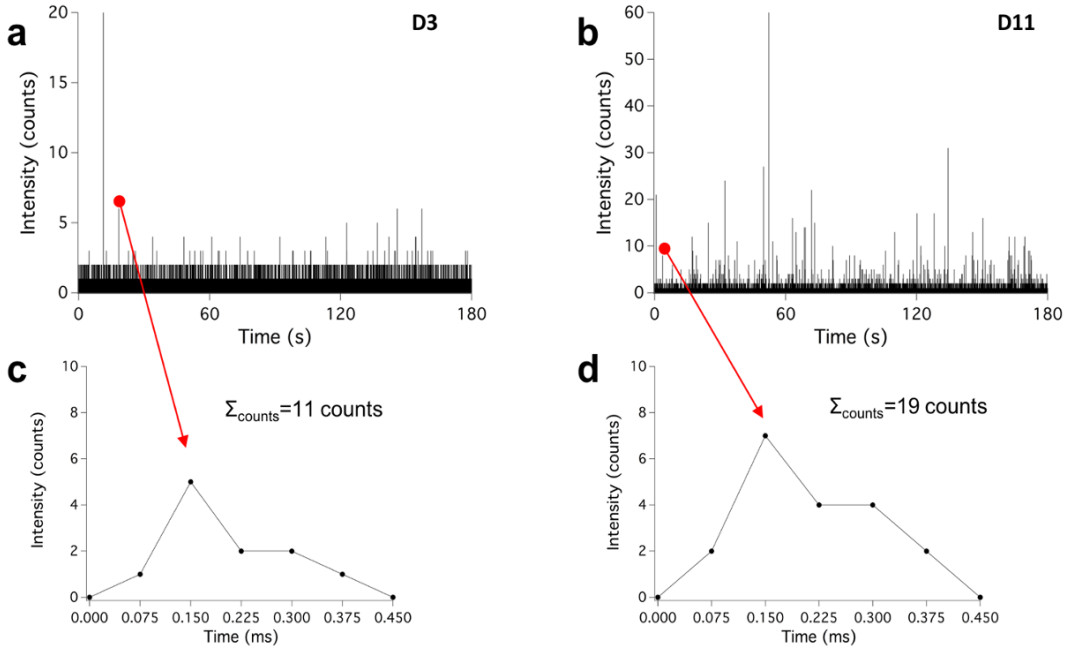

Figure 3.14 $^{107}Ag^{+}$ trace resulting from the analysis of a seawater mesocosm tank spiked with Ag^{+} on mesocosm days 3 **(a)** and 11 **(b)**. Transient signal profiles showing the presence of a particulate form of Ag on day 3 **(c)** and day 11 **(d)**, corresponding to the signal spikes shown in **(a)** and **(b)**, respectively.

The chemical behavior of ionic silver (Ag^{+}) was studied through the daily analysis of the 3 ionic silver (Ag^{+}) treated mesocosm tanks for the same experimental duration as that of AgNP treated tanks. Even though the mass concentration of Ag^{+} added daily was low, i.e., 50 ng Ag L^{-1} seawater (ppt level) for each mesocosm tank, it was still possible to monitor the presence of Ag throughout the 11-day exposure period. On day 0+2hr and day 1, Ag was only detected in its dissolved form. However, on day 2, in addition to the detection of dissolved Ag, a small number of signal spikes was also detected. This was particularly evident on day 3 when more signal spikes of higher intensity were observed (**Figure 3.14**a).

The frequency of signal spikes increased throughout the exposure experiment as can be seen from the analysis of day 11 samples (**Figure 3.14**b), in which case the signal spikes were observed at a much higher frequency and their intensities were also significantly higher than those detected during the first days of the exposure experiment. As the origin of these

signal spikes is of particular interest, their recorded duration was found to be similar to the duration times obtained for the engineered 60 nm BPEI-coated AgNPs. It can be observed from **Figure 3.14**c,d that the transient signal profiles of the detected signal spikes resembled those of engineered AgNPs in event duration and signal intensity, once the engineered AgNPs started to dissolve within the seawater mesocosm system, i.e. day 11. Assuming these signals arise from Ag-containing particles, of unknown nature, shape, and elemental composition, their actual particle diameter cannot be determined using sp-ICP-MS. It is only possible to determine the total Ag mass detected per individual particle. This mass can, however, be converted into a AgNP equivalent diameter for a hypothetical spherical particle almost purely consisting of elemental Ag. Such a calculation is a convenient way to represent the mass of this form of Ag, even though the actual particle may contain additional

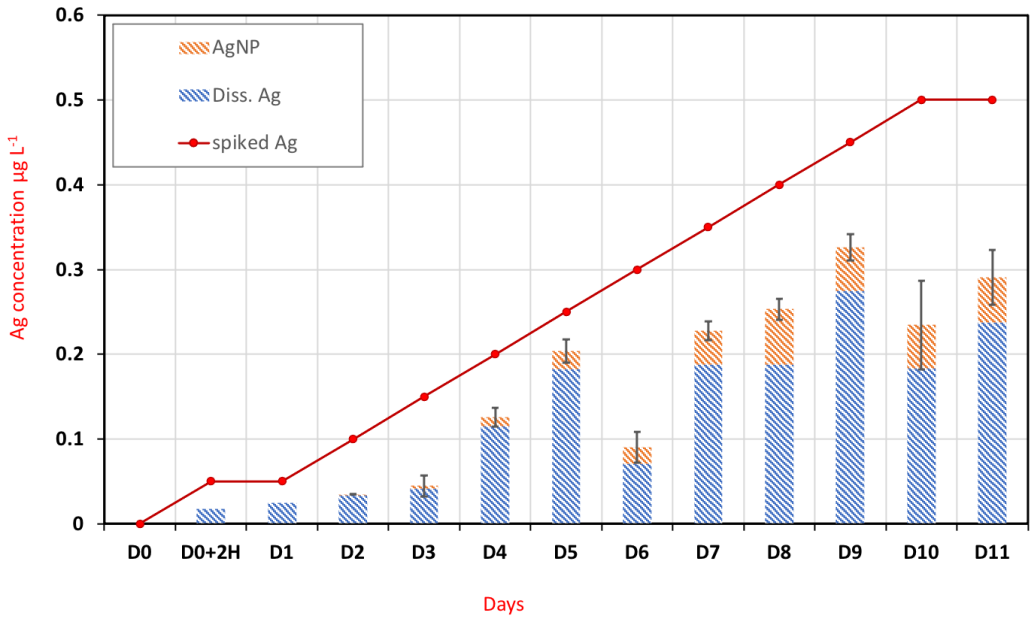

Figure 3.15 Ag mass balance for a seawater mesocosm system treated with ionic Ag (Ag^+) on a daily basis, showing the determined Ag mass concentration in the form of NPs (NP Ag), plus the dissolved Ag (Diss. Ag), in comparison to the spiked Ag. The spiked Ag amount was added daily at a mass concentration of 50 ng Ag L^{-1}, in the form of Ag^+. Each value represents the average for n=3 mesocosm tanks, and error bars represent ±1 standard deviation for n=3.

elements and other components that add size but are not detected by sp ICP-MS.

The mass balance for the ionic Ag exposure experiment is provided in **Figure 3.15**, showing that the dissolved Ag concentration increases until day 5, drops on day 6, then increases up to day 9, followed by no more increases on days 10 and 11. A particulate Ag fraction, denoted as AgNPs, starts to appear on day 2 due to the occurrence of the small

number of signal spikes, and gradually increases throughout the mesocosm duration; thus pointing to the gradual formation of Ag-containing particles. The determined total Ag mass concentration accounts for 25 to 75 % of the spiked Ag amount across the mesocosm days, with the lowest recoveries being observed during the initial days of the mesocosm experiment, i.e., day 0+2h to day 3. However, once the particulate Ag fraction appeared, Ag recoveries began to rise, with the exception of day 6. The general trend of increasing Ag recovery values with the appearance of the particulate fraction may imply the gradual growth of the Ag-containing particles, which, however, do not contain sufficient mass of Ag to be detected during the initial stages of formation, i.e., days 0-3. The determined Diss. Ag concentration on day 6 was somewhat out of trend with the values determined on the remaining days of the experiment. This was consistent for all three of the tanks from which samples were taken on day 6. This may be related to either a biological phenomenon or, less likely, an irregularity during the sampling process, which however was not possible to identify. It has to be mentioned that Day 6 mass balances were also out of trend for the AgNP treated tanks, discussed previously in **Figure 3.12**.

Regarding the nature of the detected signal spikes, these are attributed to an unknown form of particulate Ag, e.g., Ag-containing particles of unknown nature. These particles may be biogenic that have taken up or adsorbed sufficient amounts of Ag ions to be detected as particles. Other possibilities may involve AgNPs that have been formed as the result of the reduction of ionic Ag by natural organic matter such as fulvic or humic acids [58,59]. Finally, inorganic ligands, e.g. S^{2-} which is present at sufficient concentrations in seawater, may have interacted with ionic Ag resulting in the formation of Ag_2S particles [60]. Sulfide ions, in the presence of Ag^+, readily form Ag_2S, which is a very stable compound with K_{sp} as low as 5.92×10^{-51} [61,62]. Using GEOCHEM-EZ[63], a chemical speciation calculation program, and entering a seawater composition containing 5 nM S^{2-}, 50 ng Ag L^{-1}, plus other seawater salts, metals and ligands (Na^+, Mg^{2+}, Ca^{2+}, Cl^-, SO_4^{2-}, K^+, Br^-, I^-) at their expected seawater concentrations, it was calculated that 3.69% of Ag is complexed with S^{2-}, 47.13% is in solid form with S^{2-} which could be the particulate Ag that was detected, and 49.18% Ag is complexed with I^-. This points to the possibility of having Ag_2S containing nanoparticles forming during the ionic Ag exposure seawater experiment. For this to be further substantiated experimentally though, sp-ICP-MS with multi-isotope capabilities is required in order to simultaneously monitor Ag and S and attempt to determine their ratios per particle.

Wimmer *et al.* have reported on the natural formation of silver-based nanoparticles (Ag-b-NPs) in a eutrophic pre-alpine lake in Germany that contained geogenic silver traces in the sub-ng L^{-1} range, where approximately 40% of total silver (5.7 ng L^{-1}) consisted of Ag-b-NPs as detected at the lake surface. This was attributed to the reduction of Ag^{+} species to elemental Ag as a result of the presence of elevated levels of natural organic matter (NOM). Whereas in a oligotrophic lake with similar silver content, no Ag-b-NPs were detected [64]. The same authors also demonstrated the formation of Ag_2S-containing nanoparticles in lake water containing S^{2-}, with the determined nanoparticles exhibiting a relatively narrow size distribution. It is therefore noteworthy to mention that the seawater used in the present mesocosm study is regarded as oligotrophic (even though it is collected from the coastal zone), exhibiting nM concentrations of nitrogen and phosphorus, which is characteristic of this region of the Mediterranean Sea [65,66].

Figure 3.16 contains a summary of various parameters determined for the newly formed Ag-containing particles. First of all, it is evident that the Ag equivalent diameter increases

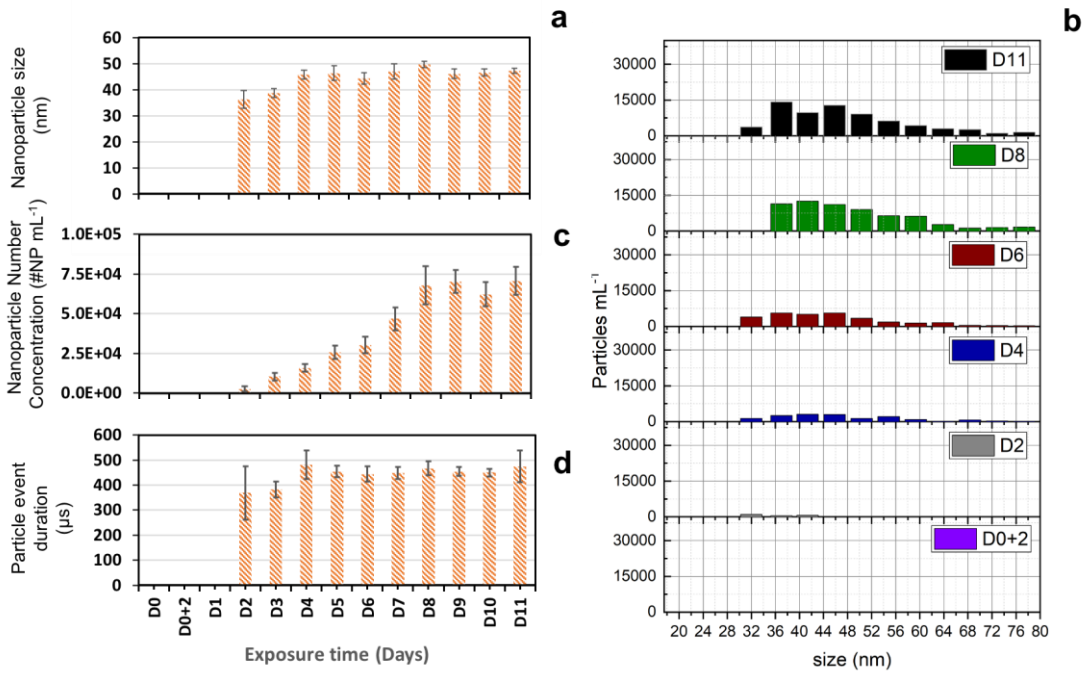

Figure 3.16 Parameters determined for a seawater mesocosm system, treated with ionic Ag (Ag^{+}) on a daily basis, showing the average Ag equivalent diameter of these Ag-containing NPs(**a**), AgNP number concentration (**c**) and average AgNP transient signal profile duration (µs) (**d**). Each bar represents the average value for n=3 mesocosm tanks, and error bars represent ±1 standard deviation for n=3. Representative Ag-containing NP size distributions are shown for selected days (**b**).

slightly from day 2 to day 4 and then seems to level off until day 11 (**Figure 3.16**a). It has been suggested that sulfides may hinder Oswald ripening[67], responsible for the increase in NP sizes, thus a narrow size distribution is expected to be observed for newly formed Ag_2S-based NPs [64]. This is also evidenced by the size (i.e., equivalent size) distribution histograms (**Figure 3.16**b**)**, showing that these NPs increase in number concentrations as a function of exposure day, whereas their size increases only gradually. The linear increase in number concentrations of the newly formed Ag-containing NPs until day 8 is clearly observed in **Figure 3.16**c. Also, as it was observed that the event duration of detected engineered AgNP was linked to their size (**Figure 3.13**), the same was observed for the newly formed Ag-containing particles in which case particle event duration times increase with increasing AgNP equivalent diameters (**Figure 3.16**a). This finding supports the presence of Ag as the main component of the detected particles, and not as an adsorbed component of much larger particles. In the latter case small changes in the amount of adsorbed Ag should not be reflected by changes in NP event duration across the mesocosm exposure days. Also, if Ag was being adsorbed onto larger particles of a wide size distribution, the amounts adsorbed should show significant variation across the mesocosm exposure days. However, that is not the case as seen from the calculated equivalent diameters, which are quite uniform for the duration of the exposure experiment from day 4 onwards (**Figure 3.16**a).

3.4 Conclusions

A data processing method (DP-µs-sp-ICP-MS) was developed in response to a need for accurate quantitation of individual metal-containing NPs in samples analyzed using µs-sp-ICP-MS. Herein, development of DP-µs-sp-ICP-MS, referred as DP-^{75}µs-sp-ICP-MS, was based on 75 µs-sp-ICP-MS acquisitions, by employing a combination of Igor Pro procedure macros for signal spike identification and integration, as well as Virtual Basic written Excel-based macros for filtration of NPs from false positive signals.

For the evaluation of DP-^{75}µs-sp-ICP-MS, 10 ms-sp-ICP-MS analysis was conducted, and the resulting raw data were processed using the automated processing of Syngistix™ Nano through the application of a 5σ threshold, referred as DP-5σ-^{10}ms-Syngistix™ Nano. The latter served as a benchmark for the evaluation of DP-^{75}µs-sp-ICP-MS. Analytical metrics including NP peak area and transport efficiency, determined from the analysis of a reference 60 nm AgNP suspension, were found to be in good agreement between DP-^{75}µs-

sp-ICP-MS and DP-5σ-^{10}ms-Syngistix™ Nano. In addition, the 2 data processing methods demonstrated good agreement on the Ag mass balance, determined for a seawater mesocosm system spiked with known amounts of Ag, as well as on the determined NP number concentration and NP size; showcasing the suitability of DP-^{75}µs-sp-ICP-MS to be used for accurate quantitation of trace amounts of Ag, present in particulate or dissolved form in samples of environmental interest.

The developed DP-^{75}µs-sp-ICP-MS was applied to study the chemical behavior of Ag in seawater mesocosm tanks, treated daily with ultrarace Ag amounts (50 ng Ag L^{-1}) in the form of engineered 60 nm AgNPs or Ag^+. The method demonstrated the capability to efficiently track the degradation of engineered 60 nm AgNPs for the generation of dissolved Ag, as well as the formation of Ag-containing particles, from an early stage of occurrence, in seawater mesocosm tanks treated with Ag^+. Chemical speciation calculations suggested that the Ag-containing NPs formed within the seawater Ag^+ tanks are likely to be attributed to silver sulfide (Ag_2S) formation.

3.5 Literature

[1] C. Degueldre, P.Y. Favarger, S. Wold, Gold colloid analysis by inductively coupled plasma-mass spectrometry in a single particle mode, Analytica Chimica Acta. 555 (2006) 263–268. https://doi.org/10.1016/j.aca.2005.09.021.

[2] I. Strenge, C. Engelhard, Capabilities of fast data acquisition with microsecond time resolution in inductively coupled plasma mass spectrometry and identification of signal artifacts from millisecond dwell times during detection of single gold nanoparticles, Journal of Analytical Atomic Spectrometry. 31 (2016) 135–144. https://doi.org/10.1039/c5ja00177c.

[3] M.D. Montaño, J.W. Olesik, A.G. Barber, K. Challis, J.F. Ranville, Single Particle ICP-MS: Advances toward routine analysis of nanomaterials, Analytical and Bioanalytical Chemistry. 408 (2016) 5053–5074. https://doi.org/10.1007/s00216-016-9676-8.

[4] C. Degueldre, P.Y. Favarger, R. Rossé, S. Wold, Uranium colloid analysis by single particle inductively coupled plasma-mass spectrometry, Talanta. 68 (2006) 623–628. https://doi.org/10.1016/j.talanta.2005.05.006.

[5] W.W. Lee, W.T. Chan, Calibration of single-particle inductively coupled plasma-mass spectrometry (SP-ICP-MS), Journal of Analytical Atomic Spectrometry. 30 (2015) 1245–1254. https://doi.org/10.1039/c4ja00408f.

[6] S. Gschwind, H. Hagendorfer, D.A. Frick, D. Günther, Mass quantification of nanoparticles by single droplet calibration using inductively coupled plasma mass spectrometry, Analytical Chemistry. 85 (2013) 5875–5883. https://doi.org/10.1021/ac400608c.

[7] B. Ramkorun-Schmidt, S.A. Pergantis, D. Esteban-Fernández, N. Jakubowski, D. Günther, Investigation of a Combined Microdroplet Generator and Pneumatic Nebulization System

for Quantitative Determination of Metal-Containing Nanoparticles Using ICPMS, Analytical Chemistry. 87 (2015) 8687–8694. https://doi.org/10.1021/acs.analchem.5b01604.

[8] H.E. Pace, N.J. Rogers, C. Jarolimek, V.A. Coleman, C.P. Higgins, J.F. Ranville, Determining Transport Efficiency for the Purpose of Counting and Sizing Nanoparticles via Single Particle Inductively Coupled Plasma Mass Spectrometry, Anal Chem. 83 (2011) 9361–9369.

[9] H.E. Pace, N.J. Rogers, C. Jarolimek, V.A. Coleman, C.P. Higgins, J.F. Ranville, Correction to Determining Transport E ffi ciency for the Purpose of Counting and Sizing Nanoparticles via Single Particle Inductively Coupled Plasma Mass Spectrometry, Anal Chem. 84 (2012) 4633–4633. https://doi.org/10.1021/ac300942m.

[10] M. Resano, M. Aramendía, E. García-Ruiz, A. Bazo, E. Bolea-Fernandez, F. Vanhaecke, Living in a transient world: ICP-MS reinvented via time-resolved analysis for monitoring single events, Chem Sci. (2022). https://doi.org/10.1039/d1sc05452j.

[11] S. Cuello-Nuñez, I. Abad-Álvaro, D. Bartczak, M.E. Del Castillo Busto, D.A. Ramsay, F. Pellegrino, H. Goenaga-Infante, The accurate determination of number concentration of inorganic nanoparticles using spICP-MS with the dynamic mass flow approach, J Anal At Spectrom. 35 (2020) 1832–1839. https://doi.org/10.1039/c9ja00415g.

[12] R.B. Reed, C.P. Higgins, P. Westerhoff, S. Tadjiki, J.F. Ranville, Overcoming challenges in analysis of polydisperse metal-containing nanoparticles by single particle inductively coupled plasma mass spectrometry, J Anal At Spectrom. 27 (2012) 1093–1100. https://doi.org/10.1039/c2ja30061c.

[13] H.E. Pace, N.J. Rogers, C. Jarolimek, V.A. Coleman, E.P. Gray, C.P. Higgins, J.F. Ranville, Single particle inductively coupled plasma-mass spectrometry: a performance evaluation and method comparison in the determination of nanoparticle size., Environ Sci Technol. 46 (2012) 12272–80. https://doi.org/10.1021/es301787d.

[14] A. Hineman, C. Stephan, E ff ect of dwell time on single particle inductively coupled plasma mass spectrometry data acquisition quality, (2014) 1252–1257. https://doi.org/10.1039/c4ja00097h.

[15] F. Laborda, J. Jiménez-Lamana, E. Bolea, J.R. Castillo, Critical considerations for the determination of nanoparticle number concentrations, size and number size distributions by single particle ICP-MS, Journal of Analytical Atomic Spectrometry. 28 (2013) 1220–1232. https://doi.org/10.1039/c3ja50100k.

[16] J. Liu, K.E. Murphy, R.I. Maccuspie, M.R. Winchester, Capabilities of single particle inductively coupled plasma mass spectrometry for the size measurement of nanoparticles: A case study on gold nanoparticles, Analytical Chemistry. 86 (2014) 3405–3414. https://doi.org/10.1021/ac403775a.

[17] D.M. Mitrano, E.K. Lesher, A. Bednar, J. Monserud, C.P. Higgins, J.F. Ranville, Detecting nanoparticulate silver using single-particle inductively coupled plasma-mass spectrometry, Environmental Toxicology and Chemistry. 31 (2012) 115–121. https://doi.org/10.1002/etc.719.

[18] J.W. Olesik, P.J. Gray, Considerations for measurement of individual nanoparticles or microparticles by ICP-MS: determination of the number of particles and the analyte mass in

each particle, Journal of Analytical Atomic Spectrometry. 27 (2012) 1143. https://doi.org/10.1039/c2ja30073g.

[19] J. Fuchs, M. Aghaei, T.D. Schachel, M. Sperling, A. Bogaerts, U. Karst, Impact of the Particle Diameter on Ion Cloud Formation from Gold Nanoparticles in ICPMS, Analytical Chemistry. 90 (2018) 10271–10278. https://doi.org/10.1021/acs.analchem.8b02007.

[20] A. Hineman, C. Stephan, Effect of dwell time on single particle inductively coupled plasma mass spectrometry data acquisition quality, Journal of Analytical Atomic Spectrometry. 29 (2014) 1252–1257. https://doi.org/10.1039/c4ja00097h.

[21] M.D. Montaño, H.R. Badiei, S. Bazargan, J.F. Ranville, Improvements in the detection and characterization of engineered nanoparticles using spICP-MS with microsecond dwell times, Environmental Science: Nano. 1 (2014) 338–346. https://doi.org/10.1039/c4en00058g.

[22] O. Borovinskaya, S. Gschwind, B. Hattendorf, M. Tanner, D. Günther, Simultaneous mass quantification of nanoparticles of different composition in a mixture by microdroplet generator-ICPTOFMS, Analytical Chemistry. 86 (2014) 8142–8148. https://doi.org/10.1021/ac501150c.

[23] H.E. Pace, N.J. Rogers, C. Jarolimek, V.A. Coleman, C.P. Higgins, J.F. Ranville, Determining Transport Efficiency for the Purpose of Counting and Sizing Nanoparticles via Single Particle Inductively Coupled Plasma Mass Spectrometry (vol 83, pg 9361, 2011), Analytical Chemistry. 84 (2012) 4633. https://doi.org/10.1021/ac300942m.

[24] J. Tuoriniemi, G. Cornelis, M. Hassellöv, Size discrimination and detection capabilities of single-particle ICPMS for environmental analysis of silver nanoparticles, Analytical Chemistry. 84 (2012) 3965–3972. https://doi.org/10.1021/ac203005r.

[25] R.B. Reed, D.G. Goodwin, K.L. Marsh, S.S. Capracotta, C.P. Higgins, D.H. Fairbrother, J.F. Ranville, Detection of single walled carbon nanotubes by monitoring embedded metals, Environmental Sciences: Processes and Impacts. 15 (2013) 204–213. https://doi.org/10.1039/c2em30717k.

[26] J. Tuoriniemi, G. Cornelis, M. Hassellöv, Improving the accuracy of single particle ICPMS for measurement of size distributions and number concentrations of nanoparticles by determining analyte partitioning during nebulisation, Journal of Analytical Atomic Spectrometry. 29 (2014) 743. https://doi.org/10.1039/c3ja50367d.

[27] F. Laborda, J. Medrano, J.R. Castillo, Quality of quantitative and semiquantitative results in inductively coupled plasma mass spectrometry, Journal of Analytical Atomic Spectrometry. 16 (2001) 732–738. https://doi.org/10.1039/b101814k.

[28] A.J. Goodman, A. Gundlach-Graham, S.G. Bevers, J.F. Ranville, Characterization of nano-scale mineral dust aerosols in snow by single particle inductively coupled plasma mass spectrometry, Environmental Science: Nano. 9 (2022) 2638–2652. https://doi.org/10.1039/d2en00277a.

[29] S. Bazargan, H. Badiei, U.S. Patent: Systems and Methods for Automated Analysis of Output in SP-ICP-MS, 2019.

[30] J. Tuoriniemi, G. Cornelis, M. Hassellöv, A new peak recognition algorithm for detection of ultra-small nano-particles by single particle ICP-MS using rapid time resolved data

acquisition on a sector-field mass spectrometer, Journal of Analytical Atomic Spectrometry. 30 (2015) 1723–1729. https://doi.org/10.1039/c5ja00113g.

[31] D. Mozhayeva, C. Engelhard, A quantitative nanoparticle extraction method for microsecond time resolved single-particle ICP-MS data in the presence of a high background, Journal of Analytical Atomic Spectrometry. 34 (2019) 1571–1580. https://doi.org/10.1039/c9ja00042a.

[32] T.E. Lockwood, R. Gonzalez De Vega, D. Clases, An interactive Python-based data processing platform for single particle and single cell ICP-MS, Journal of Analytical Atomic Spectrometry. 36 (2021) 2536–2544. https://doi.org/10.1039/d1ja00297j.

[33] E. Bolea-Fernandez, D. Leite, A. Rua-Ibarz, T. Liu, G. Woods, M. Aramendia, M. Resano, F. Vanhaecke, On the effect of using collision/reaction cell (CRC) technology in single-particle ICP-mass spectrometry (SP-ICP-MS), Analytica Chimica Acta. 1077 (2019) 95–106. https://doi.org/10.1016/j.aca.2019.05.077.

[34] P. Shaw, A. Donard, Nano-particle analysis using dwell times between 10 µs and 70 µs with an upper counting limit of greater than 3 × 107 cps and a gold nanoparticle detection limit of less than 10 nm diameter, Journal of Analytical Atomic Spectrometry. 31 (2016) 1234–1242. https://doi.org/10.1039/c6ja00047a.

[35] M. Tanner, Shorter signals for improved signal to noise ratio, the influence of Poisson distribution, Journal of Analytical Atomic Spectrometry. 25 (2010) 405. https://doi.org/10.1039/b921077f.

[36] L.A. Currie, Limits for Qualitative Detection and Quantitative Determination: Application to Radiochemistry, Analytical Chemistry. 40 (1968) 586–593. https://doi.org/10.1021/ac60259a007.

[37] L.A. Currie, International Union of Pure Nomenclature in Evaluation of Analytical Methods Including Detection Nomenclature in evaluation of analytical methods , including detect ion and quantification ca pa bi l it ies ’ (IUPAC Recommendations 1995), Pure and Applied Chemistry. 67 (1995) 1699–1723. https://doi.org/10.1287/isre.1120.0448.

[38] Project on Emerging Nanotechnologies (2013). Consumer Products Inventory, (n.d.). http://www.nanotechproject.tech/cpi (accessed November 18, 2022).

[39] M.E. Vance, T. Kuiken, E.P. Vejerano, S.P. McGinnis, M.F. Hochella, D.R. Hull, Nanotechnology in the real world: Redeveloping the nanomaterial consumer products inventory, Beilstein Journal of Nanotechnology. 6 (2015) 1769–1780. https://doi.org/10.3762/bjnano.6.181.

[40] I. Kalantzi, K. Mylona, C. Toncelli, T.D. Bucheli, K. Knauer, S.A. Pergantis, P. Pitta, A. Tsiola, M. Tsapakis, Ecotoxicity of silver nanoparticles on plankton organisms: a review, Journal of Nanoparticle Research. 21 (2019). https://doi.org/10.1007/s11051-019-4504-7.

[41] J.J. Antony, P. Sivalingam, B. Chen, Toxicological effects of silver nanoparticles, Environmental Toxicology and Pharmacology. 40 (2015) 729–732. https://doi.org/10.1016/j.etap.2015.09.003.

[42] S.L. Chinnapongse, R.I. MacCuspie, V.A. Hackley, Persistence of singly dispersed silver nanoparticles in natural freshwaters, synthetic seawater, and simulated estuarine waters, Science of the Total Environment. 409 (2011) 2443–2450. https://doi.org/10.1016/j.scitotenv.2011.03.020.

[43] W.Z. Teo, M. Pumera, Fate of silver nanoparticles in natural waters; Integrative use of conventional and electrochemical analytical techniques, RSC Advances. 4 (2014) 5006–5011. https://doi.org/10.1039/c3ra43224f.

[44] M. Sikder, J.R. Lead, G.T. Chandler, M. Baalousha, A rapid approach for measuring silver nanoparticle concentration and dissolution in seawater by UV–Vis, Science of the Total Environment. 618 (2018) 597–607. https://doi.org/10.1016/j.scitotenv.2017.04.055.

[45] C. Toncelli, K. Mylona, I. Kalantzi, A. Tsiola, P. Pitta, M. Tsapakis, S.A. Pergantis, Silver nanoparticles in seawater: A dynamic mass balance at part per trillion silver concentrations, Science of the Total Environment. 601–602 (2017) 15–21. https://doi.org/10.1016/j.scitotenv.2017.05.148.

[46] T.Y. Sun, N.A. Bornhöft, K. Hungerbühler, B. Nowack, Dynamic Probabilistic Modeling of Environmental Emissions of Engineered Nanomaterials, Environmental Science and Technology. 50 (2016) 4701–4711. https://doi.org/10.1021/acs.est.5b05828.

[47] B. Nowack, N.C. Mueller, Exposure modeling of engineered nanoparticles in the environment, EMPA Activities. 41 (2008) 63. https://doi.org/https://doi.org/10.1021/es7029637.

[48] A. Tsiola, C. Toncelli, S. Fodelianakis, G. Michoud, T.D. Bucheli, A. Gavriilidou, M. Kagiorgi, I. Kalantzi, K. Knauer, G. Kotoulas, K. Mylona, E. Papadopoulou, S. Psarra, I. Santi, M. Tsapakis, D. Daffonchio, S.A. Pergantis, P. Pitta, Low-dose addition of silver nanoparticles stresses marine plankton communities, Environmental Science: Nano. 5 (2018) 1965–1980. https://doi.org/10.1039/c8en00195b.

[49] A. Wimmer, A. Urstoeger, N.C. Funck, F.P. Adler, L. Lenz, M. Doeblinger, M. Schuster, What happens to silver-based nanoparticles if they meet seawater?, Water Research. 171 (2020). https://doi.org/10.1016/j.watres.2019.115399.

[50] J. Liu, K.E. Murphy, R.I. Maccuspie, M.R. Winchester, Capabilities of single particle inductively coupled plasma mass spectrometry for the size measurement of nanoparticles: A case study on gold nanoparticles, Analytical Chemistry. 86 (2014) 3405–3414. https://doi.org/10.1021/ac403775a.

[51] D.M. Mitrano, J.F. Ranville, A. Bednar, K. Kazor, A.S. Hering, C.P. Higgins, Tracking dissolution of silver nanoparticles at environmentally relevant concentrations in laboratory, natural, and processed waters using single particle ICP-MS (spICP-MS), Environmental Science: Nano. 1 (2014) 248–259. https://doi.org/10.1039/c3en00108c.

[52] D.M. Mitrano, A. Barber, A. Bednar, P. Westerhoff, C.P. Higgins, J.F. Ranville, Silver nanoparticle characterization using single particle ICP-MS (SP-ICP-MS) and asymmetrical flow field flow fractionation ICP-MS (AF4-ICP-MS), Journal of Analytical Atomic Spectrometry. 27 (2012) 1131–1142. https://doi.org/10.1039/c2ja30021d.

[53] E.B. and J.R.C. Francisco Laborda, Javier Jim?enez-Lamana, Selective identification, characterization and determination of dissolved silver(i) and silver nanoparticles based on single particle detection by inductively coupled plasma mass spectrometry, Journal of Analytical Atomic Spectrometry. 26 (2011) 1362. https://doi.org/10.1039/c0ja00098a.

[54] C. Toncelli, K. Mylona, M. Tsapakis, S.A. Pergantis, Flow injection with on-line dilution and single particle inductively coupled plasma – mass spectrometry for monitoring silver

nanoparticles in seawater and in marine microorganisms †, Journal of Analytical Atomic Spectrometry. 31 (2016) 1430–1439. https://doi.org/10.1039/C6JA00011H.

[55] L. Scheidemann, B. Pontiller, V. Manna, C. Cisternas-Novoa, M. Celussi, A. Tsiola, P. Pitta, I. Magiopoulos, A. Engel, Dynamics and enzymatic degradation of exopolymer particles under increasing concentrations of silver ions and nanoparticles during a marine mesocosm experiment, Frontiers in Marine Science. 9 (2022) 1–17. https://doi.org/10.3389/fmars.2022.955488.

[56] James N. Miller Jane C. Miller, Statistics and Chemometrics for Analytical Chemistry, 6th Editio, Pearson, 2010.

[57] A. Hineman, C. Stephan, Effect of dwell time on single particle inductively coupled plasma mass spectrometry data acquisition quality, Journal of Analytical Atomic Spectrometry. 29 (2014) 1252–1257. https://doi.org/10.1039/c4ja00097h.

[58] N.F. Adegboyega, V.K. Sharma, K. Siskova, R. Zbořil, M. Sohn, B.J. Schultz, S. Banerjee, Interactions of aqueous Ag+ with fulvic acids: Mechanisms of silver nanoparticle formation and investigation of stability, Environmental Science and Technology. 47 (2013) 757–764. https://doi.org/10.1021/es302305f.

[59] W.C. Hou, B. Stuart, R. Howes, R.G. Zepp, Sunlight-driven reduction of silver ions by natural organic matter: Formation and transformation of silver nanoparticles, Environmental Science and Technology. 47 (2013) 7713–7721. https://doi.org/10.1021/es400802w.

[60] J. Liu, K.G. Pennell, R.H. Hurt, Kinetics and mechanisms of nanosilver oxysulfidation, Environmental Science and Technology. 45 (2011) 7345–7353. https://doi.org/10.1021/es201539s.

[61] C. Levard, E.M. Hotze, G. V. Lowry, G.E. Brown, Environmental transformations of silver nanoparticles: Impact on stability and toxicity, Environmental Science and Technology. 46 (2012) 6900–6914. https://doi.org/10.1021/es2037405.

[62] C. Levard, B.C. Reinsch, F.M. Michel, C. Oumahi, G. V. Lowry, G.E. Brown, Sulfidation processes of PVP-coated silver nanoparticles in aqueous solution: Impact on dissolution rate, Environmental Science and Technology. 45 (2011) 5260–5266. https://doi.org/10.1021/es2007758.

[63] J.E. Shaff, B.A. Schultz, E.J. Craft, R.T. Clark, L. V. Kochian, GEOCHEM-EZ: A chemical speciation program with greater power and flexibility, Plant and Soil. 330 (2010) 207–214. https://doi.org/10.1007/s11104-009-0193-9.

[64] A. Wimmer, A. Kalinnik, M. Schuster, New insights into the formation of silver-based nanoparticles under natural and semi-natural conditions, Water Research. 141 (2018) 227–234. https://doi.org/10.1016/j.watres.2018.05.015.

[65] Y. Azov, Eastern Mediterranean-a marine desert?, Marine Pollution Bulletin. 23 (1991) 225–232. https://doi.org/10.1016/0025-326X(91)90679-M.

[66] H.R. Powley, M.D. Krom, P. Van Cappellen, Understanding the unique biogeochemistry of the Mediterranean Sea: Insights from a coupled phosphorus and nitrogen model, Global Biogeochemical Cycles. 31 (2017) 1010–1031. https://doi.org/10.1002/2017GB005648.

[67] S.T. Gentry, S.F. Kendra, M.W. Bezpalko, Ostwald ripening in metallic nanoparticles: Stochastic kinetics, Journal of Physical Chemistry C. 115 (2011) 12736–12741. https://doi.org/10.1021/jp2009786.

4 Chapter 4. Chip-based Microfluidics On-line with Inductively Coupled Plasma - Mass Spectrometry for Standard Dilution Analysis

4.1 Introduction

4.1.1 Introduction to microfluidics

Research demands for increased sample-throughput and experimental procedure automation have led to the miniaturization of analytical devices. This has brought advantages such as low reagent consumption as well as the capability to study chemical processes at biologically relevant length scales. Miniaturization mostly started in the area of micro-electro-mechanical systems (MEMSs), where fabrication developments paved the way for the fabrication of µm-dimensioned fluidic systems, e.g., microfluidics. The field of microfluidics emerged when microfluidic systems were developed to conduct analyte separations using microchip chromatography or capillary electrophoresis.[1,2] For instance, advantages of microchip capillary electrophoresis (MCE) were evident because the use of shorter and narrower separation capillaries allowed for the application of higher voltages, thus resulting in a considerable reduction of analytical time as well as improved analyte separation. The tolerance for higher voltages is owed to the characteristic of microfluidic channels for dissipation of heat generated by the high electric currents.[2,3] However, advantages of microfluidic chips were not perceived only in terms of shortening analytical time or improved quality of results, but also in terms of the possibility to design complete analytical platforms allowing for sample manipulation and detection on a single microchip. The latter was proposed in 1990 my Manz et al as a miniaturized chemical analysis system (µTAS), that is, a microfluidic chip that would integrate well-known analytical sample pretreatment procedures with detection by means of a chemical sensor.[4,5] In the following years, fundamental issues such as fabrication materials, chip designs, and fluid transport were studied, followed by a growth of bioanalytical applications. These applications include employment of microfluidics in order to manipulate and analyze single cells, intact or in a lysed state.[6–9] Moreover, upon acknowledging the capabilities of microfluidics for handling volume-limited samples, interfaces for combining microfluidics with powerful detection techniques, such as mass spectrometry were developed.[10–12]

4.1.2 Fabrication techniques

Techniques that were initially used to fabricate microfluidic chips included photolithography followed by wet etching of silicon or glass substrates. These constituted the first microfluidic chips, which were used for MCE. Execution of these fabrication techniques required specialized micro-engineering approaches as well as access to clean room facilities used to fabricate MEMSs, thus limiting researchers' accessibility to microchips. However, this changed with the introduction of polymers, especially poly(dimethylsiloxane) (PDMS) which has been the most common chip fabrication material.[13,14] This is because of the advantages of PDMS, including its transparency to visible light (helpful for microscopy measurements), its elastomeric nature (allowing tight incorporation of tubings or formulation of structures such as pneumatic valves), good compatibility with aqueous solutions typically used in bioanalytical applications (salts dissolved in buffer media), non-toxicity (compatible for biological cell studies), and the flexibility to transform the hydrophobic surface of channels into hydrophilic through plasma exposure (can be used to generate double emulsions). Disadvantages include gas permeability (liquid evaporation limits long-term studies), absorption of hydrophobic molecules such as lipids or dyes (unexpected decreases in concentration can impact results of the experiment). Another chip fabrication material which has gained recognition is thiol-ene based polymers, which, unlike PDMS, are highly compatible with organic solvents, and have been used for conducting non-aqueous microchip capillary electrophoresis for the separation of lipophilic compounds.[15,16] Fabrication of thiol-ene microfluidic chips has been demonstrated using a double-molding approach, which involves the fundamental techniques for fabricating PDMS chips. Fabrication of microfluidic chips in PDMS requires the application of photolithography and soft lithography.

Photolithography is employed in order to transfer a pattern from a photolithography mask into a substrate, i.e., a silicon wafer. Typically, photolithography masks are chromium-coated glass wafers that contain an etched pattern, made by e-beam lithography or direct laser writing. A thin layer of photoresist is applied onto a silicon wafer, becomes homogeneously distributed onto the surface of the wafer via spin coating, and the photoresist-substrate system is finally heated in order to enable solvent evaporation from the photoresist and partial hardening of the structure. Photo-resists are light-sensitive materials, composed of a polymer, a sensitizer and a solvent. The solvent allows the photoresist to be spun and form thin layers, while a photochemical reaction mediated by the sensitizer may weaken or

strengthen the polymer structure upon UV irradiation. In this respect, the photolithography mask, placed on top of the photoresist-substrate system, is irradiated with UV light (i.e., from a mercury lamp at 365 nm) with the aim of altering the polymer structure of the photoresist at the points that were irradiated. Depending on the type of photoresist used, i.e., positive or negative, the irradiated points become soluble or insoluble in a developer solution, respectively, thus resulting in an exact copy of the mask onto the substrate when using a positive photoresist, or in a complimentary structure when using a negative photoresist. For the fabrication of PDMS chips, negative photoresists, such as SU-8, are typically used in order to create master molds to be used in a subsequent step, that is soft-lithography.

Soft lithography refers to molding and patterning techniques related to the use of a soft elastomer such as PDMS. Although it requires a master mold, fabricated in a clean room facility for photolithography, soft-lithography is a cheap and easy to perform technique to fabricate PDMS chips. PDMS is commercially available as a 2-component system consisting of the oligomer rubber and a curing agent, the mixing ratio of which defines the final hardness of the cured polymer. The mixed solution is poured onto the master and is hardened in the oven, resulting in a structure which is complimentary to that of the master mold. Microchips can then be cut to preferred dimensions, while holes can be punched into the PDMS for tubbing connections. PDMS chips can then be strongly adhered to a glass slide by means of plasma bonding for sealing of channels or support.

Other approaches to fabricate microfluidic chips involve dry or wet etching (commonly used with glass or silicon substrates), where etchants such as chemicals, gases or plasmas, attack and remove locations of the substrate that were left unprotected by the mask, thermoforming techniques such as hot embossing, where a heated mold is pressed over a thermoplastic sheet such as polymethyl methacrylate (PMMA) or cyclic-olefin copolymer, or direct writing on a substrate by means of laser technology.

4.1.3 Liquid flows and mixing on a microfluidic chip

Liquid flows within channels of a microfluidic chip are typically pressure-driven.[13] The pressure gradient between the inlet and outlet point of a channel that is required to generate liquid flow can be typically generated using syringe pumps, where the motorized movement of a piston pushing a syringe is correlated to liquid flow rate, or by gas pressure-driven platforms, where the pressure gradient is the difference between an added gas pressure into a reservoir and the atmospheric pressure. It has been reported that gas pressure-driven

platforms demonstrate the greatest stability even at pumping rates of low nL min^{-1}, unlike syringe-pumps for which the pulsed movement of the motor is reflected as periodicity in the recorded flow rate.[13,17] Other cases of liquid flow include electro-osmotic flow (EOF), in which case an applied potential to the microchannel drives the movement of ions that drag along the rest of the solution. Another case of generating liquid flow was by harnessing hydrostatic pressure differences. This could be achieved by liquid filling of reservoirs, fabricated on microfluidic chips, and utilizing differences in the liquid levels of 2 reservoirs in order to generate a liquid flow between these reservoirs. Combination of EOF and hydrostatic flow has also been used to initially generate liquid flow and subsequently divert it to certain microfluidic channels, the end points of which were subjected to a voltage.[18]

The pressure-driven flow generated within a microfluidic channel results in a Poiseuille flow profile. Given the dimensions of a channel that determine the fluidic resistance R, the pressure gradient Δp is related to volumetric flow rate Q by the equation $\Delta P = QR$. For instance, the fluidic resistance for a circular channel can be calculated with the following relation:

$$R = \frac{8nL}{\pi r^4} \qquad (Eq. 1)$$

, n standing for viscocity ($Pa \times s$), L for channel length (m), Q for volumetric flow rate ($m^3 s^{-1}$) and r for channel diameter (m), therefore allowing for determining the pressure gradient required to generate a given volumetric flow rate.[19]

Mixing of liquids in microfluidic channels requires knowledge of the Reynolds and Peclet number. The Reynolds number is a dimensionless number dictating the flow regime, that is laminar (Re < 2300) or turbulent (>2300), while Peclet number defines the extent of diffusion that can lead to mixing of 2 liquids at a given flow rate. While for several applications laminar flow within microfluidic channels is beneficial, laminar flow in a straight microfluidic channel does not promote mixing of 2 liquids. In a micro mixing channel configuration where the 2 liquids meet in a T-shaped or Y-shaped intersection, the 2 liquids will co-flow in a straight microfluidic channel until molecular diffusion eradicates the concentration differences.[19] Because diffusive mixing at laminar flows, conditions pertaining to liquid flows within microfluidic channels, is slow, and thus requires long channels to complete, channel structures such as serpentines or obstacles are incorporated within the microfluidic channels in order to create turbulences and secondary flows within the liquid flow.[20] These

turbulences create chaotic mixing that increases the contact area of the 2 liquids, thus resulting in rapid and efficient mixing at low Re.[13,21]

4.1.4 Microfluidic applications

Microfluidic devices have been demonstrated with pharmaceutical, medical and biochemical applications.

In the context of pharmaceutical applications, spray drying is a powerful technique that can be used to transform a drug into an amorphous powder, thus increasing the specific surface of the drug, its solubility, and thus its bioavailability. However, conventional spray drying approaches involve large dead volumes and thus require loading high drug amounts, which are usually limited at the early stages of drug formulations. For this reason, the group of Weitz introduced a microfluidic spray drying method which demonstrated fabrication of danazol nanoparticles, with sizes ranging between 20 to 60 nm, that are far lower than the lowest NP size of 100 nm attained using conventional spray drying.[22] The microfluidic spray device was made of PDMS, and consisted of a T-shaped junction where liquid flows of water and isopropanol (containing the dissolved danazol) met, co-flowed, and were finally met at the nozzle by a flow of gas for generation of the spray.

Microfluidics have also shown potential for the production of liposomes, which are vesicles emerging from the self-assembly of phospholipids when present in an aqueous solution. Liposomes are widely used in pharmaceutics and medicine, as they can serve as carriers of lipophilic (intercalated into the lipid bilayer) or water-soluble actives (trapped within the aqueous interior). Bulk methodologies for liposome production often result in vesicles of non-uniform size and lamellarity, unlike microfluidic approaches which have shown potential for higher control of the aforementioned physical properties.[23] Formation of liposomes can be achieved by co-flowing streams of water and lipids dissolved in ethanol. In this process, diffusion-based mixing of water and ethanol results in a decrease of the ethanol concentration below the solubility of lipids, thus triggering the assembly of lipids into liposomes, which are more energy-favorable structures.

Microchip capillary electrophoresis (MCE) has experienced immense use for point-of-care medical diagnosis thanks to the advantages of considerably quicker analytical runs and more efficient analyte separation than the conventional capillary electrophoresis; adding the possibility of accommodating additional sample pre-treatment approaches, such as analyte enrichment by means of monolithic plugs.[24] MCE has been applied to investigate various

forms of cancer, i.e., lung, gastric, blood, colorectal, prostate, oral, liver, gynecologic (i.e., ovarian and cervical), and bladder cancers, as well as several immune and neurological disorders through the quantitation of proteins, peptides, and nucleic acids from biological fluids. For most of these applications, detection was carried out by laser-induced fluorescence (LIF). For instance, carcinoembryonic antigen determination was conducted by an immunochemical assay, used to bind the target antigen with a primary antibody and a secondary fluorescent tag-antibody, followed by microchip electrophoretic separation in order to isolate the target antigen-antibody complex from the unreacted antibodies. This type of electrophoretic separation-coupled with LIF detection could be realized within 4 min, instead of the 60 min-time that would otherwise be required for laborious washing steps in order to isolate the target antigen-fluorescent antibody complex.

Arguably, the biggest impact of microfluidics has been on the development of biochemical applications. Chips can be designed to incorporate multiple cell culture chambers to which medium and nutrients can be delivered in a highly controllable manner, thus allowing for a considerably greater number of cell culture growth and exposure experiments than using conventional cell culturing methods.[6] Extraction of nucleic acids from bacterial or mammalian cells by means of online cell lysis has also been demonstrated, in which case, flows of sample and reagents were controlled by pneumatic pressure-actuated valves. Volumes of the cell culture, lysis reagent and diluent were directed into a rotary mixing channel, which provided enhanced mixing as opposed to diffusion-based mixing within straight channels, and the resulting lysate was passed through an on-chip integrated affinity column and finally directed to waste. The target cell-DNA or RNA could be easily recovered from the column using an appropriate elution buffer in order to be isolated or further used for subsequent manipulations.[6,25]

Cell lysis and subsequent analysis has also been demonstrated on a per cell basis, with platforms involving single cell lysis under the presence of chemical reagents or the application of a high voltage. The target analytes emerging from the cell lysate have been detected by coupling MCE to LIF or ESI-MS detection.[18,26,27] For instance, the group of Richard N. Zare introduced a microfluidic chip bearing a reaction chamber, where lysis of a single cell along with derivatization of its constituent amino acids could be performed, and a MCE separation channel for separation of the fluorescence derivatized amino acids.[26] A fluorescence microscope was used for detection of the derivatized amino acids exiting the separation channel. The reaction chamber was created at the intersection of 2 microfluidic

channels, the liquid flows of which could be blocked upon actuation of a pneumatic valve; thus, trapping a single cell for chemical lysis within a 70 pL volume and injecting the lysed contents into the MCE channel. This type of pneumatic valve was fabricated within a multilayer PDMS chip, i.e., located on top of the layer where the microfluidic channels resided, therefore pressurization of the valve blocked liquid flow in the channels. Although pioneering in the field of single-cell analysis, this method suffered from low throughput, i.e., 1 cell per 1 hour, and relatively poor resolution in amino acid separation per single cell. Using a similar detection concept, Gao et al demonstrated the use of a microfluidic chip for detection of fluorescence-derivatized glutathione (GSH) on a per cell basis.[18] Each single erythrocyte could be docked within a microfluidic channel using a combination of hydrostatic and electroosmotic manipulations, lysed under the application of high voltage (units of kV), and detected as a fluorescence pulse corresponding to the detection of fluorescence-derivatized glutathione. An improved throughput of 15 cells h^{-1} was achieved, along with reproducible cell detection (cell detection at consistent time intervals), while the determined GSH content per cell was in good agreement with that obtained from conventional lysis of massive cell populations. However, in both of these studies, sampling of a single cell was manually conducted using a microscope, while fluorescence-derivatization of the target analyte was required prior to detection; thus, limiting sample throughput. In contrast, the group of Ramsey reported on the coupling of a microfluidic chip to molecular mass spectrometry, for the purpose of online single-cell lysis and protein detection at a significantly improved throughput of 12 cells min^{-1}.[27] All processes including cell transport, lysis, electrophoretic separation, and electrospray ionization of the lysed cell content were integrated on a microfluidic chip. Briefly, individual erythrocytes suspended within a flow of isosmotic buffer were met at an intersection by the capillary electrophoresis buffer (sub-osmotic), and were lysed under the application of an increased electric potential (4 kV) and the rapid dilution of the isosmotic cell buffer. The lysed content of individual cells was separated through an electrophoretic separation channel, and the eluent was transported to an electrospray tip for ionization and subsequent MS detection. All sample and buffer flows were driven electro-osmotically (EOF). Transport of the eluent to the electrospray tip, along with stable electrospray generation, were mediated by a makeup flow, driven electro-osmotically and meeting the eluent flow at a T-type intersection prior to the electrospray nozzle. Cell detection occurred as individual pulses in the recorded ion signal of free heme

(m/z 616) and hemoglobin subunits a and b, their major peaks corresponding to 22 and 20 positive charges.

The use of microfluidics has also been shown advantageous for probing protein conformational dynamics and interactions, by means of hydrogen exchange mass spectrometry (HDX-MS).[28,29] The principle of HDX-MS is based on determining the degree of deuterium incorporation into certain backbone peptide residues of the protein via exchange with amide hydrogens. The degree of deuterium incorporation can relay peptide or residue specific structural information, such as the epitopes through which a protein interacts with a drug or another protein. Conventional HDX permits deuterium labelling times as low as 10 s, which is insufficient for proteins undergoing fast conformation changes. In this respect, a microfluidic chip has allowed for probing protein dynamics at deuterium labelling times within the range of 0.14-1.1 s, thanks to the automated and precise mixing of sample, deuterium buffer and quench buffer.[28] The quenched protein sample was subsequently proteolyzed and the resulting peptide mixture analyzed using liquid chromatography (LC)-MS to determine deuterium uptake. Later on, the same authors developed an advanced HDX chip-based methodology, the configuration of which included deglycosylation of proteins by means of immobilized enzyme reactors, disulfide bond reduction by means of an electrochemical cell, HDX, and online proteolysis, all configured on a single chip.[29]

In all of the aforementioned studies, fluidic manipulations were conducted by means of continuous liquid flows, and analyte detection was carried out in open volume space within the microfluidic channels. A less-intuitive aspect of microfluidic operation is segmented flow, allowing for analyte transport and detection within droplets. This area of microfluidics is frequently referred to as droplet microfluidics, and in its simplest realization, involves the generation of aqueous μm-sized droplets within a hydrophobic oil flow. In such a process, the immiscibility of the 2 liquids results in a reduction of their interfacial area, therefore when coming into contact, the aqueous flow breaks into droplets which are carried downstream by the oil flow.[13,30] Droplet microfluidics has revolutionized biochemical applications, offering the capability to isolate and study single biomolecules and cells within a confined volume space (μm-sized droplets typically measuring a few tens of pL)[8,9,31,32] Each droplet may constitute a separate reactor to perform reactions and assays on encased biomolecules and cells, without dispersion of reagents, cross-contamination or diffusion of analytes of interest. Various microfluidic chip designs have been introduced, including the

application of external forces, such as an electric field, for droplet fusion, fission or sorting.[7,33] All these capabilities have led to applications, including enzyme screening assays, immunochemical assays and cytotoxicity assays per single cell, by means of fluorescence detection, as well as high-throughput analysis of drugs using molecular mass spectrometry.[9,34–36]

For instance, Mazutis et al demonstrated an immunochemical assay, allowing to discriminate between single cells that secreted an antibody of interest.[9] This method's principle involved co-encapsulation of each individual cell with a concentration of trapping antibodies, streptavidin-coated beads and fluorescent probes that could bind onto the surface of the bead. After allowing cells to incubate within the droplets for 15 min, droplets were subjected to re-flow on a microfluidic channel, and their fluorescence signal was online detected. Detection of fluorescence signals signified secretion of the target antibody by the respective cell. Towards the end of their course through the microfluidic channel, droplets could take 2 different directions, one of high and one of a lower hydraulic resistance. Each time a fluorescence signal was registered, signifying detection of the target antibody, the synchronized application of an electric pulse propelled these droplets toward the channel of high hydraulic resistance by means of di-electrophoresis, whereas the rest of the droplets naturally followed the path of lower resistance. This microfluidic cell sorting approach has been shown advantageous compared to conventional flow cytometry, the use of which precludes detection of fluorogenic biomolecules excreted from the cells. In line with the same principle of fluorescence detection coupled with electrically-actuated droplet sorting, sorting of 2 strains of *E. Coli* cells based on their enzymatic activity was demonstrated by the groups of Weitz and Griffiths.[34] Briefly, 2 strains of *E. Coli* cells, one able to express the enzyme of b-galactosidase and the other expressing an inactive variant, were emulsified into individual droplets along with a fluorogenic b-galactosidase substrate, and droplets that yielded a qualifying fluorescent signal could be collected at a throughput of 2000 s^{-1}.

Moreover, Brouzes et al reported on a microfluidic platform for performing a high-throughput cytotoxicity assay on single mammalian cells.[35] In its simplest execution, the method entailed co-encapsulation of each individual cell with 2 fluorescent dyes, one of which could stain live and the other dead cells. Initially, a group of cell-containing droplets and a group of dye-containing droplets were each generated by 2 different droplet generation nozzles, operating in parallel, ultimately resulting in the 2 groups of droplets co-flowing within a central microfluidic channel in an alternating pattern. At a certain point

downstream of the channel, application of an electric field induced fusion of each cell-containing and dye-containing droplet, resulting in the co-encapsulation of a cell and the 2 dyes within a single droplet. A long microfluidic channel served as a delay line in order to enable on-line incubation of cells with the dyes. Live or dead cell scoring could be decided upon detection of fluorescent transient signals, at wavelengths relative to those of live or dead cell-staining dye. The presented platform was also demonstrated in a more advanced version, where cell viability was evaluated upon cell exposure to 8 different concentrations of mitomycin C. Initially, a library of droplets was generated, where each group of droplets contained a given concentration of the drug, along with a given concentration of a tracer dye. This meant that information on live or dead cell scoring was also combined with information on the concentration of the drug that each cell was incubated with, as the fluorescent signal intensity of the tracer dye could be correlated to a given drug exposure concentration. Excellent agreement was demonstrated between results obtained with the on-chip viability assay and those obtained with conventional assays conducted on microplates.

Droplet microfluidics interfaced to molecular mass spectrometry, by means of nanoelectrospray ionization (nanoESI), has been used to accomplish rapid, label-free and highly sensitive analysis of molecules of biological interest, such as enzyme-derived products and neurochemicals, from complex biological matrices.[11,37] For instance, the group of Kennedy demonstrated that a PDMS chip can be directly coupled to a nanoESI source by using commercially available nanoESI spray emitters in order to quantitatively monitor the catalytic activity of amine transaminase-117, present in biological solutions that contained mM concentrations of salts.[11] Continuous infusion of droplets was demonstrated for as long as 2.5 hours, over which 20000 droplets were detected without any signal degradation or chip-based MS system dysfunction, despite the continuous infusion of the fluorinated oil carrier. The oil carrier plus the aqueous flow accounted for a total flow rate of 20-500 nL min^{-1}, depending on the volume of the aqueous droplet that was generated, i.e., 65 pL or 1.2 nL. The applicability of the system was shown for the simultaneous generation of enzyme plus substrate-containing droplets along with control droplets (without the enzyme), where each set of droplets could be conveniently detected in an alternating fashion, without any occurrence of sample carry-over. Detection limits were found at the attomole level, which is quite satisfactory noting the presence of mM levels of salts that would normally require chromatographical separation in order to permit sensitive

MS detection. Moreover, in an attempt to conduct multiplexed analysis of neurochemicals down to the attomole level, the group of Vlassov fabricated an in-house silicon chip integrating a droplet generation region along with a nanoESI emitter, configured on the same chip.[37] A solution containing 6 neurochemicals could be compartmentalized in individual 7 pL aqueous plugs flowing within an oil flow toward the nanoESI emitter. The chip was mounted on a 3-dimensional micromanipulator for optimized nanospray sampling toward the MS inlet. Efficient chip-MS operation was accomplished at the low 10 nL min^{-1}, permitting sensitive MS detection of neurochemicals down to the single digit attomole level.

4.1.5 Microfluidic chip-based interfaces to ICP-MS

Owing to the capability of microfluidic systems to handle liquids of extremely low volume (nL-μL range) and the highly sensitive detection of elemental isotopes offered by inductively-coupled plasma mass spectrometry (ICP-MS), microfluidic devices have been interfaced to ICP-MS with applications mainly in the fields of elemental speciation and biological sample analysis, including intact and lysed cell populations. As early as 2002, microchip devices were used for the electrophoretic separation of inorganic species of Cr, Cu and As, with ICP-MS detection.[38,39] Subsequently, Pearson *et al.* reported on a highly efficient interface for ICP-MS, which integrated a microfluidic chip with a low flow rate cross-flow nebulization and evaporation chamber, all configured on a polytetrafluoroethylene (PTFE) block.[40] The system was demonstrated to operate at as low as 5 μL min^{-1} and provided sensitive detection without the need for excessive sample dilution by using a makeup flow. Building on the idea of analyzing nanoliter volume samples, the group of Yin fabricated and introduced microchips which featured high sensitivity, reproducible sample injection even at 0.18-0.4 nL volumes, and high accuracy considering the matrix complexity.[41,42]

Over the last decade, microfluidic systems combined with ICP-MS have been used mainly for the analysis of droplet-encapsulated single cells, as well as lysed cell populations.[43–50] Interfaces for detecting single cells include the generation of water-in-oil droplets and subsequent introduction to ICP-MS. For the removal of organic material and the undisrupted ICP operation, strategies such as a membrane desolvator for the removal of organic vapor or the addition of O_2 gas to the ICP spray chamber have been implemented.[43–46] The reported systems have been used for detection of iron (Fe) in bovine cells, zinc (Zn) in HepG2 cells, gold (Au) nanoparticles (NPs) in Hela cells, as well as for monitoring the release of Fe and platinum (Pt) in single cells following their incubation with FePt NPs.

Without the need for forming water-in-oil droplets and the addition of O_2 gas, Zhou *et al.* has reported on the coupling of a microfluidic chip with ICP-MS detection in order to conduct analysis of single HeLa cells and RAW264.7 macrophages.[47] Microfluidic chips coupled with ICP-MS have also been used for detection of trace elements in lysed cell populations with the benefits of low sample consumption, detection sensitivity and accuracy. These interfaces involve chip-based magnetic solid phase microextraction (MSPME) and chip-based array monolithic microextraction prior to ICP-MS detection, while introduction of a microHPLC between a MSPME chip and ICP-MS allowed for the speciation of Hg in HepG2 cells.[48–50]

In almost all of these approaches μL min^{-1} flow rates were supplied using syringe pumps, while connection of the chip outlet with the nebulizer was achieved through a standard fused silica capillary.

4.1.6 Standard Dilution Analysis

Standard dilution analysis (SDA) [51–55] is based on the gradient dilution of standards (analyte standard and internal standard) in the presence of a constant sample matrix. For the simplest realization of an SDA calibration, detector readings can be collected during the introduction of a mixture composed of 50% sample and 50% of a standard solution containing the analytes and an internal standard (IS) (Solution 1). With the detector continuously recording analyte and IS signals, a second mixture containing 50% sample and 50% blank (Solution 2) can be poured into the same container with Solution 1. As the two solutions mix and detection is conducted online, multiple calibration points are generated while the 2 solutions become increasingly more dilute. Because both Solution 1 and Solution 2 contain the same amount of sample, there is no change in matrix constitution as they mix. During the dilution a negative slope for the analyte and internal standard response is observed, which allows for multiple calibration points to be obtained in order to establish the analytical response in the presence of the sample matrix. Because of the presence of internal standard and the constant amount of sample matrix, the analyte response is corrected both for matrix effects and instrument drift, and the analyte concentration in the sample can be determined using the following formula:

$$C_A^{sample} = \frac{slope}{intercept} \times \frac{C_A^{std}}{C_I} \qquad (Eq. 2)$$

The slope and intercept could be obtained from the linear relationship between the ratio of analyte signal S_A over internal standard S_I and $\frac{1}{C_I}$. To establish this relationship, precise knowledge of the internal standard concentration C_I for each point of $\frac{S_A}{S_I}$ is required, let alone the manual mixing of the solutions required for SDA.[51] Recently, Jones et al demonstrated an automated SDA inductively coupled plasma optical emission spectroscopy (ICP-OES) configuration.[53] A two-channel pinch valve was used with a peristaltic pump driven flow system in order to mix and dilute the 1st calibration solution containing the analyte standard and a primary internal standard with the 2nd calibration solution containing only a secondary internal standard. The secondary internal standard was added to the blank calibration solution in order to facilitate the convenient and unbiased identification of the SDA processing region. This was an improvement as the initial demonstration of SDA required meticulous selection of the SDA window, i.e., the signal region where the 2 solutions mixed, as well as precise knowledge of the maximum signal of the primary IS in order to establish the linear relationship that would provide the slope and intercept of $Eq.2$. The two calibration solutions were mixed in sequence with the sample solution and introduced into the plasma at mL min^{-1} flow rates. The analyte concentration in the sample C_A^{sam} could be obtained by using a mathematical expression that utilizes the presence of the secondary internal standard during the mixing of solutions. Thus, the following expression was used:

$$C_A^{sam} = \frac{intercept}{slope}\frac{C_A^{std}}{S_I^{max}} \qquad (Eq.3)$$

, where C_A^{std} are the analyte concentrations contained in the 1st calibration solution, the $intercept$ and $slope$ can be obtained from the relationship of the analyte vs the primary IS, while S_I^{max} corresponds to the intercept of the linear relationship between the primary IS and secondary IS. The proposed automated SDA method proved to be effective with close to 100% analyte recoveries for eight elements evaluated across nine different sample matrices. Limited use of SDA with ICP-MS, however, has so far been reported. To the best of our knowledge a single report on SDA with inductively coupled plasma - mass spectrometry (ICP-MS) has been shown for the quantitation of As, Cr and Ni in concentrated acids.[54] Recoveries ranged from 90-114%, with samples and standards being introduced at conventional mL min^{-1} flow rates.

4.1.7 Objective

Biochemical applications have experienced tremendous growth owing to the capabilities of microfluidics in manipulating volume-limited samples. Since there has always been an interest for metal quantitation in samples of biological interest, as a result of the prominent role of metals in biological systems, there is a need to combine the power of microfluidics in nL-µL-scale sampling with a powerful atomic spectrometric technique such as inductively-coupled plasma mass spectrometry (ICP-MS). While several attempts have already been made in interfacing microfluidics to ICP-MS for the analysis of intact or lysed cell populations, mainly through the use of fused silica capillary connecting the outlet of a microfluidic chip with the inlet of a pneumatic nebulizer, technical aspects of these interfaces that could hamper a chip-based ICP-MS analysis were not discussed. Also, there is no report of an advanced quantitation approach offering matrix or instrumental drift correction when performing metal analysis using a microfluidic-ICP-MS system, other than the common external calibration, as emphasis has been on the procedures happening on the microfluidic chip. Herein, this study aims to demonstrate the successful coupling of a microfluidic chip to ICP-MS by pointing out critical technical aspects of the chip-based ICP-MS setup used to conduct metal analysis in volume-limited samples. The coupling is conducted using commercially available components, including pressure-actuated pumping systems and distribution valves to perform robust and rapid manipulations of solutions at the low µL min^{-1} flow regime. Furthermore, the feasibility of employing Standard Dilution Analysis (SDA), a novel quantitation calibration approach demonstrated to correct for both matrix effects and instrumental drift, is shown for the first time at the µL min^{-1} flow regime using the developed chip-based ICP-MS setup; when SDA has only been demonstrated for mL min^{-1} flow rates, a flow regime where fluid mixing can more readily be achieved. Optimization of instrumental parameters associated with the provision of accurate and precise flow rates, as well as reproducible solution exchanges, is conducted in order to enable reproducible mixing of solutions on the microfluidic chip, followed by a smooth introduction into the ICP-MS. These requirements are essential for conducting SDA for chip-based ICP-MS, the successful implementation of which is indicated by the method's accuracy, precision and limits of detection, as obtained from the analysis of several different sample types.

4.2 Materials and Methods

4.2.1 Chemicals and solutions

The following solutions were prepared and used in this study. The first calibration solution, referred to as the primary internal standard (PrmIS) solution, was prepared to contain both a primary internal standard, i.e., In at 5 ng mL^{-1}, as well as the analytes Cd, Co, and Pb at 5 ng mL^{-1}, and Cr and Ni at 10 ng mL^{-1}, in 3% nitric acid. The second calibration solution, referred to as the secondary internal standard (SecIS) solution was prepared to only contain the secondary internal standard, i.e., Ce at 5 ng mL^{-1}, in 3% nitric acid.

Both calibration solutions were prepared using 18 MΩ cm de- ionized (DI) water (PURELAB Option-S, Elga Labwater, UK). A set of 5 samples with the following matrices, i.e., de-ionized water (DI), TAP water (TAP), 0.1% m/v Ca, 5% v/v MeOH and digested algal cells, were prepared and spiked with specific analyte concentrations of 5 or 10 ng mL^{-1}, in order to conduct recovery studies.

Standards and samples were prepared in 3% trace-metal grade nitric acid. Methanol of LC-MS CHROMASOLVTM grade was obtained from Sigma Aldrich (Seelze, Germany). A 0.1% w/v calcium solution was prepared from calcium nitrate tetrahydrate (crystallized; ≥98%), obtained from Fluka Chemical. Digested cell samples were prepared from EDTA-washed Chlamydomonas reinhardtii CC- 1690 cells. Briefly, 30 mL of a stock cell culture were washed with 200 mL of an EDTA solution (50 mM tris(hydroxymethyl)aminomethane (Trizma base) and 1 mM ethylenediaminetetraacetic acid (EDTA), at pH 7). After centrifugation, the resulting cell pellet was digested with 150 µL of 68% w/w HNO_3 and diluted with de-ionized water to the final concentration of 10^5 cells mL^{-1}. The certified reference materials used in this study were dogfish muscle DORM-2 (NRC-CNRC) and dogfish liver DOLT-4 (NRC-CNRC). Prior to metal determination, these materials were microwave digested with 5 mL of 68% w/w nitric acid (HNO_3) and 2 mL of 30% w/w hydrogen peroxide (H_2O_2). The digestion procedure involved pre-digestion on a sandbath for 1 h at 125 °C, followed by microwave-assisted digestion for 75 min. The resulting digests were diluted with de-ionized water to a final concentration of 3% nitric acid.

4.2.2 Instrumentation and operating parameters

The microfluidic pumping system consisted of a pressure controller (OB1 MK3+, Elveflow) unit, used to apply and regulate nitrogen (N_2) pressure, up to 2000 mbar, into pressurized 50 mL Falcon-type tubes (114×28 mm) and/or 1.5 mL Eppendorf-type containers. Liquid flows were monitored as they passed through two dedicated thermal time-of-flight flow sensors (MFS 2 and 3, Elveflow). Thermal time-of-flight technology of the MFS flow sensors incorporates a heater and a sensor upstream and downstream of the flow measurement channel, respectively, and monitors flow rate by measuring the transit time of a heat pulse over a certain distance.[56] (flow metering in microfluidics ref) Flow sensor readings were fed back to the pressure controller, while gas pressures were adjusted in order to achieve the specified flow rates. **Figure 4.1** is a graphical representation of the connections amongst the pressure controller, flow sensors, as well as the 2 calibration solutions, i.e., PrmIS and SecIS, which are interchangeably mixed with the sample within the microfluidic chip.

As shown in **Figure 4.1**, two gas channels (blue lines) were used, one of which was devoted to pumping the sample solution and the other was split and used for pumping either

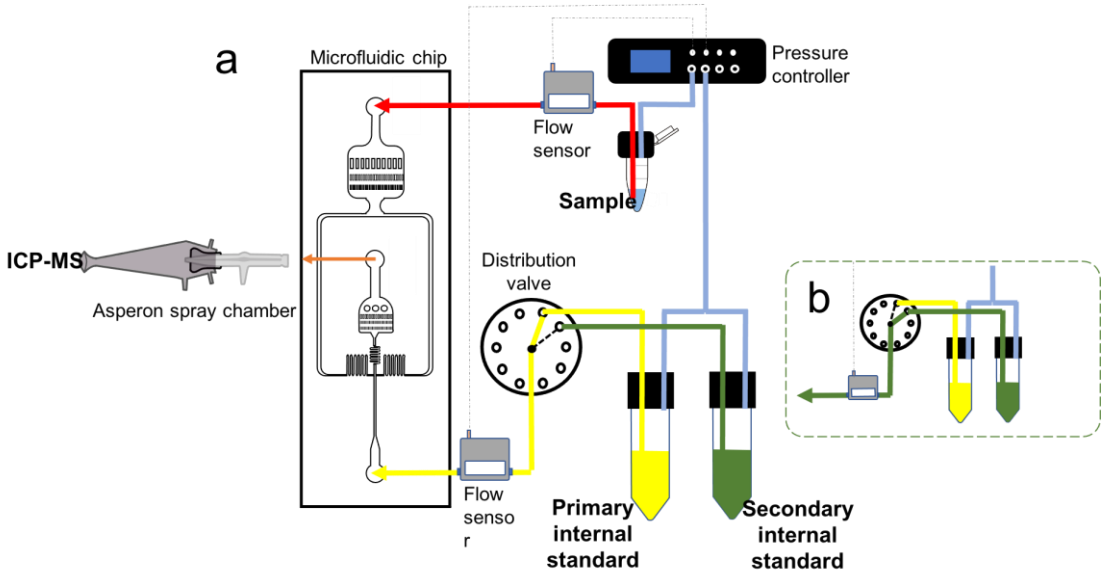

Figure 4.1 Microfluidic chip ICP-MS setup for standard dilution analysis. In (a) the setup is operating with the mixing of sample (red line) and the primary internal standard solution (PrmIS) (yellow line), whereas in inset (b) the distribution valve has been switched and the secondary internal standard solution (SecIS) (green line) is sent onto the chip for mixing with the sample. Orange line represents the mixing of the sample and the standards and their introduction into the ICP-MS. Blue lines represent gas pressure lines, and dotted lines are electrical connections. Components are not drawn to scale.

the PrmIS or the SecIS solution. The PrmIS and SecIS solutions were pumped onto the microfluidic chip (PDMS droplet gerenation chip, Elveflow) interchangeably via a MUX 10-port distribution valve (Elveflow) in order to carry out SDA analysis. The whole system integrating the pressure controller, flow sensors and distribution valve was controlled through the dedicated Elvys software (Elveflow). To evaluate the technique's precision, 4-5 independent SDA windows were obtained per sample analysis. This meant that the distribution valve was automatically switched between the PrmIS and SecIS positions every 6.5-7 min, while the two flow channels were both operated at 7.0 μL min^{-1}; the one supplying the sample and the other the PrmIS or SecIS. Therefore, the total liquid flow delivered through the chip to the nebulizer was 14.0 μL min^{-1}. Liquid solutions were transferred via polyetheretherketone (PEEK) tubing for the PrmIS and SecIS pump-flow sensor system, while PTFE tubing (0.3 mm i.d., 0.76 mm o.d.) was used for the sample solution. In addition, a piece of PEEK tubing (0.127 mm i.d., 1.587 mm o.d.) was connected to the exit port of each flow sensor to provide adequate microfluidic resistance for each pump channel. A microfluidic resistance is needed in order to ensure stable liquid flows rates when pressure-actuated pumping systems are employed, such as the one used in this study. Incorporating flow resistance along the flow path smooths out any flow instabilities that may be caused due to pressure fluctuations, or allows the pressure controller to rapidly recover liquid flows that could be momentarily obstructed within the microfluidic channels (i.e., channel clogging from a particle contamination). Also, if no fluidic resistance existed, the flow sensors would saturate at extremely low pressure values, thus prohibiting flow rate measurements. For a pressure-actuated pumping system, the pressure drop between the solution reservoir and the exit of a microfluidic channel (ΔP) is linearly related to flow rate Q, with a slope equal to the microfluidic resistance R. R can be determined, for a circular channel, using $(Eq.1)$ [19]. Based on this relation, a 26 cm long PEEK tubing (50 μm i.d.) and a 15 cm long PEEK tubing (80 μm i.d.) would be typically required for operation of the MFS2 and MFS3 flow sensors, respectively, in order to provide precise liquid flow rates across their full flow range capacity (0.4-7 μL min^{-1} and 2-80 μL min^{-1} for MFS2 and MFS3, respectively) prior to their connection with the microfluidic chip. However, it was observed that connection of the flow sensors with the microfluidic chip, containing in itself even narrower channels (i.e., 50×45, width×height), could be readily achieved using a lower microfluidic resistance (0.127 i.d. PEEK tubing) that provided extremely stable flow rates, as well as resulted in less frequent clogging issues. Connection to the microfluidic chip was achieved by direct insertion of PTFE tubing (0.3 mm

i.d., 0.76 mm o.d.) into the chip inlet and outlet ports. A 9 cm piece of the same i.d. PTFE tubing was used to connect the outlet port of the chip to the HEN nebulizer (Meinhard). A photograph of the experimental setup as configured in the lab is provided in **Figure SI1. 5**, while a graphical representation of the used microfluidic chip can be seen in **Figure SI1. 6**. Flow sensor calibration was checked gravimetrically by flowing a solution through each sensor for a 10 min period, collecting it in an Eppendorf tube, and weighing it. This allowed for the calculation of a correction factor when small flow deviations were observed.

At the end of operation, the flow sensors and microfluidic chip channels were washed with 3% HNO_3 and de-ionized water for 20 min. Subsequently, they were flushed with N_2 gas before storage.

All ICP-MS instrumental parameters are provided in **Table SI1. 2**. The ICP-MS was operated in kinetic energy discrimination mode by supplying He to the collision cell. Each acquisition was carried out in time-resolved mode with a dwell time of 500 ms, and 10 isotopes were monitored per analytical run. This resulted in registering an intensity reading for each of the 10 isotopes every 6.048 s. Given that each standard dilution window (SDA window) had a duration of approximately 360 s, it resulted in collecting approximately 60 data points per each isotope, per each SDA window.

4.3 Results and Discussion

4.3.1 Coupling the microfluidic chip to ICP-MS

Coupling of the chip-based microfluidic system to an ICP-MS was achieved using commercially available components. More specifically, a High- Efficiency Nebulizer (Meinhard, HEN) was placed in an Asperon^{TM} spray chamber (PerkinElmer), thus enabling the addition of a laminar flow of Ar makeup gas. This is a critical feature of the used interface because it allows for the HEN, a pneumatic nebulizer normally requiring 0.8-1.1 L min^{1} of Ar, to operate at much lower gas flow rates typically between 0.18 and 0.25 L min^{1}, and thus suction effects associated with the self-aspiration of the nebulizer can be minimized. The additional gas flow rate required to transport the analyte ions through the plasma is supplied via an Ar makeup flow (i.e., 0.50-0.57 L min^{1}). The diagram provided in **Figure 4.2** demonstrates how the nebulizer gas affects solution uptake and as a consequence the resulting suction exerted on the microfluidic chip. This has been achieved by simultaneously recording the signal for $^{140}Ce^{+}$, contained at 5 μg L^{-1} in the SecIS solution, and the liquid flow

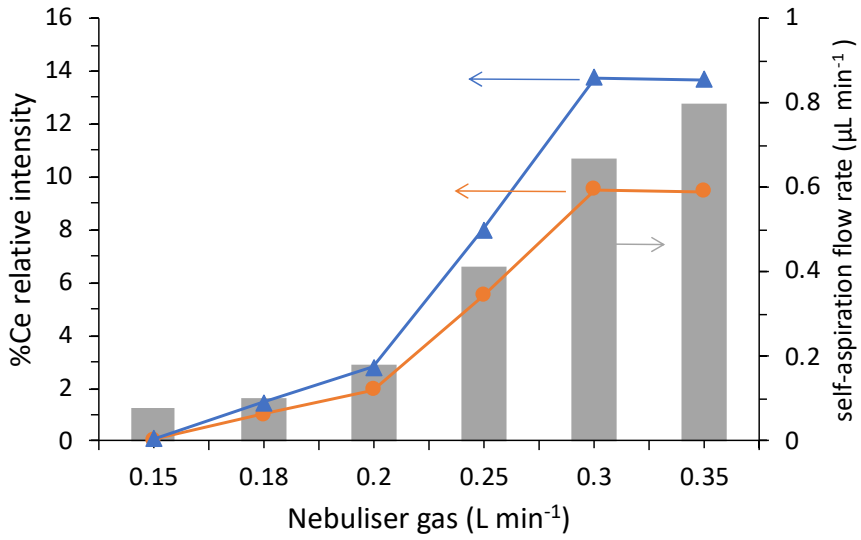

Figure 4.2 Diagram showing the effect of the nebulizer gas flow rate on the suction exerted on the microfluidic chip when the pump is not in operation. The y-axis represents the % relative intensity for the cerium isotope of $^{140}Ce^{+}$. This is defined as the absolute intensity achieved for $^{140}Ce^{+}$ when it is self-aspirated as a function of the different nebulizer gas flow rates (given on the x-axis), divided by the intensity achieved for $^{140}Ce^{+}$ when the liquid pump is operating and the nebulizer gas is either at 0.20 (blue) or 0.18 (orange) L min^{-1}. Pump in operation means that the two pump channels are delivering a total flow rate of 14.0 µL min^{-1} (5 µg L^{-1} Ce pumped at 7.0 µL min^{-1} and a blank sample pumped also at 7.0 µL min^{-1}.

rate going through the chip-ICP-MS system. In all cases the nebulizer gas, plus the makeup gas, give a total Ar flow rate of 0.75 L min^{-1}. From this diagram it is evident that upon reducing the nebulizer gas flow rate the self-aspiration flow drops substantially. This liquid flow rate, which is measured by the two flow sensors, each one dedicated to a single pump channel (**Figure 4.1**), corresponds to the uptake rate of the nebulizer when it is connected to the microfluidic chip while the two pump channels delivering the liquid flows to the chip-ICP-MS are not in operation. In a similar fashion the signal corresponding to Ce also drops. More specifically, at the commonly used in this study nebulizer flow rates of 0.18 or 0.20 L min^{-1}, self-aspiration is limited to 0.1 and 0.2 µL min^{-1}, respectively. Such low flows are negligible, approximately 1-2% of the total liquid flow of 14.0 µL min^{-1} used throughout this study, and thus are not expected to affect the operation of the chip ICP-MS system, i.e., mainly its stability. The ion signal is affected to a similar extent as is observed by the % Ce relative intensity shown in **Figure 4.2**. The % Ce relative intensity equals $^{140}Ce^{+}$ signal intensity from self-aspiration, divided by $^{140}Ce^{+}$ signal intensity recorded when both pump channels are in operation and the SecIS is being introduced. It should be mentioned that the one pump

channel was dedicated to pumping the SecIS solution (5 µg L^{-1} Ce) at 7.0 µL min^{-1} and the other to pumping a blank solution, also at 7.0 µL min^{-1}.

Signal and flow stability are also critical requirements for the efficient operation of a microfluidic interface and a prerequisite for conducting SDA. Attaining this objective was demonstrated by continuously introducing standard solutions into the ICP-MS via the chip and recording the signal intensity for $^{115}In^{+}$ and $^{140}Ce^{+}$, as well as the liquid flow rate supplied to the chip-ICP-MS (**Figure 4.3**). To conduct this stability study, the distribution valve was initially set to introduce the PrmIS solution, containing 5 µg L^{-1} In, to the chip at 7.0 µL min^{-1}, while a blank solution was also pumped onto the chip via the second pump channel, also at 7.0 µL min^{-1}. As can be seen in the inset of **Figure 4.3**, the valve switch causes a brief and negligible turbulence of 3% to the flow rate which, however, does not disturb the recorded $^{115}In^{+}$ intensity. The PrmIS solution provides a stable $^{115}In^{+}$ intensity for 8 min.

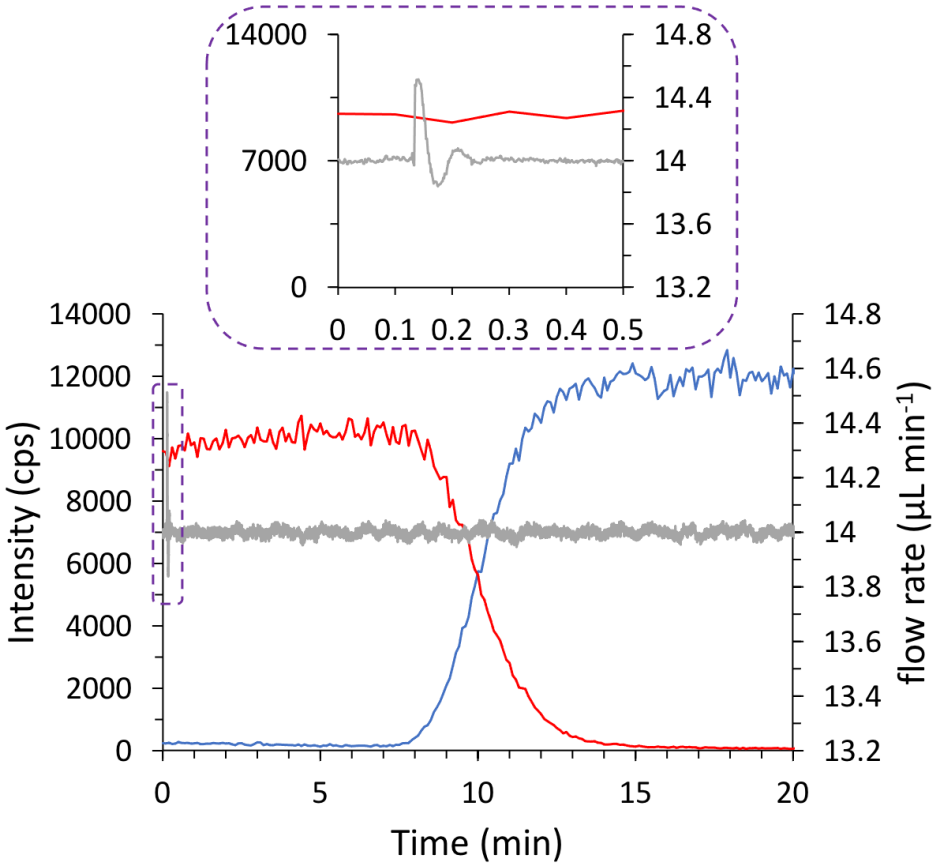

Figure 4.3 Time-resolved acquisition of the simultaneously recorded ICP-MS intensity for $140Ce^{+}$ (blue) and $115In^{+}$ (red) (scale given on left hand y-axis) and flow rate (gray) (scale given on right hand y-axis) supplied to the nebulizer. The PrmIS solution (5 µg L^{-1} In) provides a stable In signal intensity until it starts to be diluted by the SecIS solution (5 µg L^{-1} Ce) from 8-14 min. The SecIS provides a stable Ce signal intensity from 14 min until the end of the acquisition.

Between 8-14 min, **Figure 4.3** demonstrates the dilution zone of the PrmIS (5 µg L^{-1} In) by the introduced SecIS solution (5 µg L^{-1} Ce). Thereafter, a stable $^{140}Ce^{+}$ intensity is recorded until the end of the acquisition. Signal stability was in the 2.6 to 3.1 %RSD range for $^{115}In^{+}$ and $^{140}Ce^{+}$, as recorded for 0-8 and 14-20.5 min for $^{115}In^{+}$ and $^{140}Ce^{+}$, respectively. Exceptional flow rate stability was achieved by the pressure driven microfluidic pump with an RSD as low as 0.14% throughout this 20 min recording.

In addition to achieving signal stability, it was also important to demonstrate the compatibility of the PDMS microfluidic chip with the 1-3% nitric acid solutions typically used during ICP-MS analysis. Lee et al. investigated the compatibility of PDMS with various organic solvents, as well as acids.[57] In their study the authors reported that PDMS did not show any swelling in all acids and bases tested, including concentrated nitric acid (70%, 16 M). In addition, they found that concentrated nitric acid did not dissolve PDMS, in contrast with concentrated sulfuric acid and trifluoroacetic acid. Therefore, it was assumed that the PDMS chip could readily tolerate 1-3% nitric acid solutions. In addition, the occurrence of any metal leaching from the PDMS due to the dilute acid was investigated by conducting multi-elemental analysis with and without the chip being part of the microfluidic system. The recorded intensities were compared in order to evaluate the stability of the PDMS chip under the operating conditions, i.e., continuous flow of a blank 3% nitric acid aqueous solution. Most of the analyzed metals did not register an intensity increase when the chip was in-line, most importantly Si, but also Na, K, Ca, Ti, Cr, Fe, Co, Cu, As, Mo, Pd, Ru, Ag, Cd, Sn, Sb, Hg, and Pb. However, some exceptions were observed for the following m/z values: intensity at m/z 138 (possibly Ba) climbed from 10 kcps to 40 kcps, and intensity at m/z 27 (possibly Al) increased from 165 kcps to 1107 kcps, suggesting that these elements may be present in the PDMS material or that other elements from the PDMS give rise to equivalent m/z polyatomic ions and may thus cause a problem for the trace determination of Al and Ba. Overall, however, these findings show that the PDMS material is relatively inert to the use of a dilute nitric acid carrier.

4.3.2 Operation of the microfluidic chip for standard dilution analysis (SDA) using ICP-MS

For the implementation of SDA, two solutions need to be supplied simultaneously to the mixing chip, i.e., the sample solution delivered at 7.0 µL min^{-1} and either of the two calibration solutions (PrmIS or SecIS), also introduced at 7.0 µL min^{-1}. Selection of either the PrmIS or

SecIS solution for mixing with the sample was accomplished using a 10-port distributor valve. Samples were loaded onto the system from 1.5 mL Eppendorf tubes. However, only approximately 40-140 µL of solution was required for a complete analysis.

A typical multi-isotope recording obtained using the chip-based ICP-MS system is shown in **Figure 4.4** for a sample solution containing 0.1% Ca and spiked with 5 µg L^{-1} of Cd, Co, Pb and 10 µg L^{-1} Cr, Ni. From 0-5 min, both the sample and the SecIS (containing 5 µg L^{-1} Ce) solutions are mixed on the chip and delivered to the ICP-MS. This provided a steady state signal intensity for the analytes and $^{140}Ce^{+}$. At approximately 5.5 min the PrmIS (containing 5 µg L^{-1} In and the analytes in standard amounts) started to replace the SecIS solution, whereas the sample solution continued undisturbed. This resulted in a SDA window (5.5-11.5 min) which gave signals with positive slopes for the analytes ($^{52}Cr^{+}$, $^{58}Ni^{+}$, $^{59}Co^{+}$, $^{208}Pb^{+}$ and $^{114}Cd^{+}$) and $^{115}In^{+}$, present in the PrmIS solution, as well as a negative slope for $^{140}Ce^{+}$, present in the SecIS solution. Subsequently, following another switching of the

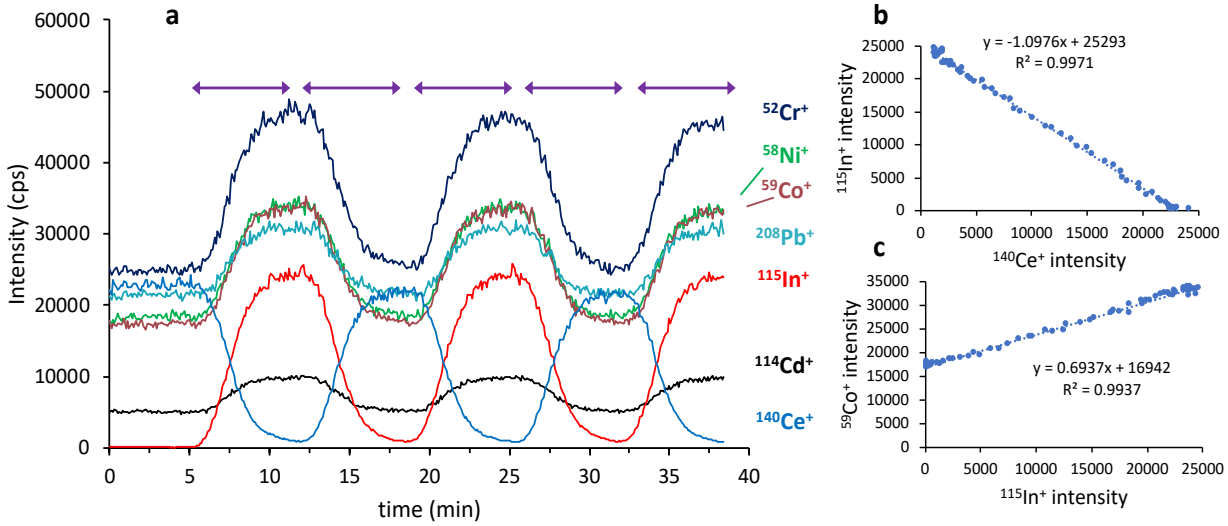

Figure 4.4 (a) Intensity traces for Ce present in the SecIS solution, followed by traces for the In internal standard and 5 analytes (Cd, Co, Pb, Cr, Ni) all of which are present in the PrmIS solution. These elemental isotope traces have been recorded while continuously introducing and mixing the two calibration solutions, one at a time, with a sample containing 0.1% w/v Ca and spiked to contain 5 µg L^{-1} of Cd, Co, Pb and 10 µg L^{-1} of Cr, Ni. A positive or negative intensity slope is observed approximately every 6.5-7 min when the SecIS is diluted by the PrmIS solution, and inversely. The purple double-arrows above the traces denote the standard dilution analysis window used in order to obtain the data needed to establish (c) the relationship for the analyte vs In (used as the primary internal standard), and (b) In vs Ce (used as the secondary internal standard).

distribution valve, the PrmIS started to be replaced by the SecIS solution. This mixing/dilution process was observed to occur between 12.5 and 18.5 min, resulting in another SDA window with negative signal slopes for the analytes and $^{115}In^{+}$, and a positive slope for $^{140}Ce^{+}$. An additional cycle of 3 consecutive exchanges between PrmIS and SecIS solutions were carried out until the end of the acquisition.

The algebraic calculations required for SDA are encapsulated in $Eq.3$, as derived and described in detail by Donati *et al.* in a recent study.[53]

$$C_A^{sam} = \frac{intercept}{slope}\frac{C_A^{std}}{S_I^{max}} \qquad (Eq.3)$$

The intercept and slope values are conveniently obtained from the plot of the analyte signal vs the In signal (used as the primary internal standard) within a SDA window (**Figure 4.4**c), and S_I^{max} is the intercept obtained from the plot of In signal vs the Ce signal (used as the secondary internal standard) within a SDA window (**Figure 4.4**b). The concentration of the analyte standard added to the PrmIS solution is represented by the term c_A^{std}. All of these values obtained from each SDA window are placed into $Eq.3$, from which the analyte concentration in the sample solution C_A^{sam} can be calculated. In **Figure 4.4**, five SDA windows are shown with the purple double arrows, and so the calculation is made five times (n=5).

The described SDA using chip-based ICP-MS yielded low limits of detection (LODs) in the sub µg L^{-1} range for Pb, Cd, Co (0.14, 0.17, 0.24 ng L^{-1}, respectively), with the exception of Cr and Ni with LODs close to 1 µg L^{-1} (1.3, 1.2 µg L^{-1}, respectively). The LODs were calculated based on 3 times the standard deviation of the blank signal.

4.3.3 Sample analysis using the SDA technique

In order to further evaluate the chip-based SDA ICP-MS approach, a variety of different samples were analyzed for their Cd, Cr, Co, Pb and Ni content. Samples were loaded from Eppendorf tubes, and thus sample exchange was conducted by changing the corresponding Eppendorf tubes. The results obtained using the SDA approach for 5 different sample matrices are shown in **Table 4.1**. All samples were spiked with the analyte mixture to contain 5 or 10 µg L^{-1} of each analyte. Concentration recoveries achieved using the chip-based SDA ICP-MS technique were close to 100% for Cd, Co, Pb and Cr with %RSDs ranging from 1.3% to 7.9%; thus demonstrating the high accuracy and precision with which metal determination can be achieved using the chip-based SDA ICP-MS system. Some

exceptions, however, were evident. For example, it should be noted that low recoveries (91.6% ± 12.0%) were determined for Ni, which originate mainly from the analysis of Ni in cell digests (72% recovery). Such a low recovery is not adequate for most analytical purposes. However, we think that it originates from a shifting elevated background, and possibly because of the need for a more suitable internal standard. It should be stressed that a stable background signal is a critical aspect of the SDA approach. For 0.1% Ca samples, percentage recoveries and %RSD were also obtained by using single point standard addition, which is an integral part of the SDA and thus no additional analysis was required. This consisted of the steady state signal for a blank, the sample and the sample plus the analyte standard. The latter serving as a single point standard addition.

Table 4.1 Percentage recovery and precision achieved from the analysis of five spiked matrices. Average values for the percentage recoveries and (%RSD) were obtained from 5 independent SDA slopes (n=5) from the analysis of each sample

Sample Type	Analytes (% Recovery ± %RSD for n=5)				
	Cd	**Co**	**Pb**	**Cr**	**Ni**
DI water	98.3±4.9	93.2±3.5	99.5± 3.5	96.4±7.9	99.4±2.1
TAP water	96.9±2.0	99.7±4.5	93.4±4.0	100.9±4.4	101.8±4.6
0.1% Ca	96.5±1.6 101.2±6.6[a]	96.3±1.3 106.5±3.1[a]	102.4±2.9 113.3±7.5[a]	97.9±3.1 100.4±5.8[a]	96.0±1.9 105.0±5.8[a]
5% MeOH	97.1±2.0	96.1±3.0	93.5±4.5	106.7±3.6	88.6±6.5
Cell digest	103.6±4.0	101.7±4.6	103.6±6.8	98.5±1.2	72.2±4.5
Average	98.5±2.9	97.4±3.3	98.5±4.8	100.1±4.1	91.6±12.0

[a]:These values give the percentage recovery and %RSD obtained from a single point standard additions calibration. The %RSD was obtained by propagating the uncertainties of the ICP-MS signals obtained from the sample and the single point standard addition measurements.

Error propagation analysis was also conducted for $Eq.3$ for a single SDA region (n=1), resulting in the following relative uncertainty expression.

$$\frac{\sigma_{C_A^{sam}}}{C_A^{sam}} = \sqrt{\left(\frac{\sigma_{intercept}}{intercept}\right)^2 + \left(\frac{\sigma_{slope}}{slope}\right)^2 + \left(\frac{\sigma_{S_I^{max}}}{S_I^{max}}\right)^2} \qquad (Eq.4)$$

A typical example is provided for the determination of Co in a 0.1 % Ca-containing sample, spiked to contain 5 μg L^{-1} of Co, using the intercept and slope provided in **Figure 4.4**b, c, as well as their associated uncertainties which were derived from linear regression analysis. Based on the above, the %RSD for the determined Co concentration, determined from one SDA window, was calculated to be 1.3%; once more indicating the excellent precision of the chip-based SDA ICP-MS.

Table 4.2 Results obtained for the determination of selected elements in DORM-2 and DOLT-4 reference materials with chip-based SDA ICP-MS, and comparisons with certified values and conventional ICP-MS. Average concentration values and (uncertainties) were obtained from regression analysis of 4 independent SDA slopes (n=4) from the analysis of each sample.

Analytes	Analyte concentration **(mg Kg^{-1} ± RSD for n=4)**					
	DORM-2			**DOLT-4**		
	certified value	**chip SDA ICP-MS**	**Conv. ICP-MS**	**certified value**	**chip SDA ICP-MS**	**Conv. ICP-MS**
Cd	0.043 ±0.008	b.d.[a]	b.d.	24.3 ±0.8	21.0 ±0.2	22.0 ±0.3
Co	0.182 ±0.031	0.173 ±0.005	0.170 ±0.003	n.p.[b]	0.193 ±0.005	0.235 ±0.002
Pb	0.065 ±0.007	0.092 ±0.004	0.031 ±0.002	0.160 ±0.040	0.097 ±0.004	0.109 ±0.009
Cr	34.7 ±5.5	30.6 ±0.4	32.1 ±1.0	n.p.	1.26 ±0.09	1.63 ±0.03
Ni	19.4 ±3.1	15.7 ±0.2	17.1 ±0.9	0.97±0.11	0.59 ±0.09	b.d.

[a]: b.d. below limit of detection; [b]: n.p. not provided.

The technique's accuracy was further evaluated through the analysis of DORM-2 and DOLT-4 certified reference materials (CRMs). As can be seen from **Table 4.2**, elemental concentrations in CRMs obtained with chip-based SDA ICP-MS were in good agreement with the certified values and the values obtained using conventional ICP-MS (external calibration with In as internal standard at 1 mL min^{-1} flow rates). Single factor analysis of variance (ANOVA) demonstrated that the differences in elemental concentrations between the certified values and those obtained with chip-based SDA and conventional ICP-MS are not statistically significant at the P=0.05 (obtained P-value of 0.98), and are thus only subject to random variation.

4.4 Conclusions

Even though microfluidic chips are important components in many types of analytical devices, their use with mass spectrometry has remained limited, especially in conjunction with atomic mass spectrometry. Herein, the coupling of a microfluidic chip with ICP-MS using commercially available components (chip, pressure-driven pump, flow sensors, connectors, nebulizer and spray chamber) is demonstrated to be conveniently achievable. The excellent stability and analytical figures of merit reported potentially open the road to highly precise and accurate measurements using microfluidics with ICP-MS. Future progress in this area will most likely include much higher throughput capabilities, advanced automation, and ultimately entire analytical workflows that require limited or no human intervention. Material compatibility, however, requires further investigation since analyte signal backgrounds must remain low and stable. SDA is a calibration approach that lends itself ideally to chip-based ICP-MS analysis.

4.5 Literature

[1] A. Manz, Y. Miyahara, J. Miura, Y. Watanabe, H. Miyagi, K. Sat, Design of an Open-tubular Column Liquid Cbromatograpb Using Silicon Chip Technology, Sensors Actuators B. Chem. (1990) 249–255.

[2] D.J. Harrison, K. Fluri, K. Seiler, Z. Fan, C.S. Effenhauser, A. Manz, Micromachining a miniaturized capillary electrophoresis-based chemical analysis system on a chip, Science (80-.). 261 (1993) 895–897. https://doi.org/10.1126/science.261.5123.895.

[3] C.S. Effenhauser, A. Manz, H.M. Widmer, Glass Chips for High-Speed Capillary Electrophoresis Separations with Submicrometer Plate Heights, Anal. Chem. 65

(1993) 2637–2642. https://doi.org/10.1021/ac00067a015.

[4] A. Manz, N. Graber, H.M. Widmer, Miniaturized total chemical analysis systems: A novel concept for chemical sensing, Sensors Actuators B. Chem. 1 (1990) 244–248. https://doi.org/10.1016/0925-4005(90)80209-I.

[5] D.R. Reyes, D. Iossifidis, P. Auroux, A. Manz, Micro Total Analysis Systems . 1 . Introduction , Theory , and Technology, 74 (2002) 2623–2636.

[6] J. El-Ali, P.K. Sorger, K.F. Jensen, Cells on chips, Nature. 442 (2006) 403–411. https://doi.org/10.1038/nature05063.

[7] S.F. Berlanda, M. Breitfeld, C.L. Dietsche, P.S. Dittrich, Recent Advances in Microfluidic Technology for Bioanalysis and Diagnostics, Anal. Chem. 93 (2021) 311–331. https://doi.org/10.1021/acs.analchem.0c04366.

[8] J.F. Edd, D. Di Carlo, K.J. Humphry, S. Köster, D. Irimia, D.A. Weitz, M. Toner, Controlled encapsulation of single-cells into monodisperse picolitre drops, Lab Chip. 8 (2008) 1262–1264. https://doi.org/10.1039/b805456h.

[9] L. Mazutis, J. Gilbert, W.L. Ung, D.A. Weitz, A.D. Griffiths, J.A. Heyman, Single-cell analysis and sorting using droplet-based microfluidics, Nat. Protoc. 8 (2013) 870–891. https://doi.org/10.1038/nprot.2013.046.

[10] L.M. Fidalgo, G. Whyte, B.T. Ruotolo, J.L.P. Benesch, F. Stengel, C. Abell, C. V. Robinson, W.T.S. Huck, Coupling microdroplet microreactors with mass spectrometry: Reading the contents of single droplets online, Angew. Chemie - Int. Ed. 48 (2009) 3665–3668. https://doi.org/10.1002/anie.200806103.

[11] D.J. Steyer, R.T. Kennedy, High-Throughput Nanoelectrospray Ionization-Mass Spectrometry Analysis of Microfluidic Droplet Samples, Anal. Chem. 91 (2019) 6645–6651. https://doi.org/10.1021/acs.analchem.9b00571.

[12] J.S. Mellors, V. Gorbounov, R.S. Ramsey, J.M. Ramsey, Fully integrated glass microfluidic device for performing high-efficiency capillary electrophoresis and electrospray ionization mass spectrometry, Anal. Chem. 80 (2008) 6881–6887. https://doi.org/10.1021/ac800428w.

[13] B. Cauli, B. Lambolez, Unravelling Single Cell Genomics, 2010. http://ebook.rsc.org/?DOI=10.1039/9781849732284.

[14] F. Zhang, Y. Fu, X.Y. Yu, Microfluidics and Interfacial Chemistry in the Atmosphere, Elsevier Inc., 2018. https://doi.org/10.1016/B978-0-12-813641-6.00009-1.

[15] D. Sticker, R. Geczy, U.O. Häfeli, J.P. Kutter, Thiol-Ene Based Polymers as Versatile Materials for Microfluidic Devices for Life Sciences Applications, ACS Appl. Mater. Interfaces. 12 (2020) 10080–10095. https://doi.org/10.1021/acsami.9b22050.

[16] N. Lu, N.J. Petersen, A.C. Kretschmann, J.P. Kutter, Non-aqueous electrophoresis integrated with electrospray ionization mass spectrometry on a thiol-ene polymer–based microchip device, Anal. Bioanal. Chem. 413 (2021) 4195–4205. https://doi.org/10.1007/s00216-021-03374-9.

[17] Elveflow, Syringe pumps and microfluidics, (2019). https://www.elveflow.com/microfluidic-reviews/microfluidic-flow-control/syringe-

pumps-and-microfluidics/.

[18] J. Gao, X.F. Yin, Z.L. Fang, Integration of single cell injection, cell lysis, separation and detection of intracellular constituents on a microfluidic chip, Lab Chip. 4 (2004) 47–52. https://doi.org/10.1039/b310552k.

[19] A. AINLA, The Multifunctional Pipette A Microfluidic Technology for the Biosciences, Chalmers University Of Technology, 2013.

[20] D. Di Carlo, Inertial microfluidics, Lab Chip. 9 (2009) 3038. https://doi.org/10.1039/b912547g.

[21] B.J. Kirby, Micro- and Nanoscale Fluid Mechanics, 2012. https://doi.org/10.1017/cbo9780511760723.

[22] J. Thiele, M. Windbergs, A.R. Abate, M. Trebbin, H.C. Shum, S. Förster, D.A. Weitz, Early development drug formulation on a chip: Fabrication of nanoparticles using a microfluidic spray dryer, Lab Chip. 11 (2011) 2362–2368. https://doi.org/10.1039/c1lc20298g.

[23] D. Carugo, E. Bottaro, J. Owen, E. Stride, C. Nastruzzi, Liposome production by microfluidics: Potential and limiting factors, Sci. Rep. 6 (2016) 1–15. https://doi.org/10.1038/srep25876.

[24] A. Wuethrich, J.P. Quirino, A decade of microchip electrophoresis for clinical diagnostics – A review of 2008–2017, Anal. Chim. Acta. 1045 (2019) 42–66. https://doi.org/10.1016/j.aca.2018.08.009.

[25] J.W. Hong, V. Studer, G. Hang, W.F. Anderson, S.R. Quake, A nanoliter-scale nucleic acid processor with parallel architecture, Nat. Biotechnol. 22 (2004) 435–439. https://doi.org/10.1038/nbt951.

[26] H. Wu, A. Wheeler, R.N. Zare, Chemical cytometry on a picoliter-scale integrated microfluidic chip, Proc. Natl. Acad. Sci. U. S. A. 101 (2004) 12809–12813. https://doi.org/10.1073/pnas.0405299101.

[27] J.S. Mellors, K. Jorabchi, L.M. Smith, J.M. Ramsey, Integrated Microfluidic Device for Automated Single Cell Analysis Using Electrophoretic Separation and Electrospray Ionization Mass Spectrometry, Anal. Chem. 82 (2010) 967–973. https://doi.org/10.1021/ac902218y.

[28] R.R. Svejdal, E.R. Dickinson, D. Sticker, J.P. Kutter, K.D. Rand, Thiol-ene Microfluidic Chip for Performing Hydrogen/Deuterium Exchange of Proteins at Subsecond Time Scales, Anal. Chem. 91 (2019) 1309–1317. https://doi.org/10.1021/acs.analchem.8b03050.

[29] G. Comamala, C.C. Krogh, V.S. Nielsen, J.P. Kutter, J. Voglmeir, K.D. Rand, Hydrogen/Deuterium Exchange Mass Spectrometry with Integrated Electrochemical Reduction and Microchip-Enabled Deglycosylation for Epitope Mapping of Heavily Glycosylated and Disulfide-Bonded Proteins, Anal. Chem. 93 (2021) 16330–16340. https://doi.org/10.1021/acs.analchem.1c01728.

[30] M. Karle, S.K. Vashist, R. Zengerle, F. von Stetten, Microfluidic solutions enabling continuous processing and monitoring of biological samples: A review, Anal. Chim.

Acta. 929 (2016) 1–22. https://doi.org/10.1016/j.aca.2016.04.055.

[31] Z. Toprakcioglu, P. Challa, C. Xu, T.P.J. Knowles, Label-Free Analysis of Protein Aggregation and Phase Behavior, ACS Nano. 13 (2019) 13940–13948. https://doi.org/10.1021/acsnano.9b05552.

[32] A. Stucki, J. Vallapurackal, T.R. Ward, P.S. Dittrich, Droplet Microfluidics and Directed Evolution of Enzymes: An Intertwined Journey, Angew. Chemie - Int. Ed. (2021) 2–22. https://doi.org/10.1002/anie.202016154.

[33] D.R. Link, E. Grasland-Mongrain, A. Duri, F. Sarrazin, Z. Cheng, G. Cristobal, M. Marquez, D.A. Weitz, Electric control of droplets in microfluidic devices, Angew. Chemie - Int. Ed. 45 (2006) 2556–2560. https://doi.org/10.1002/anie.200503540.

[34] J.C. Baret, O.J. Miller, V. Taly, M. Ryckelynck, A. El-Harrak, L. Frenz, C. Rick, M.L. Samuels, J.B. Hutchison, J.J. Agresti, D.R. Link, D.A. Weitz, A.D. Griffiths, Fluorescence-activated droplet sorting (FADS): Efficient microfluidic cell sorting based on enzymatic activity, Lab Chip. 9 (2009) 1850–1858. https://doi.org/10.1039/b902504a.

[35] E. Brouzes, M. Medkova, N. Savenelli, D. Marran, M. Twardowski, J.B. Hutchison, J.M. Rothberg, D.R. Link, N. Perrimon, M.L. Samuels, Droplet microfluidic technology for single-cell high-throughput screening, Proc. Natl. Acad. Sci. U. S. A. 106 (2009) 14195–14200. https://doi.org/10.1073/pnas.0903542106.

[36] A. Rakszewska, J. Tel, V. Chokkalingam, W.T.S. Huck, One drop at a time: Toward droplet microfluidics as a versatile tool for single-cell analysis, NPG Asia Mater. 6 (2014) 1–11. https://doi.org/10.1038/am.2014.86.

[37] Y. Zhang, K. Li, Y. Zhao, W. Shi, H. Iyer, S. Kim, C. Brenden, J. V. Sweedler, Y. Vlasov, Attomole-Level Multiplexed Detection of Neurochemicals in Picoliter Droplets by On-Chip Nanoelectrospray Ionization Coupled to Mass Spectrometry, Anal. Chem. 94 (2022) 13804–13809. https://doi.org/10.1021/acs.analchem.2c02323.

[38] Q.J. Song, G.M. Greenway, T. McCreedy, Interfacing microchip capillary electrophoresis with inductively coupled plasma mass spectrometry for chromium speciation, J. Anal. At. Spectrom. 18 (2003) 1–3. https://doi.org/10.1039/b209530k.

[39] Q.J. Song, G.M. Greenway, T. McCreedy, Interfacing a microfluidic electrophoresis chip with inductively coupled plasma mass spectrometry for rapid elemental speciation, J. Anal. At. Spectrom. 19 (2004) 883–887. https://doi.org/10.1039/b401657b.

[40] G. Pearson, G. Greenway, A highly efficient sample introduction system for interfacing microfluidic chips with ICP-MS, J. Anal. At. Spectrom. 22 (2007) 657–662. https://doi.org/10.1039/b702624b.

[41] H. Cheng, Z. Xu, J. Liu, X. Wang, X. Yin, A microfluidic system for introduction of nanolitre sample in inductively coupled plasma mass spectrometry using electrokinetic flow combined with hydrodynamic flow, J. Anal. At. Spectrom. 27 (2012) 346–353. https://doi.org/10.1039/c1ja10273g.

[42] H. Cheng, J. Liu, Z. Xu, X. Yin, A micro-fluidic sub-microliter sample introduction system for direct analysis of Chinese rice wine by inductively coupled plasma mass

spectrometry using external aqueous calibration, Spectrochim. Acta - Part B At. Spectrosc. 73 (2012) 55–61. https://doi.org/10.1016/j.sab.2012.07.010.

[43] P.E. Verboket, O. Borovinskaya, N. Meyer, D. Günther, P.S. Dittrich, A new microfluidics-based droplet dispenser for ICPMS, Anal. Chem. 86 (2014) 6012–6018. https://doi.org/10.1021/ac501149a.

[44] H. Wang, B. Chen, M. He, B. Hu, A Facile Droplet-Chip-Time-Resolved Inductively Coupled Plasma Mass Spectrometry Online System for Determination of Zinc in Single Cell, Anal. Chem. 89 (2017) 4931–4938. https://doi.org/10.1021/acs.analchem.7b00134.

[45] H. Wang, B. Chen, M. He, X. Li, P. Chen, B. Hu, Study on uptake of gold nanoparticles by single cells using droplet microfluidic chip-inductively coupled plasma mass spectrometry, Talanta. 200 (2019) 398–407. https://doi.org/10.1016/j.talanta.2019.03.075.

[46] Z. Chen, B. Chen, M. He, B. Hu, Droplet-Splitting Microchip Online Coupled with Time-Resolved ICPMS for Analysis of Released Fe and Pt in Single Cells Treated with FePt Nanoparticles, Anal. Chem. 92 (2020) 12208–12215. https://doi.org/10.1021/acs.analchem.0c01217.

[47] Y. Zhou, Z. Chen, J. Zeng, J. Zhang, D. Yu, B. Zhang, X. Yan, L. Yang, Q. Wang, Direct Infusion ICP- q MS of Lined-up Single-Cell Using an Oil-Free Passive Microfluidic System, Anal. Chem. 92 (2020) 5286–5293. https://doi.org/10.1021/acs.analchem.9b05838.s003.

[48] H. Wang, Z. Wu, B. Chen, M. He, B. Hu, Chip-based array magnetic solid phase microextraction on-line coupled with inductively coupled plasma mass spectrometry for the determination of trace heavy metals in cells, Analyst. 140 (2015) 5619–5626. https://doi.org/10.1039/c5an00736d.

[49] J. Zhang, B. Chen, H. Wang, M. He, B. Hu, Facile Chip-Based Array Monolithic Microextraction System Online Coupled with ICPMS for Fast Analysis of Trace Heavy Metals in Biological Samples, Anal. Chem. 89 (2017) 6878–6885. https://doi.org/10.1021/acs.analchem.7b01367.

[50] H. Wang, B. Chen, S. Zhu, X. Yu, M. He, B. Hu, Chip-Based Magnetic Solid-Phase Microextraction Online Coupled with MicroHPLC-ICPMS for the Determination of Mercury Species in Cells, Anal. Chem. 88 (2016) 796–802. https://doi.org/10.1021/acs.analchem.5b03130.

[51] W.B. Jones, G.L. Donati, C.P. Calloway, B.T. Jones, Standard dilution analysis, Anal. Chem. 87 (2015) 2321–2327. https://doi.org/10.1021/ac504152x.

[52] J.T. Sloop, H.J.B. Bonilla, T. Harville, B.T. Jones, G.L. Donati, Automated matrix-matching calibration using standard dilution analysis with two internal standards and a simple three-port mixing chamber, Talanta. 205 (2019) 120160. https://doi.org/10.1016/j.talanta.2019.120160.

[53] W.B. Jones, G.L. Donati, C.P. Calloway, B.T. Jones, Automated standard dilution analysis, J. Anal. At. Spectrom. 35 (2020) 178–187. https://doi.org/10.1039/c9ja00339h.

[54] A. Virgilio, D. Schiavo, L.M. Costa, J.A. Nóbrega, B.T. Jones, G.L. Donati, Inductively coupled plasma mass spectrometry and standard dilution analysis applied to concentrated acids, Talanta. 161 (2016) 826–829. https://doi.org/10.1016/j.talanta.2016.09.047.

[55] G.L. Donati, R.S. Amais, Fundamentals and new approaches to calibration in atomic spectrometry, J. Anal. At. Spectrom. 34 (2019) 2353–2369. https://doi.org/10.1039/c9ja00273a.

[56] C. Cavaniol, W. Cesar, S. Descroix, J.L. Viovy, Flowmetering for microfluidics, Lab Chip. 22 (2022) 3603–3617. https://doi.org/10.1039/d2lc00188h.

[57] J.N. Lee, C. Park, G.M. Whitesides, Solvent Compatibility of Poly (dimethylsiloxane) -Based Microfluidic Devices, Anal. Chem. 75 (2003) 6544–6554. https://doi.org/https://doi.org/10.1021/ac0346712.

5 Chapter 5. A chip-based supersonic microfluidic nebulizer for efficient sample introduction into Inductively Coupled Plasma – Mass Spectrometry Introduction

5.1 Introduction

5.1.1 Pairing a microfluidic chip with ICP-MS

Coupling a microfluidic chip with ICP-MS detection has initially been explored with the development of interfaces for capillary electrophoresis (CE) with ICP-MS, and the capabilities of the combined system were demonstrated by applications for elemental speciation. Because microfluidic chips can incorporate shorter separation channels, this allows for the application of higher voltages and therefore faster separation times can be achieved. This is extremely important as it allows for high-throughput analysis and also reduces the ICP-MS operational costs, considering that separations in conventional CE require minutes for completion. [1] The group of McCreedy were first to report on the fabrication and coupling of a CE microfluidic chip to ICP-MS using a microflow concentric nebulizer and a PEEK tubing to connect the inlet of the nebulizer with the outlet of the chip. In order to prevent any suction exerted on the separation microchannel, a makeup solution was provided to the nebulizer through a makeup reservoir in order to match its natural aspiration rate (self-aspiration).[1,2] In a later study by Cheng et al, it was demonstrated that the use of porous monolithic plugs prevented suction in a microchip electrophoresis system, resulting in considerably faster separation times and improved peak resolution between iodide and iodate, as well as higher sensitivity.[3] As the potential for nanoliter to microliter (nL-μL) volume introduction to the ICP had been revealed, the group of Greenway developed a microchip assembly incorporating a micro-cross-flow nebulizer for efficient sample introduction to the ICP at 5μL min^{-1} flow rates.[4] The group of Yin also reported on the fabrication of chips for the introduction of nL-volume samples to the ICP, using a PTFE tube connected to a microflow nebulizer.[5,6] Microfluidic chips coupled to ICP-MS have also been used for the determination of trace metal amounts in materials using chip-based microextraction methodologies on-line with ICP-MS, as well as for the separation of 14 lanthanides into distinct elemental bands followed by subsequent on-line ICP-MS detection.[7–9] Recently, attempts have been focused on interfacing microfluidic chips with ICP-MS for the analysis of cells, intact or in a lysed state.[10–18] Several studies on single cell analysis by means of ICP-MS detection involve the encapsulation of cells into aqueous

droplets within an oil flow on a microfluidic chip. In order to prevent carbon deposition on the ICP-MS cones, approaches such as droplet drying through a membrane desolvator or the addition of O_2 in the ICP have been applied.[10–13] However, individual cell detection has also been demonstrated by coupling an oil-free microfluidic chip to ICP-MS.[14] By combining low sample consumption with multiple fluid channel arrays and ICP-MS detection sensitivity, microfluidic chips, as microextraction devices, have been coupled to ICP-MS for the speciation of mercury and quantitation of trace heavy-metals in lysed cell populations.[15–18]

Based on the majority of the reported applications, the connection between a microfluidic chip and an ICP-MS has so far been achieved by using conventional nebulizers which offer little possibility to become an integrated part of a chip-based microfluidic system. These rather dimensionally large nebulizers frequently cause dead volume issues, and therefore unwanted mixing of the analyte migration zones eluting from chip-based chromatographic or CE-based separations. Moreover, for the reported nebulizers used for microchip CE-ICP-MS, an additional makeup flow is needed to match the self-aspiration rate of the microflow nebulizer; thus, contributing to overall inferior ICP-MS detection sensitivity. Self-aspiration of the micro-flow nebulizer could also pose a problem for microfluidic chip applications especially during fluid mixing and manipulations.

5.1.2 Objective

As microfluidic applications expand, there is an increasing need to introduce new efficient ways to interface microfluidic chips to ICP-MS. This study proposes that a microfluidic chip bearing a nozzle for liquid nebulization can be conveniently coupled to ICP-MS; a platform which seems to have the potential to be operated at low flow rates in applications, such as microchip CE ICP-MS, single cell analysis and single particle analysis which are typically conducted at µL and sub µL min^{-1} liquid flow rates. Hence, the objective of this study was to pair a chip-based microfluidic nebulizer (chip-µf-Neb) with ICP-MS detection. This type of nebulizer has been demonstrated to perform liquid nebulization at supersonic gas speeds, and, because of the extremely small size (~5µm) of liquid droplets that it generates it has employed in several applications demanding quick evaporation, such as nanoparticle drug formation by means of spray drying. However, it has never before been employed in ICP-MS analyses. Therefore, in this study, a number of performance characteristics of the chip-µf-Neb were evaluated, including transport efficiency, as well as the ability to introduce and

detect single cells and single nanoparticles using the ICP-MS. These characteristics were studied as a function of gas and liquid flow rates, thus mapping out the range of their values for optimum ICP-MS operation. Emphasis is given on accomplishing sensitive and efficient dissolved and nanoparticle analyte detection for a chip-μF-Neb operation at the low range of μL min^{-1} liquid flow rates (i.e., 0.5-10 μL min^{-1}). In addition, the chip-μf-Neb was tested for its ability to self-aspirate solutions, a characteristic which would be unwanted if this nebulizer were paired with other microfluidic sample manipulation techniques.

5.2 Materials and Methods

5.2.1 Chemicals and solutions

The standard solution, used for the optimization study, was prepared to contain 1 μg L^{-1} of both indium (In) and cerium (Ce) in 1% trace-metal grade nitric acid. In order to examine the transport efficiency of the chip-based microfluidic nebulizer to the ICP-MS, a 60 nm silver nanoparticle (AgNP) (NanoComposix) suspension was prepared in de-ionized (DI) water at the concentration of 200 ng Ag L^{-1}. For the analysis of single-cells, *Chlamydomonas reinhardtii* CC-1690 cells were cultivated in the presence of 20 μM sodium selenate, Na_2SeO_4 (Fluka), or 300 μM of sodium arsenate, Na_3AsO_4, as well as in their absence (controls). Cell culture aliquots were taken every 12 hours in order to monitor cell growth for selenate-incubated, arsenate-incubated and control cells, and cells were harvested at the end of the logarithmic phase of their growth. Prior to the analysis, cell culture aliquots were examined and counted under an optical microscope (Axiolab 5, Zeiss) using a Fuchs-type hemocytometer. Subsequently, cells were transferred by centrifugation from their nutrient solution to an EDTA-solution (50 mM Trizma, 1 mM EDTA, pH 7) and finally, after a second centrifugation step they were resuspended in an EDTA-solution at the working concentration of 10^5 cells mL^{-1}. An exception was made for arsenate-incubated cells which after the second centrifugation step, were resuspended in DI water in order to avoid possible argon chloride ($^{75}ArCl^+$) interference resulting from chloride contaminated buffer reagents. DI water of 18 MΩ cm resistivity was supplied by a water purification system (PURELAB Option-S, Elga Labwater, UK). All solutions supplied to the chip-based microfluidic nebulizer were filtered with 0.4 μm Whatman syringe filters (GE Healthcare). In the case of AgNP and cell suspensions, 50 μL unfiltered aliquots were added from the stock suspensions to the filtered

DI or EDTA-solution, respectively, to make the final suspensions for analysis. Solution preparation and filtering were carried out in a laminar flow hood (Bio-II-A, TELSTAR).

5.2.2 Microfluidic device fabrication

In order to make the master used for casting polydimethylsiloxane (PDMS) devices, a two-step photolithographic process was used.[19,20] In brief, a 25 μm thick negative photoresist (SU-8 3025, MicroChem) was first spin-coated onto a silicon wafer. Following exposure, a second 50-μm-thick layer (SU-8 3050, MicroChem) was then spin-coated onto the wafer and exposed under UV light. Finally, in order to remove any uncross-linked photoresist, the master was developed in propylene glycol methyl ether acetate (Sigma-Aldrich).

In order to fabricate the microfluidic devices, a 10:1 ratio of elastomer PDMS to curing agent (SYLGARD 184, Dow Corning, Midland, MI) was used. This mixture was cured for 3 hours at 65°C, and the hardened PDMS was cut and peeled off the master, while holes of 0.75 mm were punched on the PDMS. Two PDMS slabs were bonded together using a plasma bonder (Diener Electronic, Ebhausen, Germany) in order to make the 3-D microfluidic nozzle. Finally, the PDMS slabs were bonded onto a glass slide by treating with the same type of plasma bonder.

5.2.3 The chip-based microfluidic nebulizer and its coupling to ICP-MS

The chip-based microfluidic nebulizer (chip-μf-Neb) used in this study was designed to operate as a microfluidic spray device, therefore it integrates a liquid and gas channel with cross-sections ($depth \times width$) of 25×20 and 100×100 μm^2, respectively, as well as a nozzle for aerosol generation, all within a single chip. The chip has a 3D geometry, and thus the channels and nozzle are made within a PDMS block. The 3D nozzle plays an important role in the aerosol generation mechanism, as it enables the gas to entirely surround the liquid which is delivered to the nozzle. In this way, the liquid exits the nozzle in the form of a jet while PDMS surface wetting is avoided. The chip-μf-Neb was adhered horizontally onto a glass slide (1.35×3.95 cm), as can been seen in **Figure 5.1**. The in-house fabricated chip-μf-Neb has been modelled as a de Laval nozzle, that is a converging-diverging type of nozzle, which, at chocked flow conditions, can accelerate a gas to supersonic speeds, i.e., achieving a Mach number >1.[21] Chocked flow conditions occur when the mass flow rate of a gas flowing through a nozzle cannot further increase and stays constant, despite any

additional pressure drop across the flow path. Additional details on the chip-μf-Neb fabrication and operation can be found in Kartanas et al.[19,20]

Argon (Ar) gas was supplied to the gas inlet of the chip-μf-Neb, and served as the nebulization gas. A combination of quick-fit, luer lock connectors, ferrules and nuts were used to connect the Ar nebulization gas line coming from the ICP-MS with an in-line 0.4 μm syringe filter (Whatman). Attached to the other side of the syringe filter was a PTFE tubing line (i.d. 0.76 mm) the other end of which was placed directly into the gas inlet port of the chip-μf-Neb with the help of a steel adaptor tube, as shown in **Figure 5.1**. All liquid solutions and suspensions used in this study were supplied to the liquid inlet of the chip-μf-Neb using a syringe pump (Cole-Parmer). Connection between the liquid supply syringe and the chip-μf-Neb inlet was achieved using PTFE connectors and tubing (i.d. 0.3 mm). A graphical representation of the chip-μf-Neb and its gas and liquid channels connected to the supply lines is provided in **Figure SI1. 7**.

In order to interface the chip-μf-Neb with the ICP-MS, the chip-μf-Neb was inserted into an Asperon^{TM} spray chamber (Perkin Elmer), designed to allow for the addition of a laminar flow makeup gas, thus enabling single cell analysis by transporting intact cells to the ICP-MS. The chip-μf-Neb block with a width and height of 1.35 and 0.95 cm, respectively, was conveniently mounted into the Asperon^{TM} (opening of i.d. 1.62 cm) and inserted to a depth of 1.3 cm within the spray chamber, as shown in **Figure 5.1** (the red bar indicating the insertion depth). Positions at a lower insertion depth were also explored for the chip-μf-Neb, however, maximum detection sensitivity was obtained when the chip-μf-Neb was introduced within 1-1.3 cm from the opening of the spray chamber. Insertion of the chip-μf-Neb to a depth of 1.3 cm within the Asperon spray chamber caused bending to the soft PTFE tubing through which the liquid flows were supplied to the chip-μf-Neb. Therefore, in order to ensure a firm and leak-free connection between the tubing and the liquid inlet of the chip-μf-Neb, the PTFE tubing was glued to the PDMS using white silicone glue before placement of the chip-μf-Neb to the selected position within the spray chamber. In order to seal the openings between the chip-μf-Neb and the spray chamber inlet opening, Blu-tack adhesive was used to fill in these spaces (no degradation of this material was observed throughout these experiments as it did not come into contact with the sprayed solutions). This allowed for the undisrupted operation of the ICP. A diagram of the complete chip-μf-Neb - ICP-MS setup is shown in **Figure 5.1**.

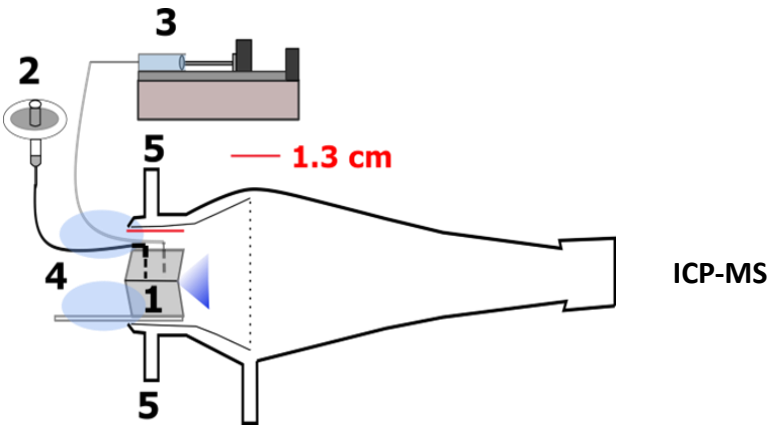

Figure 5.1 Cross-sectional view of the chip-µf-Neb–spray chamber setup. The chip-µf-Neb (1) is mounted into the AsperonTM spray chamber and inserted to a depth of 1.3 cm. The nebulization gas (2), after passing through a syringe filter, is transferred through a PTFE tube (i.d. 0.76 mm, in gray colour) to a steel adaptor (in black colour) which connects to the chip-µf-Neb gas inlet. A syringe pump (3) is used to deliver the liquid solutions through a PTFE tube (i.d. 0.3 mm, in gray colour) which is directly inserted into the liquid inlet of the chip-µf-Neb. The system is kept air-tight by filling the openings between the chip-µf-Neb and spray chamber with a removable Blu-tack adhesive (4). A makeup Ar flow (5) contributes to the transport of the produced aerosol towards the ICP-MS. All the components shown are not drawn to scale.

5.2.4 Operating Parameters

To obtain the optimum conditions for the efficient operation of the chip-µf-Neb and thus the sensitive detection of elemental isotopes, a wide range of nebulizer gas (0.28-0.42 L min^{-1}), makeup gas (0.1-0.6 L min^{-1}) and liquid flow rates (0.5-20 µL min^{-1}) were investigated. The optimum value of the nebulization and makeup gas was selected in order to perform the transport efficiency study and the single-cell analysis. To examine the transport efficiency of the chip-µf-Neb over a range of liquid flow rates (0.5-20 µL min^{-1}), a 200 ng Ag L^{-1} suspension of 60 nm AgNP was analyzed for 4 min at several different liquid flow rates. Each 4 min acquisition was split into 4 x 1 min replicates, and thus the determined NP transport efficiency and average NP intensity are reported as average values of the 4 replicates. For *Chlamydomonas reinhardtii* single-cell analysis, a 3 min acquisition was carried out for each of the control cells, those incubated in 20 µM selenate and those in 300 µM of arsenate.

The ICP-MS used in this study was a NexION 350 X (Perkin Elmer). All instrumental parameters set for the operation of the chip-µf-Neb - ICP-MS are provided in **Table SI1. 3**. A dwell time of 100 ms was used for the optimization study when introducing dissolved

metal-containing solutions, while a dwell time of 10 ms was used for the analysis of AgNPs and *Chlamydomonas reinhardtii* cell suspensions. The detection of ^{80}Se in single cells was possible by introducing O_2 in the collision cell. Besides the chip-µf-Neb, a HEN (Meinhard®) nebulizer was used for quantitation of the Se and As content per cell.

5.2.5 Cell integrity after nebulization through the chip-µf-Neb

Demonstrating the capability of the chip-µf-Neb to introduce single cells into the ICP was amongst the main objectives of this study. However, the analysis of individual cells requires that they maintain their integrity throughout their flight to the plasma. For this reason, a suspension containing *Chlamydomonas reinhardtii* cells at a concentration of 10^5 cells mL^{-1} was introduced to the chip-µf-Neb at 20 µL min^{-1}, and the chip-µf-Neb was allowed to spray for 1 min onto a microscopy slide. The sprayed cells from the resulting aerosol droplets were examined visually under an optical microscope (Axiolab 5, Zeiss) to examine cell integrity.

5.3 Results and Discussion

5.3.1 Optimization of the nebulizer and makeup gas flow rates

The performance of the chip-µf-Neb - ICP-MS system was tested and optimized with respect to the obtained indium (In) sensitivity and cerium oxide levels, expressed as the percentage of cerium oxide to cerium (CeO%). A standard solution containing In and Ce at 1 µg L^{-1} each was delivered using a syringe pump, and optimization of the nebulizer and makeup gas flow rates was carried out for 1.67, 5.00 and 10.00 µL min^{-1} liquid flow rates. The nebulizer gas flow rates of 0.28 and 0.42 L min^{-1} corresponded to backpressures of 2.13 and 2.91 bar, respectively. For both nebulizer gas flow rates, the argon gas is accelerated to supersonic speeds, achieving a Ma number of 1.03 and 1.26 for 0.28 and 0.42 L min^{-1}, respectively, hence supersonic nebulization took place. The Ma number, i.e. the ratio of the local gas velocity over the speed of sound, was calculated using isentropic relations, linking the critical pressure ratio to the Ma number for chocked flow conditions.[21] Higher nebulizer gas flow rates were not studied as mild nebulization conditions are typically preferred for single-cell analysis. For each liquid flow rate and selected nebulizer gas flow rate, the spray chamber makeup gas varied between 0.2 and 0.6 L min^{-1}. Higher values were not examined as they resulted in elevated CeO%, greater than 2.5% which is typically the desired upper level for most ICP-MS analyses. The makeup gas is a complementary laminar flow of Ar which is added into the spray chamber in order to facilitate the transport of the aerosol,

produced by the chip-μf-Neb, to the ICP. This can be achieved mainly by guiding the aerosol droplets towards the ICP and simultaneously not allowing them to impact onto the spray chamber wall; thus, compensating for limitations associated with the position or slight misalignment of the chip-μf-Neb in the spray chamber. In addition, it satisfies the requirement for additional Ar flow to transport the formed atomic ions through the plasma, especially because of the low nebulization gas volumetric flow rates used with the chip-μf-Neb. For this reason, the makeup gas flow was expected to be critical in achieving maximum

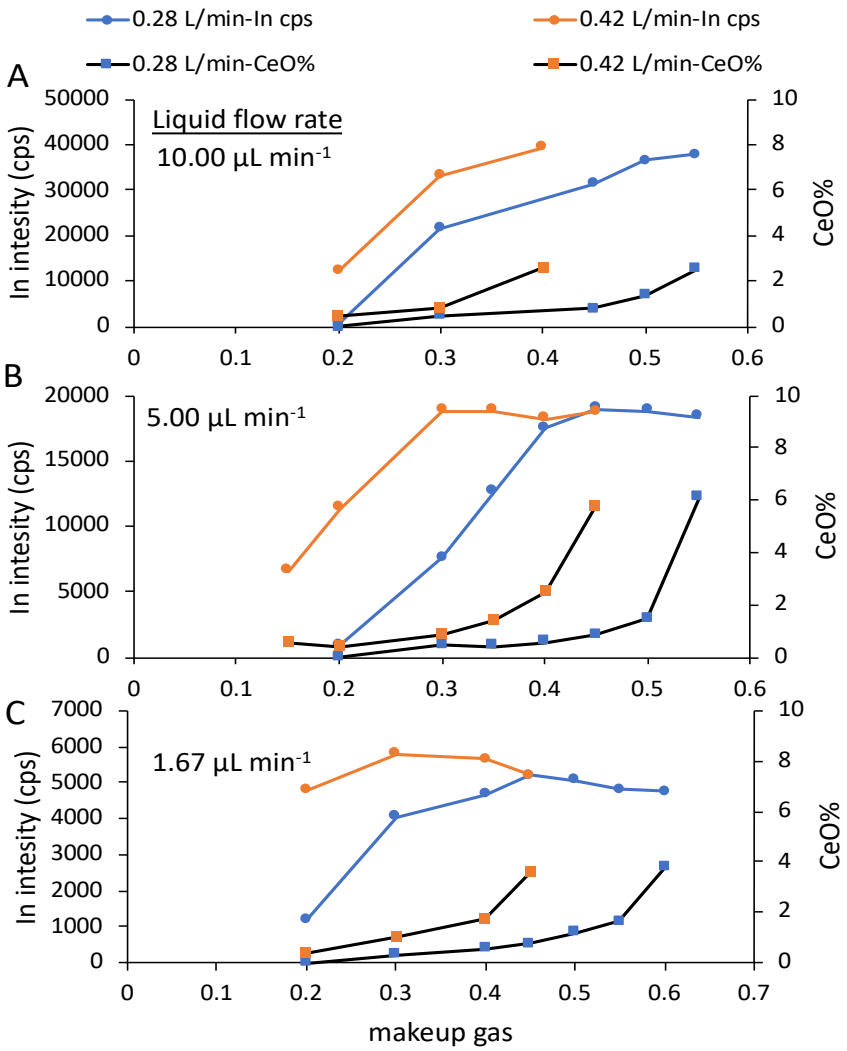

Figure 5.2. (A-C) Graphs demonstrating how the makeup gas, at nebulization gas flow rates of 0.28 (blue line) and 0.42 L min^{-1}(orange line), affects the obtained In signal (primary axis) when a solution containing In and Ce at 1 μg L^{-1} is introduced to the chip-μf-Neb - ICP-MS at 1.66 (A), 5.00 (B) and 10.00 (C) μL min^{-1} liquid flow rates. Graphs (A-C) also show the effect of the makeup gas on the obtained oxide levels, expressed as the percentage of cerium oxide to cerium (CeO%) (secondary axis), at nebulization gas flow rates of 0.28 (blue square markers) and 0.42 L min^{-1} (orange square markers).

aerosol transport efficiency and thus maximum ICP-MS sensitivity. The results for the nebulizer and makeup gas optimization are presented in **Figure 5.2**

As expected, the addition of the makeup gas is critical for the efficient transport of the produced aerosol to and through the ICP, as demonstrated in **Figure 5.2**A-C, by the marked increase in the obtained In sensitivity for all nebulizer gas flow rates and liquid flow rates tested. With respect to achieving maximum In sensitivity, the chip-μf-Neb was demonstrated to perform equally well at the lower 0.28 L min^{-1} nebulization gas flow compared to the higher 0.42 L min^{-1} by simply using slightly higher flow values of makeup gas. More specifically, significantly higher In sensitivity was obtained at 0.42 L min^{-1} nebulization gas as opposed to 0.28 L min^{-1} across a makeup gas range of 0.2-0.4 L min^{-1} for almost all liquid flow rates, except for the liquid flow rate of 5 μL min^{-1} at which the equivalent makeup gas range was 0.2-0.35 L min^{-1}. Setting 0.42 L min^{-1} of nebulization gas and exceeding 0.4 L min^{-1} of makeup gas might seem to provide even higher In sensitivity at the liquid flow rate of 10 μL min^{-1}, however, this would result in elevated CeO levels above 2.5%. Conversely at the lower 0.28 L min^{-1} nebulization gas, higher values of makeup gas (0.55 L min^{-1}) can be tolerated, and are demonstrated to yield similar In sensitivity at the liquid flow rates of 5 and 10 μL min^{-1} as opposed to using 0.42 L min^{-1} and 0.4 L min^{-1} of nebulization and makeup gas, respectively. It is noted that for the above nebulization and makeup gas combinations the total Ar flow (nebulizer plus makeup) rates delivered to the plasma are equal, at 0.82-0.83 L min^{-1}.

Because of the slightly higher gain in In sensitivity at liquid flow rates of 1.67 and 10 μL min^{-1}, the combination of 0.42 L min^{-1} and 0.4 L min^{-1} of nebulization and makeup gas, respectively, was considered optimum. The increased In sensitivity is an indication that at this higher nebulization flow rate the physical processes associated with droplet desolvation and analyte atomization and ionization within the plasma are most efficient. Kartanas et al demonstrated a progressive decrease in the average droplet diameter when the chip-μf-Neb was operated at the liquid flow rate of 200 μL h^{-1} (corresponding to 3.33 μL min^{-1}) across a backpressure range of 1.5-3 bar; with a backpressure of 3 bar yielding the lowest achievable aerosol droplet average diameter of 5.3 μm.[19] This finding may explain the gain in In sensitivity when the chip-μf-Neb - ICP-MS is operated at 0.42 L min^{-1} corresponding to a backpressure of approximately 2.9 bar.

Operating the chip-μf-Neb at a combination of 0.42 and 0.4 L min^{-1} of nebulization and makeup gas flow rate, approximately 5500, 19000 and 40000 cps $(\mu g\ L^{-1})^{-1}$ are obtained at

the liquid flow rates of 1.67, 5.00 and 10.00 μL min^{-1}, respectively. For the ICP-MS instrument used in this study (NexION 350 X, installed in our lab-Environmental Chemical Processes Laboratory, Department of Chemistry, University of Crete- in 2013), the achieved sensitivity at 10 μL min^{-1} (40000 cps (μg L^{-1})$^{-1}$) is by far superior to the one obtained by using a conventional pneumatic nebulizer at the liquid flow rate of 1 mL min^{-1} (70000 cps (μg L^{-1})$^{-1}$). If these concentration-based sensitivities (cps (μg L^{-1})$^{-1}$) are transformed to mass-based sensitivities (counts μg^{-1}), this results in 2.4×10^{11} versus 4.2×9 counts μg^{-1} for the chip-μf-Neb versus the conventional factory-based introduction system, respectively. Moreover, the chip-μF-Neb demonstrates superior sensitivity compared to other nebulizing devices operating at the μL min^{-1} flow rates. In a highly-efficient microfluidic interface reported by Pearson et al[4], the authors report 13500 cps for a 10 μg L^{-1} In solution pumped at 5 μL min^{-1}, which indicates that the chip-μf-Neb features a 14-fold advantage in In sensitivity obtained at the same liquid flow rate. Recently, a custom capillary vibrating sharp-edge spray ionization (cVSSI) device was introduced by Taylor et al for microflow sample introduction into a recently released ICP-TOF-MS (icpTOF-S2)[22]. Liquid nebulization, actuated by a piezoelectric transducer, was demonstrated across a flow rate range of 5-50 μL min^{-1}, while a maximum In mass sensitivity of 8×10^{10} counts μg^{-1} (calculated from the reported maximum concentration-based In sensitivity of 20000 cps (μg L^{-1})$^{-1}$ for a liquid flow rate of 15 μL min^{-1}). Hence, a 3-fold sensitivity advantage is marked by the chip-μF-Neb.

Another important part of this study was whether the chip-μf-Neb causes suction on the liquid sample, and thus self-aspiration, a typical characteristic of conventional pneumatic glass nebulizers.[21] In many cases, especially if microfluidics are to be used with an ICP-MS, self-aspiration would be unwanted since the exerted suction on the liquid channels could disrupt processes such as fluid mixing or result in degraded analyte separation in the case of CE ICP-MS. **Figure 5.3** illustrates the introduction of a standard solution, containing 1 μg L^{-1} of In, to the chip-μf-Neb - ICP-MS system at 1 μL min^{-1} between 0-90 s. At approximately 90 s the syringe pump is stopped and the liquid supply line is disconnected from the syringe pump; however, all gas flows remain. Moreover, the chip-μf-Neb liquid supply line is put into a vial containing the standard solution. Immediately, the In signal drops to its background level. This indicates that no self-aspiration is taking place, thus showing that the chip-μf-Neb can only operate when a liquid flow is pumped to it. At approximately

110 s the liquid supply line is reconnected, and the syringe pump is restarted to operate at a liquid flow rate of 1.67 µL min^{-1}.

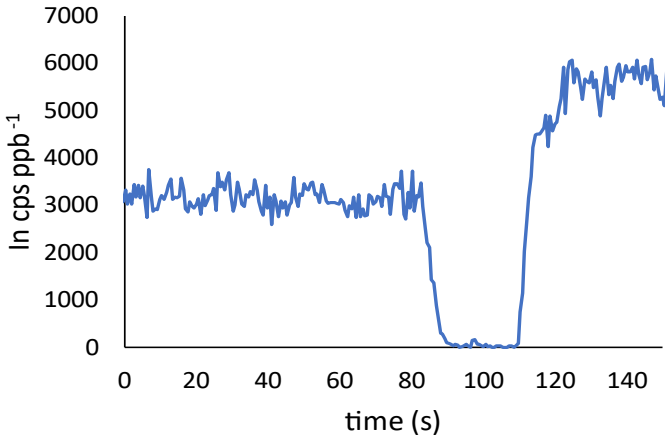

Figure 5.3 Figure showing how the obtained In signal is affected when no liquid flows are pumped to the chip-µf-Neb - ICP-MS. A standard solution, containing 1 µg L^{-1} In, is pumped to the system at 1.00 µL min^{-1} between 0-90 s. Subsequently, the syringe pump is stopped between 90-110 s, and the liquid supply line is disconnected from the syringe and put into a vial containing the same standard solution. Following this, the liquid supply line is reconnected, the syringe pump is restarted delivering the In standard solution at 1.67 µL min^{-1} until the end of the acquisition.

5.3.2 Analysis of AgNPs

Single particle ICP-MS analysis was conducted by operating the chip-µf-Neb - ICP-MS at the optimum 0.42 and 0.4 L min^{-1} values for the nebulization and makeup gas flow rate, respectively. A nanoparticle suspension containing 60 nm AgNPs at 200 ng Ag L^{-1} was introduced to the chip-µf-Neb - ICP-MS, and the system was tested at the low µL min^{-1} liquid flow rates ranging from 0.5 to 20.0 µL min^{-1}. Typical 1 min time-resolved acquisitions of AgNPs introduced at liquid flow rates of 0.5 and 5.0 µL min^{-1} are provided in **Figure 5.4**A & B, respectively. A 15% increase in the determined average NP intensity was observed when the chip-µf-Neb - ICP-MS was operated at 5 µL min^{-1} (**Figure 5.4**B) as opposed to 0.5 µL min^{-1} (**Figure 5.4**A), indicating a slightly more sensitive single nanoparticle detection at the higher liquid flow rate.

The transport efficiency of AgNPs was determined as a measure of the aerosol transport efficiency from the chip-µf-Neb to the ICP. Figure 4.4C shows the calculated % transport

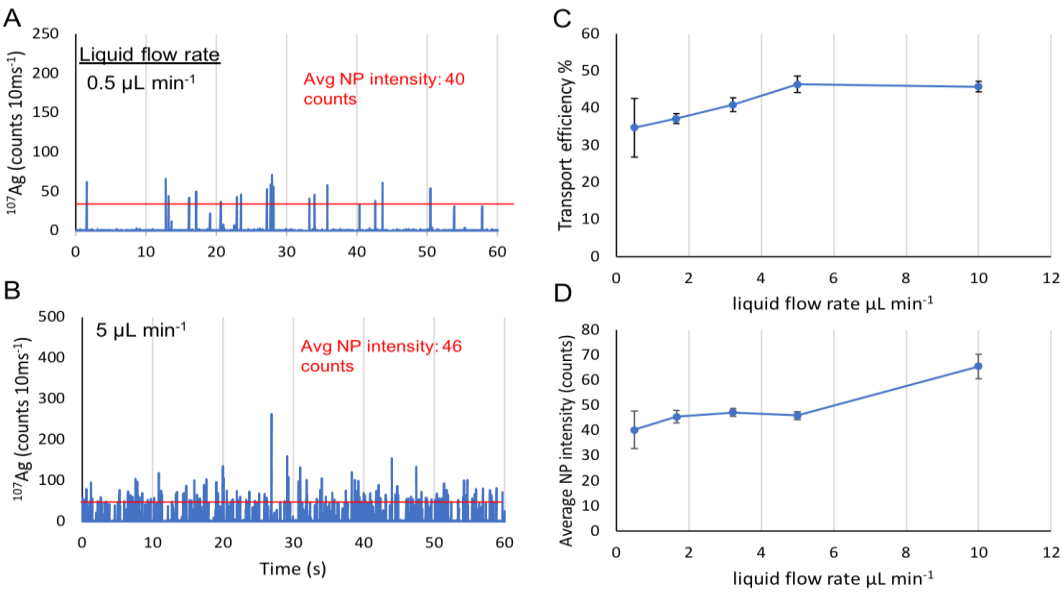

Figure 5.4 Time-resolved acquisitions (60 s) resulting from the introduction of 200 ng L^{-1} of 60 nm AgNPs to the chip-µf-Neb at liquid flow rates of 0.5 and 5.0 µL min^{-1} shown in panel A and B, respectively. The graphs in panel C and D demonstrate the obtained transport efficiency (%) and average NP intensity as a function of the liquid flow rate supplied to the chip-µf-Neb. Error bars correspond to average values resulting from 4×1 min ICP-MS acquisitions in single particle mode with a dwell time of 10 ms.

efficiency as a function of liquid flow rate ranging from 0.5 to 10.0 µL min^{-1}. Transport efficiency increased linearly from 0.5 to 5.0 µL min^{-1}, and plateaued up to 10 µL min^{-1} achieving a maximum of approximately $46 \pm 2\%$, which is significantly greater than that of a recently introduced piezoelectric nebulizer featuring a maximum transport efficiency of ~15% at 10 µL min^{-1}.[22] Compared to this study by Tailor et al, the chip-µF-Neb features highly efficient aerosol transport even at the low 0.5 µL min^{-1}.

The average NP intensity, illustrated in **Figure 5.4**D, exhibited only a slight increase as a function of liquid flow rate for values ranging from 0.5 to 5 µL min^{-1}. A greater increase of 40% was recorded at the liquid flow rate of 10 µL min^{-1}, with a maximum value of 65 ± 5 counts. To examine whether this increase can be attributed to multiple nanoparticle detection per dwell time, probability calculations using Poisson statistics were applied. For a concentration of 200 ng Ag L^{-1}, 168664 AgNPs of 60 nm are contained within 1 mL of suspension. When this suspension is pumped to the chip-µf-Neb at a liquid flow rate of 10 µL min^{-1}, theoretically 0.28 NPs are introduced per 10 ms of detection, resulting in a low 3.26% probability for multiple NP detection. In addition, **Figure SI1. 8** (panel C) demonstrates a linear increase for the number of NPs detected min^{-1} as a function of liquid

flow rate across the range of 0.5-10 μL min^{-1}, providing complimentary evidence that multiple NP detection could not have contributed to the observed increase in the average NP intensity recorded at 10 μL min^{-1}. Therefore, the chip-μf-Neb provides the most efficient and simultaneously the most sensitive AgNP detection at the liquid flow rate of 10 μL min^{-1}.

The transport efficiency dropped to 40% at the liquid flow rate of 20 μL min^{-1}, as illustrated in **Figure SI1. 8** (panel A). This is possibly attributed to multiple NP detection, as is suggested by the increase in NP intensity (panel B) and the reduced number of NPs detected min^{-1} compared to its expected value at the liquid flow rate of 20 μL min^{-1} (panel D). The expected value has been extracted upon extrapolation of the linear relationship between the number of NPs detected min^{-1} and liquid flow rate across the range of 0.5 to 10.0 μL min^{-1}, as shown in **Figure SI1. 8** (panel C). In terms of this, a more dilute AgNP suspension would provide a more accurate value for the transport efficiency at this liquid flow rate, however, at the current conditions even this small decrease in the transport efficiency would suggest that the chip-μf-Neb could be operated at this higher liquid flow rate with little to no compromise in performance.

The chip-μf-Neb was evaluated in terms of ^{107}Ag linear response across the range of 0.1-1 μg L^{-1}, by introducing dissolved standard solutions of Ag. **Figure SI1. 9** shows the calibration curve ($y=40.59+0.1814$, $R^2=0.9997$) which was established by introducing 0, 0.1, 0.5, 1 μg L^{-1} of Ag standard solutions, while Fig. SI3B shows the equivalent calibration curve ($y=52.94+0.1814$, $R^2=0.9997$) in which the response per dwell time (counts 10 ms^{-1}) is plotted versus the absolute mass of Ag introduced per dwell time (fg 10 ms^{-1}). The latter has been transformed from the units of concentration (μg L^{-1}) by taking into account the dwell time (10 ms), the liquid flow rate (10 μL min^{-1}) and the transport efficiency (46%). A satisfactory linearity can be observed from **Figure SI1. 9**. The size limit of detection for a AgNP was found to be 24.3 nm, as determined by considering 3 times × the standard deviation of the background (3σ). Using the slope of the mass flux calibration, the average NP size was determined for a 60 nm Ag NP suspension, at a concentration of 200 ng Ag L^{-1} introduced through the chip-μf-Neb at the liquid flow rate of 10 μL min^{-1}, to be 57.8 ±0.8 nm; indicating only a 3.8% deviation from the referenced value.

5.3.3 Analysis of single-cells for their Se & As content

Amongst the objectives of this study was to explore the capabilities of chip-μf-Neb to be used for the analysis of single cells. This posed a challenge as the width of the microfluidic

channels had a small cross-section of 20×25 μm^2, therefore introducing 5-7 μm sized cells could have resulted in channel blockage in case of cell aggregation. In order to conduct single-cell analysis, *Chlamydomonas reinhardtii* cell suspensions were introduced through the chip-μf-Neb. Amongst the suspensions were those containing control cells (**Figure 5.5** & **Figure 5.6**A), cells incubated in 20 μM of selenate (**Figure 5.5**B) and cells incubated in 300 μM of arsenate (**Figure 5.6**B). The cell suspensions were prepared to contain 10^5 cells mL^{-1} in order to reduce the possibility of multiple cell detection, and were introduced at either 10 or 20 μL min^{-1} liquid flow rate. Figure 4.5A and 4.B demonstrate 3 min time-resolved acquisitions resulting from the introduction of control and selenate incubated cells, respectively, while **Figure 5.6**A and B demonstrate equivalent time-resolved acquisitions for control and arsenate incubated cells.

In single-cell ICP-MS, the detection of individual cells is revealed by the presence of distinct signal pulses in the recorded signal. Therefore, the presence of distinct pulses in

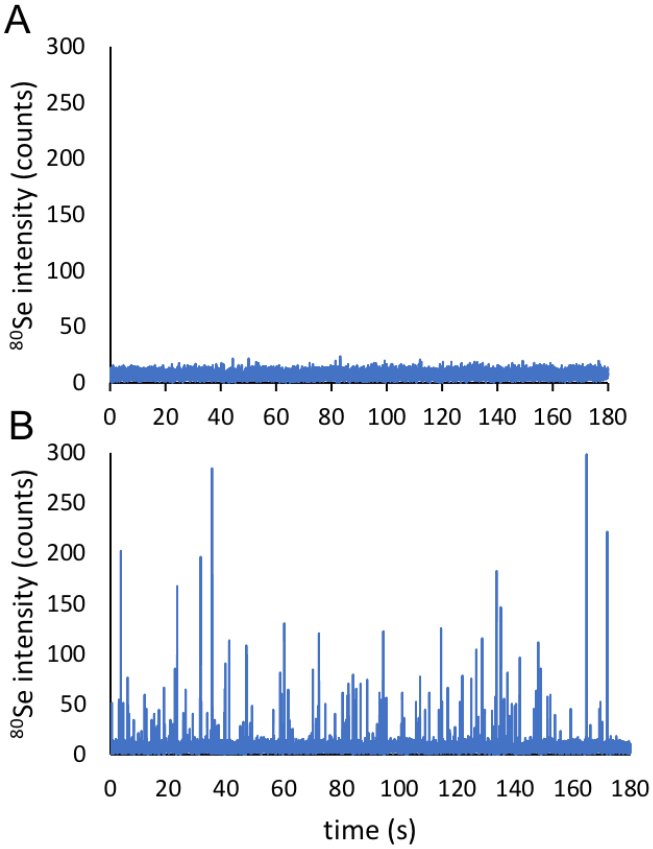

Figure 5.5 Single cell ICP-MS acquisitions resulting from the introduction of control (panel A) and 20 μM selenate incubated (panel B) *Chlamydomonas reinhardtii* cells, at a concentration of 10^5 mL^{-1}, through the chip-μf-Neb at 20 μL min^{-1}. The analysis was conducted with a 10 ms dwell time, while O_2 was introduced to the collision cell in order to reduce the background Ar_2^+ signal.

Figure 5.5B and **Figure 5.6**B indicates the detection of cells which have uptaken detectable amounts of selenate and arsenate, respectively. The detection of Se in the isotope ^{80}Se was realised by operating the instrument in the Dynamic Reaction Cell mode, which involves introducing oxygen in the collision cell. In this case, oxygen is not used to form selenium oxide ($^{96}SeO^{+}$) but rather as a knockout gas to reduce the background at the m/z 80 resulting from the Ar_2^{+} isobaric interference. The transport efficiency of the chip-μf-Neb was determined for cells incubated in selenate and arsenate with respect to ^{80}Se and ^{75}As detection, and it was found to be $7.78 \pm 0.39\%$ and $15.0 \pm 2.2\%$ for selenate and arsenate incubated cells, respectively; the uncertainty resulting from the standard deviation of 3

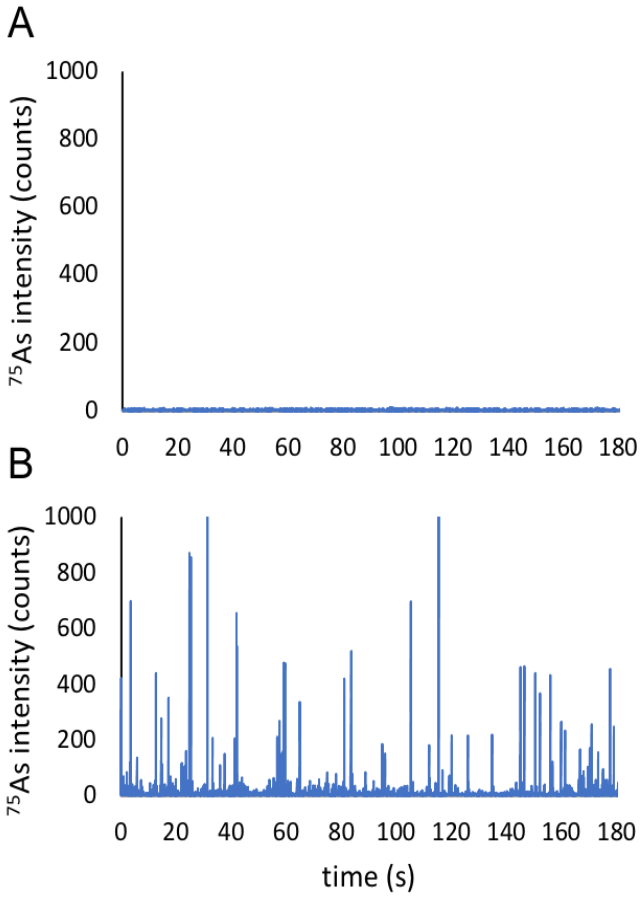

Figure 5.6 Single cell ICP-MS acquisitions resulting from the introduction of control (panel A) and 300 μM arsenate incubated (panel B) *Chlamydomonas reinhardtii* cells, at a concentration of 10^5 mL^{-1}, through the chip-μf-Neb at the liquid flow rate of 10 μL min^{-1}.

× 1 min acquisitions. Cell detection was further supported by the detection of phosphorus (P) as an intrisic element in *Chlamydomonas reinhardtii*. Detection of P was achieved by

introducing O_2 into the colission-cell through the formation of phosphorus oxide ($^{47}PO^+$), as shown in **Figure 5.7**.

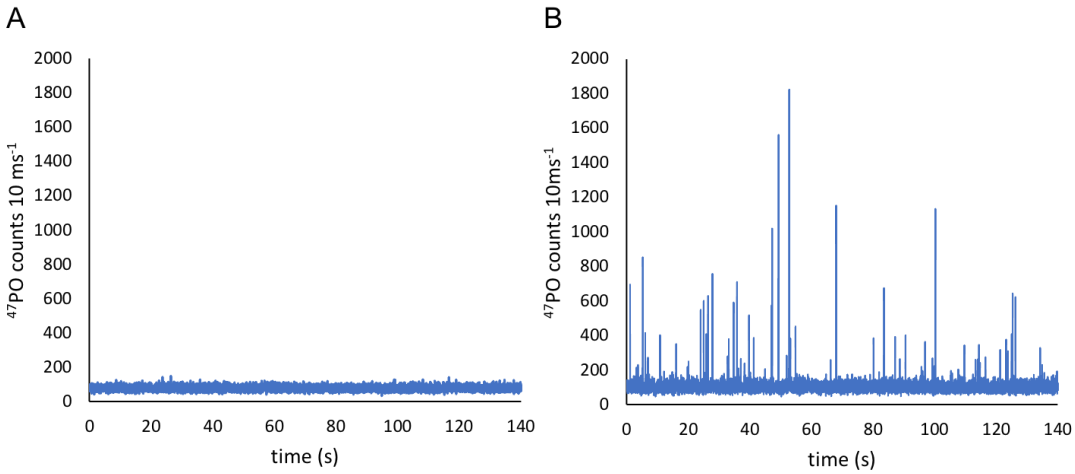

Figure 5.7 Single cell ICP-MS acquisitions resulting from the detection of phosphorus (P) as $^{47}PO^+$ by introducing oxygen in the collision-cell. Panel B shows the single-cell ICP-MS acquisition of 300 µM arsenate incubated *Chlamydomonas reinhardtii* cells at a concentration of 10^5 mL^{-1} through the chip-µf-Neb at a liquid flow rate of 10 µL min^{-1}, while panel A shows the equivalent acquisition of the blank, that is the DI water used to suspend the cells.

With respect to the detection of $^{47}PO^+$, the cell transport efficiency was found to be lower at $9.2 \pm 1.3\%$ for *chlamydomonas reinhardtii* cells incubated in arsenate as opposed to the equivalent obtained with respect to the detection of ^{75}As ($15.0 \pm 2.2\%$). The lower transport efficiency is possibly attributed to the significantly higher background intensity of $^{47}PO^+$ compared to the background intensity of ^{75}As, which were approximately 100 and 3 counts for $^{47}PO^+$ and ^{75}As, respectively. In the case of $^{80}Se^+$ and $^{47}PO^+$ single-cell ICP-MS detection, the detector settling time (4 ms) was considerable with respect to the dwell time (10 ms), and so a correction factor was established in order to account for cell signals which fell within the detector settling time and were thus not measured. This correction has previously been introduced for the detection of metal-containing NPs.[23]

The Se content was 10 fg $cell^{-1}$, whereas for As it was 4.1 fg $cell^{-1}$, as determined using a HEN (Meinhard®) nebulizer. The reason for using the HEN, instead of the chip-µf-Neb, was that when analyzing the oxoacids Se (selenate) and As (arsenate) standards with the latter, poor sensitivity was observed for both elements making their quantitation particularly problematic. The poor sensitivity for the two oxoacidic species was in contrast to high sensitivity observed for all the cationic elements analyzed in the present study (Ag, Au, In, Ce, etc.). The reason for this is not fully understood but will be investigated in future studies.

Another aspect of single-cell analysis that was investigated using the chip-μf-Neb was whether the cells maintained their structural integrity during the nebulization process. This is crucial, as the detection of pulses corresponding to cell fragments would lead to misleading results regarding the selenium or arsenate cell content. **Figure 5.8** shows a typical micrograph captured under the optical microscope for cells collected after nebulization at a backpressure of 2.9 bar. After observing multiple images like the one in **Figure 5.8**, it was concluded that cell integrity was not compromised following their nebulization. This was also supported by the measured diameter which was 6.3 ± 0.7 μm for nebulized cells (n=18) and 6.7 ± 1.0 μm for non-nebulized cells (n=22).

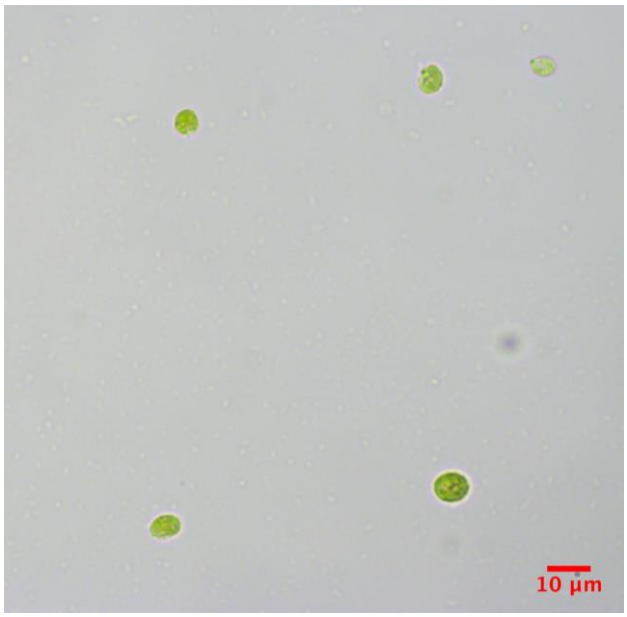

Figure 5.8 Optical micrograph showing *Chlamydomonas reinhardtii* cells that were nebulized using the chip-μf-Neb. A cell suspension containing 10^5 cells mL^{-1} was nebulized onto a microscopy slide for 1 min, and cells were visually examined under the optical microscope.

5.4 Conclusions

Although much effort has been put into interfacing microfluidic chips with ICP-MS, the majority of the developed interfaces are limited to the use of conventional full-sized glass or PFA pneumatic nebulizers. However, disadvantages such as dead volume and self-aspiration issues associated with the use of a pneumatic nebulizer require introduction of new ways to couple a microfluidic chip to ICP-MS. Herein, we report that a microfluidic chip bearing a nozzle for liquid nebulization, referred to as a chip-based microfluidic supersonic

nebulizer (chip-µf-Neb), can be coupled to an ICP-MS and operated at low and sub - µL min^{-1} flow rates. The chip-µf-Neb - ICP-MS system featured high sensitivity and transport efficiency, while the possibility to detect individual cells was also demonstrated. These results provide potential for its use in single-particle and single-cell analysis, while the absence of self-aspiration issues also render it potentially useful for coupling CE and microfluidic devices with ICP-MS. The present work constitutes a proof of concept for the coupling of chip-µf-Neb nebulizer types to ICP-MS, however, further development will be required towards making such nebulizer types powerful tools in chip-based ICP-MS. Such areas of development would potentially involve chip-µf-Neb designs which would integrate channels and a nozzle of larger cross-section, so that cell lines of larger diameter could be introduced without the occurrence of channel blockages. Other chip-µf-Neb designs could incorporate additional channels for liquid mixing or cell manipulation prior to nebulization. In addition, analytical figures of merit, such as sensitivities, background levels and limits of detection, should be demonstrated for more elemental isotopes in order for chip-µf-Neb nebulizers to be considered for universal elemental analysis and therefore a competitor to glass or PFA pneumatic nebulizers.

5.5 Literature

[1] Q.J. Song, G.M. Greenway, T. McCreedy, Interfacing a microfluidic electrophoresis chip with inductively coupled plasma mass spectrometry for rapid elemental speciation, J. Anal. At. Spectrom. 19 (2004) 883–887. https://doi.org/10.1039/b401657b.

[2] Q.J. Song, G.M. Greenway, T. McCreedy, Interfacing microchip capillary electrophoresis with inductively coupled plasma mass spectrometry for chromium speciation, J. Anal. At. Spectrom. 18 (2003) 1–3. https://doi.org/10.1039/b209530k.

[3] H. Cheng, J. Liu, X. Yin, H. Shen, Z. Xu, Elimination of suction effect in interfacing microchip electrophoresis with inductively coupled plasma mass spectrometry using porous monolithic plugs, Analyst. 137 (2012) 3111–3118. https://doi.org/10.1039/c2an35050e.

[4] G. Pearson, G. Greenway, A highly efficient sample introduction system for interfacing microfluidic chips with ICP-MS, J. Anal. At. Spectrom. 22 (2007) 657–662. https://doi.org/10.1039/b702624b.

[5] H. Cheng, Z. Xu, J. Liu, X. Wang, X. Yin, A microfluidic system for introduction of nanolitre sample in inductively coupled plasma mass spectrometry using electrokinetic flow combined with hydrodynamic flow, J. Anal. At. Spectrom. 27 (2012) 346–353. https://doi.org/10.1039/c1ja10273g.

[6] H. Cheng, J. Liu, Z. Xu, X. Yin, A micro-fluidic sub-microliter sample introduction system for direct analysis of Chinese rice wine by inductively coupled plasma mass spectrometry using external aqueous calibration, Spectrochim. Acta - Part B At. Spectrosc. 73 (2012) 55–61. https://doi.org/10.1016/j.sab.2012.07.010.

[7] T. Kagawa, M. Ohno, T. Seki, K. Chikama, Online determination of copper in aluminum alloy by microchip solvent extraction using isotope dilution ICP-MS method, Talanta. 79 (2009) 1001–1005. https://doi.org/10.1016/j.talanta.2009.02.017.

[8] J. Zhang, Z. Qin, D. Deng, J. Liao, X. Wei, N. Zhang, A novel method for the online measurement of impurities in uranium by coupling microfluidics with ICP-MS, J. Anal. At. Spectrom. 31 (2016) 934–939. https://doi.org/10.1039/c5ja00491h.

[9] H. Lackey, D. Bottenus, M. Liezers, S. Shen, S. Branch, J. Katalenich, A. Lines, A versatile and low-cost chip-to-world interface: Enabling ICP-MS characterization of isotachophoretically separated lanthanides on a microfluidic device, Anal. Chim. Acta. 1137 (2020) 11–18. https://doi.org/10.1016/j.aca.2020.08.049.

[10] P.E. Verboket, O. Borovinskaya, N. Meyer, D. Günther, P.S. Dittrich, A new microfluidics-based droplet dispenser for ICPMS, Anal. Chem. 86 (2014) 6012–6018. https://doi.org/10.1021/ac501149a.

[11] H. Wang, B. Chen, M. He, B. Hu, A Facile Droplet-Chip-Time-Resolved Inductively Coupled Plasma Mass Spectrometry Online System for Determination of Zinc in Single Cell, Anal. Chem. 89 (2017) 4931–4938. https://doi.org/10.1021/acs.analchem.7b00134.

[12] H. Wang, B. Chen, M. He, X. Li, P. Chen, B. Hu, Study on uptake of gold nanoparticles by single cells using droplet microfluidic chip-inductively coupled plasma mass spectrometry, Talanta. 200 (2019) 398–407. https://doi.org/10.1016/j.talanta.2019.03.075.

[13] Z. Chen, B. Chen, M. He, B. Hu, Droplet-Splitting Microchip Online Coupled with Time-Resolved ICPMS for Analysis of Released Fe and Pt in Single Cells Treated with FePt Nanoparticles, Anal. Chem. 92 (2020) 12208–12215. https://doi.org/10.1021/acs.analchem.0c01217.

[14] Y. Zhou, Z. Chen, J. Zeng, J. Zhang, D. Yu, B. Zhang, X. Yan, L. Yang, Q. Wang, Direct Infusion ICP- q MS of Lined-up Single-Cell Using an Oil-Free Passive Microfluidic System, Anal. Chem. 92 (2020) 5286–5293. https://doi.org/10.1021/acs.analchem.9b05838.s003.

[15] H. Wang, Z. Wu, B. Chen, M. He, B. Hu, Chip-based array magnetic solid phase microextraction on-line coupled with inductively coupled plasma mass spectrometry for the determination of trace heavy metals in cells, Analyst. 140 (2015) 5619–5626. https://doi.org/10.1039/c5an00736d.

[16] H. Wang, B. Chen, S. Zhu, X. Yu, M. He, B. Hu, Chip-Based Magnetic Solid-Phase Microextraction Online Coupled with MicroHPLC-ICPMS for the Determination of Mercury Species in Cells, Anal. Chem. 88 (2016) 796–802. https://doi.org/10.1021/acs.analchem.5b03130.

[17] J. Zhang, B. Chen, H. Wang, M. He, B. Hu, Facile Chip-Based Array Monolithic

Microextraction System Online Coupled with ICPMS for Fast Analysis of Trace Heavy Metals in Biological Samples, Anal. Chem. 89 (2017) 6878–6885. https://doi.org/10.1021/acs.analchem.7b01367.

[18] M. He, B. Chen, H. Wang, B. Hu, Microfluidic chip-inductively coupled plasma mass spectrometry for trace elements and their species analysis in cells, Appl. Spectrosc. Rev. 54 (2019) 250–263. https://doi.org/10.1080/05704928.2019.1565864.

[19] T. Kartanas, Z. Toprakcioglu, T.A. Hakala, A. Levin, T.W. Herling, R. Daly, J. Charmet, T.P.J. Knowles, Mechanism of droplet-formation in a supersonic microfluidic spray device, Appl. Phys. Lett. 116 (2020). https://doi.org/10.1063/1.5145109.

[20] T. Kartanas, A. Levin, Z. Toprakcioglu, T. Scheidt, T.A. Hakala, J. Charmet, T.P.J. Knowles, Label-Free Protein Analysis Using Liquid Chromatography with Gravimetric Detection, Anal. Chem. 93 (2021) 2848–2853. https://doi.org/10.1021/acs.analchem.0c04149.

[21] B.L. Sharp, Pneumatic nebulisers and spray chambers for inductively coupled plasma spectrometry: A review: Part 1. Nebulisers, J. Anal. At. Spectrom. 3 (1988) 613–652. https://doi.org/10.1039/JA9880300613.

[22] T.L. Taylor, A. Gundlach-Graham, Integration of capillary vibrating sharp-edge spray ionization as a nebulization device for ICP-MS, J. Anal. At. Spectrom. (2023) 16–18. https://doi.org/10.1039/d2ja00384h.

[23] B. Ramkorun-Schmidt, S.A. Pergantis, D. Esteban-Fernández, N. Jakubowski, D. Günther, Investigation of a Combined Microdroplet Generator and Pneumatic Nebulization System for Quantitative Determination of Metal-Containing Nanoparticles Using ICPMS, Anal. Chem. 87 (2015) 8687–8694. https://doi.org/10.1021/acs.analchem.5b01604.

6 Chapter 6. Cell sorting using spiral microfluidic chips combined with SC-ICP-MS

6.1 Introduction

6.1.1 Manipulation of cell/particle motion on the microscale

Precise control of the motion of cells or particles within μm-dimensioned structures and channels, a capability offered by microfluidic devices, is essential for biochemical research and medical applications.[1,2] Techniques allowing for the manipulation of particle or cell motion can be classified as active or passive, depending on whether an external field, such as acoustic waves or voltage, is applied. Active techniques include dielectrophoresis[3], acoustophoresis[4], and magnetophoresis[5]. For example, size-based sorting can be achieved via the application of an electric field in dielectrophoresis, or pressure forces via sonic waves in acoustophoresis. Both techniques can induce the lateral migration of particles across the flow streamlines, and the magnitude of the developed dielectrophoretic and acoustic forces depend on particle size. Separation of cells based on size can also be achieved with magnetophoresis, where magnetic beads are selectively attached to cells via antigen-antibody reactions. All the aforementioned active techniques can be described as field flow fractionation (FFF) techniques. Among passive techniques are hydrophoresis[6], deterministic lateral displacement[7] and gravitational separation[8]. Hydrophoresis and deterministic lateral displacement rely on the interaction of particles with obstacles along the flow, while gravitational separation relies on the concept that particles of different size will have different terminal velocities when exposed to a gravitational field. While all these techniques have found ground in achieving size-based separation, their limitation rests in low throughput. In contrast, size-based sorting of particles or cells by means of inertial focusing[1,2,9,10] can reach cell sorting speeds comparable to flow cytometry, while also being a passive cell filtration technique. By harnessing the hydrodynamic forces which develop in a laminar flow regime when inertial effects become significant, cells or particles of specific size can migrate across fluid streamlines and equilibrate at specific positions across the channel cross-section. Focused streams of cells or particles can then be collected with high purity by designing branched outlet channels to the main flow. Sorting rates of 10^6 cells min^{-1} have been reported, which are 100 times faster than other microscale sorting techniques, as well as comparable to those of flow cytometry, that is, ~ 2.4 $\times 10^6$ cells min^{-1}.[11]

6.1.2 Particle focusing-first observations

In a laminar flow pipe, suspended particles would be expected to be carried away by the fluid streamlines, as well as be randomly distributed throughout the pipe cross-section. Surprisingly, in 1961, 0.8 and 1.6 mm-sized particles flowing through cylindrical pipe of 1 cm i.d. were observed by Segré and Silberberg to congregate within a narrow annulus between the centerline and the walls of the pipe.[12] This annulus was found to form at a radial position of around 0.6 times the diameter of the pipe, and the phenomenon was called “tubular pinch effect”. At the time, the tubular pinch effect could not be explained by fluid dynamics, possibly because of the difficulties in solving the Navier-Stokes equations with the inclusion of the inertial terms.[13]

The Navier-Stokes equations are a set of equations that describe the hydrodynamic flow field of a liquid within a channel, and have been derived by combining laws for the conservation of linear momentum for a Newtonian fluid (i.e., incompressible fluid) and conservation of its mass. For instance, solutions of the Navier-Stokes equations can predict the flow profile of a fluid, whether it is Couette or Poiseuille. A Couette flow profile arises in a flow between 2 parallel plates, one of which is moving, and includes a constant velocity gradient across the channel cross-section. This case will not be discussed in this dissertation. A Poiseuille flow profile is generated in a flow between 2 parallel plates, when this flow is propelled by a pressure gradient. This flow profile is parabolic, that is, higher fluid velocities (v) found at the center of the channel and lower towards the walls, as shown in **Figure 6.2**. Due to the non-slip condition, the fluid velocity at the wall equals zero. It can be observed from **Figure 6.2** that regions near the wall have a steeper slope in the velocity field, and thus a higher velocity gradient $\frac{dv}{dy}$**.** It has been proved that the velocity gradient equals the rate of shear strain rate exerted on the fluid, i.e., the rate at which a fluid is deforming. The shear strain rate is linked to the shear stress via the viscosity co-efficient. For Newtonian fluids, i.e., incompressible liquids, the shear stress is linearly dependent upon the shear strain rate. Because the velocity gradient is greater for streamlines near the wall, these streamlines are naturally regions of greater shear forces.

Matas et al introduced the shear-gradient lift force which accurately described the phenomenon of particle focusing.[14] More specifically, for a particle flowing within a Poiseuille flow profile, the fluid velocity relative to that of a particle will be greater on the particle side closer to the wall (steeper velocity gradient) as opposed to that closer to the

centerline of the channel. This holds true with the assumption that the particle has a zero mean velocity relative to the fluid. The difference in velocities creates a pressure gradient, with the lower pressure region being that closer to the wall. Therefore, the particle starts moving towards the lower pressure region (closer to the wall), until an opposite directed force from the wall (wall-lift) pushes the particle away.[1] The observations of Segre and Silberberg were confirmed by Matas et al in 2004, who reported the equilibration of polystyrene particles in an annulus of a diameter 0.64 times the diameter of the pipe. The equilibration of particles flowing in a 8 mm pipe was observed for the Reynolds number (Re) of 60, similar to the study of Segre and Silberberg.[14] Throughout this dissertation, the term equilibration describes the state of particles or cells occupying a fixed position of a dynamical system, and may be used interchangeably with focusing.

6.1.3 Particle focusing in straight microfluidic channels

Particle focusing within channels has seen immense development with the advent of microfluidics. Although liquid flow within microfluidic channels has been commonly thought of negligible inertia, and thus described as a Stokes flow (Re close to 0) where viscous forces dominate, inertial microfluidics pertain to a flow regime where inertial forces become significant, that is Re>0.[13,15] The ratio of the inertial to viscous forces, defined by Reynolds number (Re), can be calculated:

$$Re = \rho V D_h/\mu, \qquad (Eq. 1)$$

, where ρ corresponds to the density (kg m^{-3}) of the liquid, V to the maximum velocity (m s^{-1}) of the flowing liquid, $D_h$to the hydraulic diameter of the channel (m), and μ to the liquid's dynamic viscosity (Pa s). For a microfluidic channel of rectangular cross-section, D_h equals:

$$D_h = 2(hw)/(h + w) \qquad (Eq. 2)$$

; h, w standing for channel height and width, respectively. Taking the example of a microfluidic channel of a 100×100 μm cross-section, a Re of 1.24 would correspond to a volumetric flow rate of just 5 μL min^{-1} (corresponding to a linear velocity of approximately 0.01 m s^{-1}) of an aqueous solution ($\rho = 1\ kg\ m^{-3}$). The above is used as a mere example of a microfluidic system in order to point out that inertial forces can be significant even at low volumetric flow rates. Hence, inertial microfluidics can be characterized as a middle flow regime, between Stokes flow (Re=0) and inviscid flow (negligible viscous forces, Re>>1).[13] Within this middle regime, hydrodynamic forces can determine the lateral motion of particles (migration) across flow streamlines.

In order to better understand particle focusing within curved microfluidic channels, such as spirals, the fundamentals of particle focusing need to be understood for straight microfluidic channels, the study of which laid the foundation for particle separation based on size.[16] Di Carlo et al demonstrated that 9 μm-sized fluorescent polystyrene particles, flowing within a straight microfluidic channel of square cross-section (50 μm× 50 μm), equilibrated at 4 distinct positions within the square cross-section.[16] If a square microfluidic channel is to be represented as a square prism, then the 4 symmetric equilibrium positions are located at the center of the 4 rectangular faces. These 4 positions were revealed in a confocal micrograph of the channel's square cross-section at an elevated particle Reynolds number (R_p). R_p is defined as:

$$R_p = Re\ \frac{a^2}{D_h^2}\,, \qquad (Eq.3)$$

For a specified particle size (a) and channel hydraulic diameter (D_h) R_p varies with Re, and thus with volumetric flow rate. It required elevated flow rates in order for particles to focus in 4 distinct streams. For instance, particle equilibrium positions were reached at 2.9 R_p (corresponding to 90 Re and a volumetric flow rate of 180 μL min^{-1}), as opposed to 0.5 R_p (corresponding to 16 Re and a volumetric flow rate of 30 μL min^{-1}) at which particles were uniformly distributed across the channel cross-section. Later studies demonstrated 2 equilibrium positions for particles flowing within straight microfluidic channels of rectangular cross-section. These rectangular channels had a high or low aspect ratio (height-to-width, H/W>1 or H/W<1), i.e., a very tall or very wide channel, and exhibited a non-uniform shear-gradient across the rectangular cross-section as opposed to that of a square.[17] In this case, the shear-gradient is greater across the narrowest channel dimension, forcing the particles to migrate either towards the 2 vertical walls for a high aspect ratio channel (h/w>1) or towards the 2 horizontal walls for a low aspect ratio channel (h/w<1).[17,18]. A graphic illustration of the 3 different particle configurations observed for straight microfluidic channels is provided in **Figure 6.1**.

The major forces contributing to particle migration in straight microfluidic channels have been defined as the shear-gradient lift and wall-lift forces, the magnitude of which can be estimated with the following equations.[1,13,16] The shear-gradient lift scales as:

$$F_{Shear} = \frac{f_{lift}\rho V max^2 a^3}{D_h} \qquad (Eq.4)$$

, and the wall-lift as:

$$F_{WL} = \frac{f_{WL}\rho V max^2 a^6}{D_h^4} \qquad (Eq.5)$$

Asmolov has also introduced an expression combining the 2 forces in a single inertial lift force scaling as:[11,19]

$$F_L = \frac{f_{lift}\rho V max^2 a^4}{D_h^2} \qquad (Eq.6)$$

In these expressions, f_{lift} stands for the coefficient of lift, and is a function of both the particle's position within the channel's cross-section and the Re. An average value of 0.5 has been assumed for f_{lift} for a flow through parallel plates at Re<100 [9] In addition, ρ stands for the fluid density (kg m^{-3}), and V_{max} for the maximum linear flow velocity which can be calculated as 3/2 $Vavg$ or 2 $Vavg$. A graphical representation of how the shear-gradient lift and wall-induced lift act to drive particles towards equilibrium positions is shown in **Figure 6.2**. Based on **Figure 6.2**, particles are driven towards the channel walls due to the shear-gradient lift force (F_{Shear}), while a wall-induced lift force (F_{WL}) counteracts the shear-gradient force to ultimately stabilize the particle at the equilibrium positions. The distance of these equilibrium positions from the channel wall were predicted by Di Carlo to decrease with increasing Re.[16]

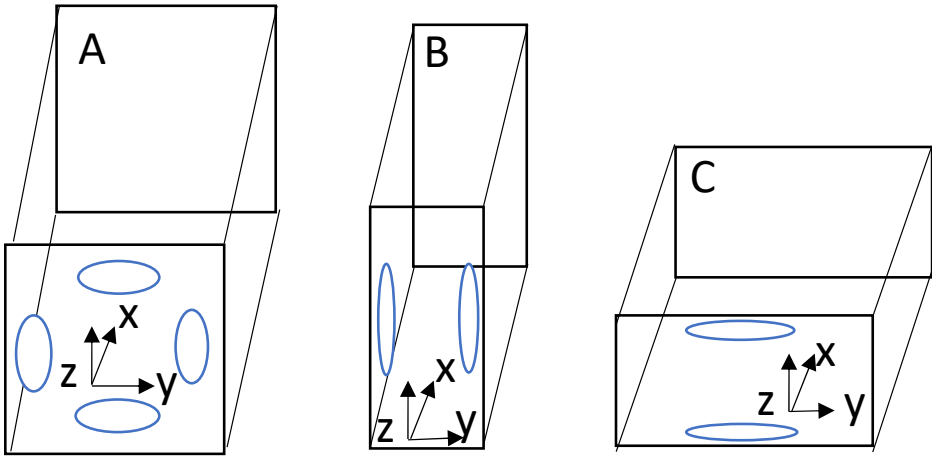

Figure 6.1 Particle configurations resulting from inertial migration in straight microfluidic channels of square cross-section (A), rectangular cross-section of high aspect ratio h/w>1 (B) and rectangular cross-section of low aspect ratio h/w<1 (C). Liquid flow is propagated in the x direction, while z and y planes stand for the channel height and width, respectively. The blue ellipses represent populations of particles equilibrating at the specified positions after inertial migration.

Furthermore, an expression was introduced to calculate the particle lateral migration velocity (V_p) by assuming that a Stokes drag force ($3\pi\mu\alpha V_p$) balances the shear-gradient lift, when the particle is driven towards the channel wall. The resulting expression allows for calculating the particle lateral migration velocity,

$$V_p = \rho V max^2 a^3 f_{lift} / 3\pi\mu D_h^2 \qquad (Eq.7)$$

and in turn, the channel length (L_I) required in order to allow for particles to migrate to their equilibrium positions. L_I is linked to V_p through the relation:

$$L_I = \frac{V_{avg}}{V_p} \times L_M \qquad (Eq.8)$$

, where V_{avg}, V_p and L_M stand for the flowing liquid average linear velocity, the particle lateral migration velocity, and the migration distance, respectively. For example, in order for a particle to migrate to a distance of 40 μm across the width of the channel, with a particle lateral migration velocity of 3.5 cm s^{-1}, in a flowing liquid of V_{avg} 1.8 m s^{-1}, 2 mm of focusing length are required. As the migration velocity had been shown to heavily depend on particle diameter, the possibility of separating different particle populations based on size was revealed.[16].

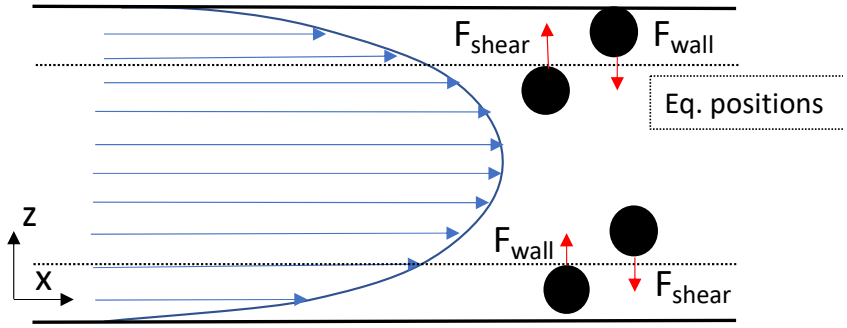

Figure 6.2 Graphical representation showing how the shear-gradient and wall-induced lift forces act on particles (black circles) to drive them to equilibrium positions. The graphical representation shows the Poiseuille flow field within a microfluidic channel of square cross-section from a side viewpoint, i.e., with respect to the channel height (z-dimension) and length (x-direction). The black colored dotted lines illustrate the 2 out of 4 particle equilibrium positions, centered at the top and bottom faces of the channel.

6.1.4 Particle focusing in curved microfluidic channels

For curved microfluidic channels, additional hydrodynamic interactions between the flow field and the flowing particles need to be considered. This is because, in a curved channel, secondary flow arises as a result of the mismatch in fluid velocity between the central regions

and wall-regions of the channel. More specifically, before entering the curve, all fluid streamlines (slow near the walls and fast at the center channel) are required to turn following the curve. Because of their higher velocity, the central fluid elements have higher inertia, and so they can change direction less rapidly than fluid elements near the wall. As a result, the central fluid elements tend to flow outwards around the curve while those near the wall flow inwards, thereby leading to the formation of 2 symmetric counter-rotating vortices at the bottom and top halves of the channel cross-section.[13] The magnitude of the secondary flow was initially established by W. R. Dean with a dimensional number, typically expressed as De, and was shown to scale as:

$$De = Re\sqrt{\frac{D_h}{2R}} \qquad (Eq.9)$$

, where Re, D_h and R stand for the channel Reynolds number, channel hydraulic diameter and the innermost radius of curvature, respectively.[20] Particles that get entrained into the Dean vortices experience a drag force (F_{dean}), defined by Di Carlo to scale as:[16]

$$F_{dean} \sim \rho V_{max}^2 \alpha D_h^2 R^{-1} \qquad (Eq.10)$$

By assuming that Dean drag resembles a Stokes drag force ($3\pi\mu\alpha V_p$), the group of Papautsky and others arrived at a different expression, according to which F_{dean} scales as:

$$F_{dean} = 3\pi\mu a V_d = 5.4\mu De^{1.63} a \qquad (Eq.11)$$

; the average dean velocity V_d equaling: [21,22]

$$V_d = 1.810^{-4} De^{1.63} \qquad (Eq.12)$$

Di Carlo et al were the first to investigate particle focusing in curved microfluidic channels, i.e., symmetric and asymmetric curvilinear channels. Curved channels led to the formation of a single particle stream, suggesting that F_{dean} acts in superposition with the lift forces F_{shear} and F_{wall} to reduce the 4 particle equilibrium positions, observed for straight microfluidic square channels, into a single one. Single stream focusing was attained for an R_p of 0.15 (corresponding to 5 Re and a volumetric flow rate of 10 μL min^{-1}) at a channel length of 3 mm. These values are significantly lower compared to the corresponding Re and channel length required for particle focusing in a straight microfluidic channel (90 Re corresponding to 180μL min^{-1}, 10 mm channel length). In addition, the authors demonstrated the significance of the ratio of particle diameter to channel hydraulic diameter (a/D_h) for particle focusing to occur, and a threshold value of 0.07 was proposed. The a/D_h ratio may also be referred to as particle confinement ratio. While conclusive evidence on the exact

mechanism and location of the superposition of inertial lift and drag forces has not yet emerged neither experimentally nor theoretically, it has been proposed that particle equilibrium positions in curved channels are determined by the inertial force ratio, R_f, defined as:

$$F_{shear}/F_{drag} \qquad (Eq. 13)$$

, and scaling as $\sim a^2$. According to this ratio, two limiting cases exist, one for $R_f \rightarrow 0$ and the other for $R_f \rightarrow \infty$. The former is indicative of an increased F_{drag} leading to particle mixing and thus defocusing, while the latter is indicative of the dominance of F_{shear} leading to particle focusing at equilibrium positions independent of the secondary flow. For intermediate values of R_f, the superposition of F_{drag} with F_{shear} can determine different equilibrium positions for particles of different sizes due to the strong dependence of R_f on particle diameter (a), ultimately providing capabilities for size-based sorting of particles.[1,13] A minimum R_f value of 0.04 has been proposed as a guideline in order for particle focusing to occur, although it has been stressed that this value does not incorporate the transient nature of the secondary flow and the cross-sectional variation of the entailed forces in order for predictions to be fully relied upon.[1]

6.1.5 Particle focusing in curved Archimedean spiral microfluidic channels

Out of all the curved channel geometries employed for particle focusing, Archimedean spirals have been studied the most. [11,23,24] To an extent that, at specified flow conditions of Re and De, and for given spiral channel characteristics, i.e., radius of curvature and channel cross-section, distinct focusing regimes for differently sized particle populations have been revealed. These focusing regimes have demonstrated cases for size-based arrangement of particles across the width of the spiral microchannel.

In a series of publications, the group of Papautsky have reported that, for mixed suspensions containing differently sized particle populations, i.e., large, medium and smaller μm-sized-particle populations, distinct particle streams are observed, with the largest sized particle population focusing nearest to the inner wall. [11,25] More specifically, Kuntaegowdanahalli et al observed populations of 10, 15 and 20 μm-sized polystyrene particles to focus in distinct streams across the width of the spiral microfluidic channel. This observation was made in spiral microfluidic channels of a low aspect ratio rectangular cross-section, i.e., 500 μm ×130 μm (width×height), when a suspension containing the 3 particle populations was introduced at 14 De (corresponding to 237 Re and a volumetric flow rate of

3 mL min^{-1}). The stream of the largest-sized particle population (20 μm-sized) was found to equilibrate nearest to the inner wall, i.e., at a position of approx. 0.13 × channel width, followed by the 15 μm-sized particles at a position of approx. 0.24 × channel width, and even farther from the inner wall, the 10 μm-sized at a position of approx. 0.36 × channel width. Hence, size-based sorting of the particle populations, from largest to smallest, was demonstrated across the width of the spiral microchannel, when initially these particle populations were randomly distributed throughout the channel cross-section, at the spiral inlet. Size-based arrangement of particles across the channel width also allowed for the independent extraction of each particle population from the initial mixed cell suspension by designing bifurcated outlet channels at the end of the main spiral channel, as shown in **Figure 6.3**.

The largest to smallest particle arrangement was explained by the balance between F_{shear} and F_{dean}. As the ratio of these forces was shown to scale with $\sim a^2$, larger particles experience a stronger F_{shear} propelling them to migrate nearest to the inner wall. In addition,

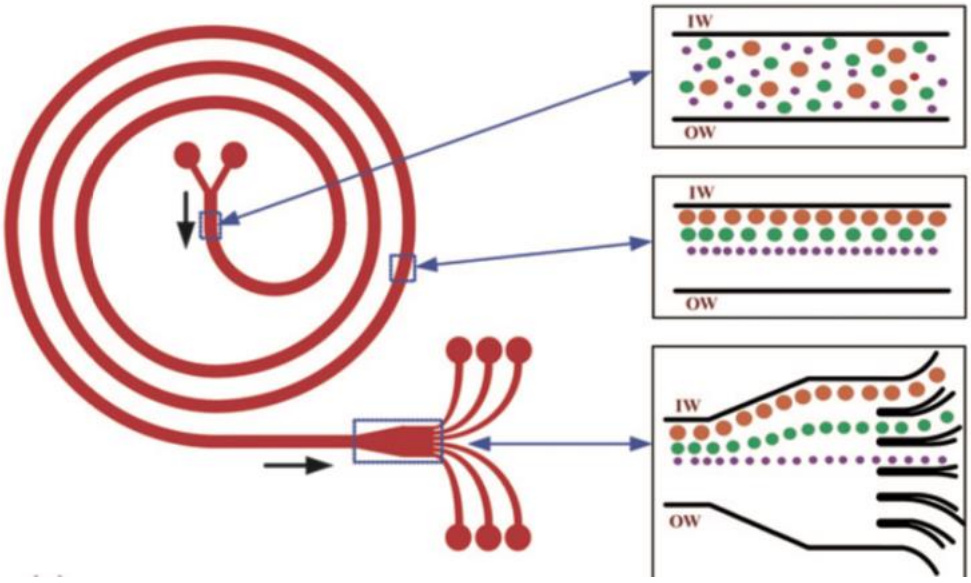

Figure 6.3 Graphical representation of the spiral microchannel used to sort 20 μm (orange), 15 μm (green) and 10 μm-sized (purple) particle populations. The panels, to the right, are inset side-views of 3 different spiral regions, i.e., a channel point close to the spiral inlet (top panel), a channel point within the 3rd spiral loop (middle panel), and a point at the bifurcated outlets (bottom panel). IW and OW stand for inner wall and outer wall, respectively. Reprinted with permission from Lab Chip, 2009, 9, 2973–2980 (Copyright 2009, Royal Society of Chemistry).

a tendency was shown for all particle sizes to occupy equilibrium focusing positions farther from the inner wall with increasing De and migrate towards the channel centerline. This tendency was a result of the increasing magnitude of F_{dean}, and was more prominent for 10 μm particles which exhibit the lowest inertial force ratio ($F_{shear}$to F_{dean}) in comparison to the other larger-sized particle populations.

Similar observations were reported by Russom et al for 10 and 7 μm particles flowing through a low-aspect ratio spiral channel.[23] While at low volumetric flow rates both particle populations overlapped in a single particle stream near the inner wall, increasing the flow rate resulted in gradual displacement of the stream away from the inner wall and ultimately in the separation of the 2 particle populations in distinct streams; the 10 μm-sized particles focusing nearest to the inner wall. In addition to showing distinct streams of differently-sized particle populations with respect to channel width, Russom et al provided indication that each of these streams, initially observed from a top-bottom view of the spiral microchannel, were comprised of 2 longitudinally ordered particle populations at the top and bottom faces of the microchannel. This was revealed by high-speed imaging which showed a train of longitudinally ordered particles, at regular spaces between each other, alternating between 2 vertical positions in the microchannel.

Because in all of the aforementioned studies De and Re were varied simultaneously by changing the volumetric flow rate at which a spiral channel was operated, Martel et al investigated particle focusing regimes using an approach which allowed for varying Re and De independently.[24] To this end, the authors employed 4 different microfluidic spiral channels, which had the same hydraulic diameter and channel length, but differed in curvature. These spiral channels were operated within a wide Re range of 1-400. Curvature was defined as the curvature ratio δ, that is, $\frac{D_h}{2r}$, taking values of 0 (straight channel), 0.0008, 0.0034, 0.0083, 0.0166. This approach meant that for the same Re, higher δ corresponded to higher De. By capturing top-down fluorescent images of the outlet channel, the focusing regimes of fluorescent 4.4, 9.9 and 15-μm sized particle populations were revealed across the channel width for each curvature ratio within the full range of tested Re. The differently sized particle populations exhibited different focusing regimes, as both Re and δ influenced their equilibrium positions. For instance, 9.9 μm particles were found to migrate towards the outer wall at high Re for a channel of δ 0.0166, while, for a δ of 0.0083 at equal Re, they formed a narrow stream nearest to the inner wall. Narrow particle streams formed nearest to the inner wall were deemed as single point equilibrium focusing positions. By combining

the focusing regimes of the 3 particle populations across the full range of Re into a single map, the spiral channels of 0.0083 and 0.0166 δ demonstrated the highest potential for separation amongst the particle populations, also showing 2 different cases for size-based sorting of particles. When operated at 140 Re (12.7 De), the spiral channel of 0.0083 δ revealed a particle spatial arrangement according to which the medium-sized (9.9 μm) particles focused nearest to the inner wall, whereas the streams of small (4.4 μm) and large-sized (15 μm) particles overlapped just before the channel centerline. Increasing Re up to 314 (28.6 De) resulted in complete separation between the large and small-sized particles, and introduced a new spatial arrangement of medium-to-large-to-small, with the medium-sized particles nearest to the inner wall. When operated at 227 Re (29.2 De), the spiral channel of 0.0166 δ showed a large-to-medium-to-small spatial arrangement, previously observed by the group of Papautsky. Hence, it was demonstrated that 2 spiral channels operating at very similar De can lead to different size-based separation mechanisms.

Further exploring particle equilibration dynamics within the rectangular channel cross-section, the same authors reported the presence of vertical particle equilibrium positions as well, as had been reported by Russom et al. Particle vertical positions were explored using bright-field microscopy with high-speed video recording. More specifically, at low Re prior to transitioning to single point equilibrium focusing positions (with respect to channel width), particles were shown to exhibit 2 vertical equilibrium positions, located at the long faces of the rectangular cross-section. As can be seen in **Figure 6.4**, these vertical equilibrium positions are close to the vertical positions at which Dean flow velocity (V_d) equals zero and thus $F_{dean} = 0$. Based on simulations describing the three-dimensional flow field throughout the rectangular cross-section, a mechanism was hypothesized to explain the size-based particle arrangements observed in rectangular channels of increasing curvature, when these channels are operated at equal Re. This mechanism is visually represented in **Figure 6.4** for large, medium and small-sized particles flowing through spiral channels of increasing curvature b-d, at a constant Re of 419.

Figure 6.4 is comprised of 3D maps showing the Poiseuille flow velocity profile developed throughout the rectangular cross-section of straight (a) and spiral microchannel (b-d). All these maps have been derived from fluid dynamics simulations at constant Re of 419, and

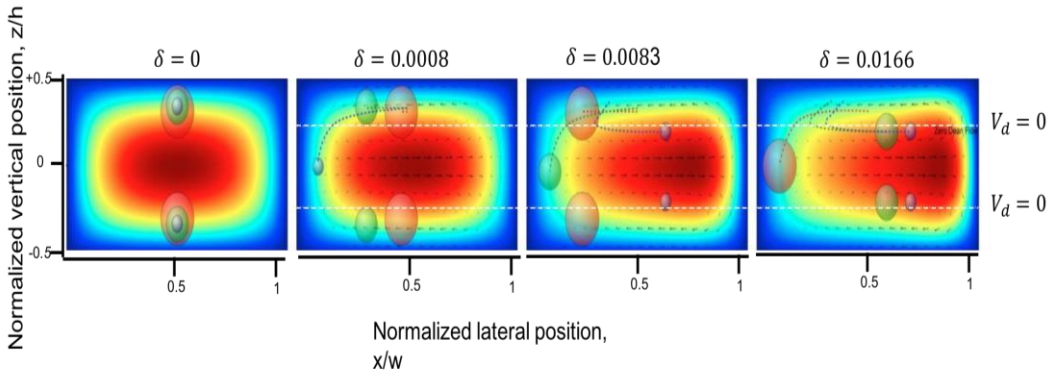

Figure 6.4 Graphical representation of the hypothetical mechanism of transition between inner and outer wall focusing positions in curved microfluidic channels. Simulated velocity profiles with normalized Dean flow vectors (black arrows) show the idealized equilibrium positions (a–d) of the three different sizes of particles (4.4 μm blue, 9.9 μm green, 15 μm red) in the cross-section of a straight channel (a) and of those of increasing curvature (left to right) b-d. The white dotted lines show the zero Dean flow ($V_d = 0$) line, above or below of which Dean velocities change direction in each of the 2 counter-rotating vortices. Figure reprinted with permission from DOI: 10.1038/srep03340 (Copyright 2013, Nature)

aid in the understanding of the size-dependent mechanism of particle equilibration positions within the cross-section of a low-aspect ratio rectangular channel, at increasing curvature values. For a straight channel, $\delta = 0$, the highest velocities (red colour) are observed at the central region of the channel, as expected for a Poiseuille flow profile, and because it is a low-aspect ratio channel, i.e., h/w<1, the shear-gradient is greater across the height of the channel. This explains that all particle sizes, i.e., small (blue), medium (green) and large-sized (red) particles, focus at 2 vertical positions (top and bottom of the channel), as a result of F_{shear} being greater across this height direction and propelling particles towards the vertical channel walls. For spiral channels of increasing curvature (b-d), counter-rotating Dean vortices (black arrows) are developed at the top and bottom vertical halves of the channel; each vortex rotating around a white line (denoting zero Dean velocity), located at a normalized vertical position x/w $\pm$0.25. Granted that all channels operate at 419Re, it is observed that the increasing curvature results in the relocation of the maximum of the velocity profile towards the outer wall (located at x/w=1). As a consequence, with increasing De, the shear-gradient lift across the height, within the inner half of the channel x/w<0.5, drops. This allows particles to cross the vertical position of zero Dean velocity and get entrained in the Dean vortex with direction towards the outer wall until F_{shear} becomes high enough to counter the Dean drag force, F_D. The dependence of this mechanism on particle

size rests on the fact that the magnitude of F_{shear} strongly depends on particle size. In terms of this, a smaller particle will require a smaller drop in the vertical shear-gradient, thus migration to a focusing position towards the outer wall can occur at lower δ than that required for larger-sized particles. Granted that Re was kept constant in this simulation, migration of smaller-sized particles towards the outer wall occurred at lower De. However, the authors have reported that single-point equilibrium positions occurring for small, medium and large-sized particles at $\delta = 0.0008,\ 0.0083$ and 0.0166, respectively, cannot be completely explained by this theory without a more detailed understanding of the 3-D variation of hydrodynamic forces within the inner half of the channel, or a greater curvature (δ) resolution.

In a more recent study on Dean flow dynamics within low aspect ratio rectangular channels, Nivedita et al.[26] demonstrated the occurrence of additional secondary Dean vortices which mediate particle/cell focusing at high De. These vortices were demonstrated by confocal microscopy observations of the recirculation pattern of a fluorescein dye throughout the channel cross-section, where secondary Dean vortices were observed to occur beyond a critical De (De_c). Confocal microscopy observations of 10 μm fluorescent particles getting trapped within secondary vortices and focusing near the outer wall at a De of 37 were also carried out, while these particles focused near the inner wall at the lower 17 De. In addition, red blood cells (RBCs) introduced through the spiral channel demonstrated very similar behavior at the same De. This, combined with the confirmation on the presence of secondary Dean vortices, suggested that cells remain focused near the outer wall as a result of getting entrained within the secondary vortices above a De_c. If not for the presence of secondary vortices, RBCs (sizes ranging between 6-8 μm) or those 10 μm particles would recirculate throughout the channel cross-section and not focus, as it is the case of smaller-sized particles.

6.1.6 Applications in cell focusing and sorting using spiral microfluidic channels

Spiral microfluidics have been demonstrated for their capabilities in focusing and size-based sorting of cells.[10,11,25,27–30] Such capabilities have contributed to the development of bioanalytical tools, including flow cytometry alternatives or droplet generators for highly efficient cell encapsulation. Compared to straight microfluidic channels, advantages of spiral channels include: quicker focusing as a result of Dean vortices propelling particles/cells towards their lateral and vertical equilibrium positions, broader

possibilities for size-based sorting, and smaller device footprint especially when a long focusing channel needs to be designed.

Detection of each cell by a flow cytometer requires that cells are focused as they travel through the flow chamber. Focusing of the cells occurs through a complicated, bulky and expensive flow chamber utilizing a flow of sheath liquid. An alternative approach to a conventional flow cytometer, with the attributes of portability, low cost and sheathless cell alignment, has been reported by Bhagat et al.[10] The authors developed a chip-based flow cytometer system, involving a spiral channel for particle and cell focusing, and a laser induced fluorescence setup to detect fluorescent signals from individual cells. For proof-of-concept, a particle suspension, containing 6 μm-sized fluorescent polystyrene particles at a 0.05% volume fraction, was infused through a 10-loop spiral channel (100 μm × 50 μm, width×height) at a De range of 0.05-2.3. Fluorescence top-down images of the channel showed particles to focus in a narrow stream close to the inner wall of the channel, while the narrowest stream was achieved at the highest De of 2.3 (corresponding to a 100 μL min^{-1}). Using a high-speed data acquisition system (300 kHz corresponding to an acquisition time window of 3.3 μs) to record the output signal from the PMT detector, each particle passing through the interrogation region within the spiral channel yielded a spike in the recorded signal. The developed system was used to detect and count SH-SY5Y neuroblastoma cells, and demonstrated excellent accuracy (99%) in the determination of the cell number concentration in the analyzed suspension.

Kemna et al has reported on the use of spiral microfluidics in order to increase the single cell encapsulation efficiency of droplet-based microfluidic systems.[27] Droplet-based microfluidic systems allow for the entrapment of individual cells into individual μm-sized aqueous droplets, thus lending themselves ideally for single-cell analysis. In such systems, cell encapsulation is governed by Poisson statistics due to the random arrival of cells to the point of droplet generation. Limitations involve low single cell encapsulation efficiencies, which are attributed to the increasingly dilute cell suspensions required in order to minimize the co-occurrence of cells in each droplet. Hence, because the droplet generation rate is not matched by the cell arrival rate as a result of the dilute suspensions used, 60-70 % of the generated droplets are empty. In the microfluidic chip introduced by Kemna et al, a 5-loop spiral channel (50 μm × 29 μm, width×height) was combined with a cross-channel configuration in a single microfluidic device. Cells exiting from the spiral channel were focused due to Dean-coupled inertial migration, forming a longitudinal train with precise

spacing (measured at 52 μm at an aqueous flow rate of 15 μL min^{-1}) between adjacent cells. A suitable cross-channel configuration was used for droplet generation, and the oil flow was optimized in order for the droplet generation rates to match the cell arrival rates (2700 s^{-1}). Using this system, single-cell encapsulation efficiencies as high as 77% were attained, overpowering the corresponding conventional Poisson-based encapsulation of 37%. In addition, the 2 types of myeloid leukemic cells (HL60 and K562 cells) encapsulated using the proposed droplet-based platform showed no significant loss in viability (>90%); losses which could have resulted from the shear stresses exerted during Dean-coupled inertial focusing.

Kuntaegowdanahalli et al were the first to demonstrate the use of a spiral microfluidic channel in the separation of particle populations and cells of different sizes by harnessing Dean coupled inertial migration.[11] The spiral channel, fabricated into a PDMS microfluidic chip, had a low aspect ratio rectangular cross-section (500 μm × 130 μm, width×height) with a continuously increasing curvature. At the end of the spiral channel, a branch of 8 outlet channels allowed for the individual collection of the sorted sample constituents, that is, SH-SY5Y neuroblastoma and C6 glioma cells neural cells, in a high- throughput fashion. Separation of these 2 cell types could be of importance in understanding their distinct role in neurodegenerative disorders. Mixed suspensions containing SH-SY5Y (avg. size of 15±5 μm) and C6 cells (avg. size of 8±3 μm), each at a concentration of 5×10^5 cells mL^{-1}, were sorted through the spiral microfluidic channel at a 12 De, resulting in the collection of the majority of the larger cells from the 1st outlet and the smaller from the 2nd outlet channel. Out of the 5×10^5 cells mL^{-1} contained per cell type in the initial suspension, a vast 90% was collected from outlet channels 1 and 2; indicating a high focusing efficiency for both cell types. However, quantitative separation between the 2 cell lines could not be achieved, i.e., 80% purity in SH-SY5Y and C6 cells was achieved for samples collected from outlets 1 and 2, respectively. This was attributed to the large variation in size, as displayed by the large standard deviation of the size distribution of both cell types. In comparison, for a mixed suspension containing 10, 15 and 20 μm-sized monodisperse polystyrene particles, separation efficiency among the 3 particle sizes reached 90%. In addition, at the operation flow rate of 3 mL min^{-1} a sorting throughput of 10^6 cells mL^{-1} was achieved using the proposed device, which is comparable to that of commercial flow cytometry (2.4×10^6) and 100× higher than other microscale sorting methods. In addition, the shear-stress exerted on

the cells during separation did not cause any substantial drop in cell viability, which was found to be >90%.

A spiral microfluidic chip, similar to that of Kuntaegowdanahalli et al, has been used by Lee et al in order to achieve high-throughput cell cycle synchronization in mammalian cell populations.[28] Synchronization of cells in different phases of the cell cycle has mediated the development of cell cycle-based therapeutics, such as cancer or stem cell therapeutics. For instance, anti-cancer drugs have been reported to act on different phases of the cell cycle, or stem cells have been reported to have higher efficiency for nuclear transfer in hosts during their G0/G1 phase. Conventional methodologies, including serum starvation or methotrexate addition, have been reported to disrupt cell metabolism, while flow cytometry (FACS) can compromise cell viability. In their study, Lee et al have demonstrated how the relationship between cell volume and cell cycle-phase can be harnessed in order to achieve enrichment of a fraction of the asynchronous cell population found in a certain phase of the cell cycle. A suspension of the asynchronous population of human bone marrow derived mesenchymal stem cells (hMSCs), at a concentration of 10^5 cells mL^{-1}, was introduced through the spiral channel, and the samples collected from outlets 1-8 were analyzed using a FACS-based methodology upon addition of propidium iodide (green fluorescence dye for cell staining) into the collected samples. Using FACs, the size distribution of the cell population in each of the collected samples was determined, and correlated to the cell cycle phase; thus, allowing for the extraction of the cell synchronization efficiency. At the operating flow rate of 2 mL min^{-1}, size-based sorting through the spiral channel resulted in a large-to-medium-to small size particle arrangement for sorted cells, which were collected from outlets 1-4. Hence, the majority of the larger-sized cells (average size of 23.5 μm), found at the mitosis stage (G2/M phase), were accumulated from the inner wall outlet (channel 1), i.e., 50% of the total cells found at the G2/M phase. Whereas the small-sized cells, found at the G0/G1, were accumulated from outlet channel 4 at an impressive 86% separation efficiency. While the achieved enrichment levels were found to be comparable to other microscale cell cycle synchronization platforms, the described Dean coupled inertial microfluidic platform attained significantly higher cell sorting throughput and viability, which were 2.5×10^5 cells min^{-1} and >95%, respectively.

Spiral microfluidics have been reported for biomedical applications, with an emphasis on handling blood samples for the purpose of blood cell sorting or enrichment of CTCs.[25,29,30] Nivedita et al has reported on the use of a spiral cell sorter optimized to

achieve efficient (~95%) separation between RBCs and WBCs in diluted blood samples.[25] Enrichment and separation of blood are essential steps in blood analysis, as independent tracking of each blood constituent, such as red (RBCs) or white blood (WBCs) cells, may provide critical information in the diagnosis of a disease, which is usually associated with changes in the cell number concentration or morphology. Limitations related to the use of conventional techniques, such as centrifugation or flow cytometry, are the occurrence of contaminations or cell lysis, as well as operational costs. To conduct separation between RBCs (avg. size of 7 μm) and WBCs (avg. size of 15 μm), a spiral channel (500 μm × 110 μm, width×height) was used, while dilution of the blood sample (44% hct) down to 0.1% hct was necessary in order to minimize cell-cell interactions associated with decreased focusing efficiency. Identification of the cell types present in the samples collected from each outlet channel was done using microscopy. The system, operated at 1.8 mL min^{-1} (corresponding to 31 De) achieved a 95 % efficiency of separation, with larger WBCs accumulating from the inner wall outlet (outlet channel 1) and the smaller RBCs from outlet 2; at concentrations of ~10^7 RBCs ml^{-1} and ~10^5 WBCs ml^{-1}. Hou et al developed and optimized a spiral sorter for the purpose of isolating CTCs from blood samples.[30] The difficulty associated with the detection of CTCs is their presence in extremely low concentrations, typically 1-100 CTCs per 10^9 blood cells. By using a 10 cm long spiral channel (500 μm × 160 μm, width×height), followed by a 2-outlet end, the larger CTCs (avg. size of 20 μm) were efficiently isolated from the rest blood cells by exiting from the inner wall outlet. High blood concentrations of 20% hct could be introduced as a result of a sheath liquid flow meeting the sample flow at the inlet. Enumeration of the sorted cells using fluorescent immuno-staining demonstrated 85% recoveries of CTCs in 20 samples collected from lung cancer patients; thus, showing the potential of the technique as robust CTC detection platform. In addition, the technique was reported to attain the highest throughput, 3 mL blood h^{-1}, among all microfluidic CTC isolation techniques.

6.1.7 Spiral microfluidic channels in conjunction with ICP-MS

So far, coupling of spiral microfluidic channels to ICP-MS has been reported by the group of Wang for the purpose of cell focusing prior to single cell detection.[31,32] While the nebulization of dilute cell suspensions, along with the use of short dwell times, statistically precludes multiple cell detection in each recorded cell detection event, the random arrival of cells to the nebulizer introduces variation to the nebulized flux of cells s^{-1}; thus biasing

quantitative results reported per cell. Recently, Zhang et al introduced a platform which involved interfacing a spiral channel (300 μm width, 50 μm height, 26.8 cm total length), fabricated into a PDMS chip, to a concentric nebulizer in order to achieve precise sampling of single cells into the ICP in a high throughput (2×10^6 cells mL^{-1}) fashion.[31] The precision in sampling of single cells was offered by the operation of the spiral channel, achieving longitudinal focusing of the cells within the channel at a wide range of flow rates 100-800 μL min^{-1}. In a later study, Wu et al developed a 2-D cytometry platform based on induced fluorescence (LIF) and ICP-MS using a spiral fused silica capillary for cell focusing.[32] Application of LIF on a terminal segment of the capillary, a few mm prior to nebulizer insertion, allowed for the online analysis of the same cell suspension using both techniques. A fluorescence detection pulse was registered with each passing cell, providing information on the spacing between adjacent cells in the focused stream and ultimately enabling determination of the cell number concentration of the suspension. For real-time ICP-MS detection, a ^{107}Ag pulse was detected with each passing cell, as cells had been previously incubated with ionic Ag. Spacing between adjacent cells was found irregular, possibly suggesting the occurrence of 2 vertical cell focusing positions, while a high recovery of 79% was achieved with respect to the theoretical cell number concentration in the suspension. The described platform could be a valuable technique in cytometry, where both information on cell number concentration and cell content are required.

6.1.8 Objective

The objective of this chapter is to explore the capabilities of spiral microfluidic chips in focusing and size-based sorting of cells prior to SC ICP-MS detection. For this reason, 3 spiral microfluidic chips, of different cross-section and channel length, are employed and studied at a range of volumetric flow rates using cell lines of different sizes. Sorted samples collected from the branched outlets of the spiral microfluidic chips are subsequently analyzed using SC ICP-MS. Upon treatment of the SC ICP-MS raw data, results are evaluated using a combination of graphs, including the number distribution of cells across outlet channels as well as contour plots linking cell size with the number of cells collected per outlet channel. The latter is made possible by demonstrating the linear relationship of phosphorus content determined per cell with cell size. The separation potential between cell lines on the 3 spiral chips is extensively discussed, as well as limitations associated with the achieved size resolution for cell suspensions. To the best of my knowledge, the work

described in this chapter constitutes the first attempt in combining spiral channels with SC ICP-MS for the purpose of size-based sorting of cell populations. As a preliminary work on the interface between inertial microfluidics and SC ICP-MS, this chapter may also serve as a foundation for future development in the field.

6.2 Materials and Methods

6.2.1 μF chips with spiral microchannels

Focusing and size-based sorting of cells was conducted on μF chips containing microchannels of Archimedean spiral geometry. The μF chips used in this study were made of Zeonor®, a cyclo-olefin polymer, and were purchased from microfluidic ChipShop GmbH. Each spiral μF chip is defined by the dimensions of its microchannels, the number of spiral turns, the spiral radius and the number of outlet channels. Three μF spiral chips (Fig.5.5) were studied with respect to their cell focusing and cell size-sorting capabilities, and their geometric characteristics are provided in **Table 6.1**. Throughout this study, the spiral μF chips will be referred to as 1, 2 and 3 in order to easily relate each μF chip with its geometric characteristics.

Table 6.1 Geometric characteristics of the 3 spiral μF chips ordered in decreasing channel cross-section, width (μm)× height (μm).

μF chip	Channel width (μm)	Channel height (μm)	Channel length (mm)	Spiral turns	Initial radius (μm)	Number of outlets
1	300	80	166	8	730	8
2	150	70	195	9	740	6
3	80	50	270	12	780	6

All the above geometric characteristics were provided by the manufacturer, apart from the spiral innermost radius of curvature. The innermost radius is required in order to determine the Dean number (De). De is a function of Re number, hydraulic diameter (D_h) and radius of curvature, and so for the given spiral μF channels used in this study (**Figure 6.5**), De will vary with the flow rate supplied to the inlet of the μF chip (Q). The μF chips used

in this study were modelled as Archimedean spirals since the distance between successive spiral loops remained relatively constant. The radius of curvature at each point in an Archimedean spiral is described by the following equation: $R = r + b \times \theta$, R denoting the radius of curvature, b the distance between loops, θ the angle of rotation and r the innermost radius. [25] The innermost radius r is the distance between the starting point of the spiral and the center of rotation. As the radius of curvature, R, linearly increases with downstream progression of the spiral, the innermost radius dictates the maximum De of the system at a given flow rate condition. This is because De scales inversely with radius of curvature, and the innermost radius is the tightest curvature in the spiral. **Figure 6.5** illustrates photographs of the μF chips 1-3, on which a cartesian system has been drawn. On this system, the chip inlet was considered the center point around which the spiral revolves. The cartesian system defines the rotation angles θ of the initial spiral turn, i.e., π/2, π, 3π/2, 2π rad. Micrographs depicting the initial rotation of the spiral from the point of origin to the angle of π/2 rad are also provided in **Figure SI1. 10** to aid in understanding the angles of rotation. Because the spiral channel is directly connected to the point of origin, the innermost radius, r, was considered zero. Instead, the radius at the short angle of π/2 rad was determined for chips 1-3, and was used as the initial radius of curvature for the calculation of De. After processing the calibrated micrographs, provided in **Figure SI1. 10**, using ImageJ, the initial radius was found to be 730, 740 and 780 for chip1, 2 and 3, respectively. The variation in the initial radius of curvature amongst chips 1-3 was below 10%, thus indicating that the differences

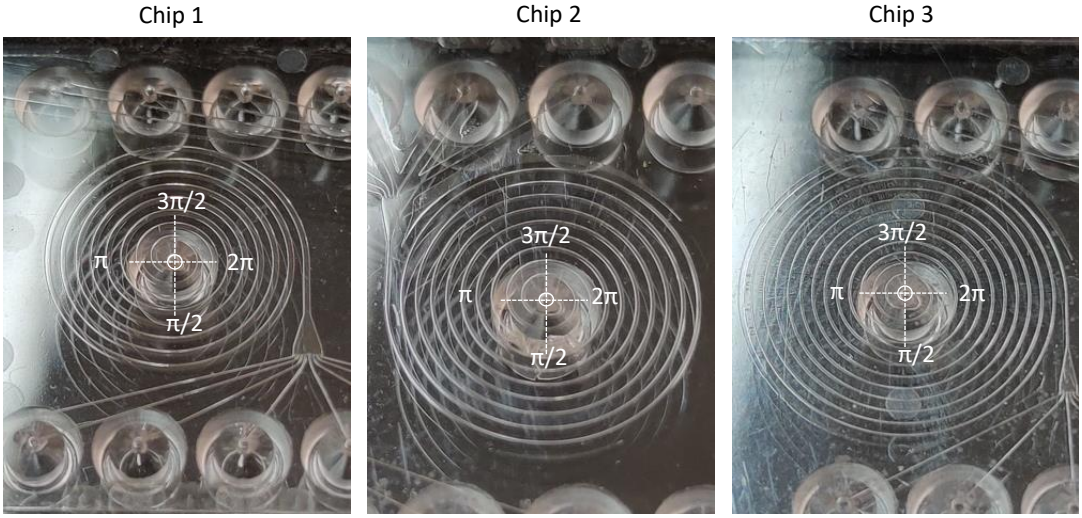

Figure 6.5 Panels A-C show photographs of the spiral μF chips 1-3, respectively. A cartesian coordinate system, with its center of origin placed at the chip inlet, is drawn, while the dotted lines denote the rotation angle θ of the initial spiral turn (π/2, π, 3π/2, 2π).

in the applied De amongst the spiral chips will be predominantly determined by the Re number and channel hydraulic diameter D_h, rather than the innermost radius r.

6.2.2 Analytical setup for cell sorting prior to SC ICP-MS analysis

In order to conduct cell sorting of the initial cell suspensions, prepared at concentrations of 10^5 - 4×10^5 mL^{-1}, two analytical setups were employed. Depending on the operating flow rate of each µF spiral chip, these setups will be referred to as low and high flow setup. The low flow setup was used in conjunction with µF chip 3, with a maximum operating flow rate at 65 µL min^{-1}, while the high flow setup was used in conjunction with µF chips 1 and 2, with a maximum operating flow rate at 300 and 1500 µL min^{-1}, respectively. The maximum operating flow rate was found experimentally, and is defined as the liquid flow rate at which a leak-free connection can be achieved between the chip and the various parts of the analytical setups. A schematic view of the analytical setups is provided in **Figure 6.6** and **Figure 6.7** for the low and high flow setup, respectively.

The low flow setup (**Figure 6.6**) is the simplest in its application, as the initial cell suspension can be loaded onto a 500 µL precision glass syringe (Hamilton) and constantly infused into the µF spiral chip inlet at a defined liquid flow rate using a syringe pump (Cole

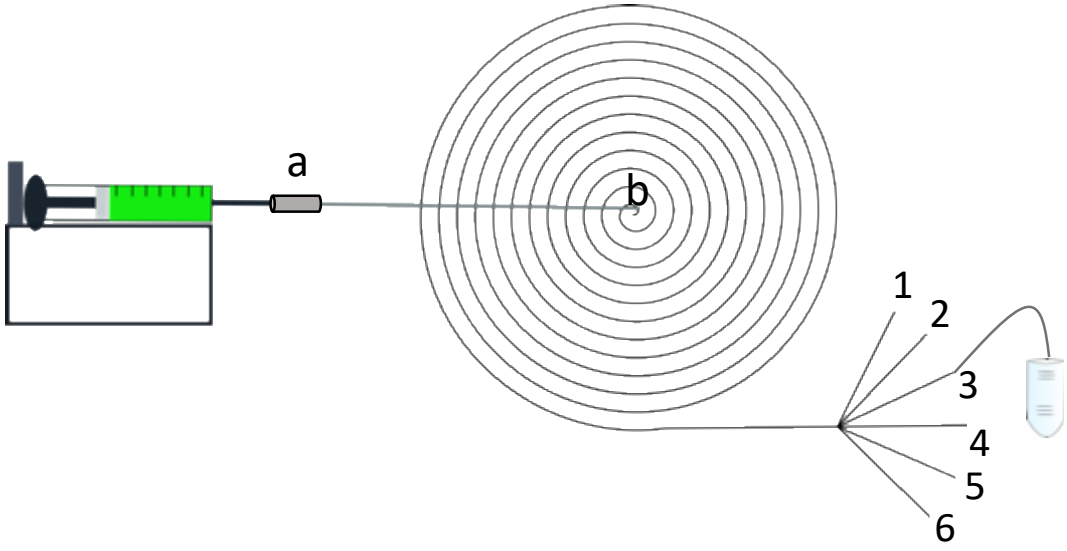

Figure 6.6 A schematic representation of the low flow analytical setup employed for cell sorting prior to SC ICP-MS analysis using the spiral µF chip 3 which requires flow rates up to 65 µL min-1. The syringe needle is connected to the spiral inlet (b) using a flexible silicone tubing (i.d. of 150 µm and total volume of 15µL) and PTFE connectors (point a). A cell suspension is constantly infused into the spiral, while the resulting samples from spiral outlet channels 1-6 are collected into Eppendorf tubes using 15 cm PTFE (300 i.d.) tubing.

Palmer). While the cell suspension is online sorted through the spiral, the liquid samples resulting from outlet channels 1-6 are collected into eppendorf tubes, each one dedicated to a given outlet channel. Connection between the glass syringe needle and the chip inlet was achieved through the use of a PTFE union (point a) and silicone tubing (i.d. 100 µm), the end of which was directly connected to a thermoplastic elastomer (TPE) luer connector, fitting into the chip spiral inlet (point b). TPE mini luer connectors were also used to interface the chip outlet ports (connecting to the spiral outlet channels) with 15 cm PTFE tubings (i.d. 300 µm) in order to collect the resulting samples into the eppendorf tubes. A photograph showing the low flow setup in operation can be found in **Figure SI1. 11**.

In order to perform cell sorting of the initial cell suspensions using µF chips 1 and 2, higher flow rates were required, that is, 250-1500 µL min^{-1} and 150-350 µL min^{-1} for chip 1 and 2, respectively. Because the syringe pump cannot provide flow rates above 100 µL min^{-1}, the high flow setup consisting of a LC pump and a 6-port injector valve (**Figure 6.7**) was

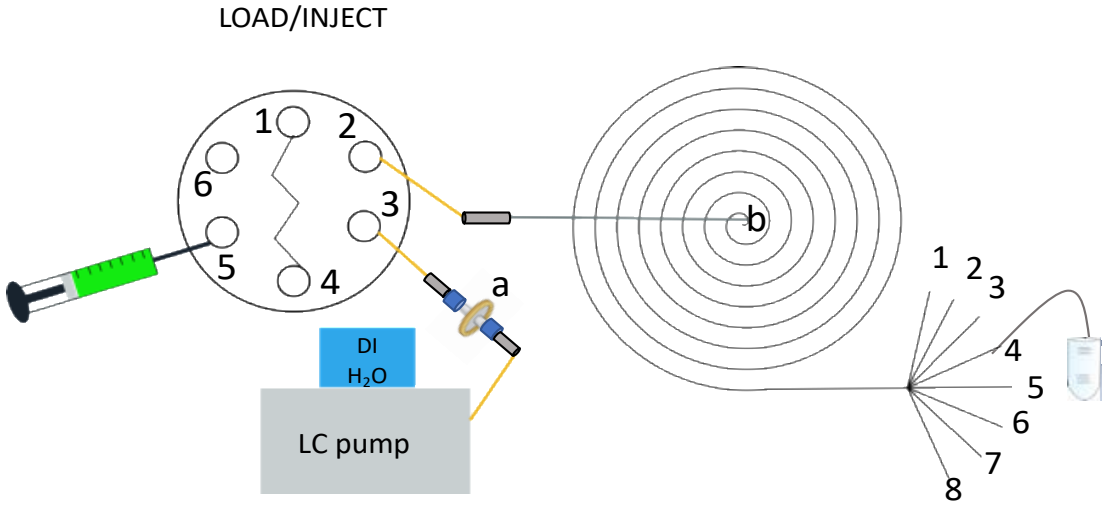

Figure 6.7 A schematic representation of the high flow analytical setup employed for cell sorting prior to SC ICP-MS analysis using the spiral µF chips 1 and 2, operated at flow rates up to 1500 and 300 µL min^{-1} for chip 1 and 2, respectively. A cell suspension is injected through a 6-port load/inject valve while an online filtered de-ionised water carrier flow is supplied through a LC pump. Connection between the LC pump and the valve is achieved at (point a) through a combination of male/female luer lock fittings (blue) and flexible silicone tubing (gray). The cell suspension is loaded into a 500 µL loop (ports 1-4) and is carried to the chip spiral inlet (point b) through a 17 cm (127 µm i.d.) PEEK tubing and a 100 cm (500 µm i.d.) PTFE tubing. The samples resulting from the spiral outlet channels 1-8 are collected into separate Eppendorf tubes using 20 cm (300 µm i.d.) PTFE tubings.

employed instead. **Figure 6.7** provides a schematic representation of the high flow setup used in conjunction with chip 1.

The same setup was also used with chip 2 which contained 6 outlet channels. De-ionized water (18.2 MΩ cm resistivity) was used as a carrier flow, while it was online filtered in order to prevent possible clogging of the μF channels. Connection of the LC pump (Shimadzu 2000xxx) and port-3 of the valve was achieved through the use of PEEK tubing, a 0.4 μM Whatman filter and male/female luer lock connectors, as shown in point a (**Figure 6.7**). Contrary to the low flow setup, the initial cell suspension cannot be constantly infused into the spiral as this would require that the cell suspension be put to flow through the pump's internal plumbing. As the latter would be unwanted, the initial cell suspension was loaded into a 500 μL loop, and injected into the system at a given time through port-2 of the valve. Connection between port-2 and the chip spiral inlet was achieved using a 17 cm PEEK tubing (i.d. 127 μm) and a 100 cm PTFE tubing (i.d. 500 μm), the end of which was connected to a TPE luer connector fitting into the chip spiral inlet. Typically, 1-2 injections were needed in order to collect sufficient sample volume into the eppendorf containers dedicated to collecting samples from the distinct chip outlets. Similarly to the low flow setup, TPE luer connectors were used to interface the chip outlet ports with 20 cm PTFE tubings (300 μm i.d.) in order to collect the samples resulting from the chip outlet channels to the Eppendorf containers. A photograph showing the connections required for the high flow setup is provided in **Figure SI1. 12**.

6.2.3 Cell lines and operating conditions for cell sorting prior to SC ICP-MS

Using the analytical setups described in section 6.2.2, focusing and size-based sorting of 4 different cell types was explored. The cell types included cyanobacteria cells *Synechocystis sp. PCC 6803,* algal cells such as *Chlorella sorokiniana and Chlamydomonas reinhardtii,* as well as murine bone marrow-derived macrophages (BMDMS). The cell size of the aforementioned cell lines was determined from optical microscopy images captured using a 40x lens under an optical microscope (Axiolab 5, Zeiss). Multiple micrographs of each cell line ,as shown in **Figure 6.8**, were processed with ImageJ (National Institutes of Health) in order to determine the average cell diameter, which was found to be 1.64 $\pm$ 0.23 (N=71 cells), 3.76 $\pm$ 0.55 (N=109 cells), 7.34 $\pm$ 1.41 (N=55 cells) and 11.99 $\pm$ 2.59 (N=97 cells) for *Synechocystis sp. PCC 6803, Chlorella sorokiniana, Chlamydomonas reinhardtii* and BMDMS, respectively.

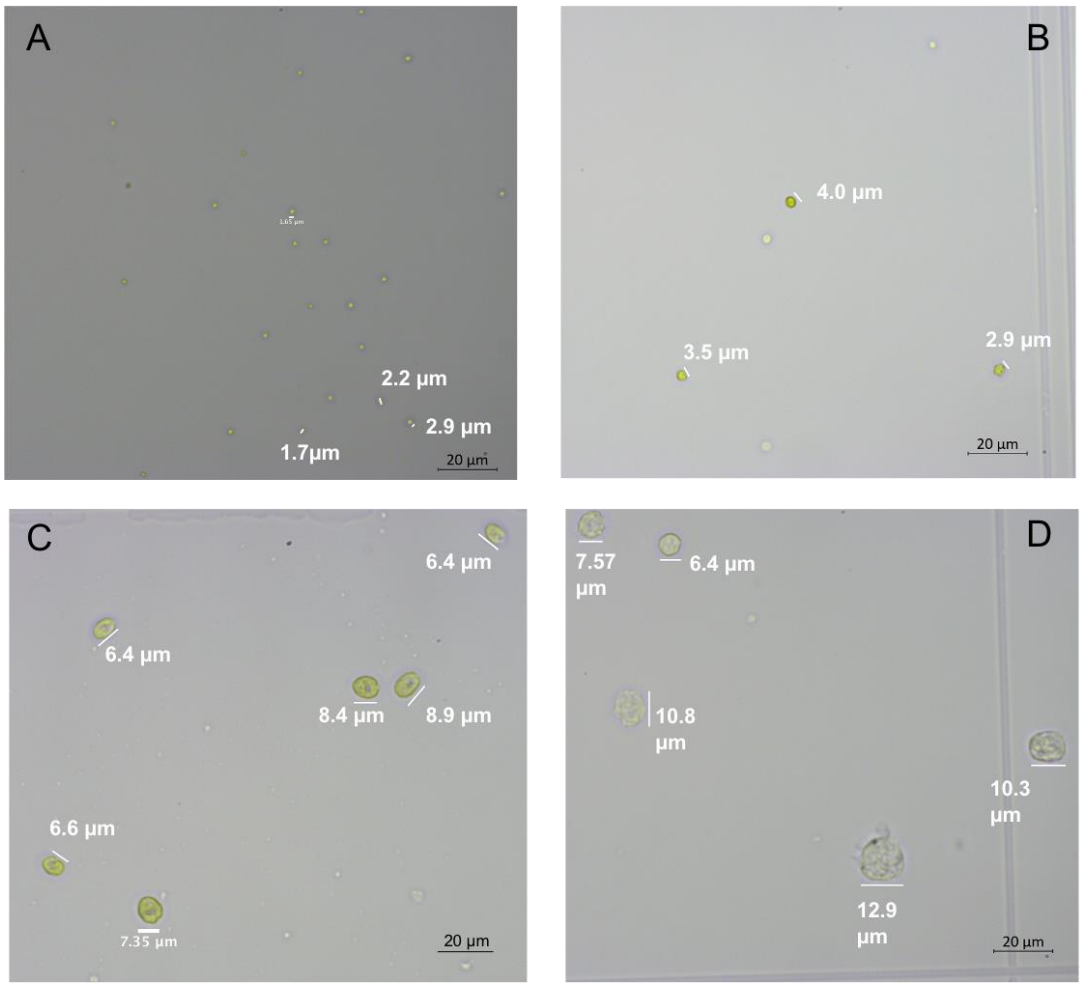

Figure 6.8 Micrographs of *Synechocystis sp. PCC 6803 (A)*, *Chlorella sorokiniana* (B), *Chlamydomonas reinhardtii* (C) *and* bone marrow-derived murine macrophages (BMDMS) (D) captured using a 40X lens under an optical microscope. The micrographs are provided to the same scale in order to demonstrate the increase in cell size from A to D.

Examining a statistically significant number of cells also allowed for the determination of the cell size (diameter) distribution, as shown in **Figure 6.9**. While *Synechocystis, Chlorella* and *C. reinhardtii* cell populations can be fully distinguished, a significant overlap between *C. reinhardtii* and BMDMS populations is observed due to their wider size distributions. This overlap is estimated to be around 34% as both distributions share sizes approximately within 1 σ from the average values which were 7.34 ± 1.41 and 11.99 ± 2.59 for *C. reinhardtii* and BMDMS cell lines, respectively.

In this work, the size-based sorting of cell populations and ultimately separation between different cell lines was not explored in cell suspensions of mixed cell lines. Each cell suspension, consisting of a single cell line, was introduced individually into a spiral chip with

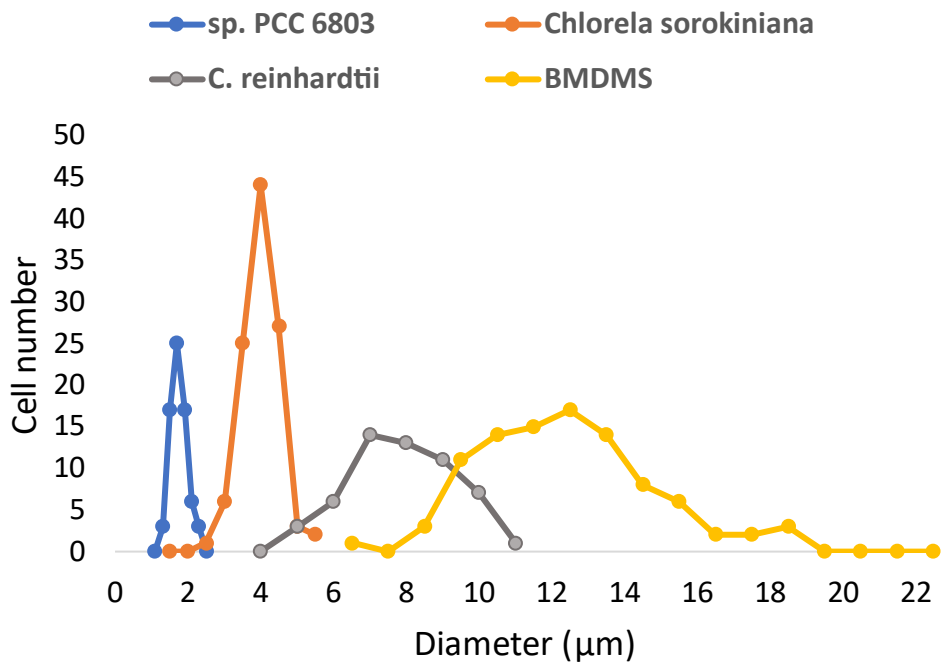

Figure 6.9 Graph illustrating the size distributions of *sp. PCC 6803* (blue), *Chlorella sorokiniana* (orange), *C. reinhardtii* (grey) and BMDMS (yellow) cell lines, as obtained upon measurement of 71, 109, 55 and 97 cell populations of each cell line, respectively.

the aim of producing focused streams of cells, which would result in cell-enriched and cell-clean outlet channels. As a consequence, presented results reporting separation between the 2 cell lines were obtained from 2 individual experiments, each one dedicated to a cell line sorted on the same spiral chip at the same flow rate. However, if 2 individual experiments conducted using the same spiral chip demonstrate 2 cell lines to accumulate at different outlet channels, this may be a good indication that the 2 cell lines can be separated when present in a mixed cell suspension of a sufficiently low cell volume fraction. The cell concentration is critical for optimal focusing behavior and accuracy, as excessive values may result in steric crowding effects. Di Carlo introduced the term of length fraction (λ), for which values >1 would result in steric crowding effects that could disrupt focusing.[13] λ can be determined using the formula:

$$\lambda = \frac{6 \times W \times H \times V_f}{\pi \times \alpha^2} \qquad Eq\ (13)$$

, where W and H stand for the width and height of the rectangular microfluidic channel, respectively, V_f is the volume fraction of cells in the suspension, and α is the particle/cell diameter. It is calculated that λ is below 1 for all cell lines, at the cell concentrations of 10^5-4×10^5 mL^{-1} that cells are sorted. In addition, Martel et al has reported an upper limit in

particle/cell volume fraction of 1-3% above which focusing is disrupted.[1] The cell volume fractions used in this study are below 0.04% at the highest cell concentration of 4×10^5. For instance, for a possible mixture of BMDMs and *C. reinhardtii* at concentrations of 4×10^5 $mL^{-1}$and 10^5 mL^{-1}, respectively, these cell lines account for a total cell volume fraction of 0.037%. All the above provide a strong indication that results obtained from individual sorting experiments on 2 cell lines should be similar to those obtained upon sorting a mixture of these cell lines at the given concentrations.

Focusing and sorting of *C. reinhardtii* cells was studied on all spiral chips under different chip input flow rates (Q), Reynolds number (Re) and Dean number (De), while the rest of the cell lines were studied in comparison to *C. reinhardtii* at equal flow rates. A table compiling the different experiments conducted for all cell lines is provided in **Table 6.2**. In this work, De could only be studied in conjunction to Re number on which De linearly depends on, unlike the work of Martel et al in which the effects of Re and De could be studied separately.[24] In this work, comparisons on the results of these experiments will be mostly discussed with regard to De.

Table 6.2 Conducted cell sorting experiments of cell lines on chips 1, 2, 3 at variable volumetric flow rates (Q), Reynolds number (Re) and Dean number (De).

	Chip 1			Chip 2			Chip 3	
Q ($\mu L\ min^{-1}$)	250	1500	2000	150	250	8	20	65
Re	328	196.7	262.3	34.0	56.6	3.1	7.7	24.9
De	7.8	46.6	62.1	10.2	17.0	0.7	1.8	5.7
Synechocystis	✓					✓	✓	✓
Chlorella		✓	✓	✓	✓		✓	✓
C. reinhardtii	✓	✓	✓	✓	✓		✓	✓
BMDMS	✓	✓						✓

The cell lines were introduced into the spiral chips as dilute cell suspensions. Typically, stock cell cultures of 10^7-10^8 cells μL^{-1} were washed once or twice with a solution, containing 1 mM EDTA, 50 mM Trizma base, 0.1% NaCl, in order to remove the cell culture medium. This step was carried out by centrifuging the cells using an Eppendorf centrifuge (Eppendorf™ Minispin™) for the generation of a cell pellet. The applied RCF varied

depending on the robustness of each cell line, i.e, 4300 rcf (8000 rpm) for *C. reinhardtii* and *Synechocystis* cells, 605 rcf (3000 rpm) for *Chlorella* cells and 151 rcf (1500 rpm) for BMDMs. Upon removal of the culture medium, the pelleted cells were resuspended in 0.1 % NaCl and diluted to a final concentration of 10^4-10^5 cells mL^{-1}. The cell concentration in the final suspension was selected based on the abundance of the acquired cell signals during ICP-MS detection of an unsorted cell suspension. This was required because the nebulization of the larger and more delicate BMDMs cells was less efficient, so a higher concentration of 4×10^5 cells mL^{-1} was used to compared to the rest of the cell lines prepared at, ie., 2×10^4-10^5 for *Synechocystis* and 10^5 cells mL^{-1} for *Chlorella* and *C. reinhardtii* cells.

Sorting of cell suspensions using the analytical setups presented in section 6.2.2 required collection of the sample volume resulting from each outlet channel into Eppendorf tubes. Prior to sample collection, the dead volume of the analytical setups was taken into account in order to avoid diluting the sorted samples. For example, several components of the high flow setup that contributed to the dead volume included a PEEK tubing (2 µL), PTFE tubing (196 µL), spiral channel (4 µL), as well as the soft PTFE tubings (15 µL each) used for transferring the resulting volume to the Eppendorf containers; all of the aforementioned parts accounting for a total of 337 µL as opposed to a 500 µL sample loop. To avoid diluting the sorted samples with the carrier solution, a time delay was considered before initiating sample collection.

For the determination of this time delay, flow rate measurements were conducted for each analytical setup in order to determine the flow rate at the outlet channels. This proved important as the initial flow rate that was provided to the spiral inlet was not split equally amongst the outlet channels, as can been seen from **Table 6.3** for typical flow rates used for the high and low flow setups. Instead, the center outlet channels operated at a higher flow rate than those closer to the inner and outer wall (**Table 6.3**), which can be attributed to the parabolic flow profile at low Re numbers. The time delay before sample collection was

calculated based on the outlet channel that operated at the lowest flow rate. Typical examples for calculating the time delay for the high and low flow setup are provided. For instance, for the high flow setup coupled to chip 1 and operating at 1500 µL min^{-1}, the time delay was calculated as follows: The total dead volume of the PEEK (2 µL), PTFE tubing (196 µL) and spiral (4 µL) will be distributed amongst the outlet channels according to the percentage volume distributed per channel, which is 8.72, 11.41, 16.22, 26.70, 8.50, 8.55, 11.43, 8.46 % for outlet channels 1-8, respectively. The percentage volume can be determined from the measurements of the individual flow rates per channel. Consequently, the absolute dead volume that will be distributed per outlet channel can be determined, and was found to be 17.64, 23.09, 32.84, 54.05, 17.21, 17.32, 23.13 and 17.11 µL for outlet channels 1-8, respectively. Added to each of these values is the 15 µL of a PTFE tubing (used for transferring the sample to the Eppendorf tubes). Because the chip input flow rate

Table 6.3 Flow rate measurements on the individual outlet channels of chip 1, 2 and 3 operating at an input flow rate (Q) of 1500, 150 and 65 µL min^{-1}, respectively.

Q (µL min^{-1})/ outlet channel flow rate (µL min^{-1})	Chip 1 1500 µL min^{-1}	Chip 2 150 µL min^{-1}	Chip 3 65 µL min^{-1}
Outlet ch1	131 µL min^{-1}	21 µL min^{-1}	8 µL min^{-1}
Outlet ch2	171 µL min^{-1}	26 µL min^{-1}	12 µL min^{-1}
Outlet ch3	243 µL min^{-1}	36 µL min^{-1}	17 µL min^{-1}
Outlet ch4	400 µL min^{-1}	29 µL min^{-1}	13 µL min^{-1}
Outlet ch5	127 µL min^{-1}	19 µL min^{-1}	8 µL min^{-1}
Outlet ch6	128 µL min^{-1}	14 µL min^{-1}	6 µL min^{-1}
Outlet ch7	171 µL min^{-1}		
Outlet ch8	127 µL min^{-1}		
Total flow rate [(a)]	1498 µL min^{-1}	145 µL min^{-1}	64 µL min^{-1}

(a) The total flow rate is the sum of the individual flow rates measured per outlet channel, and the slight deviation from the input flow rate (0.13, 3.3, 1.0 % for chip 1, 2 and 3, respectively) reflects the uncertainty of the chip input flow rate provided by the pumps.

(1500 μL min^{-1}) is distributed unequally amongst the outlet channels, each outlet channel will require a different time in order to dispense its dead volume. Therefore, the dispense time required per channel was determined to be 0.24, 0.22, 0.19, 0.17, 0.25, 0.25, 0.22, 0.25 min for outlet channels 1-8, respectively, and sample collection was started 0.25 min (15 s) after the injection. The delay time was based on the slower channel. Considering a 500 μL sample loop, the injection volume collected per Eppendorf tube should be 43, 52, 68, 103, 42, 42, 52, and 42 μL for tubes dedicated to channel outlets 1-8, respectively. Under the operating flow rate of 1500 μL min^{-1}, 0.33 min were required to collect a sorted 500 μL sample loop. The collected sample volume (μL) from outlets 2, 3 and 4 was lower than the 68, 103 and 42 μL min^{-1} calculated above. This is because these outlets were operating at a higher flow rate, thus a few tens of μL were wasted due to the 0.25 min delay. Nevertheless, the collected sample volume was sufficient to be subsequently analyzed with SC ICP-MS. The same procedure for calculating the time delay was followed for all flow conditions and chips operated with the high flow setup.

The dead volume in the low flow setup consists of a soft silicone tubing (15 μL) which connects the syringe needle directly to the inlet of chip 3 (1.08 μL). According to the flow rate measurements (**Table 6.3**), for chip 3 operating at an input flow rate of 65 μL min^{-1}, the calculated percentage volume distributed per outlet channel is 12.9, 18.9, 26.7, 19.8, 12.2, 9.5 %. It follows that the absolute dead volume distributed per outlet channel is 2.08, 3.03, 4.29, 3.18, 1.96 and 1.53 μL, and added to each of these values is the 15 μL of a PTFE tubing (used for transferring the sample to the Eppendorf tubes). Consequently, the dispense time for the dead volume per channel was calculated to be 2.07, 1.50, 1.13, 1.44, 2.19 and 2.73 min for outlet channels 1-6, respectively. By considering a delay of 2.73 min and a chip input flow rate of 65 μL min^{-1}, 174 μL were dispensed from a 500 μL sample loaded syringe before sample collection was started. Out of a 500 μL sample loaded syringe, 59, 79, 106, 83, 57 and 47 μL were collected to Eppendorf tubes dedicated for outlet channels 1-6, respectively. The collected sample volume (μL) from outlets 1, 2, 3, 4 and 5 was lower than expected because these outlets were operating at a higher flow rate, thus a few tens of μL were wasted due to the 2.73 min delay.

6.2.4 Analysis of sorted samples using SC ICP-MS

The samples that were collected in Eppendorf tubes, as described in the previous sections, were subsequently analyzed using SC ICP-MS. Sample introduction into the ICP-

MS was carried out using a highly efficient cell nebulization system (discussed in previous chapters), which consisted of the Asperon spray chamber (Perkin Elmer) and a high-efficiency glass nebulizer (HEN-90-A0.2, Meinhard). The HEN nebulizer was operated at 0.35 L min^{-1} Ar gas, while a makeup flow of 0.65 L min^{-1} Ar was also supplied to the Asperon spray chamber for a total input of 1 L min^{-1} Ar into the ICP. At 0.35 L min^{-1} of nebulizer gas, sample introduction was performed in self-aspiration mode at a sample uptake rate of 45 µL min^{-1}. Cell detection was achieved by monitoring phosphorus, as an intrinsic cell element, in the form of $^{48}PO^{+}$ in DRC mode (Dynamic Reaction Cell) by introducing 0.3-0.35 mL min^{-1} oxygen (O_2) into the collision cell. In addition, the ICP-MS was operated in Time-resolved analysis mode using a 10 ms dwell time. Under these operating conditions, a 40 µL sample volume was sufficient to produce a 50 s ICP-MS signal which could either show a steady $^{48}PO^{+}$ background intensity (dissolved phosphorus) and thus indicate a cell-free outlet, or reveal pulses in the recorded $^{48}PO^{+}$ intensity (cell detection) and thus indicate a cell-enriched outlet.

6.3 Results and Discussion

6.3.1 SC ICP-MS analysis of *C. reinhardtii* cells sorted using µF chip1

C. reinhardtii was selected as a model organism in order to investigate the effect of hydrodynamic forces on a cell population, with an average size of 7.3 µm, when it is subjected to flow within spiral microfluidic channels of different cross-section and spiral length. Therefore, *C. reinhardtii* cell populations were studied on chips 1, 2 and 3 at increasing flow rates, and Dean numbers (De).

Figure 6.10 demonstrates time-resolved acquisitions that were obtained from SC ICP-MS analysis of samples collected from outlet channels 1-8 (Outlet ch1-Outlet ch8) after a *C. reinhardtii* cell suspension, containing 10^5 cells mL^{-1}, was introduced into chip 1 at an input flow rate (Q) of 250 µL min^{-1} and a Dean number (De) of 7.8.

Prior to the analysis of each outlet, a 0.1% NaCl solution was introduced into the ICP as a blank for approximately 0-40 s, resulting in a $^{47}PO^{+}$ intensity of approximately 30 counts 10 ms^{-1} (**Figure SI1. 13**). Between 40-100 s, the recorded signal reflects the introduction of outlet samples from outlet channels 1-8. It can be observed that the majority of outlet channels produce a cell-free acquisition, while the frequent presence of signal pulses in outlets ch2 and ch3 reveals the formation of a focused *C. reinhardtii* cell stream which can be collected from outlet channels 2 and 3.

SC ICP-MS data processing allows for differentiating the background intensity from the pulses corresponding to cell events. Therefore, processing of the 40-100 s segment of signal in the time-resolved acquisitions (**Figure 6.10**) will allow for cell counting, and in turn determination of the number distribution of the cell population across the 1-8 outlet channels. The results obtained from SC ICP-MS data processing are illustrated in **Figure 6.11**, in which the number of cells determined per channel is expressed as a relative percent of the total number of cells determined from all outlet channels. More specifically, 70% of the cell population was collected from outlet channel 2, while another 20% was collected from outlet

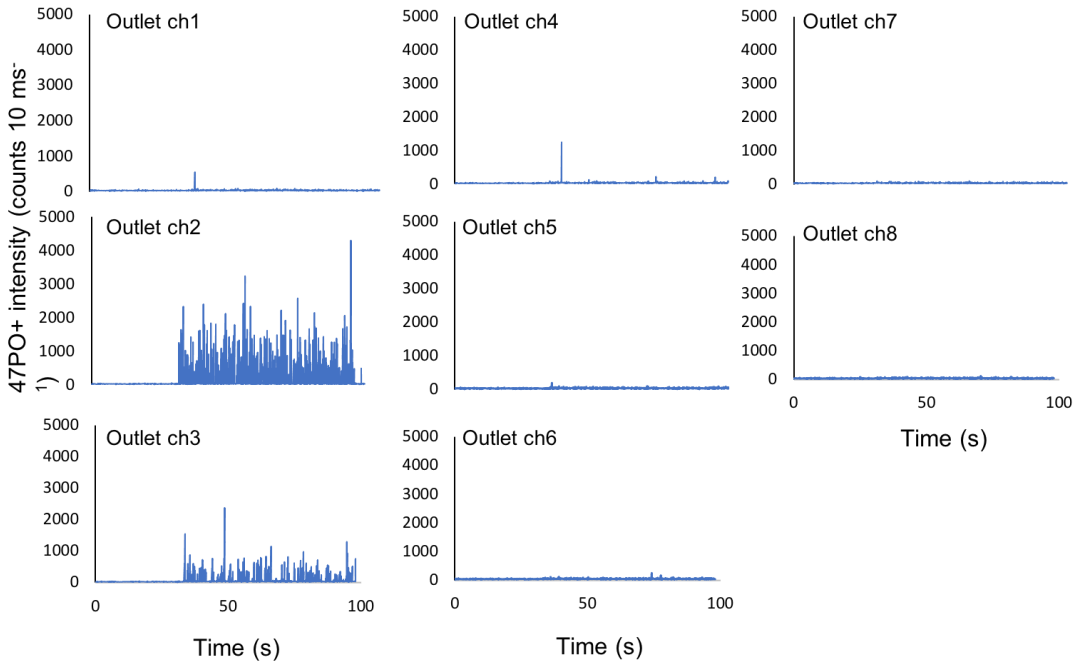

Figure 6.10 Time-resolved acquisitions obtained from SC ICP-MS analysis of samples collected from outlet channels 1-8 (outlet ch1-8) of chip 1, after a *C. reinhardtii* cell suspension was introduced at a chip input flow rate (Q) of 250 µL min^{-1} and 7.8 De. $^{47}PO^{+}$ was monitored using a dwell time of 10 ms, while *C. reinhardtii* cells were introduced at a concentration of 10^5 mL^{-1}.

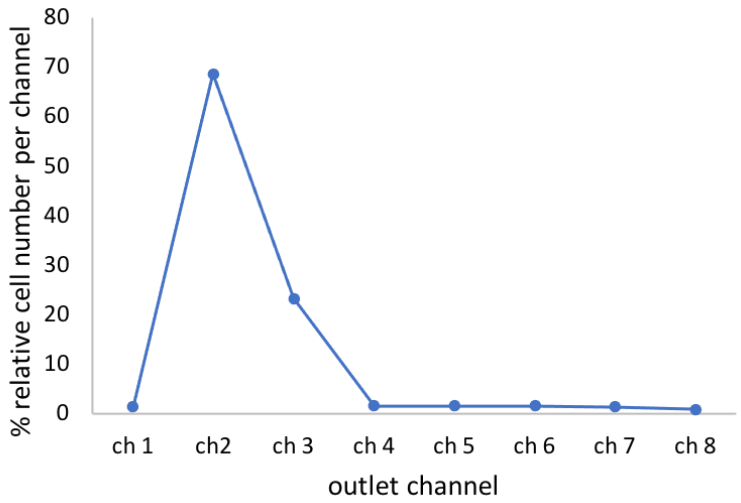

Figure 6.11 Graph illustrating the number distribution of *C. reinhardtii* cell population across the outlet channels 1-8 of spiral chip 1, operated at an input flow rate of 250 µL min^{-1} and 7.8 De. The number of cells detected per outlet channel has been normalized to the total number of cells detected from all outlet channels, and therefore it is expressed as % relative cell number per channel. *C. reinhardtii* cells were introduced at a concentration of 10^5 mL^{-1}.

channel 3. This indicates that *C. reinhardtii* cells, which were randomly dispersed in the initial suspension, produced a focused stream by the end of their course through the spiral µF channel. The width of the produced cell stream spanned from oulet 2 to 3, resulting in 2 cell-enriched outlet channels. The degree of focusing for *C. reinhardtii* under this flow condition (250 µL min^{-1}, 7.8 De) was taken at channel 2 which exhibited maximum cell focusing, i.e., 70% of the entire cell population.

SC ICP-MS analysis is not limited to cell counting, but also allows for metal quantitation per individual cell. Phosphorus (P) is an intrinsic element to the cells, largely present as a phosphate group in chemical compounds including DNA, RNA, ATP and phospholipids. In terms of this, a cell-to-cell variation in phosphorus content may also reflect cell size variation, granted that a larger cell requires higher phosphorus amounts to sustain its life cycle. In this study, absolute phosphorus amounts per cell were not determined. However, by principle, the ICP-MS $^{47}PO^+$ intensity recorded for each cell event is proportional to the P mass per cell which can be related to cell volume providing that the P concentration is equal for all cells. If the latter is true, a linear correlation between cell intensity and cell volume is expected.

Figure 6.12 demonstrates the correlation of the registered $^{47}PO^{+}$ intensity per cell with the cell volume for *C. reinhardtii* (panel A) and BMDMS (panel B) cell lines. The procedure to construct panel A and B diagrams has been introduced by Lau et al who used elemental Mg as an indicator to reveal cell size variation in *Chlorella vulgaris* cell populations.[33] Briefly,

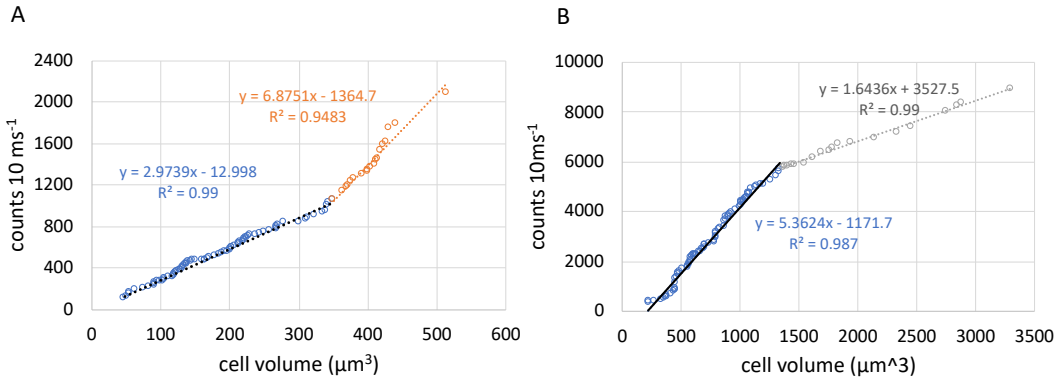

Figure 6.12 Diagrams demonstrating how the $^{47}PO^{+}$ intensity registered per cell (obtained from SC ICP-MS analysis of *C. reinhardtii* and BMDMS cell suspensions) correlates with cell volume (obtained from optical microscopy) for *C. reinhardtii* (panel A) and BMDMS (panel B) cell lines. Cell intensity and volume datasets were ranked in percentiles, and the diagrams illustrate the relationship for equivalent percentiles of the cell intensity and cell volume. The blue and orange slopes (Panel A) were obtained from the linear regression of 2-79% and 79-97% percentile ranges, respectively, while the blue and gray slopes (panel B) from 1-80% and 81-99% percentile ranges, respectively.

---

cell intensity data (counts 10 ms^{-1}) were obtained from the analysis of *C. reinhardtii* and BMDMS cell populations using SC ICP-MS, while cell volume data (μm^3) were calculated, with the assumption of sphericity, from the cell diameters obtained using optical microscopy. Subsequently, the cell intensity and volume data were sorted in ascending order, and ranked in percentiles with increments of 1%. The diagrams in panel A and B illustrate the relationship for equivalent percentiles of the cell intensity and cell volume. It is apparent from **Figure 6.12**A and B that the linear dependence of cell intensity on cell volume can be described by 2 linear ranges. More specifically, cell intensity for *C. reinhardtii* increases linearly as a function of cell volume within a 1st range of 50-350 μm^3 (corresponding to cell diameters of 4.5-9.1 µm), and demonstrates a slope of 2.97 counts μm^3. A 2nd linear range can be observed within 350-500 μm^3, demonstrating a higher slope of 6.87 counts μm^3. The difference in the observed slopes may be attributed to the insufficient linear dynamic range of the detector in pulse-counting mode, receiving instantaneous ion count rates (expressed in counts s^{-1}) from cell detection events above the pulse counting limit of 2×10^6 cps. Olesik

et al and Lee et al demonstrated that the cap count rate (2×10^6 cps) of the ICP-MS detector, when operating in pulse mode, can easily be exceeded when transient signals from single particles are measured as opposed to those from dissolved ions.[34,35] This is attributed to the transient nature of single particle signals which yield high ion count rates across their short signal duration (hundreds of µs), even if a dwell time longer than the particle's signal duration is used. As a consequence of the high ion count rates registered from the detection of NP signals, a limited linear range for NP size determination has been reported when pulse-counting detector mode is employed. In addition, SC ICP-MS analysis of *C. reinhardtii* cell suspensions using a 75 µs dwell time was used to investigate the profile of the *C. reinhardtii* detection events, revealing an average duration of 1.3 ms for a $^{47}PO^+$ cell detection event. This average duration corresponded to 18 individual intensity data points (75 µs spent for each intensity data point) which were summed to yield an integrated intensity. It was revealed that the cell detection events with integrated intensities above 600 counts were found to yield ion count rates $>2\times10^6$ cps (cap of pulse counting mode for NexION 350X) at intensity data points (d.ps) close to the peak apex. With increasing integrated intensity (>900 counts), the number of d.ps exceeding the pulse counting limit increased, as well as the count rates. Because the established relationship of cell intensity vs cell volume using 10 ms was similar to that of 75 µs, i.e., the cell volume range described by the 2nd slope was 50-350 and 50-400 µm^3 for 10 ms and 75 µs, respectively, it is likely that the cell detection events corresponding to the orange slope (**Figure 6.12**A) were captured by employing the analog mode of the detector. While SC ICP-MS detection of *C. reinhardtii* cells was carried out in dual detector mode, theoretically allowing for a wide linear detection range up to10^9 cps (for NexION 350 X), it may be possible that pulse and analog response were not subjected to a cross-calibration prior to these experiments; thus, explaining the change in the observed linear response in **Figure 6.12**A. Further experiments are required to test the validity of the aforementioned conclusion. However, limited linear range, even though dual detector mode was employed, has also been reported in the determination of Au NPs using SP ICP-MS. Liu et al established a linear response for Au across a range of Au NP sizes up to 70 nm (corresponding to 1000 Au counts per particle), while deviation from linearity was observed for NP sizes above the reported limits. A good linear correlation between cell intensity and cell volume is also observed for the larger BMDMS cells (**Figure 6.12**B). The blue slope (**Figure 6.12**B) representing BMDMS cells within 250-1250 µm^3 suggests that the analog mode was employed throughout the reported

volume range, as the lower range limit of cell volume of this slope (**Figure 6.12**B) coincides with the upper range limit of the blue slope (**Figure 6.12**A) (250-350 μm^3) above which the analog mode was employed to register *C. reinhardtii* cell events. A 2nd decreased slope (**Figure 6.12**B) is observed when 1250 μm^3 are exceeded. This decrease could be due to incomplete cell vaporization in the plasma or local plasma cooling, leading to a lower cell response. A similar behavior has been observed for µm-sized SiO_2 particles.[34] However, both diagrams in panels A and B demonstrate a satisfactory correlation between cell intensity and cell volume, thus suggesting that higher $^{47}PO^+$ intensities are linked to bigger cell sizes.

Therefore, the $^{47}PO^+$ intensity of cell events can be used to provide evidence of cell size variation amongst cells collected from individual outlets, considering that *C. reinhardtii* exhibit a wide size distribution with cell diameters spreading from 4 to 11 µm. In order to investigate the possibility that cells of specific sizes exit from different outlet channels, cells were binned according to their recorded $^{47}PO^+$ intensities. This allowed for constructing a heat map linking $^{47}PO^+$ intensity with the cell number detected per outlet channel.

More specifically, it can be observed from **Figure 6.13** that the majority of the cells are accumulated in channel 2, and exhibit intensities ranging from 200 to 1600 counts 10 ms^{-1}, with the most frequent intensities in the region of 400-800 counts 10 ms^{-1}. Channel 3 shares considerable cell numbers only within the 200-800 counts 10 ms^{-1} range. However, the appearance of a significant number of cells within the 1000 to 1600 counts 10 ms^{-1} range exclusively in channel 2 indicates the tendency of the larger cell sizes to equilibrate closer to the inner wall of the spiral channel. These observations suggest that the initial *C. reinhardtii* cell population was, to a certain extent, subjected to sorting based on cell size, as outlet ch3 was found to contain the low to middle range recorded cell intensities (400-800 counts 10 ms^{-1}). As the most frequent intensity of the cell population was found at 600 counts 10 ms^{-1}, most possibly reflecting the average and most frequent cell diameter (7.34 µm as seen from **Figure 6.9**), this would suggest that ch3 most possibly contained cell sizes within the left half of the *C. reinhardtii* size distribution.

For the following experiments that will be discussed in this dissertation, time-resolved acquisitions such as those in **Figure 6.10** will be provided in the Supporting information.

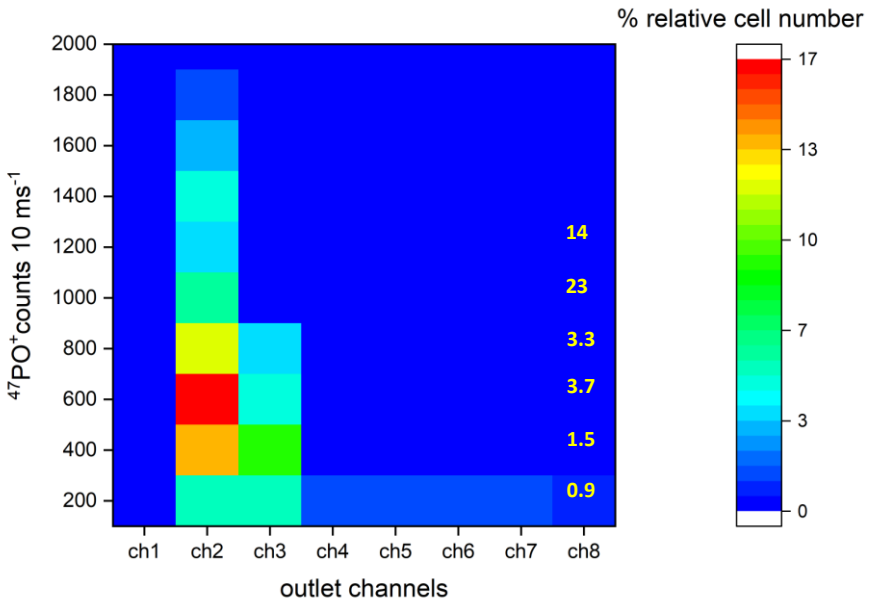

Figure 6.13 Heat map illustrating the distribution of *C. reinhardtii* cells with respect to their recorded $^{47}PO^{+}$ intensity across outlet channels 1-8 of chip 1, operated at an input flow rate of 250 µL min^{-1} or 11.2 De. The y and x-axis show the recorded $^{47}PO^{+}$ intensity per cell event in counts per 10 ms^{-1} and the number of outlet channels, respectively, while the z-axis indicates the number of cells (expressed as a percentage of the total number of cells detected) showing a specific intensity. Cell events were arranged in intensity bins of 200 counts 10 ms^{-1} which are illustrated as colored squares (varying from blue to red with increasing % relative cell number) in this heatmap. Cell numbers from equivalent intensity bins obtained from ch2 and ch3 are compared, and the resulting ratio of ch2 over ch3 (yellow values) is provided in the right-hand side of this chart for each pair of intensity bins (200-1200 counts per 10 ms^{-1}).

Focusing and sorting of *C. reinhardtii* cells on chip 1 was also explored for higher flow rates and De, and results are provided comparatively for all 3 flow conditions tested (**Figure 6.14**). A right shift of the distribution can be observed with the application of higher De, as evidenced by the relocation of the maximum of the distribution from channel 2 at 11.2 De to channel 4 at 69.9 or 93.2 De. This suggests that, with increasing De, the cells are subjected to a higher Dean drag force (F_{dean}) which transposes the focused cell stream to a position farther from the inner wall. This finding is in agreement with Kuntaegowdanahalli et al who observed that streams of 10, 15 and 20 µm particles, initially focused near the inner wall, started to move away from the inner wall above a critical De; therefore, indicating the dominance of F_{dean} over the shear-gradient force (F_{shear}) or net lift force F_L.[11] The net lift force, when dominant, would cause particle focusing at positions, closer to the inner wall .

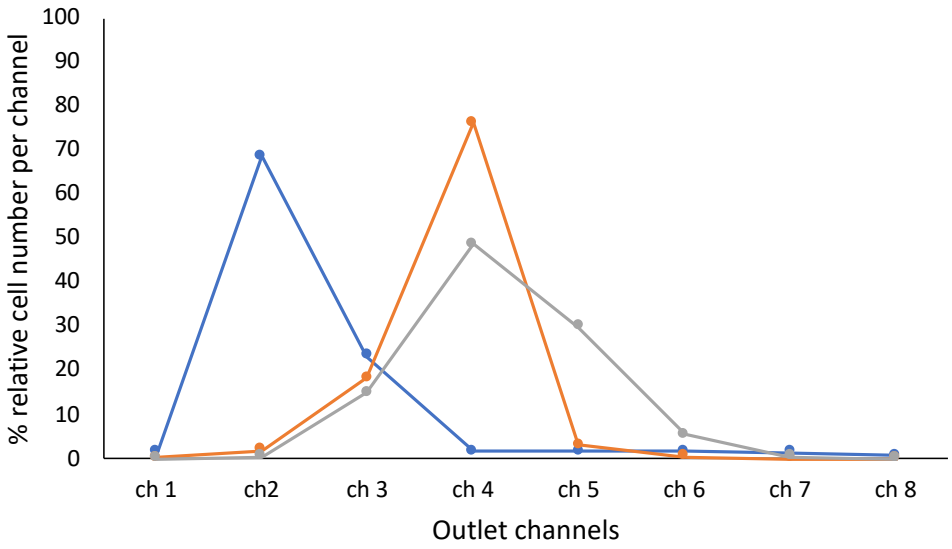

Figure 6.14 Graph illustrating the distribution of *C. reinhardtii* cell population across the outlet channels 1-8 of spiral chip 1, operated at chip input flow rates of 250 (blue), 1500 (orange)and 2000 (gray) μL min^{-1} which correspond to 11.2, 69.9 and 93.2 De, respectively. The number of cells detected per outlet channel has been normalized to the total number of cells detected from all outlet channels, and therefore it is expressed as % relative cell number per channel. The cell concentration was kept at 10^5 mL^{-1} for all flow conditions.

A similar observation was made by Russom et al who observed the lateral displacement of a focused stream of 7 and 10 μm particles away from the inner wall with increasing Re and thus De.[23] Increasing De from 11.2 to 69.9 increased the cell focusing efficiency from approximately 70% to 80%, as determined for outlet ch 2 and 4 at De 11.2 and 69.9, respectively. In addition, the distributions maintained the same width, both spreading across 2 cell-enriched outlets, i.e., ch2-ch3 and ch3-ch4 for De 7.8 and 69.9, respectively. A further increase to 93.2 De is observed to decrease the focusing efficiency to approximately 50%, noted at outlet ch4, and simultaneously increase the width of the distribution, now spanning from ch3 and ch6. Therefore, at this flow rate, the developed Dean flow field disrupts cell focusing by widening the produced cell stream across the channel width, which results in 2 additional cell-enriched outlet channels. This observation fits well with studies reporting particle defocusing above a critical De. [23,26]

In both of their studies, Rusom et al and Kuntaegowdanahalli et al attribute particle focusing near the inner wall of the μF channel to the dominance of F_{shear}(or expressed as lift force F_L) over F_{dean}. In addition, it has been mentioned that particle focusing in low aspect ratio curved μF channels (height-to-width, h/w <1) is determined by the ratio of particle diameter (α) to channel height, α/h. For particles to focus, a/h values greater than 0.07 and 0.1 have

been reported by Kuntaegowdanahalli et al and Rusom et al, respectively. In this work, an a/h value of 0.09 is calculated for *C. reinhadtii* cells flowing through chip 1, considering an average cell diameter (7.3 μm) and the cross-section of chip 1 (300, 80 μm width and height, respectively); thus, meeting the criterion reported in the literature. However, the dominance of F_{shear} over F_{dean} is not mathematically observed for any of the 3 flow rate conditions studied in this work, but rather the inverse. Using $Eq.4$ and $Eq.11$ to calculate F_{shear} and $F_{dean,}$ we report values of 1.1× 10^{-11} N and 3.5× 10^{-10} N at 7.8 De (250 μL min^{-1}) for the F_{shear} and F_{dean}, respectively, indicating the dominance of F_{dean},, already from the low 7.8 De. Although Kuntaegowdanahalli et al do not demonstrate a theoretical calculation for F_{shear} and F_{dean} in their study, a typical calculation was conducted in this work for the sake of comparing their system with the present *C. reinhardtii*-chip1 system. By using the geometrical characteristics of the Archimedean spiral (500, 90-140 μm width, height and 1 cm innermost radius) and subsequently using $Eq4$ and $Eq.11$, it is highly unlikely that F_{shear} acting on 10 μm particles is greater over F_{dean} across the range of the applied De. This implies that focusing near the inner wall may not necessarily require the dominance of F_{shear} over F_{dean}, but may rather be determined by a certain ratio of F_{shear} over F_{dean} acting on particles. Di Carlo argued that different inertial force ratios (F_{shear}/ F_{dean}, R_f) may lead to different particle focusing positions along the channel width, while a R_f threshold of 0.04 was proposed in order for particle focusing to occur within rectangular and continuously curving microfluidic channels.[16][13] However, he pointed out to the complexity of the behavior of these forces, and that the accuracy of the proposed criterion required further experiments. For the present *C. reinhardtii* - chip 1 system, R_f ratios are calculated to be 0.018, 0.035 and 0.039 at 11.2, 69.9 and 93.2 De (250, 1500, 2000 μL min^{-1}), respectively. These values reveal a tendency of F_{shear} to increase with increasing De, which is contradicting to the argument for the dominance of the dean drag force (F_{dean}) over the lift force (F_{shear}) with increasing De. An explanation to this phenomenon was offered by the group of Papautsky, who although argued that F_{shear} should increase with greater flow velocities (and thus De), greater flow velocities decrease the lift coefficient (f_{lift}, related to F_{shear}), and thus result in the decreased values of F_{shear} [11,19]. f_{lift} was reported to scale as ~$-Re^{0.5}$.

Upon binning the cell detection events in 200 counts 10 ms^{-1} intensity bins, heat maps linking $^{47}PO^{+}$ intensity with the number of cells detected per channel are provided in **Figure 6.15** and **Figure 6.16** for *C. reinhardtii* sorted at flow rates of 1500 and 2000 μL min^{-1} (corresponding to 69.9 and 93.2 De, respectively). It has to be mentioned that the cell

intensities illustrated in **Figure 6.13** (11.2 De) cannot be directly compared with those in **Figure 6.15** (69.9 De) and **Figure 6.16** (93.2 De), as the cells introduced at 11.2 De had previously been washed twice with an EDTA solution compared to the cells at the larger De, previously washed once with EDTA. Thus, slight differences in the $^{47}PO^{+}$ cell response may be expected, especially for cells within the low end of the size distribution. This is because a double washing step could result in a lower background signal due to the lower concentration of dissolved P species, thus allowing for a lower limit of detection. Evidence of the higher background signal recorded for $^{47}PO^{+}$ can be observed in **Figure SI1. 14**showing the dissolved signal (red baseline) for *C. reinhardtii* cells introduced at 69.9 De (500 counts 10 ms^{-1}) and 93.2 De (283 counts 10 ms^{-1}), respectively, as opposed to *C. reinhardtii* introduced at 11.2 De (34 counts 10 ms^{-1}). The difference in the dissolved intensity between 69.9 and 93.2 De could be attributed to the fact that these 2 individual

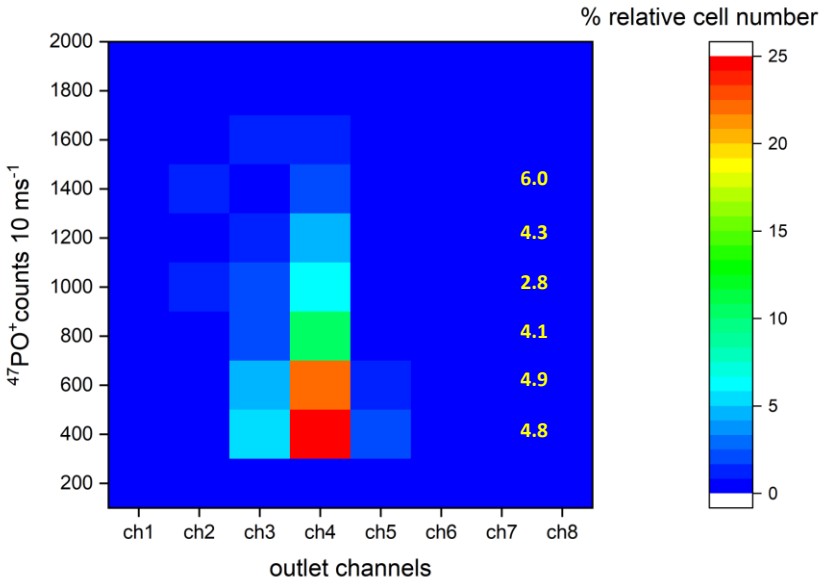

Figure 6.15 Heat map illustrating the distribution of *C. reinhardtii* cells with respect to their recorded $^{47}PO^{+}$ intensity across outlet channels 1-8 of chip 1, operated at an input flow rate of 1500 µL min^{-1} or 69.9 De. The y and x-axis show the recorded $^{47}PO^{+}$ intensity per cell event in counts per 10 ms^{-1} and the number of outlet channels, respectively, while the z-axis indicates the number of cells (expressed as a percentage of the total number of cells detected) showing a specific intensity. Cell events were arranged in intensity bins of 200 counts 10 ms^{-1} which are illustrated as colored squares (varying from blue to red with increasing % relative cell number) in this heatmap. Cell numbers from equivalent intensity bins obtained from ch3 and ch4 are compared, and the resulting ratio of ch4 over ch3 (yellow values) is provided in the right-hand side of this chart for each pair (ch4/ch3) of intensity bins (400-1400 counts per 10 ms^{-1}).

experiments were conducted on different analytical days. Hence, instrumental response, background levels prior to sample analysis and sample preparation errors could have contributed to the observed differences.

From the distribution of the detected cell intensities illustrated in **Figure 6.15** for *C. reinhardtii* introduced at 69.9 De, it can be observed that the majority of the detected cells are accumulated in outlet ch4, and exhibit intensities ranging from 400 to1400 counts 10 ms^{-1}, with the most frequent intensities in the region of 400-600 counts 10 ms^{-1}. In addition, ch3 demonstrates a similar intensity distribution pattern to ch4, i.e., cell detection events within 400-1200 counts 10 ms^{-1}, but shares considerably lower percentages of the cell population. This is supported by the ratio of cell numbers obtained from ch4 over those obtained from ch3 for equivalent intensity bins (yellow values, **Figure 6.15**) It can be observed that this ratio stays relatively constant for a relatively wide range of cell intensities (400-1200 counts 10 ms^{-1}), thus indicating that ch3 accumulated a similar array of cell sizes

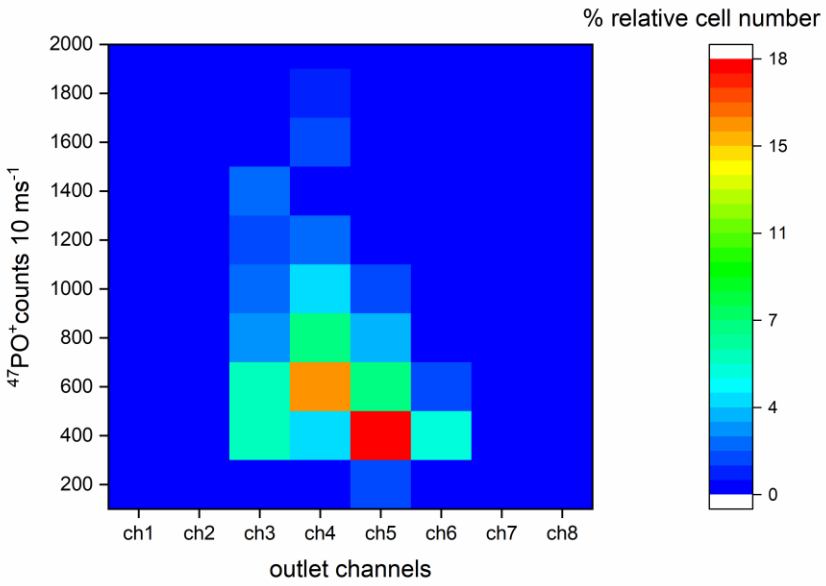

Figure 6.16 Heat map illustrating the distribution of *C. reinhardtii* cells with respect to their recorded $^{47}PO^{+}$ intensity across outlet channels 1-8 of chip 1, operated at an input flow rate of 2000 µL min^{-1} or 93.2 De. The y and x-axis show the recorded $^{47}PO^{+}$ intensity per cell event in counts per 10 ms^{-1} and the number of outlet channels, respectively, while the z-axis indicates the number of cells (expressed as a percentage of the total number of cells detected) showing a specific intensity. Cell events were arranged in intensity bins of 200 counts 10 ms^{-1} which are illustrated as colored squares (varying from blue to red with increasing % relative cell number) in this heatmap.

as ch4, but in lower abundance. Therefore, minimal occurrence of cell size discrimination can be observed between the 2 outlet channels. This obtained size distribution pattern for cells collected from outlets ch3-ch4 at 69.9 De (1500 µL min^{-1}) is quite different compared to that obtained for cells collected from ch2-ch3 at the lower 11.2 De (250 µL min^{-1}) where size-based sorting within the cell population was observed. The latter was supported by the fact that ch3 was found to contain only a portion of the cell size distribution, i.e., cell events within the low to medium $^{47}PO_4^+$intensity range compared to ch2 which covered a broad range of cell intensities (200-1800 counts 10 ms^{-1}). Supporting this observation is the significantly greater variation of the ratio of cell numbers obtained from ch2 over those obtained from ch3 for equivalent intensity bins at 11.2 De (yellow values, **Figure 6.13**) as opposed to the ratio of ch4 over ch3 corresponding to 69.9 De (yellow values, **Figure 6.15**).

Focusing of *C. reinhardtii* was disrupted at the higher De of 93.2, resulting in the dispersion of the cell population across outlets ch3-ch6 (**Figure 6.16**).

These results could prove significant for separations between *C. reinhardtii* and cell lines of higher sizes, as the accumulation of *C. reinhardtii* at the center outlets ch3-ch4 will possibly allow for the collection of a larger-sized cell line from the inner wall outlets 1, 2 as a consequence of a higher F_{shear} acting on the larger cells.

6.3.2 SC ICP-MS analysis of *C. reinhardtii* cells sorted using µF chip 2

Sorting of *C. reinhardtii* was explored on chip 2 containing channels of smaller cross-section (150 ×70 µm width×height). Unlike chip1, the smaller cross-section of chip 2 did not allow for the use of flow rates in the range of mL min^{-1}, as the interface connecting the liquid flow to the chip inlet could not sustain backpressures corresponding to flow rates above 250 µL min^{-1}. Sorting experiments were thus carried out using the high flow setup at 150 and 250 µL min^{-1} corresponding to 10.2 and 17.0 De, respectively.

Figure SI1. 15 and **Figure SI1. 16** demonstrate time-resolved acquisitions that were obtained from SC ICP-MS analysis of samples collected from outlet channels 1-6 (ch1-ch6) after a *C. reinhardtii* cell suspension, containing 10^5 cells mL^{-1}, was introduced into chip 2 at input flow rates (Q) of 150 (10.2 De) or 250 µL min^{-1} (17.0 De). The time-resolved acquisitions were very similar for both flow rate conditions, although slightly better focusing can be observed at the lower 10.2 De. An additional difference between the 2 sets of time-resolved acquisitions can be observed in the $^{47}PO^+$ background intensity (corresponding to the dissolved P species in the cell suspension) which was 150 and 300 counts 10 ms^{-1} at

10.2 and 17.0 De, respectively. As the same initial cell suspension was used for both of these experiments, the time difference between the 2 experiments could have resulted in a loss of viable cells and hence to an increase in the dissolved P levels.

The distributions of the sorted *C. reinhardtii* cells at 150 μL min^{-1} (10.2 De) and 250 μL min^{-1} (17.0 De) across outlets ch1-ch6 of chip 2 are shown in **Figure 6.17**. It is apparent that the accumulation of approximately 80 % of the cell population in ch2 indicates a high degree of cell focusing. This was expected as the present *C. reinhardtii* - chip 2 system meets an α/h value of 0.104 considering an average cell diameter of 7.3 μm and the cross-section of chip 2 (150, 70 μm width and height, respectively). This α/h value agrees with the proposed 0.07 and 0.1 values for which particle focusing was observed. The widths of the distributions are extremely narrow, as 80% of the cell population focused at ch2 while ch1 and ch3 shared the remaining 20 % of the cell population.

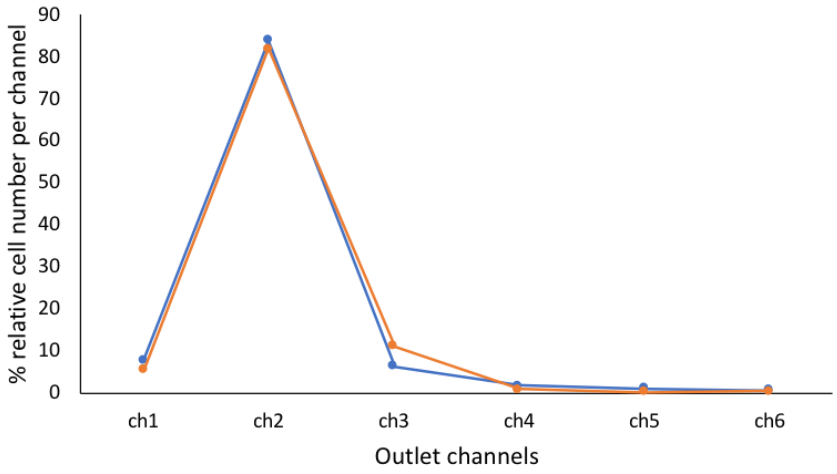

Figure 6.17 Graph illustrating the distribution of *C. reinhardtii* cell population across the outlet channels 1-6 of spiral chip 2, operated at chip input flow rates of 150 (blue) and 250 (orange) μL min^{-1} which correspond to 10.2 and 17.0 De, respectively. The number of cells detected per outlet channel has been normalized to the total number of cells detected from all outlet channels, and therefore it is expressed as % relative cell number per channel. The cell concentration was kept at 10^5 mL^{-1} for all flow conditions.

From the distribution of the recorded cell intensities illustrated in **Figure 6.18** for *C. reinhardtii* sorted at 10.2 and 17.0 De, a very similar sorting pattern can be obtained for both flow rate conditions. Almost the entirety of the introduced cell population was accumulated

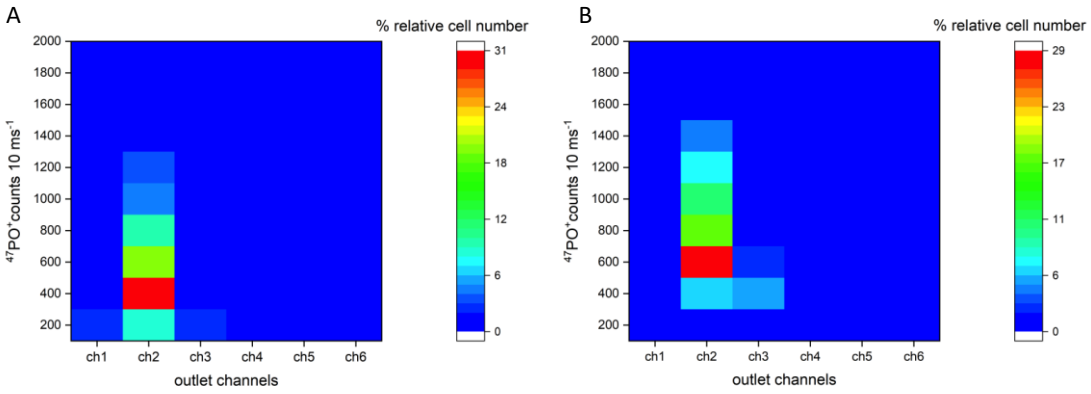

Figure 6.18 Heatmaps illustrating the distribution of *C. reinhardtii* cells with respect to their recorded $^{47}PO^{+}$ intensity across outlet channels 1-6 of spiral chip 2, operated at chip input flow rates of 150 (A) and 250 (B) µL min^{-1} (corresponding to 10.2 and 17.0 De, respectively). The y and x-axis show the recorded $^{47}PO^{+}$ intensity per cell event in counts per 10 ms^{-1} and the number of outlet channels, respectively, while the z-axis indicates the number of cells (expressed as a percentage of the total number of cells detected) showing a specific intensity. Cell events were arranged in intensity bins of 200 counts 10 ms^{-1} which are illustrated as colored squares (varying from blue to red with increasing % relative cell number) in this heatmap.

in ch2 with intensities ranging from 200-1200 and 400-1400 counts 10 ms^{-1} for 10.2 and 17.0 De, respectively. The elevated $^{47}PO^{+}$ background intensity recorded from the analysis of cells sorted at 17.0 De (300 counts 10 ms^{-1}) as opposed to 10.2 De (150 counts 10 ms^{-1}) resulted in an elevated LOD, thus preventing the detection of cell sizes at the low 200 count range. Collection of a minor proportion of the cell population from ch3 indicates a slightly higher degree of focusing for cells sorted at 10.2 De as opposed to 17.0 De. This small proportion of the cell population, contained in ch3 (closer to the outer wall), had the lowest detected intensities recorded for *C. reinhardtii* at 17.0 De, thus corresponding to the lowest detectable cell sizes. This agrees with the findings for *C. reinhardtii* sorted on chip 1, where smaller cell sizes tended to occupy channels farther from the inner wall with increasing De.

6.3.3 SC ICP-MS analysis of *C. reinhardtii* cells sorted using μF chip 3

Sorting of *C. reinhardtii* was investigated on chip 3 which contained spiral channels of the smallest possible cross section (80 ×50 μm width×height) and longest channel length (270 mm). The backpressure due to the narrow channels allowed chip input flow rates up to 65 μL min^{-1}. Therefore, experiments on *C. reinhardtii* were conducted at 20 and 65 μL min^{-1}, corresponding to 1.8 and 5.7 De, respectively.

The number distributions of *C. reinhardtii* cells sorted at 1.8 De and 5.7 De across outlets ch1-ch6 of chip 3 are shown in **Figure 6.19**. Both flow rate conditions produced very similar cell number distributions, spreading from ch2 to ch4. A similar degree of cell focusing was also observed, with a maximum value of 75% at ch2. This high degree of focusing was expected for *C. reinhardtii* cells sorted on chip 3, as the system meets an a/h value of 0.146. Unlike the results for *C. reinhardtii* sorted on chip1 at 250 (11.2 De) and 1500 μL min^{-1} (69.9 De), the increase of De to a maximum of 5.7 could not relocate the cell focusing position away from the inner wall. Hence, considering the size range of *C. reinhardtii* (5-10 μm), it may be unlikely that chip 3 can separate *C. reinhardtii* from slightly larger sized cells, i.e., BMDMS, at these flow conditions. Furthermore, the intensities of the registered $^{47}PO^{+}$ cell

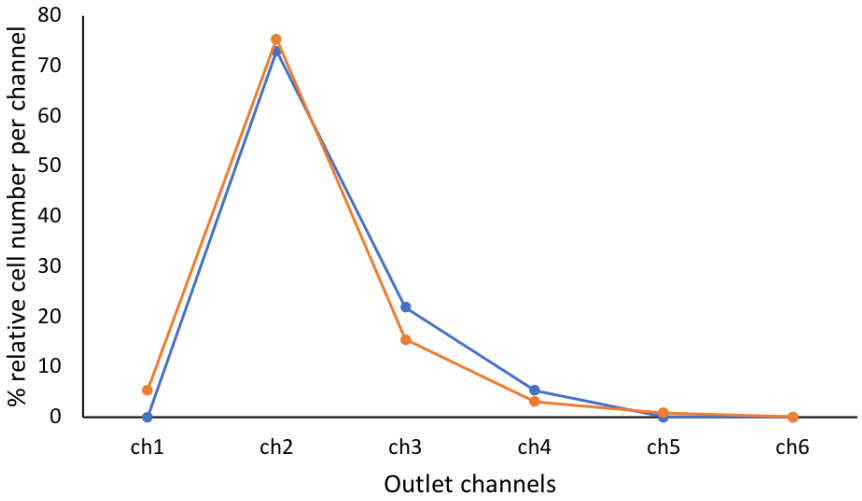

Figure 6.19 Graph illustrating the distribution of *C. reinhardtii* cell population across the outlet channels 1-6 of spiral chip 3, operated at chip input flow rates of 20 (blue) and 65 (orange) μL min^{-1} which correspond to 1.8 and 5.7 De, respectively. The number of cells detected per outlet channel has been normalized to the total number of cells detected from all outlet channels, and therefore it is expressed as % relative cell number per channel. The cell concentration was kept at 10^5 mL^{-1} for all flow conditions.

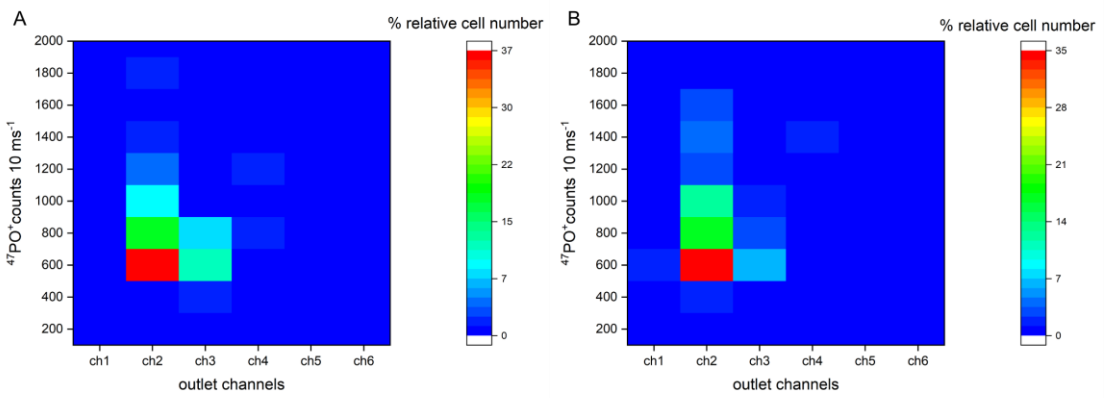

Figure 6.20 Heatmaps illustrating the distribution of *C. reinhardtii* cells with respect to their recorded $^{47}PO^{+}$ intensity across outlet channels 1-6 of spiral chip 3, operated at chip input flow rates of 20 (A) and 65 (B) µL min^{-1} (corresponding to 1.8 and 5.7 De, respectively). The y and x-axis show the recorded $^{47}PO^{+}$ intensity per cell event in counts per 10 ms^{-1} and the number of outlet channels, respectively, while the z-axis indicates the number of cells (expressed as a percentage of the total number of cells detected) showing a specific intensity. Cell events were arranged in intensity bins of 200 counts 10 ms^{-1} which are illustrated as colored squares (varying from blue to red with increasing % relative cell number) in this heatmap.

events are distributed in an identical pattern across outlets ch1-ch6 (**Figure 6.20**) for both flow rate conditions.

6.3.4 Discussion on chip 1, 2, 3 cell sorting capabilities

This section will attempt to make an overview of the empirical data obtained using spiral chips 1-3 to sort *C. reinhardtii* cells, with respect to the degree of focusing and cell intensity distribution pattern across the chip outlet channels, while also discuss how these empirical data compare to theoretical calculations using current mathematical relations.

In almost all the flow conditions tested, all three chips demonstrated a high capability to focus *C. reinhardtii* cells. More specifically, outlet channel 2 demonstrated the highest cell enrichment by accumulating 70-80% of the total cell population at flow conditions of 250 µL min^{-1} (32.8 Re, 11.6 De), 150 or 250 µL min^{-1} (34.0 Re, 10.2 De or 56.6 Re, 17.0 De) and 20 or 65 µL min^{-1} (7.7 Re, 1.8 or 24.9 Re, 5.7 De) for chip 1, 2 and 3, respectively. For *C. reinhardtii* with a particle to channel height ratio (a/h) of 0.087, 0.104 and 0.146 on chip 1, 2 and 3, respectively, the high degree of focusing closely matches findings by Rusom et al who observed particles meeting a/h $\geq$ 0.1 to focus in single streams within an intermediate 2-12 De regime. Theoretical calculations for a straight microfluidic channel also suggest that focusing of *C. reinhardtii* can be conveniently achieved on chips 1-3 at these flow conditions.

For example, the channel length required to focus *C. reinhardtii* (focusing length) on chips 1-3 under the specified flow conditions can be derived using:

$$V_p = \rho V max^2 a^3 f_{lift} / 3\pi\mu D_h^2 \qquad (Eq.7)$$

$$L_I = \frac{V_{avg}}{V_p} \times L_M \qquad (Eq.8)$$

where V_{avg} is the liquid's average linear velocity (mm s^{-1}), L_M is the migration distance, and V_p is the particle lateral migration velocity which can be obtained by balancing the shear-gradient force and a Stokes drag force $(Eq.7)$. In order to calculate the L_I, the common value of 0.5 was considered for the coefficient of lift, f_{lift} for all flow conditions and particle diameters. More specifically, in order for a 7 μm particle (corresponding to the avg. size of *C. reinhardtii*) to migrate half-width of a microfluidic channel, 167 and 27.9 mm of focusing length are required for chip 1 operated at 250 and 1500 μL min^{-1}, respectively, 34.8 or 20.9 mm for chip 2 operated at 150 or 250 μL min^{-1}, and 22.1 or 6.8 mm for chip 3 operated at 20 or 65 μL min^{-1}, respectively. These values are well within the capacity of chips 1,2 and 3, containing 166, 195 and 270 mm of channel length, respectively; especially considering that the introduction of Dean flow has been demonstrated to shorten the channel length required for particle focusing.[13] An additional parameter shown to determine focusing is the inertial force ratio, Rf, defined as the ratio of shear gradient lift over dean drag. A minimum value of 0.04 has been proposed by Di carlo et al for particle focusing to occur, although in the present study flow conditions providing Rf values < 0.04 resulted in focusing nonetheless.

Unlike chips 2 and 3, chip 1 could be operated at higher flow rates due to its larger cross-section. Operation of chip 1 at 1500 μL min^{-1} (69.9 De) posed the most interesting case as it displaced *C. reinhardtii* farther from the wall, while cell focusing was maintained at a sufficient degree; thus, indicating potential for separation of *C. reinhardtii* from a larger-sized cell population. Chips 2-3 may prove interesting cases as well due to the high degree of cell focusing that they exhibited. However, unless restrictions in flow rate are overcome so that these chips can be operated at increased De, it is highly unlikely that chips 2 and 3 can perform such kind of separations. However, this conclusion is based on the assumption of a large-to-medium-to-small particle arrangement (arranged from the inner to outer wall). Without studying chips 1-3 in a wide range of flow rates, the underlying mechanisms dictating cell sorting are difficult to be established.

6.3.5 Sorting of BMDMs from *C. reinhardtii* cells on chip 1 & 3

Sorting of BMDMs was explored on chip 1 at 250 and 1500 μL min^{-1}, corresponding to 11.6 and 69.9 De, respectively. Time-resolved acquisitions of BMDMs sorted on chip1 can be seen in **Figure SI1. 17**. The number distributions of BMDMS cells across outlet channels 1-8 on chip 1 are presented in **Figure 6.21** comparatively with the equivalent number distributions of *C. reinhardtii*, obtained at the specified flow conditions.

The number distributions of BMDMs across outlets ch1-ch8 are quite different between experiments conducted at 250μL min^{-1} (11.6 De) and 1500 μL min^{-1} (69.9 De). The

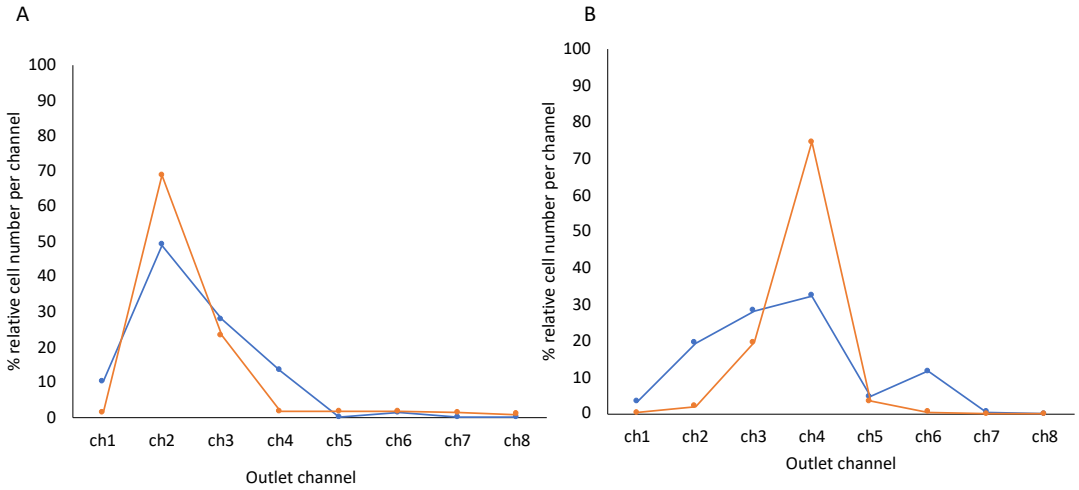

Figure 6.21 Graph illustrating the number distribution of BMDMs (blue) in comparison to *C. reinhardtii* (orange) sorted on chip 1 at 250 μL min^{-1} (A) and 1500 μL min^{-1} (B), corresponding to 11.6 and 69.9 De. The number of cells detected per outlet channel has been normalized to the total number of cells detected from all outlet channels, and therefore it is expressed as % relative cell number per channel. For both flow conditions, BMDMs were introduced at a cell concentration of 4× 10^5 mL^{-1}, while *C. reinhardtii* were introduced at 10^5 mL^{-1}.

distribution of BMDMS in **Figure 6.21**A spans from outlet ch1 to ch4, while a maximum cell focusing of around 50% is achieved at ch2. The rest 50% of the cell population is shared among ch1, ch3 and ch4, indicating the formation of a relatively wide cell stream compared to the equivalent of *C. reinhardtii* at 11.6 De. The larger width of the distribution of BMDMs sorted at 69.9 De (**Figure 6.21**B), extending from outlet ch1 to ch6, indicates an even wider cell stream than that for cells sorted at 11.6 De. Also, a lower degree of cell focusing is observed, where ch3 and ch4 almost equally share 60% of the total cell population. It is observed that the increased 69.9 De relocated the focusing position of the produced cell stream away from the inner wall compared to the lower 11.6 De, by shifting the position of

maximum focus to outlets ch3-ch4. Shifting of the BMDMs (avg. cell diameter of 11.9 μm) stream away from the inner wall at elevated De indicated that a significant proportion of the larger sized cell population could not resist the Dean drag. When compared to *C. reinhardtii*, the lower degree of cell focusing and the wider number distribution of BMDMS across outlets ch1-ch8 are apparent for both flow conditions, even though BMDMS meet a higher a/h ratio than *C. reinhardtii* on chip1 (0.15 for BMDMs against 0.09 for *C. reinhardtii*), and thus a convenient focusing of this cell line would be expected. The inferior focusing observed for BMDMs could be attributed to their significantly wider size distribution, which shows a 4σ width of 10.4 μm compared to 5.64 μm for *C. reinhardtii* (size distributions of both cell lines approximated as Gaussian), as shown in **Figure 6.9**. Furthermore, **Figure 6.21** revealed the potential for separation of BMDMs from *C. reinhardtii*, if the 2 cell lines were to be introduced as a mixed cell suspension. More specifically, **Figure 6.21**A (250 μL min^{-1}, 11.6 De) demonstrates outlet ch1 to almost exclusively contain BMDMs, while **Figure 6.21**B (1500 μL min^{-1}, 69.9 De) demonstrates that BMDMs cells can be collected with high purity from outlets ch1-ch2 and ch6. Percentage purities of BMDMs, infused at 69.9 De, were found to be 100 and 80 % at ch1 and ch2, respectively, whereas for *C. reinhardtii* (avg diameter of 7.3 μm) 70% at ch4

In order to illustrate the distribution of BMDMS with respect to their recorded $^{47}PO^{+}$ intensity across outlets ch1-ch8 of spiral chip 1, contour plots were employed instead of heatmaps. So far, a heatmap was preferred over a contour plot since the outlet channels, denoting the x-variable, take discrete values from 1-6 or 1-8, and they thus do not reflect a continuous variable. However, it was found that a contour plot can better demonstrate separations between 2 cell populations especially in the case a cell population exhibiting a broad intensity distribution.

Contour plots illustrating the intensity distribution of BMDMs across outlets ch1-ch8 on chip 1 are shown in **Figure 6.22** for experiments carried out at 11.6 (panel A) and 69.9 De (panel B). Both graphs reveal 2 major sub-populations within the initial BMDMs cell suspension, the one containing cell events below 1000 counts and another containing cell events within 1000-9000 counts. The contour plot in panel A (BMDMs sorted at 11.6 De) reveals that the majority of the larger sized cells (cell intensities within 3000-8000) are shared between outlets ch1-ch2, while the smaller sized sub-population has mostly accumulated between outlets ch3-ch4. In contrast, the contour plot in panel B (BMDMs sorted at 69.9 De) clearly shows a right shift of the BMDMs distributed intensities, as outlets

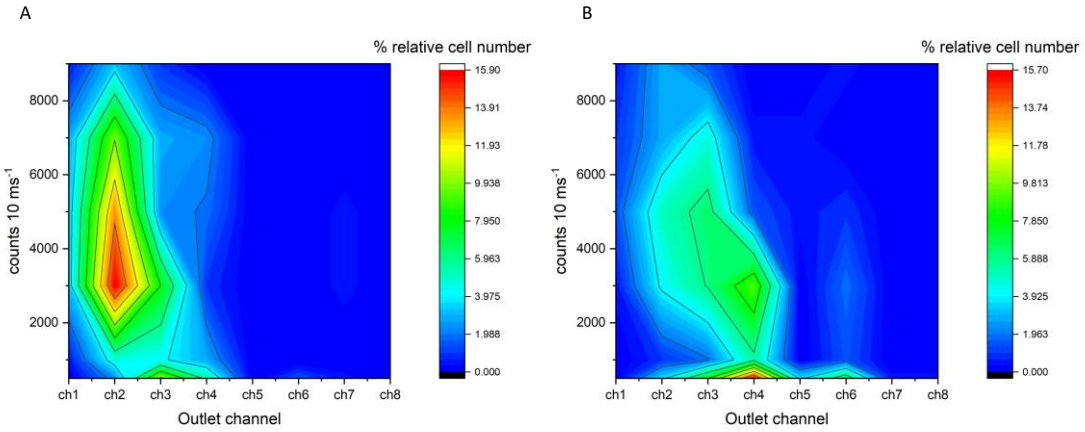

Figure 6.22 Contour plots illustrating the distribution of BMDMs cells with respect to their recorded $^{47}PO^{+}$ intensity across outlet channels 1-8 of spiral chip 1, operated at chip input flow rates of 250 (A) and 1500 (B) µL min^{-1} (corresponding to 11.6 and 69.9 De, respectively). The y and x-axis show the recorded $^{47}PO^{+}$ intensity per cell event in counts per 10 ms^{-1} and the number of outlet channels, respectively, while the z-axis indicates the number of cells (expressed as a percentage of the total number of cells detected) showing a specific intensity. Cell events were initially arranged in intensity bins of 500 counts for cell intensities up to 1000 counts 10 ms^{-1} above which a bin of 2000 counts was used to arrange the remaining cell intensities.

---

ch1-ch2 were stripped of several cell numbers from the region of the most frequently observed intensities. These cells moved to outlets ch3-ch4, however, ch1-ch2 retained a considerable cell population with intensities above 4000 counts 10 ms^{-1}. The latter is an indication that the high purity of outlets ch1-ch2 in BMDMs cell numbers as against *C. reinhardtii*, as shown in **Figure 6.21**, is attributed to the larger sized BMDMs sub-population that retains its focusing position close to the inner wall at the increased 69.9 De. The above observations suggest that size-based sorting within the BMDMs cell population is even more prominent compared to *C. reinhardtii* due to their wider size distribution.

The equivalent contour plots which illustrate the distributed intensities of *C. reinhardtii* sorted at 11.6 and 69.9 De are provided in **Figure SI1. 18**. Distributed intensities of *C. reinhardtii* reach up to 1000 counts 10 ms^{-1}, and accumulated between outlets ch2-ch3 and ch3-ch4 for cells sorted at 11.6 and 69.9 De, respectively.

If the distributed intensities of BMDMs and *C. reinhardtii* are combined in a single contour plot, this strategy would simulate the experiment of sorting a mixed cell suspension containing the 2 cell lines. Such a contour plot is provided in **Figure 6.23**, illustrating distributed intensities of 224 and 136 cell events of BMDMs and *C. reinhardtii*, respectively, sorted at 11.6 and 69.9 De. A lower number of *C. reinhardtii* cell events was plotted in order to enhance the separation between the 2 cell lines. This is because *C. reinhardtii* are overlapping with the lower-sized sub-population of BMDMs, thus significantly increasing the % relative cell number around the 1000 counts 10 ms^{-1} intensity section and simultaneously making the larger-sized BMDMs sub-population difficult to discern. For instance, 821 *C. reinhardtii* cells were detected in 68 s from outlets ch1-ch8 for a cell suspension of 10^5 mL^{-1}. Plotting 143 cell events (corresponding to a detection time of 12 s instead of 68 s) instead of 821 cell events is similar to diluting the *C. reinhardtii* to a concentration of 1.7× 10^4 cells mL^{-1}, which would be needed in order to optimize the separation of the 2 cell lines for spiral sorting SC ICP-MS. These dilutions will not be required if complete separation between BMDMS and *C. reinhardtii* is achieved in the future.

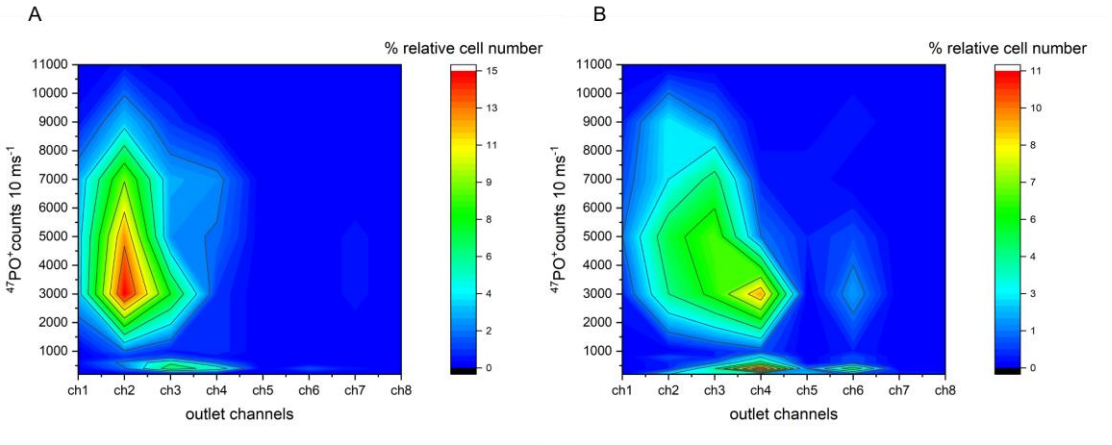

Figure 6.23 Contour plots illustrating how the distributed intensities of BMDMs cells compare to those of *C. reinhardtii* for sorting experiments conducted at 250 µL min^{-1}, 11.6 De (A) and 1500 µL min^{-1}, 69.9 De (B). The compiled cell intensities of the 2 cell lines were initially arranged in 200 count bins for cell intensities up to 1000 counts 10 ms^{-1} above which a 2000 count bin was used for the remaining cell intensities.

A good separation between BMDMs and *C. reinhardtii* can be observed from both **Figure 6.23**A and B. The distributed intensities of *C. reinhardtii* overlap with the lower sized subpopulation of BMDMs, demonstrating intensities up to 1000 counts 10 ms^{-1}, for both flow conditions. While *C. reinhardtii* and a significant portion of BMDMs moved towards ch4 at

the increased 69.9 De, the larger sized BMDMs population resisted the Dean drag and remained between ch1-ch2. Results on BMDMs and *C. reinhardtii* suggest that chip 1 achieves cell sorting based on the conventional particle arrangement of large-to-medium-to-small. Considering that BMDMs exhibited a wide size distribution, the lower-sized part of which overlapped with *C. reinhardtii*, It is likely that sorting of a mixture of *C. reinhardtii* and a cell line larger than BMDMs on chip 1 at 69.9 De can result in complete fractionation of a cell suspension into its constituent cell lines.

Sorting of BMDMs was also explored on chip 3 at the flow rate of 65 μL min, corresponding to 5.7 De. Considering a spiral channel width of 80 μm, BMDMs meet a a/h ratio of 0.24 which is even greater than the equivalent of chip 1 (a/h 0.149). Despite the higher a/h ratio, BMDMs could not be focused in a narrow cell stream, as shown in **Figure 6.24**A. Instead, they demonstrated a wide number distribution spanning from outlets ch1-ch5, with outlets ch2, 3 and 4 accumulating the higher percentages of the cell population, i.e., 30, 40 and 25% for ch2, 3, and 4 respectively. However, it is extremely interesting that BMDMs exhibited a right shift towards outlets away from the inner wall, resulting in the accumulation of a considerably greater number of BMDMs than *C. reinhardtii* cells at ch3-ch4. More specifically, increasing purity in BMDMs as against *C. reinhardtii* is calculated for ch2, ch3 and ch4, i.e. 30, 70 and > 80 % respectively. In addition, It can be observed from **Figure 6.24**B that the larger sized BMDMs (intensities >4000 counts 10 ms^{-1}) accumulated

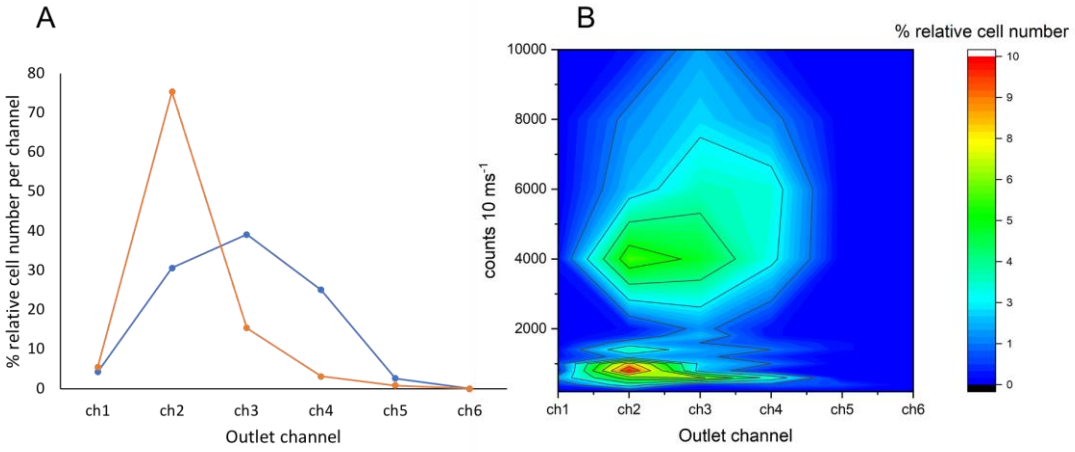

Figure 6.24 Graph A illustrates the number distribution of BMDMs (blue) as against *C. reinhardtii* (orange) across outlets ch1-ch6 on chip 3 at 65 μL min^{-1} (5.7 De), while graph B is a contour plot illustrating the distributed intensities of BMDMs and *C. reinhardtii* across outlets ch1-ch6. In order to construct graph B, the compiled cell intensities of the 2 cell lines were initially arranged in 200 count bins for cell intensities up to 1000 counts 10 ms^{-1} above which a 2000 count bin was used for the remaining cell intensities.

in outlets ch3-ch4, while *C. reinhardtii* or the lower and medium sized BMDMs (<4000 counts 10 ms^{-1}) accumulated mainly in outlet ch2. The observed separation pattern attained by chip 3 at 5.7 De is inverse to that of chip 1 at 69.9 De which demonstrated high percentages of BMDMs in cell populations collected from inner wall outlets, i.e., 100% and 80% purity in BMDMs for ch1 and ch2, respectively. Sorting of a cell line smaller than *C. reinhardtii* or larger than BMDMs might provide further insight into the type of particle/cell size arrangement that can be attained using chip 1 and 3 at the specified flow conditions.

6.3.6 Sorting of *Chlorella sorokiniana* from *C. reinhardtii* cells on chip 1, 2, 3

Sorting of *Chlorela sorokiniana* cells was initially explored on chip 1 at 1500 and 2000 μL min^{-1}, corresponding to 69.9 and 93.2 De, respectively. Time-resolved acquisitions of cell populations sorted on chip1 can be seen in **Figure SI1. 19**. Amongst the analyzed outlets, ch3-ch5 exhibited major cell-enrichment. The recorded average $^{47}PO^{+}$ intensity of the cell events accumulated in ch4, which contained the largest percentage of the cell population, was 10^5 counts 10 ms^{-1}.

Despite *Chlorela* (average diameter of 3.8 μm) meeting an a/h value of 0.047 on chip 1(300 μm × 80 μm, width×height), a decent 60% portion of the cell population focused at the center outlet, ch4. The number distributions of *Chlorela sorokiniana* cells across outlet channels 1-8 on chip 1 are presented in **Figure 6.25** comparatively with the equivalent

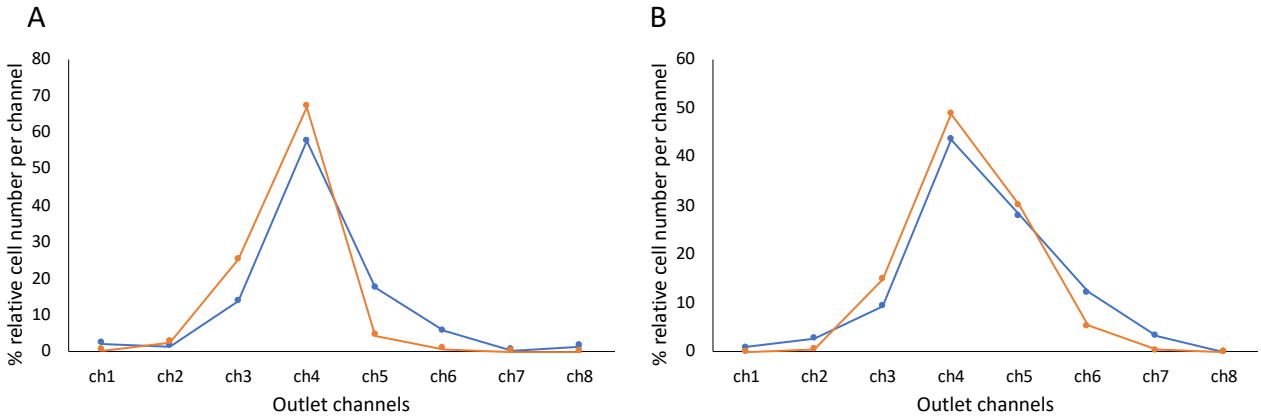

Figure 6.25 Graphs illustrating the number distribution of *Chlorella sorokinana* (blue) in comparison to *C. reinhardtii* (orange) sorted on chip 1 at 1500 μL min^{-1} (A) and 2000 μL min^{-1} (B), corresponding to 69.9 and 93.2 De. The number of cells detected per outlet channel has been normalized to the total number of cells detected from all outlet channels, and therefore it is expressed as % relative cell number per channel. For both flow conditions, both cell lines were introduced at a cell concentration of 10^5 mL^{-1}.

number distributions of *C. reinhardtii*, obtained at the specified flow conditions. At both flow conditions, *Chlorela* and *C. reinhardtii* cells exhibited very similar number distributions spanning from outlets ch3-ch6. However, it can be observed that *Chlorela* cells exhibit a slight right shift in their number distribution compared to *C. reinhardtii* cells at 69.9 De, thus allowing for the collection of 80 and 100% pure *Chlorela* populations from outlets ch5 and ch6, respectively. These percentage purities represent the fraction of *Chlorella* cells within the total number of cells, i.e., *Chlorella* and *C. reinhardtii* combined, counted per individual outlet. At 93.3 De the number distributions of both cell lines widen as the increased Dean drag deteriorates the cell focusing achieved at 69.9 De. The flow condition at 93.3 De does not pose an interesting case because no apparent separation between the 2 cell lines can be discerned.

The distributed cell intensities of *Chlorela* (n=276) and *C. reinhardtii* (n=287) cells across outlets ch1-ch8 are illustrated in the combined contour plot in **Figure 6.26**. A clear distinction between the 2 cell lines was achieved. More specifically, *C. reinhardtii* were distributed within the 300-1200 intensity region and *Chlorela* within the 75-150 count region. While a homogenous size distribution of *C. reinhardtii* can be seen within outlets ch3-ch4, there seems to be a tendency for the lower-sized *chlorella sorokiniana* cells to migrate away from

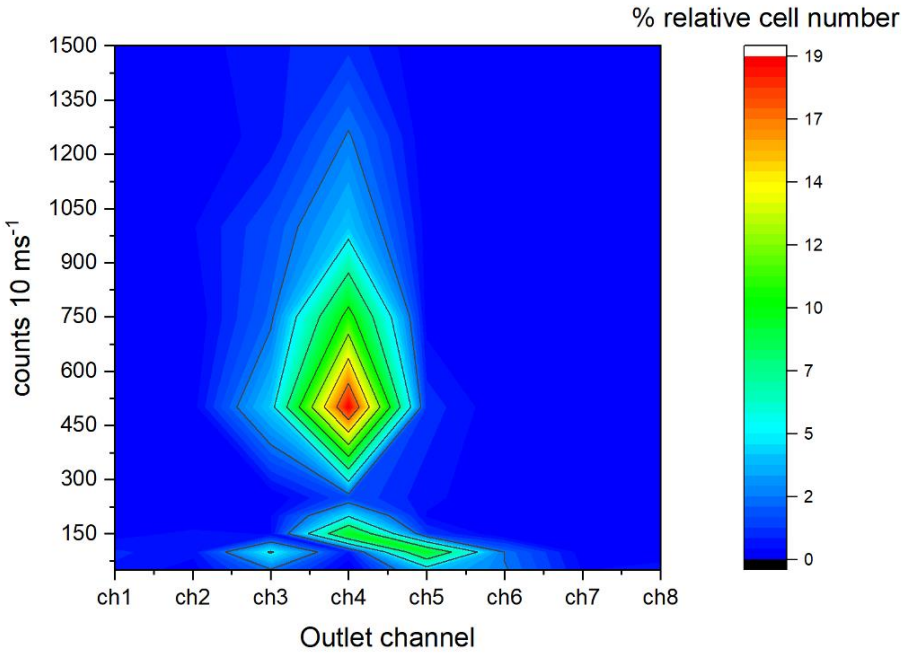

Figure 6.26 Contour plot illustrating the distributed intensities of *Chlorella* and *C. reinhardtii* across outlets ch1-ch6 of chip 1, operated at 1500 µL min^{-1} (69.9 De). The compiled intensities of the 2 cell lines were initially arranged in 50 count bins for cell intensities up to 250 counts 10 ms^{-1}, above which a 250 count bin was used for the remaining cell intensities.

the center channel towards outlets ch5, ch6. In combination with findings on the separation between BMDMs and *C. reinhardtii*, this finding suggests that a conventional large-to-medium-to-small particle/cell size arrangement might be the sorting pattern of chip 1 at 69.9 De.

Chip 2 (300 μm × 80 μm, width×height) and chip 3 were also employed in order to examine the sorting behavior on *Chlorella* cells in contrast to *C. reinhardtii* at the flow conditions of 150 (10.2 De) and 250 μL min^{-1} (17.0 De) on chip 2, as well as 20 (1.76 De), 65 μL min^{-1} (5.7 De) on chip 3. Both pairs of flow conditions tested for chip 2 and chip 3 produced identical results. For this reason, the flow conditions of 150 μL min^{-1} (10.2 De) and 65 μL min^{-1} (5.7 De) were selected to demonstrate the number distributions of *Chlorella* and *C. reinhardtii* across ch1-ch6 of chip 2 and 3, as shown in **Figure 6.27**.

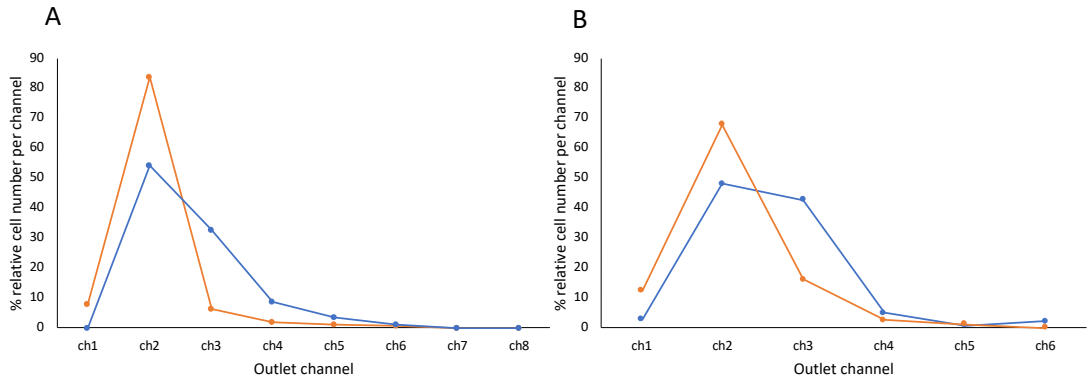

Figure 6.27. Graphs illustrating the number distribution of *Chlorella sorokinana* (blue) in comparison to *C. reinhardtii* (orange) sorted at 150 μL min^{-1} (10.2 De) on chip 2(A) and at 65 μL min^{-1} (5.7 De) (B) on chip 3. The number of cells detected per outlet channel has been normalized to the total number of cells detected from all outlet channels, and therefore it is expressed as % relative cell number per channel. For both flow conditions, both cell lines were introduced at a cell concentration of 10^5 mL^{-1}.

In comparison to the results obtained using chip 1, *Chlorella* populations on chips 2, 3 accumulated in outlet channels closer to the inner wall, as can be observed from **Figure 6.27**A &B. More specifically for chip 2, *Chlorella* cells were distributed across outlets ch2-ch5, with outlets ch2 and ch3 containing the majority of the cell population, i.e, 50% and 35%. Regarding chip 3, *chlorella* cells demonstrated a similar distribution width, however, focusing was slightly inferior as outlets ch2 and ch3 shared almost equal percentages of the cell population. For both chips and flow conditions, *chlorella* cells exhibited a wider number distribution than *C. reinhardtii*, and thus inferior degree of focusing compared to results for chip 1. This does not agree with theoretical predictions which suggest focusing of *chlorella*

to be increasingly easier in channels of smaller cross-section, considering the increase of the a/h ratio, i.e., 0.047, 0.054 and 0.076 for chip 1, 2, and 3, respectively. The theoretical channel length L_I required for focusing *Chlorella* cells is also within the limits of chips 1-3, i.e., 197, 247 and 48 mm required for focusing cells on chip 1, 2, 3 operated at the specified flow conditions, while 166, 195, 270 mm is the channel length of the devices. At present, this behavior cannot be explained, however, it has to be noted that these mathematical formulas for determination of L_I do not take into account Dean flow, as they have been expressed for straight microfluidic channels. Flow dynamics simulations could aid in better predicting the behavior of small-sized cells in the future.

To the best of our knowledge, only one study reports focusing of 3.2 μm particles (close to the average diameter of a *chlorella* cell) in a narrow stream and collection from a single 100 μm width inner wall outlet channel. This was done by employing a spiral sorter chip (20 μm × 20 μm square cross-section, initial radius of 2.12 mm, operated at 10 μL min^{-1}.[36] These flow conditions correspond to 12. 4 Re and 0.85 De. In our study, similar low flow conditions using chip 3 (80× 50 μm, i.e., 20 μL min^{-1}, 7.66 Re, 1.8 De) did not lead to a better focusing. The difficulty to focus particles, closely sized to *chlorella,* is further demonstrated by Rusom et al. In their work, 10 μm particles were collected from a narrow 50 μm outlet channel, while 3 μm particles were collected from a wide 950 μm outlet channel as they remained unfocused.[23]

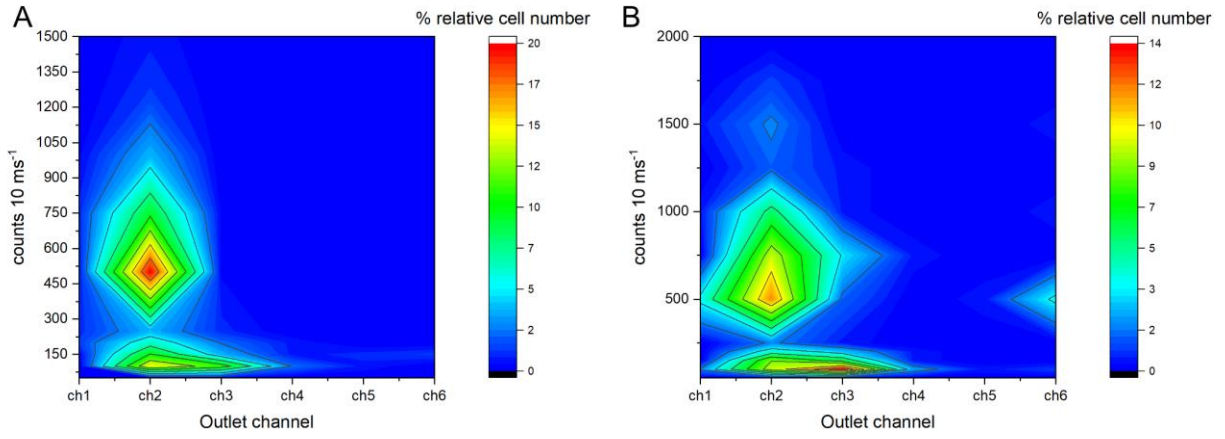

Figure 6.28 Contour plot illustrating the distributed intensities of *Chlorella* and *C. reinhardtii* across outlets ch1-ch6 of chip 2 (A) and chip 3 (B), operated at 150 μL min^{-1} (10.2 De) and 65 μL min^{-1} (5.7 De), respectively. The compiled intensities of the 2 cell lines were initially arranged in 50 count bins for cell intensities up to 250 counts 10 ms^{-1}, above which a 250 count bin was used for the remaining cell intensities. Both contour plots were constructed out of an equal number of cell events from each cell line, accounting for a total of 280 and 220 for plot A and B, respectively.

Contour plots illustrating the distributed intensities of *Chlorella* and *C. reinhardtii* are provided in **Figure 6.28** for cells sorted on chip 2 (A) and chip 3 (B). Occurrence of size-based sorting within *Chlorella* populations cannot be observed, if only slightly for chip 2 **Figure 6.28**A, as the whole size range of detected cells is almost equally shared between the two major cell-enriched outlets, ch2 and ch3.

6.3.7 Sorting of Synechocystis sp. PCC 6803 from C. reinhardtii cells on chip 1, 3

Focusing and sorting of *Synechocystis sp. PCC 6803*, the smallest accessible cell line with an average diameter of 1.6 µm, was explored on chip 1 operated at 250 µL min^{-1} (11.6 De) and chip 3 operated at 8 (0.8 De), 20 (1.9 De) or 65 µL min^{-1} (6.2 De), respectively. No occurrence of cell focusing can be seen from **Figure 6.29**A &C for *Synechocystis* introduced into chip 1, but rather a homogeneous distribution of cells across all outlet channels, ch1-ch8. This suggests that the diameter of the cell (meeting a a/h ratio of 0.02) is extremely small for a sufficient lift force F_{shear} to counteract the dean drag F_{dean}. Therefore, it seems that cells are constantly circulating throughout the channel cross-section. The theoretically calculated channel length to focus *Synechocystis sp. PCC 6803* also prohibits any

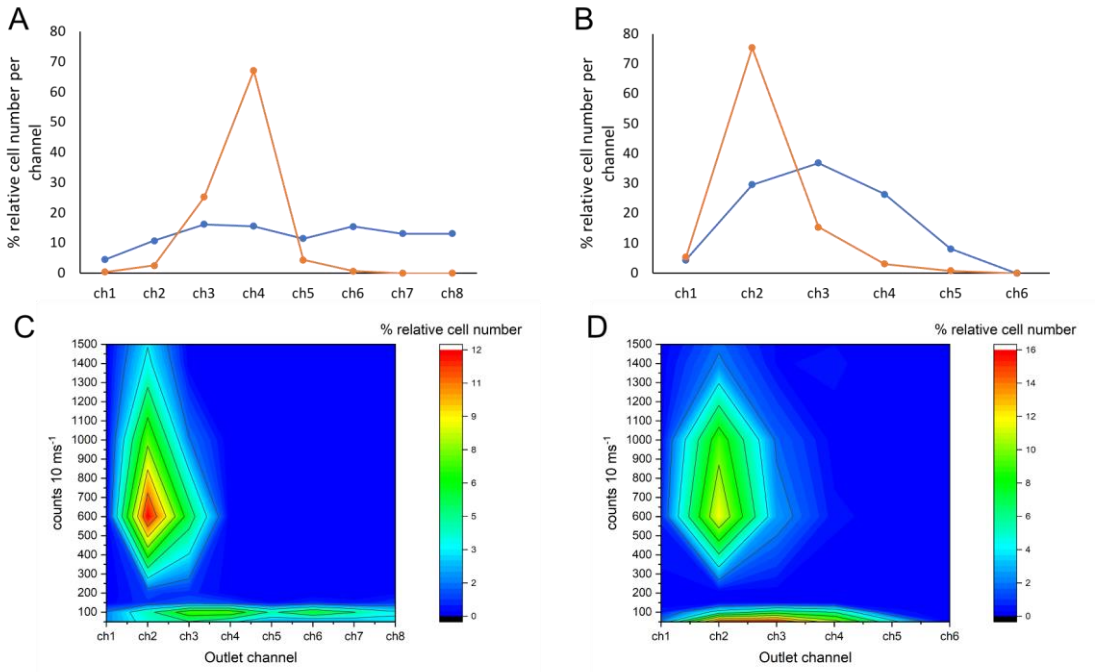

Figure 6.29 Graphs A & B illustrate the number distribution of *Synechocystis sp. PCC 6803* (blue) as against that of *C. reinhardtii* (orange) across outlet channels of chip 1 (A) and chip 3 (B), operated at 250 µL min^{-1} (11.6 De) and 65 µL min^{-1}(6.2 De), respectively. Contour plots illustrate the distributed intensities of the 2 cell lines across outlet channels of chip 1 (C) and chip 3 (D) at 250 and 65 µL min^{-1}, respectively.

occurrence of focusing, i.e, 15906 mm of a straight microfluidic channel length required as against the 166 mm available on chip1. The use of chip 3, on which *Synechocystis sp. PCC 6803* meet a a/h ratio of 0.03, provided improved cell focusing capability (**Figure 6.29**B). All flow conditions used for chip 3 produced similar results, and so the flow condition of 65 µL min^{-1} was selected for demonstration in **Figure 6.29**B & D. It can be observed that cells are distributed almost equally among 3 major outlets, ch2-ch4. However, the flow field was not sufficient to transpose *Synechocystis* away from the inner wall channels, so that a separation from *C. reinhardtii* could be achieved. To the best of our knowledge, a single paper by Bhagat et al reports on the separation of 1.9 and 7.3 µm particles through an Archimedean spiral sorter (100 µm × 50 µm width× height, initial radius of 3 mm) containing 2 outlets.[21] The 1.9 µm particles were transposed to a wide outer wall outlet channel so that the bigger 7.32 could be collected from an inner wall outlet channel. The migration of the 1.9 µm particles to the outer wall agreed with theoretical calculations predicting the required focusing length for these small particles. However, the theoretical calculation was based on the Dean velocity $V_d\ (Eq.13)$ rather than the lateral migration velocity $V_p\ (Eq.7)$ that has already been shown in section 6.3.4. The authors did this with the assumption of the Dean drag significantly dominating inertial lift for these small-sized particles at all flow conditions. Similar flow conditions to the study by Bhagat et al (10 µL, 4.4 Re, 0.47 De) were also used for sorting *Synechocystis* on chip 3 (8 µL, 3 Re, De 0.8), however complete migration to the outer wall channels could not be achieved. Failure might be attributed to the channel length of chip 3 (266 mm) which was much larger than the predicted (23.14 mm), while in the work by Bhagat et al the predicted length (12.8 mm) closely matched the actual length of the sorting channel (13 mm).

6.3.8 Overview of the potential for separation among BMDMs, *C. reinhardtii* and *Chlorella sorokiniana*

The distributions of a large (BMDMs), medium (*C.reinhardtii*) and a smaller-sized (*Chlorella sorokiniana*) cell line across the outlet channels of chips 1 & 3 may provide an insight into the cell/particle separation potential of these chips, as well as the regimes of separation, that is, the arrangement of particles by size across the width of the spiral microfluidic channel. Chip 2 is left out of this section due to the lack of sorting experiments on BMDMs cells. Furthermore, *Synechocystis sp. PCC 6803* are not discussed as their smaller diameter presented limitations in cell focusing.

Figure 6.30 demonstrates results obtained by operating chip 1 at 1500 µL min^{-1} and chip 3 at 65 µL min^{-1}. It is evident that a complete separation, i.e., collection of each cell line from a different outlet channel, cannot be attained using either spiral chip at these flow conditions. The possibility of collecting a highly pure cell population occurs only for BMDMs which can be collected with a >90 % purity from outlet ch2 and ch4 of chip 1 and 3, respectively. However, while the separation potential of chip 1 has been explored in a wider range of Re numbers, i.e, 23 Re (250 µL min^{-1}) and 196 Re (1500 µL min^{-1}), chip 3 was only operated within 7.6 Re (20 µL min^{-1})-25 Re (65 µL min^{-1}). For instance, on a spiral chip (100 µm × 50 µm, 2 cm inner radius), Martel et al observed complete separation of 5, 10 and 15 µm particles at 314 Re (28.6 De), while distributions of 5 and 15 µm-sized particles overlapped at the lower 140 Re (12.7 De).[24] Thus, to achieve comparable De on chip 3 (80 µm × 50

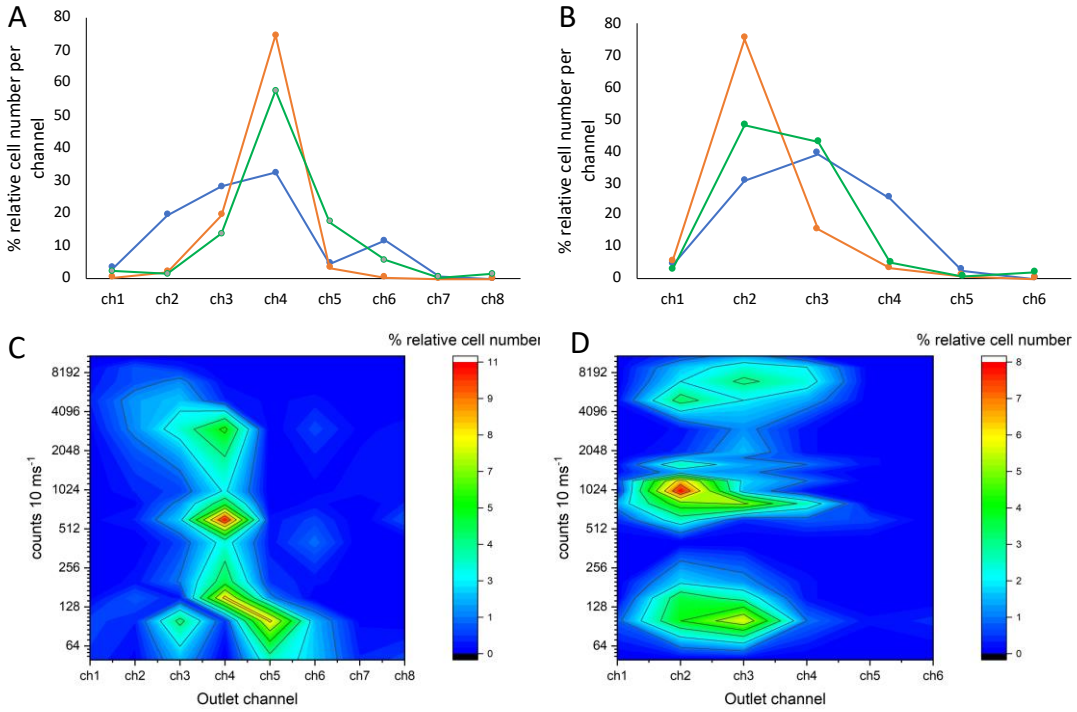

Figure 6.30 Graphs A&B illustrate the number distribution of BMDMs (blue) against *C. reinhardtii* (orange) and *Chlorella sorokiniana* (green) across outlet channels of chip 1 (A) and chip 3 (B), operated at 1500 µL min^{-1} and 65 µL min^{-1}, respectively. Contour plots illustrate the distributed intensities of the 2 cell lines across outlet channels of chip 1 (C) and chip 3 (D) at the 250 and 65 µL min^{-1}, respectively. The data used to plot graphs A-C were not acquired upon sorting a mixed cell suspension, but acquired from independent sorting experiments on BMDMs, *C. reinhardtii* and *Chlorella sorokiniana* at the specified flow rates.

μm, 0.5 cm inner radius), chip 3 has to be operated at much higher flow rates, i.e., 200 μL min^{-1} and 320 μL min^{-1}, than those used in this study.

The number distributions (**Figure 6.30** A&B) in combination with the contour plots of the distributed cell intensities (**Figure 6.30** C&D) suggest different regimes of separation for the 3 cell lines between chips 1 and 3. More specifically for chip 1, accumulated BMDMs between ch1-ch2 are observed to represent the portion of the large-sized BMDMs cells as they exhibit intensities >4000 counts. Whereas accumulated c*hlorella sorokiniana* cells in ch5 are observed to represent the smaller sized sub-population of *Chlorella sorokiniana* cells, i.e., intensities<100 counts. Outlet channels ch3, ch4 accumulated the entire *C. reinhardtii* population, as well as portions of the other cell lines which were difficult to separate due to limitations in cell size resolution. A large-to-medium-to-small arrangement of cell sizes (sizes arranged from inner to outer wall) is proposed for chip 1 operated at 1500 μL min^{-1}.

In comparison, **Figure 6.30** B&D shows the larger sized sub-population of BMDMs and a portion of *Chlorella* cells to migrate to the outer wall outlets, ch3-ch4, whereas the majority of *C. reinhardtii* focused in outlet ch2. For clarification, it has to be mentioned that although the population of C. reinhardtii seems to extend towards ch3, this extension is due to the lower-sized sub-population of BMDMs exhibiting intensities within 600-800 counts. These cell size distributions shown for chip 3 resemble a less common particle separation regime, unveiled by Martel et al [24], where medium-sized particles focus near the inner wall as opposed to the small and large which overlap at the center of the channel width. At higher flow rates this regime has been observed to lead to a medium-to-large-to-small particle arrangement, therefore it is possible that a higher degree of separation can be achieved using chip 3 at higher flow rates.

6.4 Conclusions

Analysis of cell populations using SC ICP-MS allows for determining the elemental content of a cell population on a per cell basis. This method often unveils large variations in the elemental content within the cell population, but cannot pinpoint the causes contributing to these variations, such as a wide size distribution characterizing the cell population. In addition, information on elemental content might seem more complicated, in the case of analysis of an unknown cell suspension containing mixed cell lines. In this study, a method combining inertial microfluidics for size-based sorting of cell populations prior to SC ICP-MS analysis was developed. Three microfluidic chips containing spiral channels of different cross-section were used to explore capabilities for focusing and sorting a large-sized (BMDMs), medium-sized (*C. reinhardtii*) and small sized *Chlorella sorokiniana or* Synechocystis *sp. PCC 6803* cell line across a range of flow rates. While complete fractionation of a mixed cell suspension into its 3 constituent cell lines could not be achieved, sorting cell lines in pairs resulted in obtaining highly pure cell lines from specific outlet channels. By establishing a correlation between $^{47}PO^{+}$ intensity per cell detection event and cell size, insights into the sorting mechanism of 2 chips could be provided. Contour plots linking $^{47}PO^{+}$ intensity with the percentage of cells accumulated in each outlet resulted in complete visual discrimination between 2 cell lines, thus equipping SC ICP-MS with flow cytometry capabilities. While this study constitutes preliminary work on the combination of cell sorting with SC ICP-MS, it lays the foundation for the advancement of inertial microfluidics for SC ICP-MS. Future developments could focus on interfacing spiral sorter chips online to ICP-MS, so that the contents of each outlet channel could be monitored real-time. Specialized distributor valves can be used to direct the flow of a selected outlet into the ICP-MS spray chamber, and simultaneously allow for the uninterrupted operation of all other outlet channels. During the real-time analysis of an outlet channel, the other outlets could all be flowing into a waste vial. By improving the analytical configuration as such, spiral chips could be studied at their full spectrum of flow rates in a time-efficient manner. Also, the probability of experimental errors, such as sample cross-contamination that may occur during off-line sample collection, will be eliminated. In addition, more chips customized for sorting of specific cell lines should be tested in order to validate theoretical calculations, granted that the field of inertial microfluidics has grown considerably through empirical studies. Flow dynamics simulations using relevant software, such as COMSOL Multiphysics®, are expected to aid in better predicting the behavior of different cell or particle

sizes within microfluidic spiral channels of certain geometry, or aid in the design of suitable channel geometries to enhance separations.

6.5 References

[1] J.M. Martel, M. Toner, Inertial focusing in microfluidics, Annu. Rev. Biomed. Eng. 16 (2014) 371–396. https://doi.org/10.1146/annurev-bioeng-121813-120704.

[2] Microfluidic cell sorting: a review of the advances in the separation of cells from debulking to rare cell isolation, Lab Chip. 15 (2015) 1230–1249. https://doi.org/10.1039/C4LC01246A

[3] J.G. Kralj, M.T.W. Lis, M.A. Schmidt, K.F. Jensen, Continuous dielectrophoretic size-based particle sorting, Anal. Chem. 78 (2006) 5019–5025. https://doi.org/10.1021/ac0601314.

[4] F. Petersson, L. Åberg, A.-M. Swärd-Nilsson, T. Laurell, Free Flow Acoustophoresis: Microfluidic-Based Mode of Particle and Cell Separation, Anal. Chem. 79 (2007) 5117–5123. https://doi.org/10.1021/ac070444e.

[5] S. Miltenyi, W. Müller, W. Weichel, A. Radbruch, High gradient magnetic cell separation with MACS, Cytometry. 11 (1990) 231–238. https://doi.org/10.1002/cyto.990110203.

[6] S. Choi, S. Song, C. Choi, J.K. Park, Hydrophoretic sorting of micrometer and submicrometer particles using anisotropic microfluidic obstacles, Anal. Chem. 81 (2009) 50–55. https://doi.org/10.1021/ac801720x.

[7] K. Loutherback, K.S. Chou, J. Newman, J. Puchalla, R.H. Austin, J.C. Sturm, Improved performance of deterministic lateral displacement arrays with triangular posts, Microfluid. Nanofluidics. 9 (2010) 1143–1149. https://doi.org/10.1007/s10404-010-0635-y.

[8] D. Huh, J.H. Bahng, Y. Ling, H.H. Wei, O.D. Kripfgans, J.B. Fowlkes, J.B. Grotberg, S. Takayama, Gravity-driven microfluidic particle sorting device with hydrodynamic separation amplification, Anal. Chem. 79 (2007) 1369–1376. https://doi.org/10.1021/ac061542n.

[9] J. Zhang, S. Yan, D. Yuan, G. Alici, N.T. Nguyen, M. Ebrahimi Warkiani, W. Li, Fundamentals and applications of inertial microfluidics: A review, Lab Chip. 16 (2016) 10–34. https://doi.org/10.1039/c5lc01159k.

[10] A.A.S. Bhagat, S.S. Kuntaegowdanahalli, N. Kaval, C.J. Seliskar, I. Papautsky, Inertial microfluidics for sheath-less high-throughput flow cytometry, Biomed. Microdevices. 12 (2010) 187–195. https://doi.org/10.1007/s10544-009-9374-9.

[11] S.S. Kuntaegowdanahalli, A.A.S. Bhagat, G. Kumar, I. Papautsky, Inertial microfluidics for continuous particle separation in spiral microchannels, Lab Chip. 9 (2009) 2973–2980. https://doi.org/10.1039/b908271a.

[12] G. Segre, A. Silberg, Radial Particle Displacements in Poiseuille Flow of Suspensions, Nature. 189 (1961) 209–210. http://dx.doi.org/10.1038/189209a0.

[13] D. Di Carlo, Inertial microfluidics, Lab Chip. 9 (2009) 3038. https://doi.org/10.1039/b912547g.

[14] J. Matas, J. Morris, E. Guazzelli, Lateral Forces on a Sphere, Oil Gas Sci. Technol. 59 (2004) 59–70. https://doi.org/10.2516/ogst:2004006.

[15] D. Stoecklein, D. Di Carlo, Nonlinear Microfluidics, Anal. Chem. 91 (2019) 296–314. https://doi.org/10.1021/acs.analchem.8b05042.

[16] D. Di Carlo, D. Irimia, R.G. Tompkins, M. Toner, Continuous inertial focusing, ordering, and separation of particles in microchannels, Proc. Natl. Acad. Sci. U. S. A. 104 (2007) 18892–18897. https://doi.org/10.1073/pnas.0704958104.

[17] A.A.S. Bhagat, S.S. Kuntaegowdanahalli, I. Papautsky, Inertial microfluidics for continuous particle filtration and extraction, Microfluid. Nanofluidics. 7 (2009) 217–226. https://doi.org/10.1007/s10404-008-0377-2.

[18] J.F. Edd, D. Di Carlo, K.J. Humphry, S. Köster, D. Irimia, D.A. Weitz, M. Toner, Controlled encapsulation of single-cells into monodisperse picolitre drops, Lab Chip. 8 (2008) 1262–1264. https://doi.org/10.1039/b805456h.

[19] J. Zhou, I. Papautsky, Fundamentals of inertial focusing in microchannels, Lab Chip. 13 (2013) 1121–1132. https://doi.org/10.1039/c2lc41248a.

[20] W.R. Dean, LXXII. The stream-line motion of fluid in a curved pipe (Second paper) , London, Edinburgh, Dublin Philos. Mag. J. Sci. 5 (1928) 673–695. https://doi.org/10.1080/14786440408564513.

[21] A.A.S. Bhagat, S.S. Kuntaegowdanahalli, I. Papautsky, Continuous particle separation in spiral microchannels using dean flows and differential migration, Lab Chip. 8 (2008) 1906–1914. https://doi.org/10.1039/b807107a.

[22] S. Ookawara, D. Street, K. Ogawa, Numerical study on development of particle concentration profiles in a curved microchannel, Chem. Eng. Sci. 61 (2006) 3714–3724. https://doi.org/10.1016/j.ces.2006.01.016.

[23] A. Russom, A.K. Gupta, S. Nagrath, D. Di Carlo, J.F. Edd, M. Toner, Differential inertial focusing of particles in curved low-aspect-ratio microchannels, New J. Phys. 11 (2009). https://doi.org/10.1088/1367-2630/11/7/075025.

[24] J.M. Martel, M. Toner, Particle focusing in curved microfluidic channels, Sci. Rep. 3 (2013). https://doi.org/10.1038/srep03340.

[25] N. Nivedita, I. Papautsky, Continuous separation of blood cells in spiral microfluidic devices, Biomicrofluidics. 7 (2013). https://doi.org/10.1063/1.4819275.

[26] N. Nivedita, P. Ligrani, I. Papautsky, Dean Flow Dynamics in Low-Aspect Ratio Spiral Microchannels, Sci. Rep. 7 (2017) 1–10. https://doi.org/10.1038/srep44072.

[27] E.W.M. Kemna, R.M. Schoeman, F. Wolbers, I. Vermes, D.A. Weitz, A. Van Den Berg, High-yield cell ordering and deterministic cell-in-droplet encapsulation using Dean flow in a curved microchannel, Lab Chip. 12 (2012) 2881–2887. https://doi.org/10.1039/c2lc00013j.

[28] W.C. Lee, A.A.S. Bhagat, S. Huang, K.J. Van Vliet, J. Han, C.T. Lim, High-throughput cell cycle synchronization using inertial forces in spiral microchannels, Lab Chip. 11

(2011) 1359–1367. https://doi.org/10.1039/c0lc00579g.

[29] J. Sun, C. Liu, M. Li, J. Wang, Y. Xianyu, G. Hu, X. Jiang, Size-based hydrodynamic rare tumor cell separation in curved microfluidic channels, Biomicrofluidics. 7 (2013). https://doi.org/10.1063/1.4774311.

[30] H.W. Hou, M.E. Warkiani, B.L. Khoo, Z.R. Li, R.A. Soo, D.S.W. Tan, W.T. Lim, J. Han, A.A.S. Bhagat, C.T. Lim, Isolation and retrieval of circulating tumor cells using centrifugal forces, Sci. Rep. 3 (2013) 1–8. https://doi.org/10.1038/srep01259.

[31] X. Zhang, X. Wei, X. Men, Z. Jiang, W.Q. Ye, M.L. Chen, T. Yang, Z.R. Xu, J.H. Wang, Inertial-Force-Assisted, High-Throughput, Droplet-Free, Single-Cell Sampling Coupled with ICP-MS for Real-Time Cell Analysis, Anal. Chem. 92 (2020) 6604–6612. https://doi.org/10.1021/acs.analchem.0c00376.

[32] C. Wu, X. Wei, X. Men, X. Zhang, Y.-L. Yu, Z.-R. Xu, M.-L. Chen, J.-H. Wang, Two-Dimensional Cytometry Platform for Single-Particle/Cell Analysis with Laser-Induced Fluorescence and ICP–MS, Anal. Chem. 93 (2021) 8203–8209. https://doi.org/10.1021/acs.analchem.1c00484.

[33] W.Y. Lau, K.H. Chun, W.T. Chan, Correlation of single-cell ICP-MS intensity distributions for the study of heterogeneous cellular responses to environmental stresses, J. Anal. At. Spectrom. 32 (2017) 807–815. https://doi.org/10.1039/c6ja00348f.

[34] J.W. Olesik, P.J. Gray, Considerations for measurement of individual nanoparticles or microparticles by ICP-MS: Determination of the number of particles and the analyte mass in each particle, J. Anal. At. Spectrom. 27 (2012) 1143–1155. https://doi.org/10.1039/c2ja30073g.

[35] X. Bi, S. Lee, J.F. Ranville, P. Sattigeri, A. Spanias, P. Herckes, P. Westerhoff, Quantitative resolution of nanoparticle sizes using single particle inductively coupled plasma mass spectrometry with the K-means clustering algorithm, J. Anal. At. Spectrom. 29 (2014) 1630–1639. https://doi.org/10.1039/c4ja00109e.

[36] I.D. Johnston, M.B. McDonnell, C.K.L. Tan, D.K. McCluskey, M.J. Davies, M.C. Tracey, Dean flow focusing and separation of small microspheres within a narrow size range, Microfluid. Nanofluidics. 17 (2014) 509–518. https://doi.org/10.1007/s10404-013-1322-6.

7 Conclusions-Future perspective

Novel atomic spectrometric methods were developed for the analysis of single cells and single nanoparticles.

The development and application of SC-ICP-MS provided novel analytical metrics that were evidenced to be more suitable to characterize the uptake of arsenate by *C. reinhardtii* cells. Compared to conventional analytical schemes, SC-ICP-MS could reveal the lognormal distribution of As among single cells, as well as allowed for obtaining metrics such as the most frequent As mass $cell^{-1}$ and the lognormal mean As mass $cell^{-1}$. Simultaneous quantitation of intracellular, cell wall-bound and dissolved As was demonstrated. SC-ICP-MS required minimum sample preparation, just a simple dilution or cell washing was performed, while it only consumed a few μL of sample (e.g., 18000 cells). Therefore, thanks to its sensitivity, efficiency and simple execution, SC-ICP-MS is envisioned to be used as a powerful bioanalytical tool for rapid screening of cell populations for drug or toxicant uptake, as well as for intrinsic cell elements.

The developed data processing method for μs-sp-ICP-MS (DP-μs-sp-ICP-MS) demonstrated great accuracy in the simultaneous quantitation of nanoparticulate and dissolved Ag. Its applicability was further demonstrated in its use for the study of the behaviour of ppt-levels of Ag in a seawater mesocosm experiment. Compared to the well-documented ms-scale sp-ICP-MS, it provided unique information such as the time profiles of the transient nanoparticle signals. In comparison to other equivalent in-house data processing methods built using programming languages, DP-μs-sp-ICP-MS was developed using a combination of commercially available software, with straightforward and fully visible computation steps, as well as a more user-friendly interface. DP-μs-sp-ICP-MS constitutes an independent data treatment approach that is not bound to any particular ICP-MS instrument, and can be employed either in sp-ICP-MS or SC-ICP-MS analyses.

Pairing of microfluidic chips to ICP-MS was demonstrated using pneumatic liquid nebulisation, either with the use of a high-efficiency nebuliser or with direct coupling of microfluidic supersonic nebuliser (chip-μf-Neb). In the former case, the efficient operation of a chip-based ICP-MS system was demonstrated with the application of standard dilution analysis (SDA) which required precise and reproducible mixing of standard solutions on chip. The use of SDA as a powerful calibration approach, enabling matrix and instrumental drift correction, was employed for the first time for microfluidic chip-based ICP-MS at the low μL min^{-1} flow regime. Its excellent quantitation capability and minimum sample consumption

(140 µL per sample) can be harnessed as a bioanalytical tool for the efficient metal analysis of biological samples.

A microfluidic supersonic nebuliser was coupled for the first time to an ICP-MS (chip-µf-Neb), featuring highly efficient and sensitive metal analysis of volume-limited samples, including single particles and single cells. Because of the µm-sized liquid channels and nebulisation of liquids directly to an ICP-MS, metal analysis can be conducted with minimum dead volumes, associated with analyte diffusion or memory effects. Also, nebulisation occurs without liquid suction on microfluidic channels, which renders chip-µf-Neb ideal for microchip capillary electrophoresis followed by metal determination. Because of its simple and cost-efficient fabrication in PDMS, new designs of channels can be explored so that multiple fluidic processes can be accommodated on chip prior to liquid nebulisation. These processes may include encapsulation of single cells within aqueous droplets that can be individually be detected with ICP-MS or molecular MS. These droplets will provide flexibility to perform several biochemical experiments on cells, including individual cell lysis, in order to provide a readout in terms of elemental, metabolite or protein content per cell.

Microfluidic chips with spiral channels showed potential to be combined with SC-ICP-MS in order to focus or sort cell populations prior to elemental detection. Mixed cell suspensions containing BMDMs and *C. reinhardtii* could be sorted in order to obtain samples that were highly pure in BMDMS or *C. reinhardtii*. This provides new possibilities to SC-ICP-MS, which has only been used for elemental determination of a single cell line; thus, equipping SC-ICP-MS with label-free cell cytometry capabilities. The latter can be achieved with online coupling of a spiral chip to ICP-MS. This will also aid in devising quicker experiments, so that more experimental parameters can be optimized, i.e., flow rates, cell concentrations. Chip interfaces with tubings for liquid transport can be suitably sealed to allow for the application of higher flow rates, especially for spiral channels of narrow cross-section.

8 Supporting Information 1

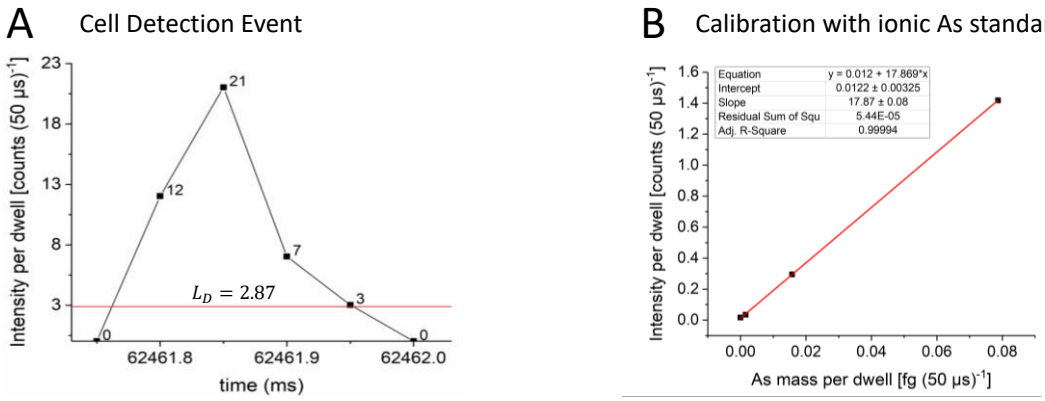

$$Peak\ Area\ (PA) = \Sigma_{Intensity\ per\ dwell}$$
$$= 12 + 21 + 7 + 3$$
$$= 43 \text{ counts } (1)$$

$$Slope = 17.87 \frac{counts}{fg} \ (2)$$

$$(1), (2) \Rightarrow As\ mass\ per\ cell\ event\ (fg) = \frac{PA}{slope} = \frac{43}{17.87} = 2.41 \text{ fg}$$

Figure SI1. 1 Step-by-step transformation of the intensity registered for the cell event shown in Panel A into As mass. This was achieved by summing the intensities of all 4 cell event points and converting their sum into As mass. This conversion was based on the ionic As mass flux calibration shown in Panel B. Numerical values and calculations are given below the two panels.

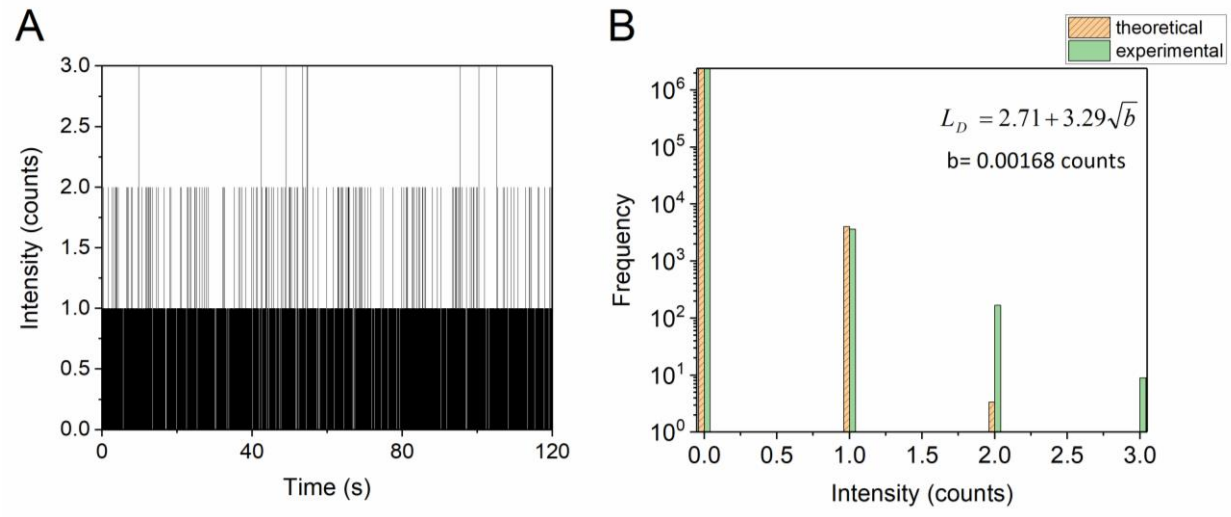

Figure SI1. 2 Time Resolved Acquisition (TRA) of $^{75}As^{+}$ for control C. reinhardtii cell suspension for 120 s acquisition, B) Comparison of the plotted as histogram ^{75}As intensity (experimental) with the corresponding (theoretical) Poisson distribution with a mean value b of 0.00168.

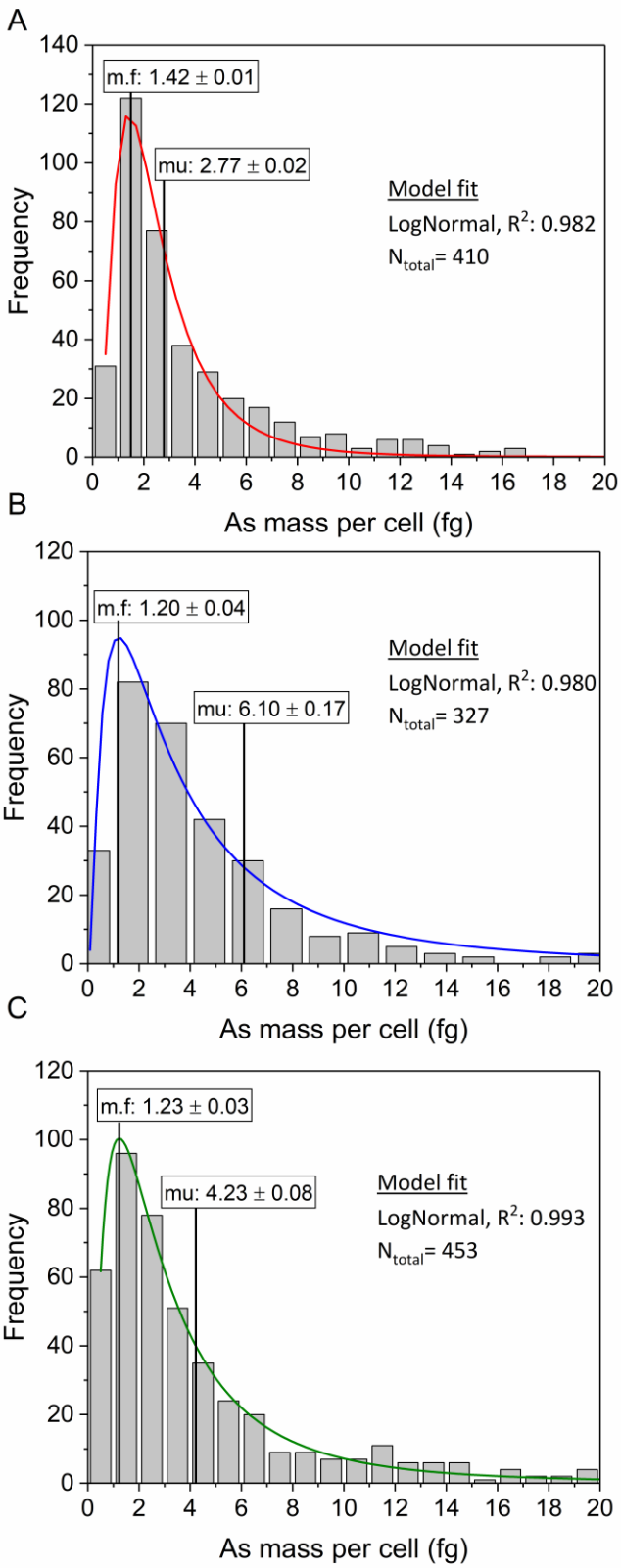

Figure SI1. 3 As mass distribution histograms for unwashed C. reinhardtii cells grown in 15 (A), 22.5 (B) and 30 µg mL^{-1} As (C); A, C binned at 1 fg and B at 1.5 fg. The lognormal probability function has been fitted to the mass histogram data in all three cases. Values for mu and m.f denote the lognormal mean and most frequently observed As mass per cell, respectively.

Table SI1. 1 Precision indicative data on the 3 independent technical replicates.

Cell Samples	Most Freq. Mass (fg)	Mean Mass (fg)	No. of Peaks	Mean Intensity (counts)	Dissolved Intensity (counts)
Incubated in 15 ppm As Rep. 1	1.96	4.66	97	82.44	3.10E-03
Incubated in 15 ppm As Rep. 2	2.16	4.63	99	81.80	3.03E-03
Incubated in 15 ppm As Rep. 3	2.16	4.27	90	75.38	3.06E-03
Average	2.09	4.52	95.3	79.87	3.06E-03
Stdev	0.12	0.22	4.73	3.91	3.33E-05
stdev%	5.53	4.82	4.96	4.89	1.09
Incubated in 22.5 ppm As Rep. 1	2.36	5.94	120	105.21	4.86E-03
Incubated in 22.5 ppm As Rep. 2	2.46	7.59	137	134.76	5.13E-03
Incubated in 22.5 ppm As Rep. 3	2.46	6.55	95	116.05	5.08E-03
Average	2.42	6.69	117.3	118.67	5.02E-03
Stdev	0.06	0.84	21.13	14.95	1.43E-04
stdev%	2.38	12.49	18.01	12.60	2.85
Incubated in 30 ppm As Rep. 1	2.16	4.46	104	78.78	3.85E-03
Incubated in 30 ppm As Rep. 2	2.31	4.84	83	79.98	3.90E-03
Incubated in 30 ppm As Rep. 3	2.31	4.47	101	74.35	3.91E-03
Average	2.26	4.59	96.0	77.70	3.89E-03
Stdev	0.09	0.21	11.36	2.97	2.90E-05
stdev%	3.84	4.64	11.83	3.82	0.75

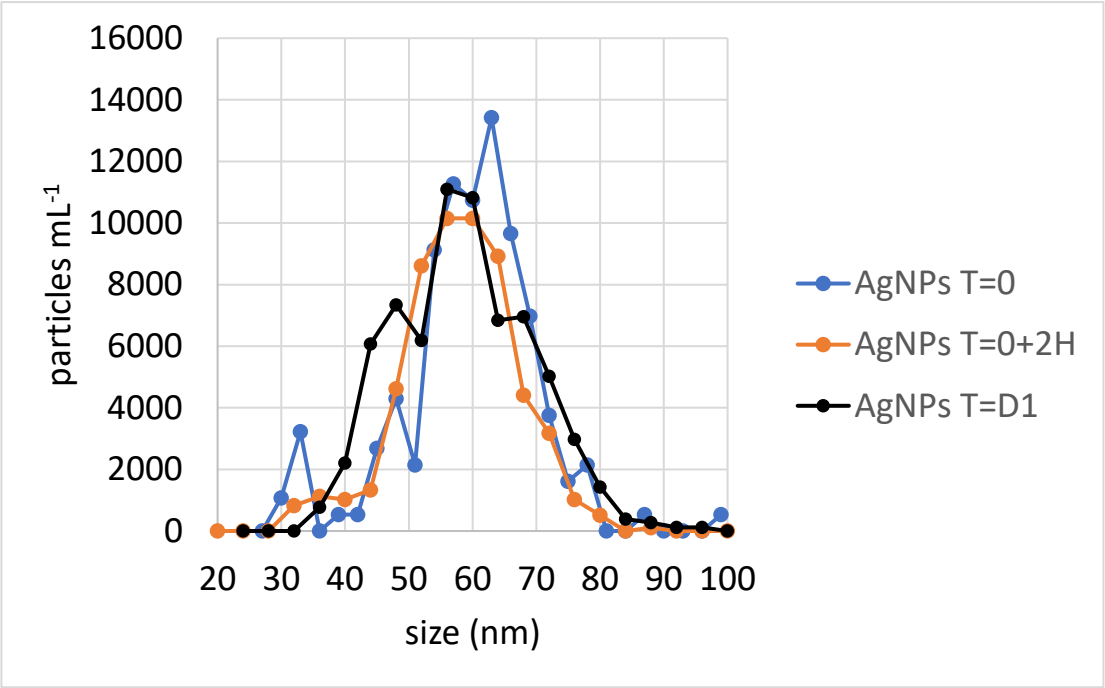

Figure SI1. 4 Silver nanoparticles (AgNPs) size distributions corresponding to a AgNP seawater suspension analyzed directly after spiking (AgNPs T=0-blue curve), a AgNP treated mesocosm tank analyzed 2 hours after spiking (AgNPs T=0+2H-orange curve), and a AgNP treated mesocosm tank analyzed 1 day after spiking (AgNPs T=D1-black curve). The blue curve was obtained from the analysis of the 60 nm Ag NPs nanoComposix suspension, used as calibrant, at a concentration of 100 ng Ag L-1, while the orange and black curve from the analysis of the three AgNP treated mesocosm tanks (spiked with 50 ng Ag L-1) on D0+2H and D1 mesocosm days, respectively.

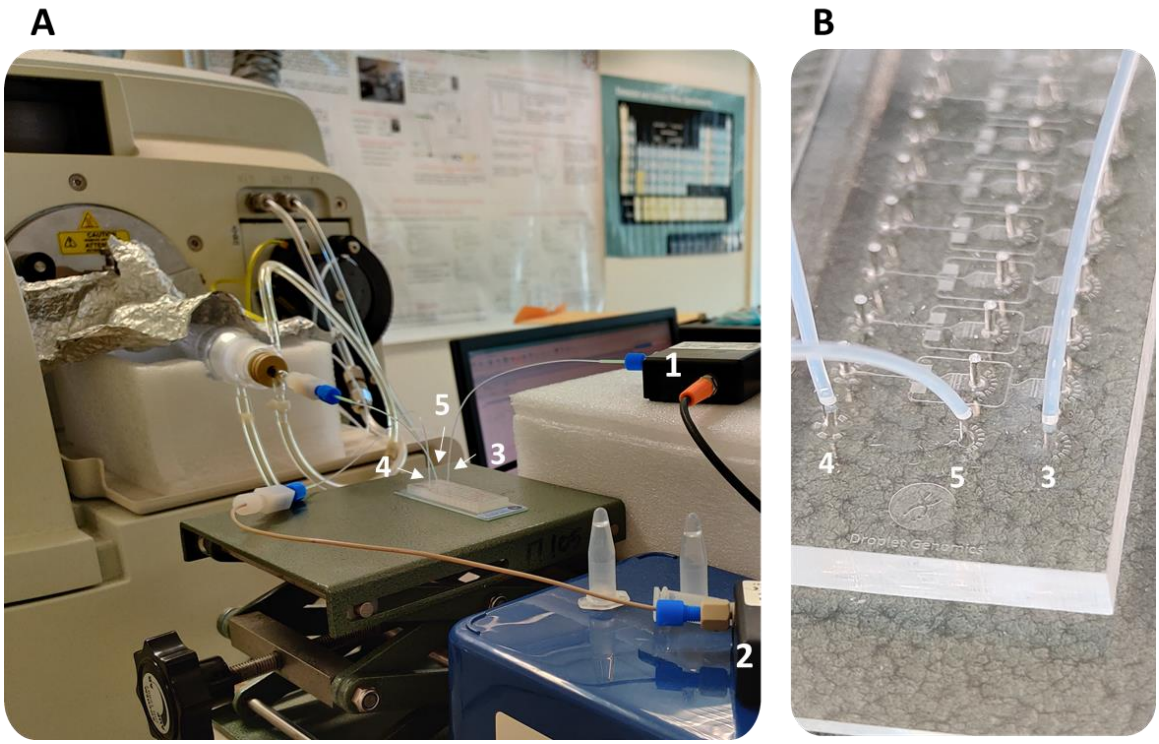

Figure SI1. 5 Photograph of the microfluidic chip coupled online to the ICP-MS. The numbers are representative of the microfluidic connections and include (1) the PrimIS/SecIS flow sensor and its PTFE tubing (0.3 mm i.d.) connecting it to chip inlet (3) shown in detail in panel B, (2) the sample flow sensor connected through PTFE tubing (0.3 mm i.d.) with its respective chip inlet (4) shown in detail in panel (B), and (5) represents the PTFE tubing (0.3 mm i.d.) connecting the chip outlet to the High-Efficiency Nebulizer (Meinhard, HEN) located inside the Asperon^{TM} spray chamber (PerkinElmer). (B) Close-up photograph of the microfluidic chip. Each chip unit contains 10 independent microfluidic systems placed in parallel configuration. One of these microfluidic systems was used in this study, the channels of which are transparent in this photograph because of the water they contain. The channels in the microfluidic systems that are next to it can be seen because they contain air.

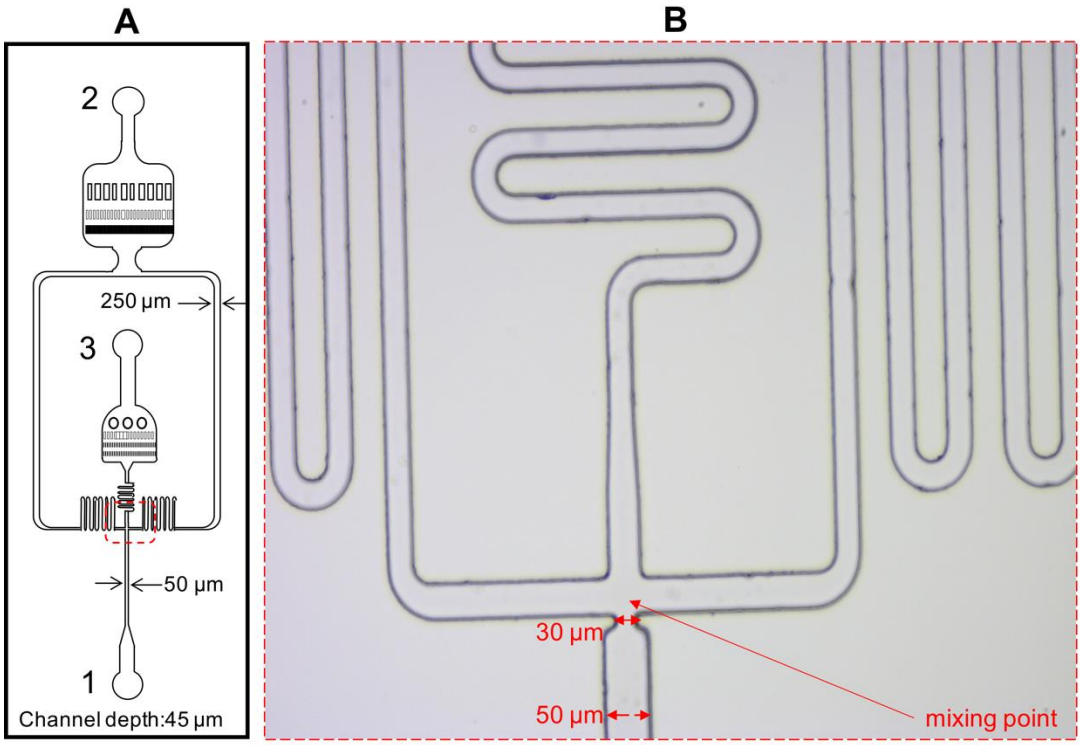

Figure SI1. 6 Representation of the microfluidic chip used throughout this work. The red dashed-line rectangle indicates the intersection where flows from the 2 channels, sample (2) and PrmIS/SecIS (1), start to mix. A closer look at the mixing point and part of the serpentine collection channel (3) is offered in panel (B), which is a picture of the microfluidic chip captured under an optical microscope with a 10X lens.

Table SI1. 2 Operation parameters for microfluidic system, ICP-MS and interface.

ICP-MS	
Collision-cell gas (He)	1.5 mL min^{-1}
Plasma gas	15 L min^{-1}
Auxiliary gas	1.5 L min^{-1}
Isotopes	^{114}Cd, ^{59}Co, ^{207}Pb, ^{208}Pb, ^{52}Cr, ^{53}Cr, ^{58}Ni, ^{60}Ni,
Dwell time	500 ms
Interface	
Nebulizer type	Meinhard HEN-090-A0.2
Chamber type	Asperon^{TM} spray chamber
Nebulizer gas (Ar)	0.18 L min^{-1}
Makeup gas (Ar)	0.6 L min^{-1}
Microfluidic system	
MFS2 flow sensor	7 µL min^{-1}
MFS3 flow sensor	7 µL min^{-1}
Stable or fast (P value)	0.001 /0.001 (MFS2/MFS3)
Smooth or Responsive (I value)	0.005/0.434 (MFS2/MFS3)

*MFS2 was the flow sensor dedicated to the pump channel of the sample solution, whereas MFS3 was dedicated to the pump channel of the two calibration solutions required for SDA, the *PrmIS* or *SecIS* solutions. The P, I values were set to basic for the MFS2 sensor, whereas for the MFS3 were set to Large Reservoir.

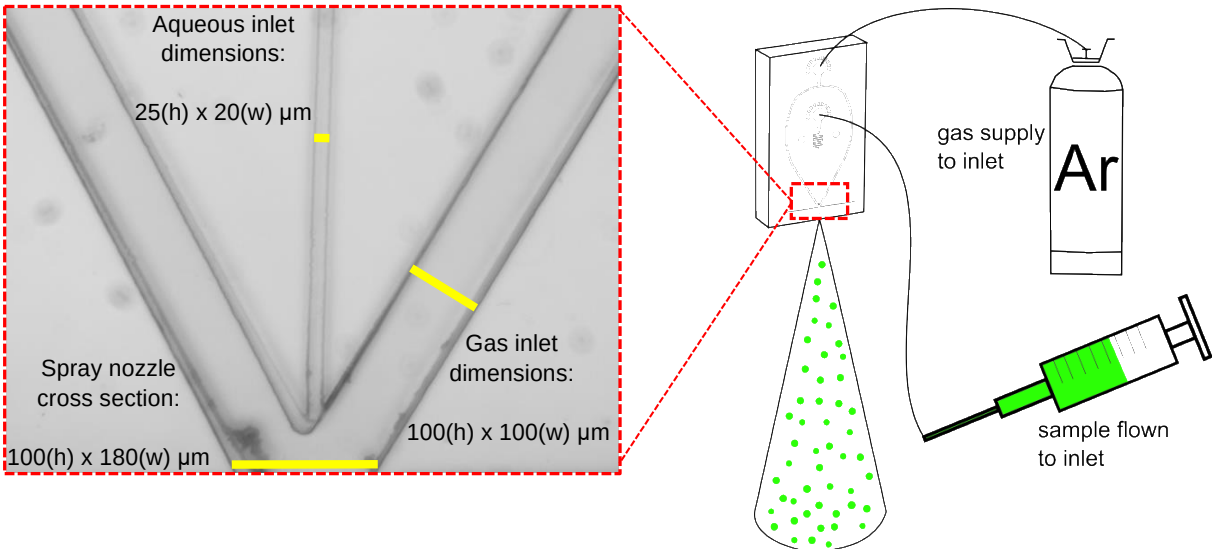

Figure SI1. 7 A graphical illustration (right hand corner) showing how the nebulisation gas and liquid supply lines are connected to the inlets of the chip-µf-Neb in order for it to convert the supplied liquid to a fine aerosol. The inset image (left hand corner) is a micrograph of the chip-µF-Neb, showing the intersection of the gas and liquid channels right before the spray nozzle. Within this micrograph, dimensions are provided for the cross-section (height (h)× width (w)) of the gas and aqueous inlet channels, as well as for the nozzle.

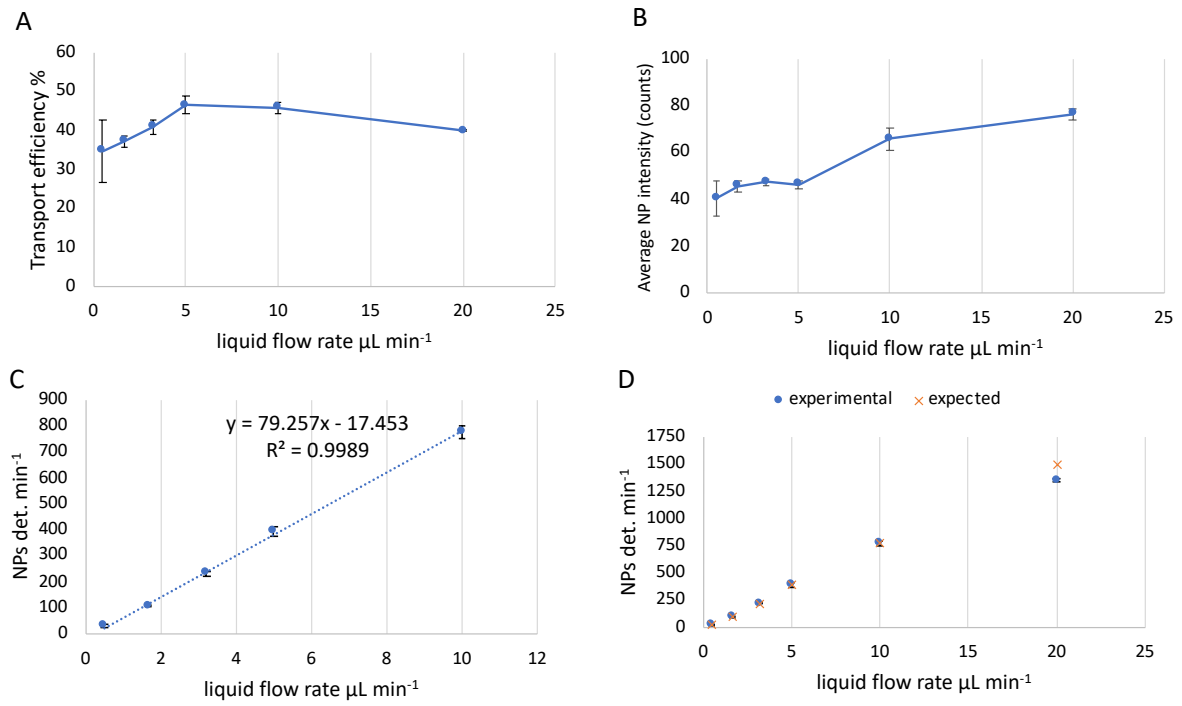

Figure SI1. 8 The graphs in panels A and B demonstrate the obtained transport efficiency (%) and average NP intensity as a function of the liquid flow rate accross the range of 0.5-20.0 µL min^{-1}. The graph in panel C illustrates the range of liquid flow rates (0.5-10 µL min^{-1}) at which the number of NPs detected per min increase linearly, while the graph in panel D extends the range of liquid flow rates up to 20 µL min^{-1} and shows how the experimental number of NPs detected per min deviates from the expected value at the liquid flow rate of 20 µL min^{-1}. Error bars correspond to average values resulting from 4×1 min ICP-MS acquisitions in single particle mode with a dwell time of 10 ms.

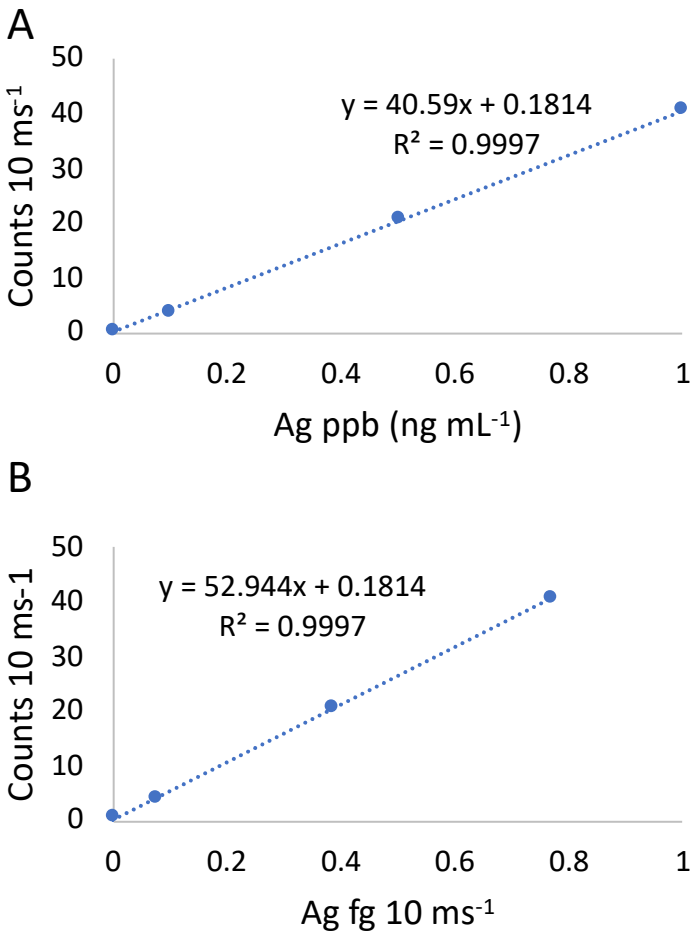

Figure SI1. 9 Panel A shows the ^{107}Ag calibration curve resulted from the introduction of dissolved Ag standard solutions accross the concentration range of 0.1-1 ppb (ng mL^{-1}). Panel B shows the mass flux calibration curve resulting from panel A by converting from concentration units (ng mL^{-1}) to the absolute mass Ag introduced per dwell time (fg 10 ms^{-1}).

Table SI1. 3 Operation parameters for microfluidic system, ICP-MS and interface.

ICP-MS (for dissolved solutions)	
Plasma gas	15 L min^{-1}
Auxiliary gas	1.5 L min^{-1}
Isotopes	^{115}In, ^{140}Ce, ^{156}CeO
Dwell time	100 ms
ICP-MS (for single-particle and single-cell analysis)	
O_2 gas (DRC mode) (for single-cell detection)	1.25 mL min^{-1}
Plasma gas	15 L min^{-1}
Auxiliary gas	1.5 L min^{-1}
Isotopes	^{107}Ag, ^{80}Se
Dwell time	10 ms
chip-µf-Neb interface	
Spray chamber type	Asperon™ spray chamber
Nebulisation gas (Ar)	1.5 L min^{-1}
Makeup gas (Ar)	0.5 L min^{-1}

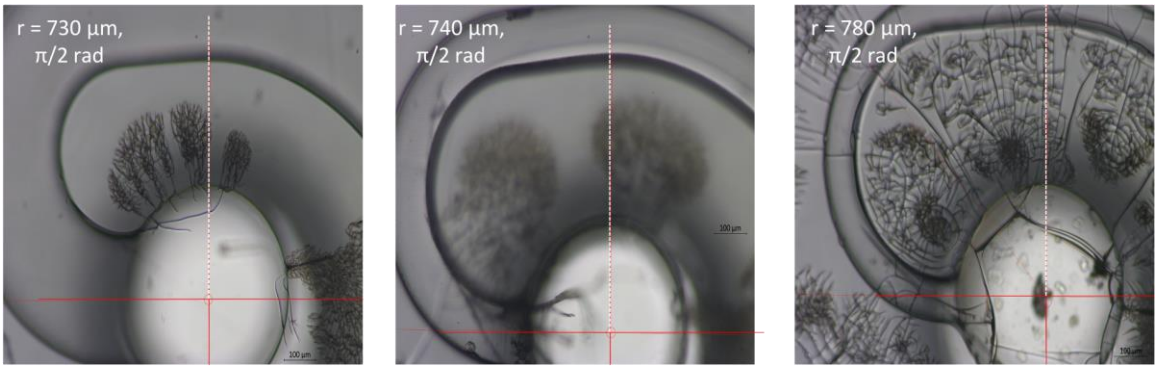

Figure SI1. 10 Micrographs depicting the initial rotation of the spiral from the point of origin to the angle of π/2 rad for spiral chips 1, 2, and 3 from left to right.

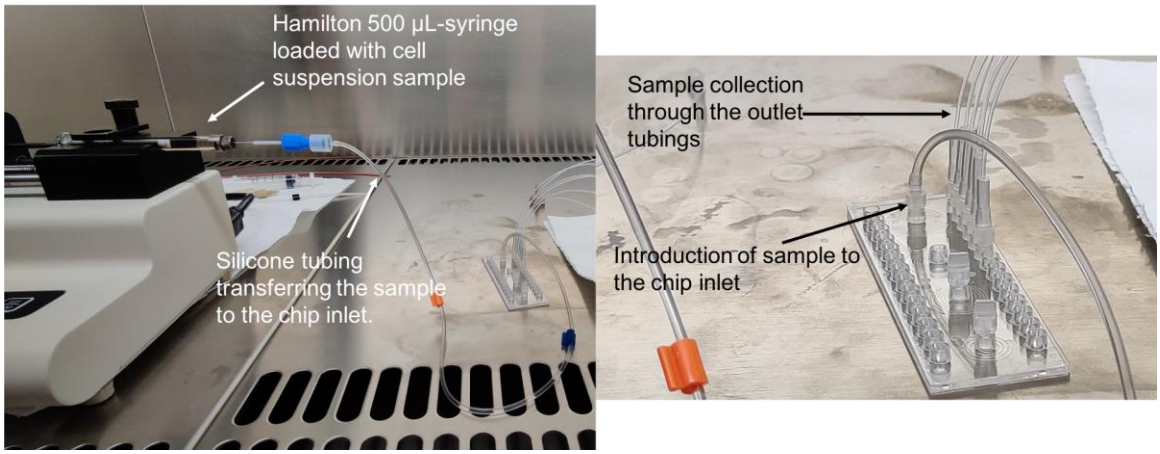

Figure SI1. 11 Liquid connections of the low flow setup

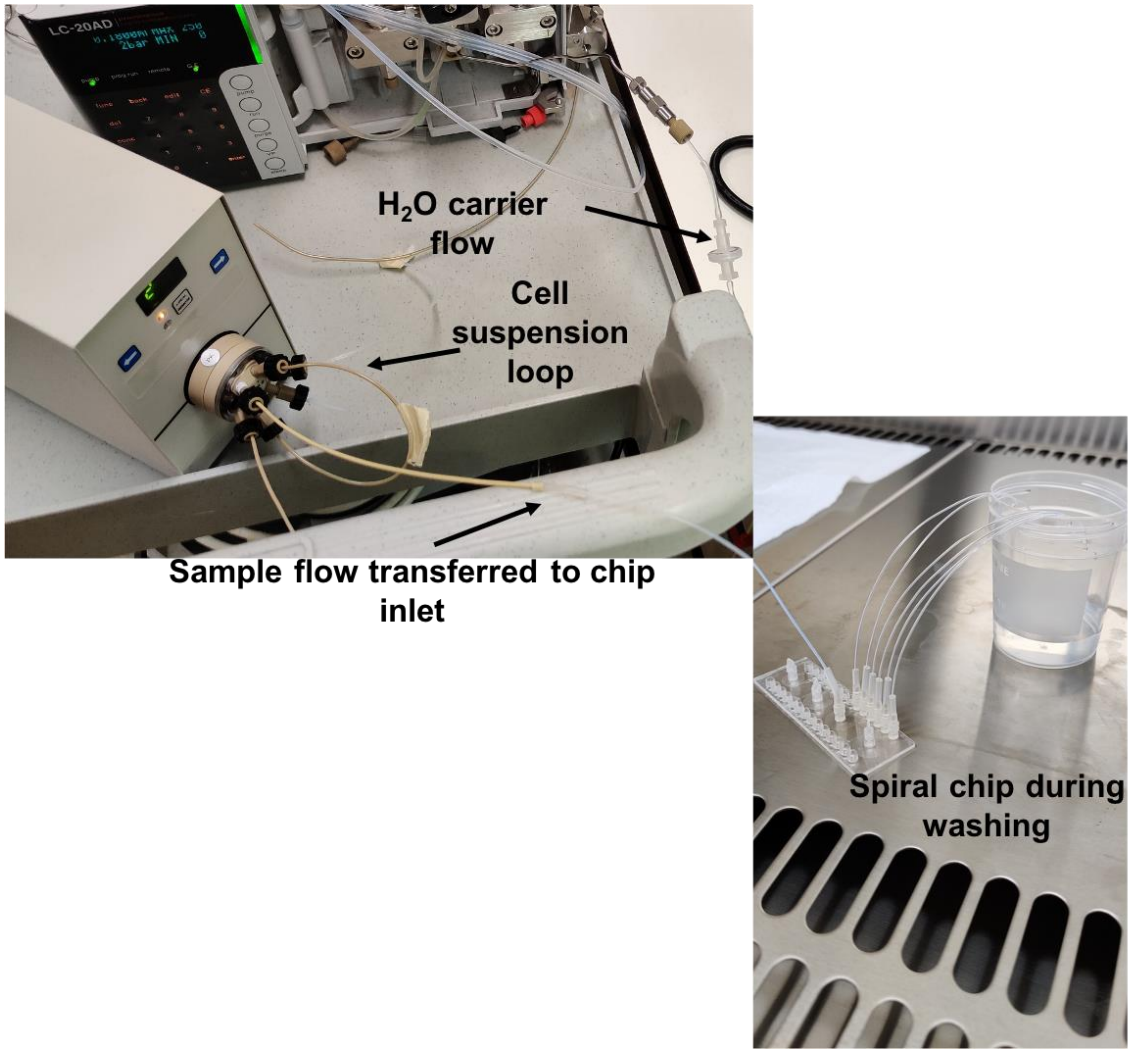

Figure SI1. 12 Liquid connections of the high flow setup, as configured in the lab.

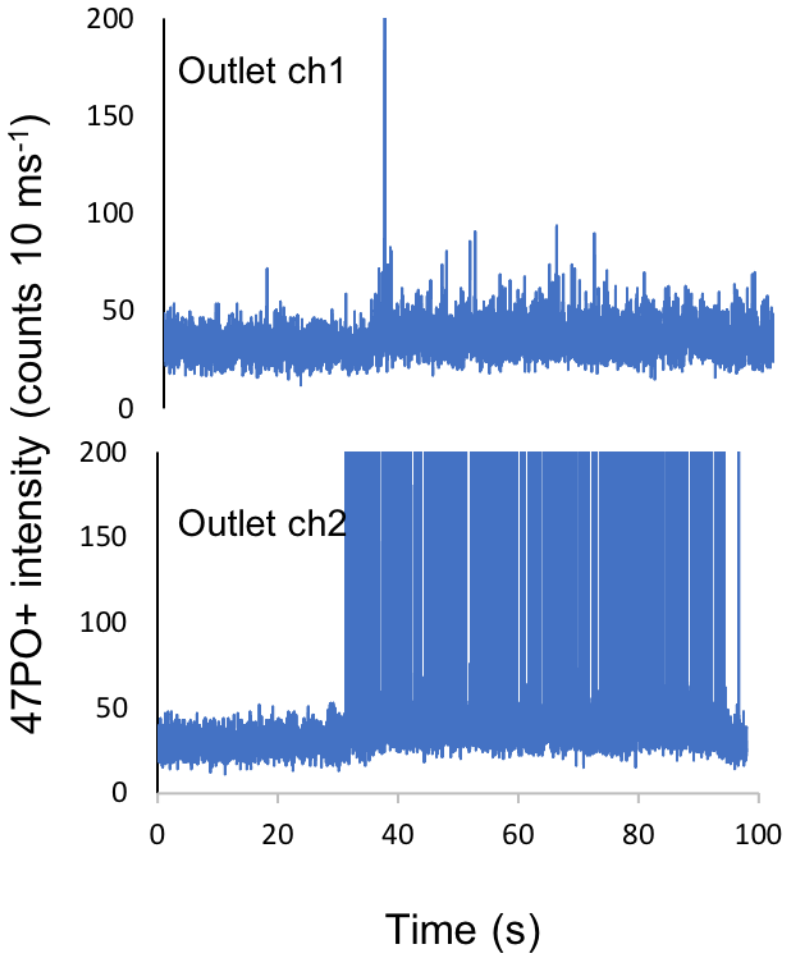

Figure SI1. 13 Time-resolved analysis of outlet channel 1 and 2, with a close up view of the time region of 0-40 s (outlet ch2) in order to show the signal from the introduction of a 0.1% NaCl solution. From 40-100 s, the signal rises due to the arrival of the cells.

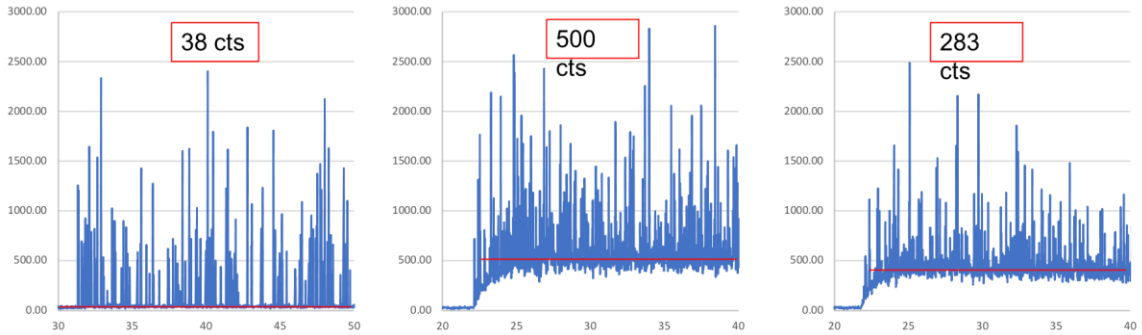

Figure SI1. 14 Background signals observed from the analysis of cell enriched outlet channels for cells sorted on chip 1 at 11.2, 69.9, and 93.2 De, from left to right, respectively.

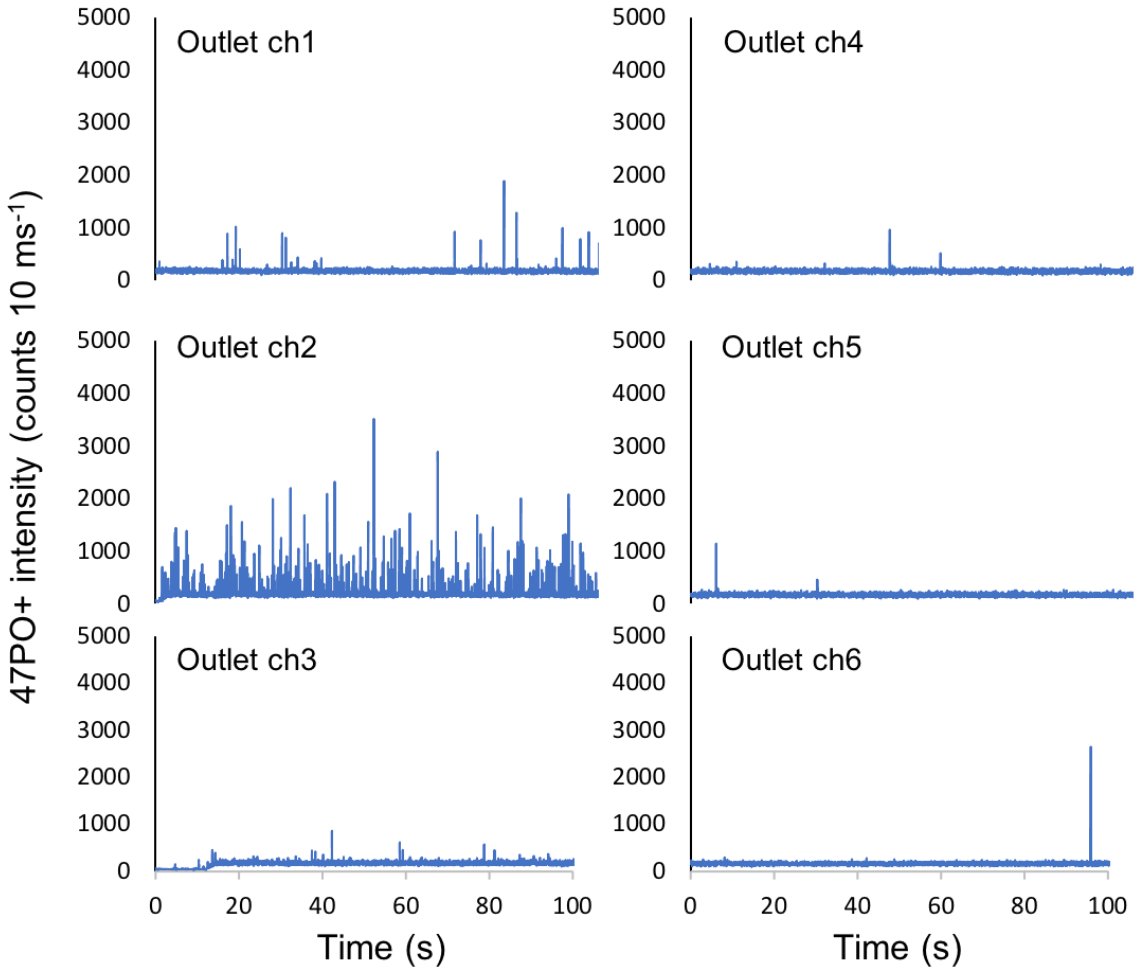

Figure SI1. 15 Time-resolved acquisitions that were obtained from SC ICP-MS analysis of samples collected from outlet channels 1-6 (ch1-ch6) after a *C. reinhardtii* cell suspension, containing 10^5 cells mL^{-1}, was introduced into chip 2 at input flow rate (Q) of 150 (10.2 De).

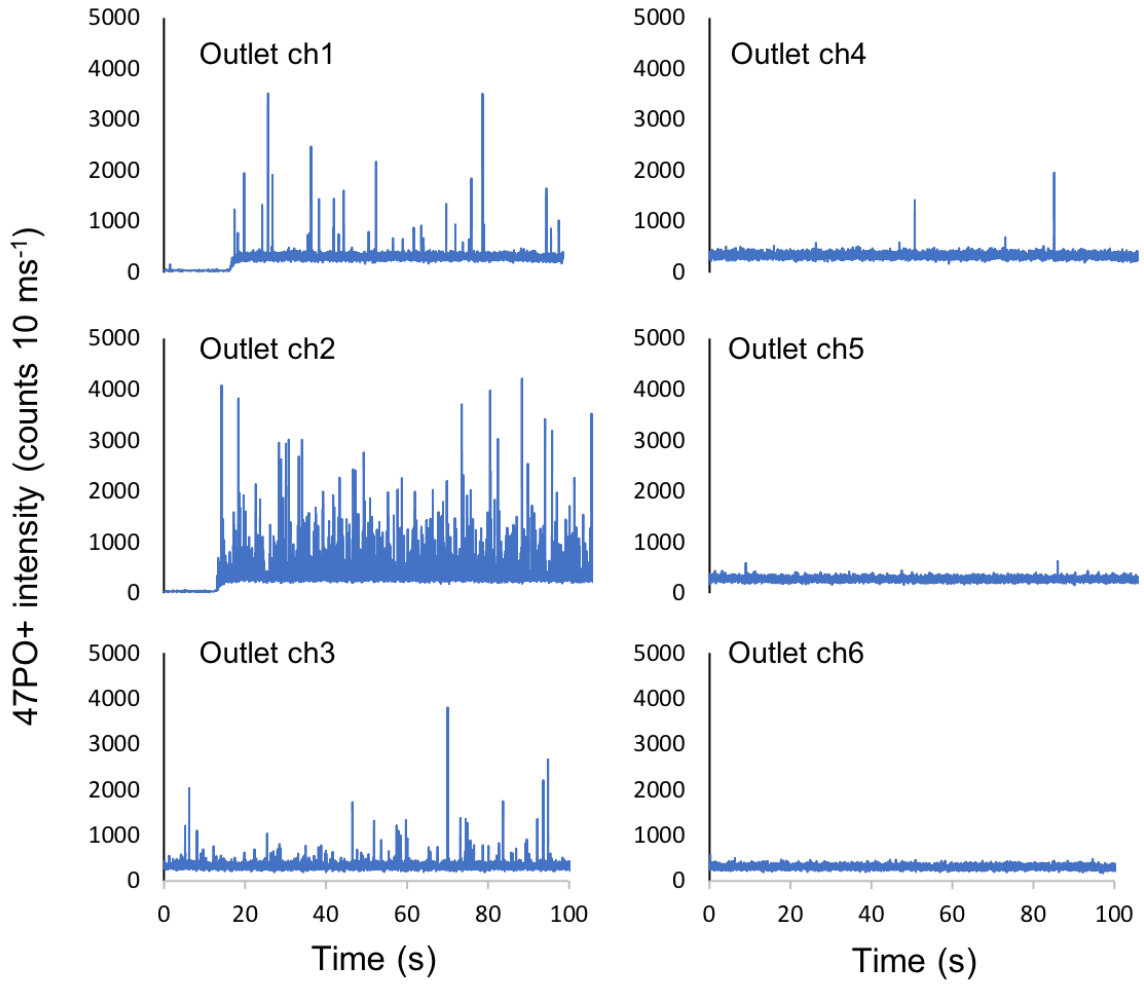

Figure SI1. 16 Time-resolved acquisitions that were obtained from SC ICP-MS analysis of samples collected from outlet channels 1-6 (ch1-ch6) after a *C. reinhardtii* cell suspension, containing 10^5 cells mL^{-1}, was introduced into chip 2 at input flow rate (Q) of 250 µL min^{-1} (17.0 De)

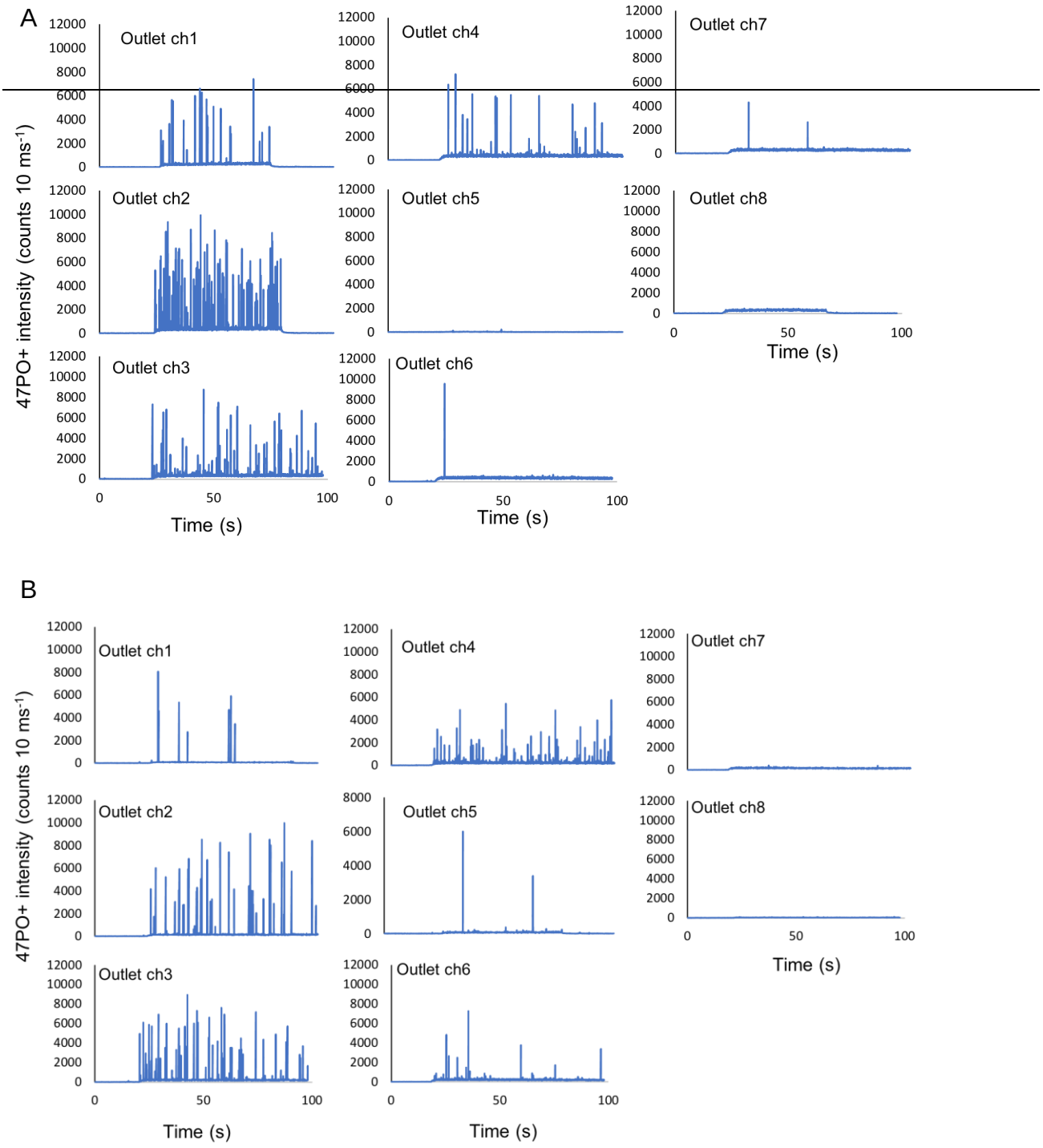

Figure SI1. 17 Time-resolved acquisitions that were obtained from SC ICP-MS analysis of samples collected from outlet channels 1-6 (ch1-ch6) after a BDMS cell suspension, containing 4×10^5 cells mL^{-1}, was introduced into chip 1 at input flow rate (Q) of 250 µL min^{-1} (11.6 De) (A) and (B) 1500 µL min^{-1} (69.9 De)

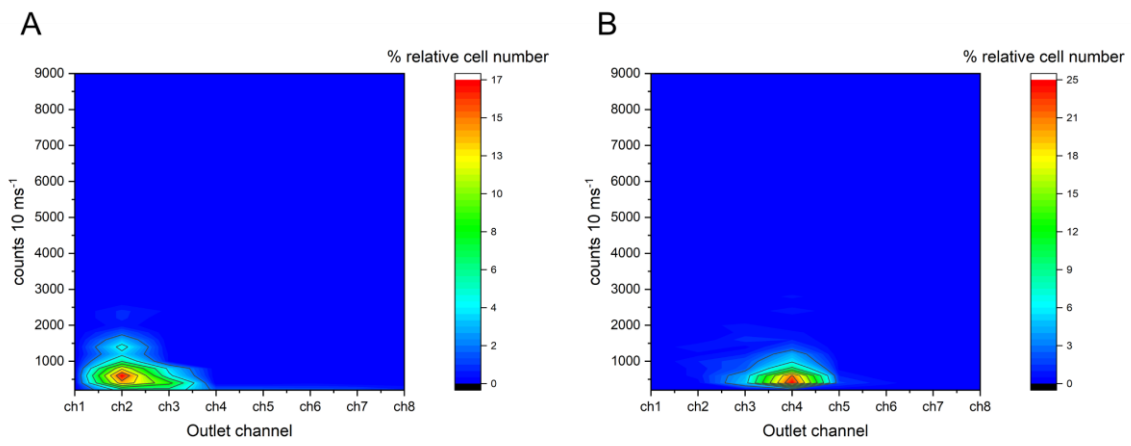

Figure SI1. 18 Contour plots illustrating the distribution of *C. reinhardtii* cells with respect to their recorded $^{47}PO^{+}$ intensity across outlet channels 1-8 of spiral chip 1, operated at chip input flow rates of 250 (A) and 1500 (B) µL min^{-1} (corresponding to 11.6 and 69.9 De, respectively).

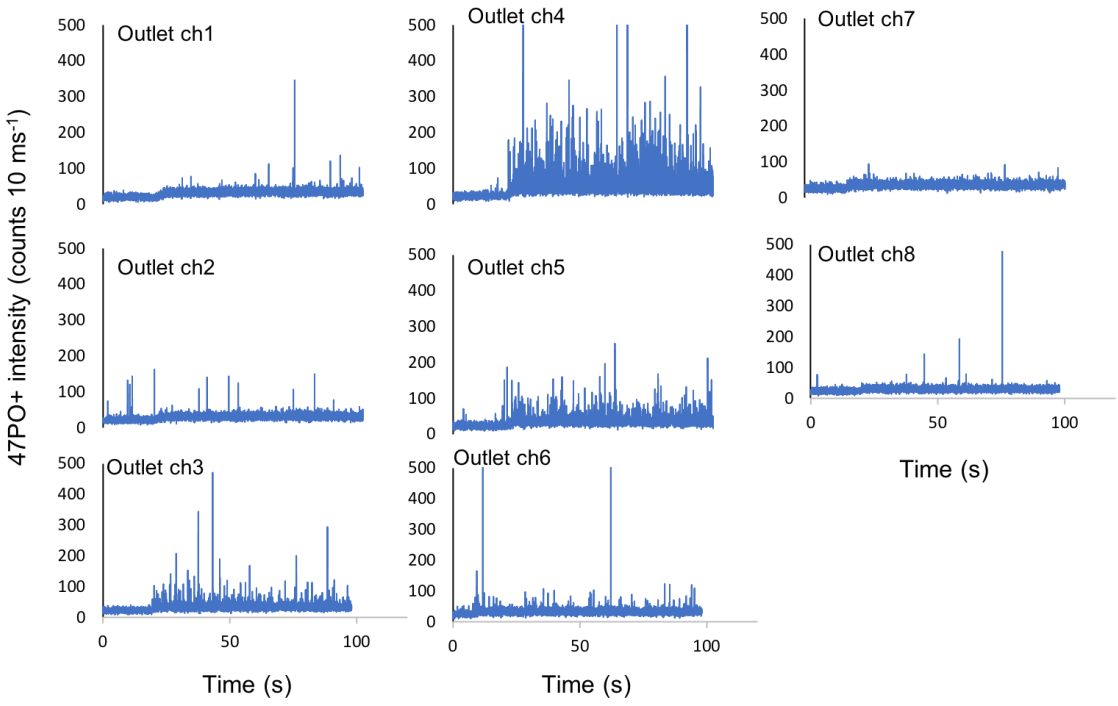

Figure SI1. 19 Time-resolved acquisitions of *Chlorela sorokiniana* cell populations at a concentration of 10^5 cells mL^{-1}, sorted on chip1 at 1500 or 2000 µL min^{-1}, corresponding to 69.9 and 93.2 De, respectively.

9 Supporting Information 2

Peer-reviewed publications

Chapter 2. Investigating the Uptake of Arsenate by *Chlamydomonas reinhardtii* Cells using Single Cell ICP-MS

Investigating the Uptake of Arsenate by Chlamydomonas reinhardtii Cells and its Effect on their Lipid Profile using Single Cell ICP−MS and Easy Ambient Sonic-Spray Ionization−MS, Anal. Chem. 2019, 91, 9590−9598, doi: http://dx.doi.org/10.1021/acs.analchem.9b00917

Chapter 3. Development of data processing for µs-sp-ICP-MS

“Investigating the Behavior of Ultratrace Levels of Nanoparticulate and Ionic Silver in a Seawater Mesocosm Using Single Particle Inductively Coupled Plasma – Mass Spectrometry” Currently under peer-review in Chemosphere (May 2023)

Chapter 4. Chip-based Microfluidics On-line with Inductively Coupled Plasma - Mass Spectrometry for Standard Dilution Analysis

“Chip-based microfluidics on-line with inductively coupled plasma - mass spectrometry for standard dilution analysis”, Analytica Chimica Acta 1179 (2021) 338830, https://doi.org/10.1016/j.aca.2021.338830

Chapter 5. A chip-based supersonic microfluidic nebulizer for efficient sample introduction into Inductively Coupled Plasma – Mass Spectrometry Introduction

A chip-based supersonic microfluidic nebulizer for efficient sample introduction into inductively coupled plasma – Mass spectrometry”, Analytica Chimica Acta 1229 (2022) 340342, https://doi.org/10.1016/j.aca.2022.340342

10 CURRICULUM VITAE

Emmanouil (Manos) Mavrakis

Date of birth	28/05/1993
Place of birth	Heraklion, Crete, Greece
e-mail	mavr.manos@gmail.com

Education

Feb. 2018 - April 2023	Ph.D. Degree in Chemistry (supervisor Prof. Spiros Pergantis)
Oct. 2015 – Feb. 2018	M.Sc. Degree in Chemistry (supervisor Prof. Spiros Pergantis) with specialization in Analytical Chemistry, University of Crete, Greece
Sept. 2011 – July 2015	B.Sc. Degree in Chemistry, University of Crete, Greece

Publications in peer-reviewed journals

Investigating the Behavior of Ultratrace Levels of Nanoparticulate and Ionic Silver in a Seawater Mesocosm Using Single Particle Inductively Coupled Plasma – Mass Spectrometry, M. Chronakis, **E. Mavrakis**, R. Álvarez García, M. Montes-Bayón, J. Bettmer, P. Pitta, E. Tsapakis, I. Kalantzi, A. Tsiola, S. A. Pergantis, prepared for submission in the Science of Total Environment (submitted in Chemosphere-currently under peer review)

A chip-based supersonic microfluidic nebulizer for efficient sample introduction into inductively coupled plasma – Mass spectrometry, **E. Mavrakis**, Z. Toprakcioglu, N. Lydakis-Simantiris, T.P.J. Knowles, S.A. Pergantis, *Analytica Chimica Acta.* 2022, 1229, 340342. https://doi.org/10.1016/j.aca.2022.340342

Gold nanoclusters as elemental label for the sequential quantification of apolipoprotein E and metallothionein 2A in individual human cells of the retinal pigment epithelium using single cell-ICP-MS, A. Lores-Padín, **E. Mavrakis**, B. Fernández, M. García, H. González-Iglesias, R. Pereiro, Spiros A. Pergantis, *Analytica Chimica Acta*. 2022, 1203, 339701. https://doi.org/10.1016/j.talanta.2020.121489

Chip-based microfluidics on-line with inductively coupled plasma - mass spectrometry for standard dilution analysis, **E. Mavrakis**, S. Pergantis, *Analytica Chimica Acta*. 2021, 1179, 338830. https://doi.org/10.1016/j.aca.2021.338830

Versatile Dual-Inlet Sample Introduction System for Multi-Mode Single Particle Inductively Coupled Plasma Mass Spectrometry Analysis and Validation, D. Rosenkranz, F. Kriegel, **E. Mavrakis**, S. Pergantis, P. Reichardt, J. Tentschert, N. Jakubowski, P. Laux, U. Panne, *J Vis Exp.* 2020, 163. https://doi.org/10.3791/61653.

Improved Validation for Single Particle ICP-MS Analysis Using a Pneumatic Nebulizer / Microdroplet Generator Sample Introduction System for Multi-mode Nanoparticle

Determination, D. Rosenkranz, F. Kriegel, **E. Mavrakis**, S. Pergantis, P. Reichardt, J. Tentschert, N. Jakubowski, P. Laux, U. Panne, A. Luch, *Analytica Chimica Acta*. 2020, 1099, 16-25. https://doi.org/10.1016/j.aca.2019.11.043

Investigating the Uptake of Arsenate by *Chlamydomonas reinhardtii* Cells and its Effect on their Lipid Profile using Single Cell ICP- MS and Easy Ambient Sonic-Spray Ionization – MS, **E. Mavrakis**, L. Mavroudakis, N. Lydakis-Simantiris, S. Pergantis, *Anal. Chem.* 2019, 91, 15, 9590-9598. https://pubs.acs.org/doi/abs/10.1021/acs.analchem.9b00917

Determination of chlorate, perchlorate and bromate anions in water samples by microbore reversed-phase liquid chromatography coupled to sonic-spray ionization mass spectrometry, L. Mavroudakis, **E. Mavrakis**, A. Kouvarakis and S. Pergantis, *Rapid Commun. Mass Spectrom.* 2017, 31, 911–918. https://doi.org/10.1002/rcm.7866

Conference presentations

(the underline indicates the presenter)

'Advances in Single Cell ICP-MS via Chip-Based Microfluidics for Cell Sorting and Nebulization', **E. Mavrakis,** E. Zkeri, N. Lydakis-Simantiris, Z. Toprakcioglu, T. P. J. Knowles, S. Pergantis, oral presentation: 2022 Conference on Plasma Spectrochemistry, January 16-22, 2022, Tucson, Arizona

'Selenate uptake by *Chlamydomonas reinhardtii* Algal Cells, its Transformation and its Effect on Membrane Lipid Profiles', **E. Mavrakis**, G. Panagou, S. Grafanaki, E. Zkeri, S. Pergantis, N. Lydakis-Simantiris, oral presentation: 17th International Conference on Environmental Science & Technology, September 01-04, 2021, Athens, Greece

'Advancements and challenges for the determination of metals in individual cells using single cell inductively coupled plasma - mass spectrometry', **E. Mavrakis**, N. Lydakis-Simantiris, S. Pergantis, oral presentation: 11th International Conference on Instrumental Methods of Analysis, September 22-25, 2019, Ioannina, Greece

"Application of single particle inductively coupled plasma-mass spectrometry for the detection and characterization of metal containing nanoparticles in seawater samples", M.I. Chronakis, **E. Mavrakis**, S. Pergantis, R.Á. Fernández García, M. Montes - Bayón, J. Bettmer, A. Tsiola, A. Gondikas, M. Tsapakis, poster presentation: 11th International Conference on Instrumental Methods of Analysis, September 22-25, 2019, Ioannina, Greece

"Investigating the Uptake of Arsenate by *Chlamydomonas reinhardtii* Cells and its Effect on their Lipid Profile using Single Cell ICP-MS and Easy Ambient Sonic-Spray Ionization – MS", **E. Mavrakis**, L. Mavroudakis, N. Lydakis-Simantiris, S. Pergantis, oral presentation: BAM-BfR Seminar 2019 (Scientific exchange between BAM and Department „Chemical and Product Safety" of BfR), March 21st, Berlin, Germany

"Investigating arsenate uptake in *C. reinhardtii* cells using Single Cell ICP-MS and its effect on lipid remodelling using ambient MS '', **E. Mavrakis**, L. Mavroudakis, N. Lydakis-Simantiris, S. Pergantis, oral presentation: European Winter Conference on Plasma Spectrochemistry, February 3-8, 2019, Pau, France

“Determination of heavy metal (Cd & As species) uptake by *Chlamydomonas reinhardtii* cells by means of Single-Cell ICP-MS using Conventional and High Efficiency Introduction Systems”, **E. Mavrakis**, N. Lydakis-Simantiris, S. Pergantis, poster presentation: 11th Aegean Analytical Chemistry Days, September 25-29, Chania, Crete, Greece

‘’Investigating heavy metal (Pb and As species) uptake by *Chlamydomonas reinhardtii* cells by means of Single-Cell ICP-MS’’, **E. Mavrakis**, N. Lydakis-Simantiris, C. Stephan, R. Magarini, S. Pergantis, poster presentation: 10th International Conference on Instrumental Methods of Analysis, Modern Trends and Applications, September 17-21, 2017, Heraklion, Crete

‘’Arsenic accumulation in *Chlamydomonas reinhardtii* cells grown in As-contaminated media’’, **E. Mavrakis**, L. Sakelaraki, M. Gaulier, A. Riaudel, S. Pergantis, N. Lydakis-Simantiris, oral presentation: 15**th** International Conference on Environmental Science And Technology, August 31-September 2, 2017, Rhodes, Greece

“Advances in single-cell ICP-MS for determining elemental distributions in cell populations”, **E. Mavrakis**, N. Lydakis-Symantiris, C. Stephan, R. Magarini, S. Pergantis, oral presentation: European Winter Conference on Plasma Spectrochemistry, February 19-24, 2017, St Anton, Austria

‘’Determination of Lead (Pb) distribution in individual *Chlamydomonas reinhardtii* cells by means of Single-Cell ICP-MS’’, **E. Mavrakis**, N. Lydakis-Simantiris, C. Stephan, R. Magarini, S. Pergantis, poster presentation: European Winter Conference on Plasma Spectrochemistry, February 19-24, 2017, St Anton, Austria

‘’Paired-Ion Sonic-Spray Ionization Mass Spectrometry (PI-SSI-MS) for the analysis of anions: Progress towards even lower limits of detection’’, **E. Mavrakis**, L. Mavroudakis, S. Pergantis, poster presentation: 64th American Society for Mass Spectrometry Conference, June 5-9, 2016, San Antonio, TX

“Evaluation of Sonic Spray Mass Spectrometry for Proteomics Analysis”, S.Pergantis, K. Kanaki and **E. Mavrakis**, poster presentation: 63RD ASMS Conference on Mass Spectrometry and Allied Topics, May 31-June 4 , 2015, St. Louis, Missouri, USA

Other publications

Monitoring the Fate of Silver Nanoparticles in Seawater Using Single Particle ICP-MS, M.I. Chronakis, **E. Mavrakis**, S. Pergantis, R.Á. Fernández García, Chady Stephan, Application Note, Perkin Elmer Inc. Woodbridge, ON, Canada

Acting reviewer for peer-reviewed journals

Metallomics by OXFORD ACADEMIC

Workshops/Seminars

" Analysis of Nano-Particles, Approaches and Applications" organized by ANTISEL (partner of Perkin-Elmer), 2015, Univ. of. Crete.

Participation in “MITOS”, a 2-month educational series of courses on Capacity Building for the commercialization of research and technology (i.e. theoretical practice on affairs of researcher and Technology Transfer Office), organized for phD students and post-docs of Univ. of. Crete, September-November 2020

Certificates on foreign languages

2009 Proficiency in English, University of Michigan
2009 Proficiency in English, University of Cambridge

Awards/Scholarships

2022-2023 12-month scholarship granted by the Greek States Scholarships Foundation (IKY) in the context of the Act “Enhancing Human Resources Research Potential by undertaking a Doctoral Research” Sub-action 2: IKY Scholarship Programme for PhD candidates in the Greek Universities»

2020-2021 “Maria Michail Manasaki” bequest Fellowship awarded by the Dept. of. Chemistry for demonstrated excellence in academic progress.

2019 Monetary award conferred by the Dept. of Chemistry, Univ. of Crete for demonstrated excellence in academic progress. The conference was held within the Dept. of Chemistry in memory of Maria Hatzimarinaki, an excellent student of the Dept. of Chemistry.

2019 Student grant awarded by the scientific committee of the European Winter Conference on Plasma Spectrochemistry, 2019, held in Pau, France, for an oral presentation of high-scientific impact. (https://winterplasma19.sciencesconf.org/resource/page/id/33.html).

2018 Werner Baltes Fellowship- 3 month stay as a guest scientist in the Guest Programme of Promoting Talents and Scientific Careers at the Federal Institute for Risk Assessment (BfR), in Berlin.

2009 Monetary award conferred to me by KRIS English Tuition center by virtue of accumulating the highest score in the Cambridge Proficiency examination of all the students in class

Computer competences

- Good command of Microsoft Office (Word, Excel, PowerPoint). Operation of Excel includes writing of Macro procedures in Visual Basic for raw data manipulation.

- Good command of OriginPro
- Good command of Igor Pro (i.e. procedures for integrating multiple peaks, or pulse-type signals relating to Single-particle or Single-cell ICP-MS
- Good command of Syngistix for NeXION 350X or 2000 (ICP-Mass Spectrometers), as well as Syngistix Nano and Single-Cell App Module for determination of single-particles and single-cells.
- Adequate command of Zeiss Axio Lab.A1 optical microscope and Image-J (micrograph post-processing for cell size measurements)
- Adequate command of Xcalibur, software for operating Thermo Mass Spectrometers such as LCQ (ion-trap type), TSQ (triple-quadrupole type) and Q-exactive Plus (Orbitrap) Mass Spectrometers
- Good command of Zoom, MS teams, TeamViewer

Work experience

Throughout my M.Sc and Ph.D. studies, I worked on the deliverables of projects related to metal determination using ICP-MS, as outlined below:

- Multi-elemental determination using ICP-MS on water samples originating from hotel units in Crete in the framework of developing a risk assessment strategy for the presence of Legionella bacteria. ICP-MS sample preparation (acidification, internal standard addition) and analysis of hundreds of samples amongst my main research projects promoted skills such as work-load tolerance and time-organization under stress.
- Multi-elemental determination using ICP-MS in samples of industrial interest such as stretch films and netwraps for crop baling, polymer balls for plastic production or activated-carbon filters. Prior to ICP-MS analysis, solid samples were dissoluted using microwave-assisted acid-digestion.
- Multi-elemental determination in biological samples (including digested fish tissue or cell cultures) or application of HPLC-ICP-MS (size-exclusion chromatography) to quantitate protein-bound metal amounts in lysed cell populations.

Statement of research Interests and objectives

My research goal has been set on developing powerful analytical chemistry methods that will allow for answering pertinent biological questions or overcoming existing analytical challenges related to bioanalysis. In this context, emphasis is put on microfluidic and its pairing with powerful detection methods, including but not limited to mass spectrometry. Granted the heterogeneity of biological populations, it is also of interest to determine biomolecules or elemental content on a per cell basis. As all the above research interests require expanding on multiple disciplines, working and growing in an interdisciplinary environment is highly anticipated and pursued.